TECHNISCHE UNIVERSITÄT MÜNCHEN

Munich School of Engineering

Research group „Control of renewable energy systems“

Dissertation

Synchronous optimal PWM for two-level inverter fed salient-pole synchronous machines in automotive applications

Athina Birda

TECHNISCHE UNIVERSITÄT MÜNCHEN
Munich School of Engineering
Research group „Control of renewable energy systems“

Synchronous optimal PWM for two-level inverter fed salient-pole synchronous machines in automotive applications

Athina Birda

Vollständiger Abdruck der von der Munich School of Engineering der Technischen Universität München zur Erlangung des akademischen Grades eines

Doktor–Ingenieurs (Dr.-Ing.)

genehmigten Dissertation.

Vorsitzender:		Prof. Dr.-Ing. Rolf Witzmann, TUM
Prüfer der Dissertation:	1.	Prof. Dr.-Ing. Christoph M. Hackl, HM
	2.	Prof. Dr. rer. nat. Thomas Hamacher, TUM

Die Dissertation wurde am 18.08.2020 bei der Technischen Universität München eingereicht und durch die Munich School of Engineering am 20.09.2021 angenommen.

Ich erkläre an Eides statt, dass ich die bei der promotionsführenden Einrichtung

Munich School of Engineering

der TUM zur Promotionsprüfung vorgelegte Arbeit mit dem Titel:

Synchronous optimal PWM for two-level inverter fed salient-pole synchronous machines in automotive applications

in Munich School of Engineering unter der Anleitung und Betreuung durch:

Prof. Dr.-Ing. Christoph M. Hackl

ohne sonstige Hilfe erstellt und bei der Abfassung nur die gemäß §6 Abs. 6 und 7 Satz 2 angegebenen Hilfsmittel benutzt habe.

- [x] Ich habe keine Organisation eingeschaltet, die gegen Entgelt Betreuerinnen und Betreuer für die Anfertigung von Dissertationen sucht, oder die mir obliegenden Pflichten hinsichtlich der Prüfungsleistungen für mich ganz oder teilweise erledigt.
- [x] Ich habe die Dissertation in dieser oder ähnlicher Form in keinem anderen Prüfungsverfahren als Prüfungsleistung vorgelegt.
- [ ] Die vollständige Dissertation wurde in ___ veröffentlicht. Die promotionsführende Einrichtung Munich School of Engineering hat der Vorveröffentlichung zugestimmt.
- [x] Ich habe den angestrebten Doktorgrad noch nicht erworben und bin nicht in einem früheren Promotionsverfahren für den angestrebten Doktorgrad endgültig gescheitert.
- [ ] Ich habe bereits am ___ bei der Fakultät für ___ der Hochschule ___ unter Vorlage einer Dissertation mit dem Thema ___ die Zulassung zur Promotion beantragt mit dem Ergebnis: ___

Die öffentlich zugängliche Promotionsordnung der TUM ist mir bekannt, insbesondere habe ich die Bedeutung von §28 (Nichtigkeit der Promotion) und §29 (Entzug des Doktorgrades) zur Kenntnis genommen. Ich bin mir der Konsequenzen einer falschen Eidesstattlichen Erklärung bewusst. Mit der Aufnahme meiner personenbezogenen Daten in die Alumni-Datei bei der TUM bin ich

- [x] einverstanden,
- [ ] nicht einverstanden.

Ort, Datum Unterschrift

This document is typeset with LaTeX/TeX.

Acknowledgements

I want to express my deepest gratitude to my supervisor, Prof. Dr.-Ing. Christoph Hackl, for his continued support, valuable advice and for the confidence he placed in me. I would also like to thank deeply my supervisor at BMW AG, Mr. Jörg Reuss, for his professional support and guidance. Both of them gave me the opportunity to work on the topic that I love and helped me develop a great understanding about the control of power electronics. I truly enjoyed discussing with them about various scientific topics from a theoretical and practical point of view. Furthermore, I had the opportunity to visit many conferences and workshops and exchange ideas with people from academia and industry. For this I would also like to sincerely thank my mentor Prof. Dr.-Ing. Ralph Kennel.

The research involved a lot of measurements that had not been possible without the support of Mr. René Richter, Mr. Johann Obermaier and Mr. Christian Dietrich at BMW AG. I am also grateful to the students whom I supervised for their valuable cooperation. Financial support by the BMW AG is also deeply acknowledged.

Finally, I owe my sincere gratitude to my family for their love, patience and encouragement. None of this would have happened without their continued support.

Munich, March 2020 Athina Birda

Contents

List of Figures

List of Tables

Nomenclature

Symbol	Definition
$\mathbb{N}$	$:= \{1, 2, 3, \dots\}$, natural numbers
$\mathbb{N}_0$	$:= \mathbb{N} \cup \{0\}$, natural numbers included zero
$\mathbb{Z}$	$:= \{\dots, -2, -1, 0, 1, 2, \dots\}$, integers
$\mathbb{R}$	$:= (-\infty, \infty)$, real numbers
$\mathbb{R}_{\geq 0}$	$:= [0, \infty)$, real non-negative numbers
$\mathbb{R}_{>0}$	$:= (0, \infty)$, real positive numbers
$\mathbb{C}$	Set of complex numbers, where $s = x + jy \in \mathbb{C}$ with x, $y \in \mathbb{R}$ and imaginary unit j.
$\Re(s)$	Real part of complex number s
$\Im(s)$	Imaginary part of complex number s
Vectors and Matrices	
$\boldsymbol{x}$	$:= \begin{pmatrix} x_1 \\ \dots \\ x_n \end{pmatrix} \in \mathbb{R}^n$, vector
$\boldsymbol{x}^\top$	$:= \begin{pmatrix} x_1 & \dots & x_n \end{pmatrix}$, transpose of vector $\boldsymbol{x}$
$\boldsymbol{A}$	$:= \begin{bmatrix} a_{11} & \dots & a_{1m} \\ \vdots & & \vdots \\ a_{n1} & \dots & a_{nm} \end{bmatrix} \in \mathbb{R}^{n \times m}$, matrix with real values, $n, m \in \mathbb{N}$
$\boldsymbol{A}^\top$	$:= \begin{bmatrix} a_{11} & \dots & a_{n1} \\ \vdots & & \vdots \\ a_{1m} & \dots & a_{nm} \end{bmatrix} \in \mathbb{R}^{m \times n}$, transpose of matrix $\boldsymbol{A} \in \mathbb{R}^{n \times m}$
$\boldsymbol{A}^{-1}$	inverse of matrix $\boldsymbol{A} \in \mathbb{R}^{n \times m}$
Generic variable usage conventions	
$\widetilde{x}$	normalized value
$\hat{x}$	estimated value
X	phasor

Specific variable usage definitions

Symbol	Meaning	Definition
a_ν, b_ν	Fourier coefficients of each harmonic component ν	V·$\mathbb{R}$
C	dc-link capacitance	F·$\mathbb{R}_{\geq 0}$
c	switching time counter	$\mathbb{N}_0$
d	normalized current harmonic distortion factor	$\mathbb{R}_{\geq 0}$
f_{FPGA}	FPGA clock frequency	Hz·$\mathbb{R}_{\geq 0}$
f_{r}	electrical frequency	Hz·$\mathbb{R}$

Symbol	Meaning	Definition
f_{sw}	inverter switching frequency	$\mathrm{Hz}\cdot\mathbb{R}_{\geq 0}$
i_{c}	dc-link capacitor current	$\mathrm{A}\cdot\mathbb{R}$
i_{inv}	inverter current	$\mathrm{A}\cdot\mathbb{R}$
$\boldsymbol{i}_{\mathrm{s}}^{uvw}$	machine phase currents in the uvw-frame	$\mathrm{A}\cdot\mathbb{R}^3$
$\boldsymbol{i}_{\mathrm{s}}^{k}$	machine phase currents in the dq-frame	$\mathrm{A}\cdot\mathbb{R}^2$
ℓ	number of optimized inverter switching angles	$\mathbb{N}_0$
L	machine leakage inductance	$\mathrm{H}\cdot\mathbb{R}_{\geq 0}$
L_{bat}	inductance of the battery simulator	$\mathrm{H}\cdot\mathbb{R}_{\geq 0}$
L_{s}^{d}, L_{s}^{q}	stator self-inductances in the dq-frame	$\mathrm{H}\cdot\mathbb{R}_{\geq 0}$
m	modulation index	$[0, 4/\pi]$
n	processor model trigger instant	$\mathbb{N}_0$
n_{p}	pole pair number of the machine	$\mathbb{N}$
n_{m}	machine speed	$\mathrm{rpm}\cdot\mathbb{R}$
p	trigger instant for the FPGA inputs	$\mathbb{N}_0$
q	inverter pulse number over an electrical period	$\mathbb{N}_0$
R_{bat}	resistance of the battery simulator	$\Omega\cdot\mathbb{R}_{\geq 0}$
R_{ESR}	dc-link capacitor equivalent series resistance	$\Omega\cdot\mathbb{R}_{\geq 0}$
R_{s}	stator resistance	$\Omega\cdot\mathbb{R}_{\geq 0}$
$\boldsymbol{s}^{uvw}$	inverter gate signals	$\mathbb{R}^3$
t	time	$\mathrm{s}\cdot\mathbb{R}_{\geq 0}$
T	machine torque	$\mathrm{Nm}\cdot\mathbb{R}$
$\boldsymbol{T}_{\mathrm{c}}$	Clarke transformation matrix	$\mathbb{R}^{2\mathrm{x}3}$
$\boldsymbol{T}_{\mathrm{p}}$	Park transformation matrix	$\mathbb{R}^{2\mathrm{x}2}$
u_{bat}	dc voltage produced by the battery simulator	$\mathrm{V}\cdot\mathbb{R}$
u_{dc}	dc-link voltage	$\mathrm{V}\cdot\mathbb{R}$
$\boldsymbol{u}_{\mathrm{o}}^{uvw}$	inverter output voltages relative to the inverter midpoint o	$\mathrm{V}\cdot\mathbb{R}^3$
$\boldsymbol{u}_{\mathrm{s}}^{uvw}$	machine phase voltages in the uvw-frame	$\mathrm{V}\cdot\mathbb{R}^3$
$\boldsymbol{u}_{\mathrm{s}}^{k}$	machine phase voltages in the dq-frame	$\mathrm{V}\cdot\mathbb{R}^2$
Z_{bat}	impedance in the battery simulator and cable	$\mathbb{C}$
Z_{c}	impedance of the dc-link capacitor	$\mathbb{C}$
$\boldsymbol{\alpha}$	optimized inverter switching angles	$\mathrm{rad}\cdot\mathbb{R}_{\geq 0}^{\ell}$
γ	voltage phase angle of the Fourier vectors $\boldsymbol{a}_1$ and $\boldsymbol{b}_1$ in the dq-frame	$\mathrm{rad}\cdot\mathbb{R}$
θ	voltage phase angle in the uvw-frame	$\mathrm{rad}\cdot\mathbb{R}$
θ_{m}	mechanical rotor position	$\mathrm{rad}\cdot\mathbb{R}$
θ_{r}	electrical rotor position	$\mathrm{rad}\cdot\mathbb{R}$
θ_{u}	voltage phase angle in the dq-frame	$\mathrm{rad}\cdot\mathbb{R}$
λ	machine anisotropic factor or saliency ratio	$\mathbb{R}_{\geq 0}$
ν	harmonic order	$\mathbb{N}$
σ	current harmonic distortion factor (objective function of the optimization problem)	$\mathbb{R}_{\geq}0$
ϕ_0	initial electrical rotor position	$\mathrm{rad}\cdot\mathbb{R}$
ψ_{PM}	PM flux linkage	$\mathrm{Wb}\cdot\mathbb{R}$
ω_{m}	mechanical angular velocity	$\frac{\mathrm{rad}}{\mathrm{s}}\cdot\mathbb{R}$
ω_{r}	electrical angular velocity	$\frac{\mathrm{rad}}{\mathrm{s}}\cdot\mathbb{R}$
ω_{u}	angular velocity of the machine voltage vector	$\frac{\mathrm{rad}}{\mathrm{s}}\cdot\mathbb{R}$

Further subscripts and superscripts

ac	alternating current
aniso	anisotropic
cor	corrected
d, q	rotor-fixed Cartesian axes
dc	direct current
dev	deviation
dif	difference
DT	dead time
FF	feedforward
h	harmonic content
init	initial
iso	isotropic
k	synchronously rotating dq-frame
max	maximum value
opt	optimal value
PI	proportional integral
PLL	phase-locked loop
PO	percentage overshoot
ref	reference value
RMS	root mean square
SP	sampling point
TAT	turnaround time of the processor model
THD	total harmonic distortion
uvw	stationary uvw-frame
2SP, 4SP	two and four sampling points

Kurzzusammenfassung

In den letzten Jahren haben die Automobilunternehmen stark in die Forschung und Entwicklung von Elektrofahrzeugen investiert. Ihr Hauptziel ist, den Einsatzbereich der Elektrofahrzeuge zu erweitern und gleichzeitig Größe und Kosten der eingesetzten mechanischen und elektrischen Komponenten zu reduzieren. Eine Möglichkeit, dies zu erreichen, besteht darin, ein geeignetes Modulationsverfahren zur Ansteuerung des Wechselrichters zu wählen und damit die Gesamtleistung des Traktionssystems des Elektrofahrzeugs weiter zu optimieren. Die programmierte Pulsweitenmodulation (PWM) ist eine attraktive Wahl, da sie die Reduzierung der Schaltfrequenz des Wechselrichters bei gleichzeitiger Optimierung der Motorverluste ermöglicht. Darüber hinaus kann eine Erhöhung der Spitzenleistung durch die programmierte PWM erreicht werden, da sie den Wechselrichterbetrieb im Übermodulationsbereich bis zur Blockkommutierung ermöglicht.

Die programmierte PWM wurde in den letzten Jahrzehnten umfassend auf die Steuerung von Mittelspannungs-Hochleistungs-Asynchronantrieben untersucht und stellt ein gängiges Modulationsverfahren für elektrische Eisenbahnantriebsumrichter dar. Das Verfahren der optimierten Pulsmuster (engl.: synchronous optimal PWM, SOPWM) ist eine vielversprechende Methode, die zur Kategorie der programmierten PWM gehört. In dieser Arbeit wird das SOPWM-Schema für die Ansteuerung eines Fahrzeugtraktionssystems diskutiert, das aus einem zweistufigen Wechselrichter mit Gleichspannungs-Zwischenkreis und einem permanentmagneterregten Synchronmotor mit hoher betriebspunktabhängiger magnetischer Anisotropie besteht.

Diese Arbeit soll zeigen, dass die anisotropen Eigenschaften der Maschine die Qualität der Stromverzerrung der Maschine beeinflussen und bei der Optimierung der Motorverluste berücksichtigt werden sollten. Um diese Aussage zu belegen, werden analytische Formulierungen der Maschinenphasenströme in Bezug auf die Schaltwinkel des Wechselrichters, den Anisotropiefaktor und der Spannungsphase abgeleitet und ihre Richtigkeit durch Simulationen und Messungen gezeigt.

Der getaktete Wechselrichterbetrieb beeinflusst nicht nur die Motoreffizienz, sondern erzeugt auch eine Stromwelligkeit im Zwischenkreis, die sich auf die Größe und Kosten des Zwischenkreiskondensators auswirkt. Aufgrund des begrenzten Platzes in Elektrofahrzeugen ist die Reduzierung der Größe des Zwischenkreiskondensators von höchster Bedeutung. Der analytische Ausdruck der Stromwelligkeit des Zwischenkreiskondensators wird in dieser Arbeit in Bezug auf die PWM-Schaltwinkel abgeleitet. Auf diese Weise kann der Einfluss unterschiedlicher Pulsmuster auf die Stromwelligkeit des Zwischenkreiskondensators quantifiziert werden.

Nicht zuletzt wird in dieser Arbeit eine einfache Implementierungsmethode vorgeschlagen, die die Integration von SOPWM in ein feldorientiertes Regelungssystem mit geschlossenem Stromregelkreis ermöglicht. Der Grundwellenanteil des Rückkopplungsstroms lässt sich effektiv abschätzen, indem der gemessene Strom zu bestimmten Zeitpunkten abgetastet wird. Diese Methode ist unabhängig von den Lastparametern, und der erforderliche Rechenaufwand kann von einem standardmäßigen industriellen digitalen Signalprozessorsystem bewältigt werden. Experimentelle Ergebnisse bestätigen das ausreichend hohe dynamische Verhalten dieser Methode für Automobilanwendungen.

Abstract

In the recent years, automotive companies invested heavily in the research and development of electric vehicles (EVs). Their major goal is to extend the operational range of EVs and at the same time to reduce size and cost of mechanical and electrical components in EVs. One way to achieve this is by choosing the appropriate modulation scheme for inverter control in order to improve the overall performance of the EV traction system. Programmed pulsewidth modulation (PWM) is an attractive choice since it allows for the reduction of the inverter switching frequency while optimizing the motor power losses. Furthermore, an increase in the peak electrical power can be accomplished by programmed PWM since it enables the inverter operation in the overmodulation region up to six-step mode.

Programmed PWM has been extensively investigated over the last decades for the control of medium voltage high power induction motor drives and is a common modulation scheme for electric railway traction converters. Synchronous optimal PWM (SOPWM) is a very promising method, which belongs to the category of programmed PWM. In this thesis, the SOPWM scheme will be evaluated for the control of an automotive traction system, which consists of a two-level voltage source inverter and an interior permanent magnet synchronous motor with highly motor operating point dependent magnetic anisotropy.

This thesis aspires to demonstrate that the machine anisotropic properties influence the machine current harmonic quality and should be taken into account when optimizing the motor power losses. To prove this statement, analytical formulations of the machine phase currents with respect to the inverter switching angles, machine anisotropic factor and voltage phase angle are derived and their correctness is validated by simulations and measurements.

The inverter operation in switched mode does not only influence the motor efficiency but also generates current ripple in the dc-link, which affects the size and cost of the dc-link capacitor. Due to the limited space available in EVs, the reduction of the dc-link capacitor size is of outmost importance. The analytical expression of the dc-link capacitor current ripple is deduced in this thesis with respect to the PWM switching angles. In this way, the influence of different pulse patterns on the dc-link capacitor current ripple is examined.

Last but not least, a simple implementation method is proposed in this thesis which allows the integration of SOPWM into a field oriented control system with closed-loop current control. The fundamental feedback current is effectively estimated by sampling the measured current at specific points in time. This method is independent of load parameters and the computational effort required is within the capability of a standard industrial digital signal processor system. Experimental results confirm its sufficiently high dynamic performance for automotive applications.

Scientific environment and outcomes

This research was carried out during the years 2016 to 2019 and is the result of a cooperative project between the research group "Control of renewable energy systems" (CRES) at the Technical University of Munich (TUM) and the research department of electrical drives at Bayerische Motoren Werke Aktiengesellschaft (BMW AG). The total number of publications were 4 papers divided into one conference publication and three journal articles. Furthermore, a patent application is submitted to the European Patent Office.

Publications

1. A. Birda, J. Reuss, and C. Hackl, "Synchronous optimal pulse-width modulation with differently modulated waveform symmetry properties for feeding synchronous motor with high magnetic anisotropy," *19th European Conference on Power Electronics and Applications (EPE'17 ECCE Europe)*, Sep. 2017.

2. A. Birda, J. Reuss, and C. M. Hackl, "Simple fundamental current estimation and smooth transition between synchronous optimal PWM and asynchronous SVM," *IEEE Transactions on Industrial Electronics*, vol. 67, no. 8, pp. 6354-6364, Sept. 2019.

3. A. Birda, J. Reuss, and C. Hackl, "Synchronous optimal PWM for synchronous machines with highly operating point dependent magnetic anisotropy," *IEEE Transactions on Industrial Electronics*, Apr. 2020.

4. A. Birda, C. Grabher, C. Hackl, and J. Reuss, "Dc-link capacitor and inverter current ripples in anisotropic synchronous motor drives produced by synchronous optimal PWM," *IEEE Transactions on Industrial Electronics*, Manuscript submitted for publication.

Patent application

1. A. Birda and J. Reuss, "Strommessverfahren für synchrones Steuerverfahren mit geringer Modulationsfrequenz", Patent application EP18206341.2, submitted to European Patent Office on 14.11.2018

Chapter 1

Introduction

1.1 Motivation

As part of the global effort to decrease the dependency on fossil fuels and, thus, reduce the CO_2 emissions, emission reduction targets have been set for vehicles by legislation on national and international level [1]. In order to comply with these regulations, the interest of the automotive industry over the last decades has been focused on the concept of electric mobility. Hybrid electric vehicles (HEVs) can reduce fuel consumption in comparison to conventional vehicles, while battery electric vehicles (BEVs) provide an ultimate solution for sustainable mobility, since the electricity they consume can be generated from a wide range of fossil free and renewable sources.

Nowadays, most major automotive manufacturers make great investments in developing their electrified product portfolio. Still, the limited operational range, mainly influenced by the electrical drive system performance, and increased price of electric vehicles (EVs) remain the most important obstacles for their wide spread [2]. In this light, the primary objectives of the automotive research activity lie on the efficiency enhancement and cost reduction of the electrical drive system. This includes, not only the optimal design of each electric propulsion component - the battery, the electrical machine and the power electronics system - but also the optimal control of the overall electrical system. Most electrical drives are not operated at their energy optimum operating point. Consequently, improvements in the control of electrical drives can still be made.

In electric vehicles, the available dc-link voltage produced by the battery stack should be fully utilized. The maximum inverter output voltage, which is delivered to the electrical machine, depends on the pulsewidth modulation (PWM) strategy [3, 4]. Therefore, the performance of the modulator is primarily determined by its dc-link voltage utilization level. The traditional space vector modulation (SVM), used in EVs nowadays, cannot fully exploit the available dc-link voltage [3, 4]. Subsequently, an alternative modulator has to be implemented, especially in the field-weakening region.

The efficiency of the electrical drive system and thereafter the operating range of electric vehicles can be improved by optimizing the inverter as well as the motor power losses. Interior permanent magnet synchronous motors (IPMSMs) are commonly used in automotive traction systems, since they provide higher efficiency, reliability and power density in comparison to induction motor drives [5,6]. The salient properties of IPMSM further increase the motor performance, due to the additional reluctance torque. Furthermore, the rotor configuration does not have any windings and copper losses on the rotor do not exist. For this reason, the harmonic losses are lower in PMSMs than in induction motors allowing for a motor operation with reduced switching frequencies [7]. A dc-ac voltage source inverter (VSI), usually with insulated-gate bipolar transistors (IGBTs), performs the power conversion in switched mode. The inverter switching

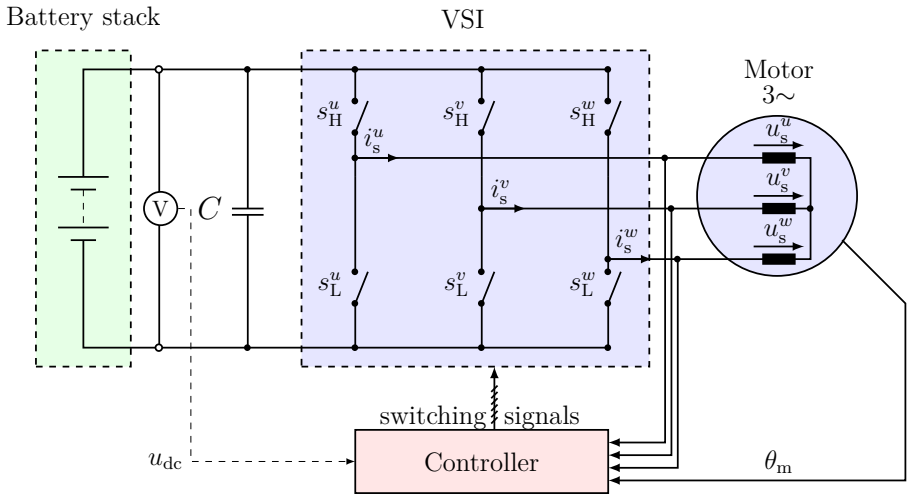

Figure 1.1: *The electrical drive system of an electric vehicle ($u_{\mathrm{s}}^{u}, u_{\mathrm{s}}^{v}, u_{\mathrm{s}}^{w}$: machine phase voltages, $i_{\mathrm{s}}^{u}, i_{\mathrm{s}}^{v}, i_{\mathrm{s}}^{w}$: machine phase currents, u_{dc}: dc-link voltage, C: dc-link capacitor, θ_{m}: mechanical rotor position, $s_{\mathrm{H}}^{u}, s_{\mathrm{H}}^{v}, s_{\mathrm{H}}^{w}, s_{\mathrm{L}}^{u}, s_{\mathrm{L}}^{v}, s_{\mathrm{L}}^{w}$: switching signals).*

losses are proportional to the switching frequency of the semiconductor devices and have a major contribution to the overall losses of the drive system. The requirements of low motor and inverter power losses cannot be simultaneously fulfilled, when carrier based modulation is employed for inverter control [8, 9].

For all these reasons, the concept of low switching frequency modulation or programmed PWM [9–11] is investigated in this thesis. The dc-link voltage can be fully exploited with programmed PWM, since the inverter can be operated up to six-step mode. Furthermore, programmed PWM allows for the reduction of the switching frequency without compromising the motor current quality. However, a little variation in the optimized switching angles has significant impact on the harmonic distortion of machine voltages and currents, since the inverter is operated at reduced switching frequencies and the number of switching instants over the fundamental period is small. For this reason, the objective function of the optimization problem must be carefully formulated in programmed PWM based on the features of the used electrical drive system.

Programmed PWM is primarily employed in medium voltage high power induction motor drive applications, where the reduction of switching losses is of outmost importance [9–11]. Moreover, it is a common modulation strategy for electric railway traction converters [12] adopted by GE [13] as well as by SIEMENS [14]. Programmed PWM applied in low voltage IPMSM drives of electric vehicles with non-negligible saliency, which varies due to magnetic saturation and cross-saturation effects, has not yet been explored. This is the main motivation of this thesis.

1.2 Pulsewidth modulation

The traction system of electric vehicles, as shown in Fig. 1.1, consists of a three-phase ac machine, which is fed by a battery stack. A dc-ac VSI performs the conversion of dc to ac power in switched mode. Power semiconductor switches (usually IGBTs) are turned on and off connecting the three phases of the motor with the two dc terminals of the battery stack. A very efficient method to control the inverter switches and, thus, the inverter output power is the pulsewidth modulation.

The main principle of pulsewidth modulation is illustrated in Fig. 1.2. PWM controls the power

semiconductor switches in order to form the output voltage of each inverter phase leg. The motor phase voltage is influenced by the PWM waveforms of all three inverter phases. By controlling the conduction time of each switch, the desired motor fundamental phase voltage can be produced. The resulting motor phase current faces significant waveform quality deterioration due to the inverter operation in switched mode. Although the machine leakage inductances and the inertia of the mechanical system suppress a major part of the switching harmonic content acting as a low-pass filter, they do not eliminate it [15, 16]. The remaining current harmonic distortion has a major influence on the machine losses and the instantaneous torque ripple.

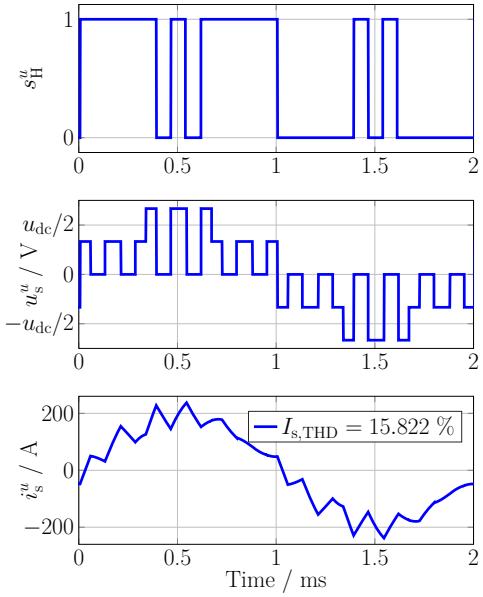

(a) $f_{\mathrm{sw}} = 2.5\,\mathrm{kHz}$.

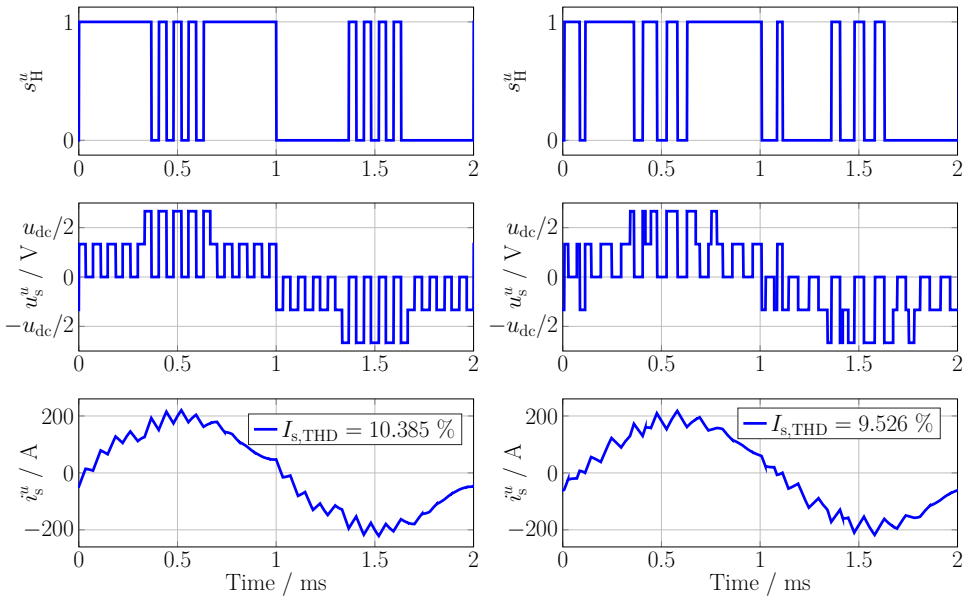

(b) $f_{\mathrm{sw}} = 4.5\,\mathrm{kHz}$.

(c) $f_{\mathrm{sw}} = 4.5\,\mathrm{kHz}$.

Figure 1.2: *Main principle of pulsewidth modulation.*

One way to increase the motor current quality is to operate the inverter at higher switching frequencies f_{sw} (compare Fig. 1.2a with Fig. 1.2b). Nevertheless, this results in increased inverter

switching losses. This leads to a conflicting situation and the tradeoff has to be found [16]. However, the location of the switching events does also influence the harmonic distortion of the motor current waveform $I_{\mathrm{s,THD}}$. In Fig. 1.2b and Fig. 1.2c, the inverter is operated with the same switching frequency. However, the different pulse trains affect the motor current distortion differently. Consequently, another way to enhance the current harmonic quality is to optimize the inverter pulse patterns.

The main objective of PWM is to control the inverter switching devices efficiently and to form high quality motor voltages and currents with the desired frequency and magnitude [17]. Over the last decades intensive research has been conducted and various PWM techniques have been introduced. The performance of each modulator depends on the motor operating point and there is no single modulator, which provides an optimal performance in the whole motor operating range. The performance of each PWM scheme is mainly evaluated based on the following criteria [15, 16, 18]:

- **Dc-link voltage utilization level**: The available dc-link voltage produced by the battery stack must be fully utilized, in order to extend the torque and power density of the electrical drive system. The modulation index [19, p. 86]

$$m := \frac{u_{\mathrm{s,1}}^{u}}{\frac{u_{\mathrm{dc}}}{2}} \tag{1.1}$$

  can be used as a measure of the dc-link voltage utilization level and is defined as the ratio of the fundamental voltage component $u_{\mathrm{s,1}}^{u}$ to the half dc-link voltage u_{dc}. Full dc-link voltage utilization can be reached in six-step operating mode, where $m_{\mathrm{six-step}} := \frac{4}{\pi}$. The maximum inverter output voltage, which is delivered to the electrical machine, depends on the used PWM strategy [3, 4, 20]. For that reason, the performance of each modulator is primarily determined by its maximum dc-link voltage utilization level.

- **Current harmonics**: The inverter operation in switched mode has negative effects on the motor performance because current waveforms with increased harmonic content cause motor heating. The current harmonic quality primarily determines the motor copper losses, which have a major contribution to the overall machine losses [16] especially for low speeds [21, 22]. Current harmonics produce also torque ripple, which may cause mechanical resonance [20, 23, 24].

- **Switching losses**: When a semiconductor device switches from the blocking to the conducting state and vice versa, high values of current and voltage occur simultaneously, causing energy losses in the device. The energy losses depend on the collector current. The overall switching losses are proportionally increasing with the switching frequency [25, 26], which can be controlled by the modulator. The conduction losses of the switching devices and the free-wheeling diodes depend mainly on the load current and are only marginally affected by the modulation method [27].

- **Dynamic performance and implementation simplicity**: Traditionally, the drive system is controlled based on the field oriented control (FOC) principle with closed-loop current control. The dynamic performance of the system is essentially affected by the response time of the current controller as well as the switching frequency and the used PWM scheme. Furthermore, the feedback currents must be free from harmonics. Filtering these signals deteriorates the control dynamics [15]. Other computationally expensive methods to estimate the fundamental component of the measured currents may not be the preferred solution for industrial applications with limited hardware resources.

1.2.1 Programmed PWM - "State of the art"

According to the conventional SVM, the modulator combines the two zero vectors and two active vectors closest to the reference voltage vector to generate the three-phase pulse sequences for each cycle. The number and location of the pulses are fixed for a given cycle duration and modulation index. Hence, the only way to control the current harmonic distortion is by manipulating the cycle duration, i.e. the switching frequency.

The constraint of fixed pulse location over each cycle can be omitted by employing the concept of programmed PWM. According to this concept, the inverter switching events are allowed to take place freely over the electrical period. The inverter pulse patterns, i.e. inverter switching angles, are optimized offline which either eliminate predefined low order voltage harmonics or minimize the harmful effects of the harmonics [11]. In this way, the inverter switching frequency can be reduced without compromising the motor current quality. This is the main idea behind programmed PWM. The main features of programmed PWM can be summarized as follows [10, 28]:

- Low harmonic distorted voltage and current waveforms with low inverter switching frequencies.
- High dc-link voltage utilization. The inverter can be operated in the overmodulation region and six-step mode.
- Low filtering requirements.
- The harmonics can be controlled so that different performance criteria can be optimized according to the requirements of each application.

Programmed PWM techniques were firstly investigated in the 1960's and 1970's [29–32] due to the advent of thyristor semiconductors, which were by nature slow. Nowadays, faster switching devices such as metal-oxide-semiconductor field-effect transistors (MOSFETs) and IGBTs have been developed. Thus, these modulation schemes are primarily employed in medium voltage high power induction motor drive applications, where the reduction of switching losses is of outmost importance [9–11]. Programmed PWM techniques applied in synchronous motors and especially highly anisotropic PMSMs have only recently been explored in depth [7,33–41].

1.2.1.1 Selective harmonic elimination PWM

The principal idea behind selective harmonic elimination PWM (SHEPWM) is the elimination of undesirable low order harmonics in the inverter output waveforms, which cannot be easily attenuated using filter circuits [29]. SHEPWM was introduced in the early 1960's in [29], where it was found out that low order harmonics can be eliminated by utilizing additional switching angles in a square wave voltage. This idea was further developed some years later in [30], where Fourier analysis was employed to express the inverter output voltages and generalized methods were introduced to suppress a fixed number of voltage harmonics.

SHEPWM has been investigated for two-level inverters [33, 34, 42–52] and various multilevel inverters [20, 44, 45, 53–59]. Furthermore, different symmetry properties on the PWM waveform have been studied. Primarily, half-wave symmetry (HWS) and quarter-wave symmetry (QWS) properties are imposed on the PWM waveform in order to simplify the optimization procedure. In this case, $\ell - 1$ harmonics can be eliminated using ℓ switching angles per quarter electrical period [10]. However, in [42–47,53,54], the optimized switching angles for SHEPWM are presented, when the PWM waveform possesses only HWS, while the QWS constraint is relaxed. In [53], multiple sets of solutions are reported for three-level inverters and classified in terms of harmonic

distribution, pulsewidth and total harmonic distortion. Furthermore, different HWS formulations have been examined in [46,47] and the SHEPWM solutions have been evaluated in terms of harmonic performance. In addition to QWS, HWS is also dropped in [42,43], [55] and [56] for a two-, three- and a five-level inverter, respectively. However, this leads to the presence of undesired even order harmonics in the PWM waveform.

In [33,34], SHEPWM is applied to IPMSM drives. [33] shows, that the elimination of low order voltage harmonics does not guarantee the additional elimination of current harmonics due to the anisotropic properties of the IPMSM.

The main disadvantage of SHEPWM is that elimination of certain low order voltage harmonics does not lead to optimal motor behavior, since the remaining harmonics are arbitrarily adjusted and their amplitudes may increase [11,48]. Different SHEPWM solutions yield different harmonic distortions [52,53] and motor losses [48]. Furthermore, SHEPWM solutions may not be available when the inverter is operated at high modulation indices [20,32]. For these reasons, the concept of synchronous optimal PWM (SOPWM) has been developed to optimize the motor performance, while operating the inverter at low switching frequencies.

1.2.1.2 Synchronous optimal PWM

SOPWM is a combination of synchronous and optimal PWM. Synchronous PWM guarantees the elimination of all subharmonic components in the PWM waveform, since the inverter switching frequency is always synchronized with the voltage fundamental frequency [11]. Optimal PWM guarantees low inverter switching frequency operation, while maintaining a sufficient high motor performance.

The SOPWM has been developed based on the fact that minimization of the unwanted effects of harmonics is more advantageous than complete elimination of predefined low order harmonics. The inverter pulse patterns are determined by optimizing a certain performance index. The optimization procedure is conducted offline assuming steady-state operation and the resulting optimized switching angles are stored in look up tables (LUTs). During real time operation, the appropriate switching angles are retrieved from the LUTs and the modulator generates the pulse patterns. The pulse patterns are optimal in steady-state operation but not during transient conditions [60].

The SOPWM scheme has been applied to two-level [23,32,36,37,39–41,48–50,61–66], multilevel [11,20,24,35,38,57,60,67–81] and modular multilevel [82] converters. In the following paragraphs, the main features of SOPWM will be discussed in more detail.

1.2.1.2.1 Performance criteria

The SOPWM scheme has been extensively investigated over the last years for optimizing the performance of induction motor drives. The root mean square (RMS) value of each current harmonic can be approximated by [64,83]

$$I_{\mathrm{s},\nu,\mathrm{RMS}} = \frac{U_{\mathrm{s},\nu,\mathrm{RMS}}}{\nu\omega_{\mathrm{r}}L}, \tag{1.2}$$

where $U_{\mathrm{s},\nu,\mathrm{RMS}}$ is the RMS value of each voltage harmonic, ω_{r} is electrical angular velocity of the machine, L is the machine leakage inductance and ν is the harmonic order. The machine resistance in (1.2) is neglected. Based on this formulation, the normalized current harmonic

distortion factor

$$d := \frac{I_{\mathrm{s,h,RMS}}}{I_{\mathrm{s,h,RMS}}\Big|_{\mathrm{six-step}}} \overset{(1.2)}{=} \sqrt{\frac{\sum_{\nu\neq 1} U^2_{\mathrm{s},\nu,\mathrm{RMS}}/\nu^2}{\sum_{\nu\neq 1} U^2_{\mathrm{s},\nu,\mathrm{RMS}}\Big|_{\mathrm{six-step}}/\nu^2}} \tag{1.3}$$

is defined as the ratio of the phase current ripple $I_{\mathrm{s,h,RMS}}$ and the current ripple in six-step mode $I_{\mathrm{s,h,RMS}}\Big|_{\mathrm{six-step}}$, where $U_{\mathrm{s},\nu,\mathrm{RMS}}\Big|_{\mathrm{six-step}}$ is the RMS value of each voltage harmonic in six-step mode. This factor is the preferred choice for optimizing the motor current quality [32, 74–82, 84, 85]. Furthermore, the weighted total harmonic distortion (WTHD) factor [83]

$$\mathrm{WTHD} := \frac{I_{\mathrm{s,h,RMS}}}{I_{\mathrm{s,1,RMS}}} \overset{(1.2)}{=} \frac{\sqrt{\sum_{\nu\neq 1} U^2_{\mathrm{s},\nu,\mathrm{RMS}}/\nu^2}}{U_{\mathrm{s,1,RMS}}} \tag{1.4}$$

is also a very common performance index found in the literature [61,62,65,83]. Both d and WTHD are a measure of the current harmonic distortion and, for isotropic machines, are independent of the machine's magnetic properties. This feature simplifies the optimization problem.

Further performance criteria can also be found in the literature. In [23,24,63], the minimization of torque ripple is targeted, while in [49], the overall motor losses are optimized. In [48, 50, 86], different SHEPWM and SOPWM pulse patterns are evaluated considering motor power losses and torque ripple and, in [20], SOPWM is compared to SHEPWM in terms of maximum modulation index and frequency spectrum of voltage and current. Lastly, SOPWM is employed in [57] to solve the problem of floating capacitor voltage balancing of a 5-level converter.

On the contrary, little research has been conducted when the SOPWM strategy is employed for the control of synchronous motor drives [7, 35–41]. In [7, 35, 36], the RMS harmonic current of an isotropic PMSM drive is minimized, which is proportional to

$$I_{\mathrm{s,h,RMS}} = \frac{1}{\omega_{\mathrm{r}} L}\sqrt{\sum_{\nu\neq 1}\left(\frac{U_{\mathrm{s},\nu,\mathrm{RMS}}}{\nu}\right)^2} \propto \sqrt{\sum_{\nu\neq 1}\left(\frac{U_{\mathrm{s},\nu,\mathrm{RMS}}}{\nu}\right)^2}. \tag{1.5}$$

The same objective function is utilized in [37] for a salient pole PMSM, ignoring the machine anisotropic properties in the objective function formulation. However, this objective function cannot describe the influence of the salient pole characteristics on the PMSM harmonic currents. Improved optimization criteria for separately excited synchronous motors have been proposed in [38–40] considering the anisotropic motor magnetic properties in the optimization of the inverter pulse patterns. These criteria can also be applied to salient pole PMSMs. However, they are derived assuming that the load angle is zero. Consequently, the influence of the load angle on the PMSM current harmonics cannot be evaluated using these optimization indices.

The analytical expressions for a salient pole PMSM harmonic current with respect to machine saliency ratio and voltage phase angle were recently presented in [33] using quarter- and half-wave symmetric PWM waveforms. Based on this analysis, a new current harmonic evaluation index is proposed in [41] ignoring the stator resistance in the analytical expression of the machine phase current. Optimization and experimental results are presented using a PMSM with constant saliency ratio as load.

1.2.1.2.2 PWM waveform symmetry properties

SOPWM is commonly examined imposing QWS and HWS conditions on the PWM waveform. The HWS property guarantees the elimination of all even harmonics. On the contrary,

the only contribution of QWS is to simplify the optimization procedure. The QWS condition is relaxed in [61,62] and in [87,88] for two- and three-level inverter fed induction motor drives, respectively, and improved solutions are obtained.

1.2.1.2.3 Dynamic performance

Fast current control at reduced switching frequency requires closed-loop control methods, where the fundamental component must be fed back. The dynamic performance of the system is essentially affected by the current control loop. The fundamental component of the feedback current is inherently obtained when the SVM is used, by sampling the measured currents at the center of the zero vector time interval [16]. In contrast to SVM, the SOPWM strategy does not offer this feature, since the measured and sampled current contains a significant harmonic content [71].

A variety of methods have been developed to estimate the fundamental component of the measured currents when SOPWM is utilized. One possibility is to filter out the harmonics of the measured currents [35, 36]. Nevertheless, this increases the response time of the current control loop. The problem of slow control dynamics can be fixed by using an observer to identify the fundamental components of stator current and flux linkage vectors of induction motors [67–71,89]. However, the implementation of an observer is rather complex. Lastly, model predictive control (MPC) combined with optimal PWM [72,73] seems to be a very effective but computationally expensive method, which enables a very fast dynamic response without the need of a complex observer.

1.2.1.2.4 Implementation

The inverter switching angles of all programmed pulse patterns are stored in LUTs. Thereby, considerable computing resources and hardware memory requirements may be involved in generating the pulse patterns. Another important aspect, concerning the implementation of SOPWM, involves the transition between different pulse patterns. SOPWM is a synchronous modulation scheme. The inverter switching frequency f_{sw} is synchronized with the fundamental electrical frequency f_{r} and their ratio defines the pulse number [11]

$$q := \frac{f_{\mathrm{sw}}}{f_{\mathrm{r}}} \tag{1.6}$$

over an electrical period, which is always an integer.

Using the same pulse number in the whole motor frequency range is not recommended since the inverter switching frequency decreases with the electrical frequency and the motor phase current quality deteriorates [16]. For that reason, the pulse number must increase with reducing electrical frequencies, i.e. $f_{\mathrm{r}} \searrow \Rightarrow q \nearrow$. The use of different pulse patterns implies that the amplitude and phase angle of the current harmonics also differ. Consequently, the switching transition may cause current and torque transients and even overcurrent tripping.

For very low electrical frequencies it is not possible to use a high pulse number and, thus, to increase the inverter switching frequency, due to the limited resource capabilities of the processor. Furthermore, the optimization procedure is not effective in this range, due to the increased computation time. Consequently, the performance of SOPWM degrades and it is more advantageous to use SVM in the lower electrical frequency range. This imposes the requirement of a smooth switching transition between these modulation modes to prevent overcurrent conditions.

An effective but computationally rather expensive method is presented in [71] for an induction motor drive system. According to this method, the tracking error between the optimal and

actual flux trajectory, caused by the transition between different pulse patterns, is compensated by manipulating the optimized inverter switching instants. The optimal flux trajectory is reconstructed in real time using the optimized inverter switching angles, whereas the actual one is estimated by an observer. In [58, 59], the switching transition between SVM and SHEPWM is investigated. In [58], the switching transition is enabled at a fixed vector angle, while in [59] the switching is optimized, such that no more than one switching state changes during transition. However, these methods do not consider a switching between two modulation schemes with highly different switching frequencies and current harmonic distortions. A rather complex transition strategy between different SHEPWM solutions is presented in [51], according to which the transition at each of the three phases is activated when the corresponding phase current is around zero. In other words, the transitions at each of the three phases occur at different time instants.

1.3 Contribution of this thesis

The primary objective of this thesis is to investigate the performance of the SOPWM strategy for the control of a two-level VSI at reduced switching frequencies, while optimizing the current quality of a salient-pole IPMSM. The contribution of this thesis can be summarized in the following points:

A. *Evaluation of the influence of the IPMSM anisotropic properties on the optimization of the inverter pulse patterns.*

   This thesis aims at minimizing the current harmonic distortion of a salient-pole IPMSM, whose magnetic anisotropic properties vary due to magnetic saturation and cross-saturation effects and depend on the operating point. For this purpose, the analytical formulations of the motor phase currents in the time and frequency domain with respect to the inverter switching angles are derived. The analysis of [33, 41] is extended in this thesis for the case of *only half-wave symmetric* PWM waveforms and optimization results are presented considering also the varying IPMSM saliency ratio. In this way, the influence of the saliency ratio and voltage phase angle on the optimized switching angles is examined. Both optimized half-wave symmetric pulse patterns of an isotropic and an anisotropic PMSM are adopted for the control of a salient pole IPMSM drive and experimental results evaluate and compare their performance. Lastly, both static and dynamic optimal operation of the drive system in the whole torque/speed range is examined.

   This work has been partly published in the *European Conference on Power Electronics and Applications* [66] and parts have been accepted for publication in *IEEE Transactions on Industrial Electronics* [90].

B. *Evaluation of the influence of the optimized inverter pulse patterns on the dc-link capacitor current ripple.*

   An accurate identification of the dc-link capacitor current is crucial for the design of the dc-link capacitor as the capacitor current ripple affects lifetime, size, weight and cost of the VSI. In this thesis, analytical expressions for the inverter current and the dc-link capacitor current are deduced in the time and frequency domain with respect to the inverter switching angles when the SOPWM is employed for the control of a salient pole IPMSM drive. The magnetic anisotropic properties of the IPMSM are considered and half-wave symmetric PWM signals are utilized. The effect of various pulse patterns on the produced dc-link capacitor current ripples is evaluated and the correctness of the derived equations is validated by experimental results.

This work was developed as part of the supervised master's thesis [91] and was submitted to *IEEE Transactions on Industrial Electronics* [92] for publication.

C. *Relaxation of the PWM quarter-wave symmetry property.*

The elimination of the QWS property of the PWM waveform extends the solution space and improved solutions are obtained. Optimization results, which prove this statement, are already published in [66] for an anisotropic PMSM and are not included in this thesis. In this thesis, half-wave symmetric PWM waveforms are adopted and further investigated.

D. *Integration of SOPWM into a FOC scheme with closed-loop current control.*

An important topic in this thesis involves the integration of SOPWM into a FOC scheme with closed-loop current control since robustness, reliability and implementation simplicity of the modulator and control algorithms are of outmost importance for automotive applications. A simple implementation method is proposed, according to which the optimized inverter switching angles are translated into switching time counters. This allows to use the same modulator for both SVM and SOPWM schemes.

Furthermore, traditional proportional integral (PI) controllers are utilized for current control for both SVM and SOPWM schemes. When the SOPWM is in use, the measured currents contain a significant harmonic content. A simple yet very effective fundamental current estimation method is proposed in this thesis, which eliminates the undesired harmonics in the measured currents by sampling at specific points in time. In this way, the integration of the SOPWM into a FOC scheme can be realized without using a complex observer. The main feature of this method is its implementation simplicity, since the computational effort required is within the capability of a standard industrial digital signal processor (DSP) system. Furthermore, it is independent of the load parameters. The proposed method is an attractive alternative to a complex observer or MPC for EVs and other industrial applications, where implementation simplicity is needed.

A patent application is submitted to the *European Patent Office* [93], which presents the main principle of the proposed fundamental current estimation method. Furthermore, its performance is investigated using a three-phase inductive load and the outcomes are published in *IEEE Transactions on Industrial Electronics* [94]. In this thesis, this method is adopted for the control of a salient-pole IPMSM.

E. *Smooth switching transition between SVM and SOPWM.*

At speed ranges lower than the rated speed the motor is driven based on the asynchronous SVM scheme with a constant switching frequency, whereas at higher speeds and especially in the field-weakening region the better dc-link voltage utilization capability of the SOPWM scheme is exploited. The transition between the asynchronous SVM and the synchronous SOPWM should be smooth to prevent overcurrent tripping. In this thesis and in [94], a simple method is introduced to synchronize the SVM switching frequency with the electrical frequency before the switching transition takes place. In this way, a smooth transition is ensured even when the switching frequencies of both modulation schemes are highly different.

This thesis is organized as follows: In Chapter 2, the analytical formulations of the machine voltages and currents as well as the dc-link capacitor current are derived with respect to the inverter switching angles. Moreover, the optimization problem is formulated and the optimization results are presented. Chapter 3 discusses in detail the implementation of SOPWM and validates

the outcomes of this thesis via experimental results. Finally, Chapter 4 concludes this thesis and illustrates the propositions for future work.

An overview of the used test bench is given in the Appendix (see A). It should be noted, that a VSI with IGBT semiconductor devices, conventionally used in electric vehicles, was not available for use in this thesis. Nevertheless, the contributions of this thesis can still be experimentally validated with the presented test bench.

Chapter 2

Optimization

2.1 Mathematical preliminaries

2.1.1 Trigonometric equations

The following trigonometric equations [95] have been used throughout this thesis, where x, $y \in \mathbb{R}$ and $j \in \mathbb{C}$:

$$\sin(x \pm y) := \sin(x)\cos(y) \pm \cos(x)\sin(y) \tag{2.1}$$

$$\cos(x \pm y) := \cos(x)\cos(y) \mp \sin(x)\sin(y) \tag{2.2}$$

$$e^{jx} := \cos(x) + j\sin(x) \tag{2.3}$$

$$\arctan\left(\frac{y}{x}\right) := \begin{cases} \tan^{-1}\left(\frac{y}{x}\right) & x > 0 \\ \tan^{-1}\left(\frac{y}{x}\right) + \pi & y \geq 0,\ x < 0 \\ \tan^{-1}\left(\frac{y}{x}\right) - \pi & y < 0,\ x < 0 \\ +\frac{\pi}{2} & y > 0,\ x = 0 \\ -\frac{\pi}{2} & y < 0,\ x = 0 \\ \text{undefined} & y = 0,\ x = 0 \end{cases} \tag{2.4}$$

The command $\arctan(y/x)$ returns the four-quadrant inverse tangent $\tan^{-1}$ of y and x (see Matlab function $\text{atan2}(y, x)$ [96]).

2.1.2 Fourier transform theory

Based on the Fourier transform theory [19, 97], any time-varying function $g(t)$ with constant fundamental angular velocity ω can be expressed by

$$g(t) := \frac{a_0}{2} + \sum_{\nu=1}^{\infty} a_\nu \cos(\nu\omega t) + b_\nu \sin(\nu\omega t) \tag{2.5}$$

as a infinite sum of the harmonic components, where ν represents the order of each harmonic component and a_0, a_ν, b_ν constitute the Fourier coefficients, which are given by

$$a_0 := \frac{1}{\pi}\int_0^{2\pi} g(\omega t)d(\omega t) \tag{2.6}$$

$$a_\nu := \frac{1}{\pi}\int_0^{2\pi} g(\omega t)\cos(\nu\omega t)d(\omega t)$$
$$b_\nu := \frac{1}{\pi}\int_0^{2\pi} g(\omega t)\sin(\nu\omega t)d(\omega t).$$

The signal $g(t)$ may possess quarter-wave symmetry (QWS) and half-wave symmetry (HWS) properties, which simplify the derivation of the Fourier coefficients [19]:

- **HWS:** The signal $g(t)$ is half-wave symmetric, if the second half period is inverted with respect to the first one, i.e. $g(t) = -g(t - \frac{\pi}{\omega})$. In this case, the Fourier coefficients simplify to

$$\begin{aligned} a_0 &= 0 \\ a_\nu &= \begin{cases} \frac{2}{\pi}\int_0^{\pi} g(\omega t)\cos(\nu\omega t)d(\omega t) & \text{for odd } \nu \\ 0 & \text{for even } \nu \end{cases} \\ b_\nu &= \begin{cases} \frac{2}{\pi}\int_0^{\pi} g(\omega t)\sin(\nu\omega t)d(\omega t) & \text{for odd } \nu \\ 0 & \text{for even } \nu. \end{cases} \end{aligned} \tag{2.7}$$

  Thereupon, only odd harmonic components exist, whereas the dc and the even order harmonics are zero.

- **HWS and QWS:** If $g(t)$ possesses in addition to HWS also QWS properties, i.e. $g(t) = -g(t - \frac{\pi}{\omega})$ and $g(t) = g(\frac{\pi}{\omega} - t)$, then the Fourier coefficients are given by

$$\begin{aligned} a_0 &= 0 \\ a_\nu &= 0 \\ b_\nu &= \begin{cases} \frac{4}{\pi}\int_0^{\pi/2} g(\omega t)\sin(\nu\omega t)d(\omega t) & \text{for odd } \nu \\ 0 & \text{for even } \nu. \end{cases} \end{aligned} \tag{2.8}$$

  In this case, the dc and the even order harmonics are still absent. Moreover, since

$$g(t) \overset{(2.5),(2.8)}{=} \sum_{\nu=1}^{\infty} b_\nu \sin(\nu\omega t),$$

  all harmonics $b_\nu \sin(\nu\omega t)$ are either in phase with the fundamental vector $b_1 \sin(\omega t)$ or shifted by $\pm\pi$ rad depending on the signs of b_1 and b_ν.

2.1.3 Phasor theory

A phasor is a complex number used to represent a sinusoidal function whose amplitude, angular frequency and initial phase are real numbers and time-invariant [98, Chapter 9].

Suppose a sinusoid

$$g(t) := h\cos(\omega t + \delta) \tag{2.9}$$

with amplitude h, angular frequency ω and initial phase angle δ. Eq. (2.9) represents the sinusoid in the time domain. Using the Euler's formula in the rectangular form [98, Chapter 9] gives

$$ge^{j(\omega t+\delta)} \overset{(2.3)}{=} h\cos(\omega t + \delta) + jh\sin(\omega t + \delta). \tag{2.10}$$

Eq. (2.9) can be written as follows

$$g(t) = \Re\left(he^{j(\omega t+\delta)}\right) = \Re\left(he^{j\delta}e^{j\omega t}\right) = \Re\left(\mathrm{G}e^{j\omega t}\right), \tag{2.11}$$

where G is the phasor of $g(t)$. In other words, the sinusoid $g(t)$ can be expressed in the phasor domain by a complex number G called the phasor according to the rule

$$\mathrm{G} := he^{j\delta}. \tag{2.12}$$

A phasor can be converted from the rectangular to the polar form. The transformation yields

$$\mathrm{G} := h\angle\delta. \tag{2.13}$$

The following rules can be applied to phasors [98, Chapter 9]:

1. **Linearity rule:**
   The linear combination of n sinusoids
   $$\sum_{k=1}^{n} x_k g_k(t) \tag{2.14}$$
   can be represented by
   $$\sum_{k=1}^{n} x_k \mathrm{G}_k, \tag{2.15}$$
   where $x_k \in \mathbb{R}$.

2. **Differentiation rule:**
   G is the phasor of a given sinusoid $h\cos(\omega t + \delta)$ if and only if $j\omega\mathrm{G}$ is the phasor of its derivative $\frac{\mathrm{d}}{\mathrm{d}t}\left(h\cos(\omega t + \delta)\right)$, i.e.
   $$\Re\left(j\omega\mathrm{G}e^{j\omega t}\right) = \frac{\mathrm{d}}{\mathrm{d}t}\left(\Re\left(\mathrm{G}e^{j\omega t}\right)\right). \tag{2.16}$$

2.2 Electrical drive system model

Fig. 2.1 illustrates the electrical three-phase system used in this thesis, which consists of a battery simulator, a two-level VSI and an IPMSM. The battery simulator and the dc-link cable are modelled as a $R_{\mathrm{bat}}L_{\mathrm{bat}}$-element with a dc voltage source u_{bat}. The dc-link capacitor with capacitance C and equivalent series resistance R_{ESR} is located close to the VSI to reduce stray inductance between these two components.

In this section, the analytical formulations of the

- inverter output voltages $\boldsymbol{u}_{\mathrm{o}}^{uvw}(\boldsymbol{\alpha}) := (u_{\mathrm{o}}^{u}(\boldsymbol{\alpha}), u_{\mathrm{o}}^{v}(\boldsymbol{\alpha}), u_{\mathrm{o}}^{w}(\boldsymbol{\alpha}))^{\top}$ relative to the inverter midpoint o and machine phase voltages $\boldsymbol{u}_{\mathrm{s}}^{uvw}(\boldsymbol{\alpha}) := (u_{\mathrm{s}}^{u}(\boldsymbol{\alpha}), u_{\mathrm{s}}^{v}(\boldsymbol{\alpha}), u_{\mathrm{s}}^{w}(\boldsymbol{\alpha}))^{\top}$ (see Sec. 2.2.1);
- machine phase currents $\boldsymbol{i}_{\mathrm{s}}^{uvw}(\boldsymbol{\alpha}) := (i_{\mathrm{s}}^{u}(\boldsymbol{\alpha}), i_{\mathrm{s}}^{v}(\boldsymbol{\alpha}), i_{\mathrm{s}}^{w}(\boldsymbol{\alpha}))^{\top}$ (see Sec. 2.2.2); and
- gate signals $\boldsymbol{s}^{uvw}(\boldsymbol{\alpha}) := (s^{u}(\boldsymbol{\alpha}), s^{v}(\boldsymbol{\alpha}), s^{w}(\boldsymbol{\alpha}))^{\top}$, inverter current $i_{\mathrm{inv}}(\boldsymbol{\alpha})$ and dc-link capacitor current $i_{\mathrm{c}}(\boldsymbol{\alpha})$ (see Sec. 2.2.3);

will be derived in the time domain with respect to the independent inverter switching angles

$$\boldsymbol{\alpha} := (\alpha_1, \ldots, \alpha_\ell)^{\top}, \tag{2.17}$$

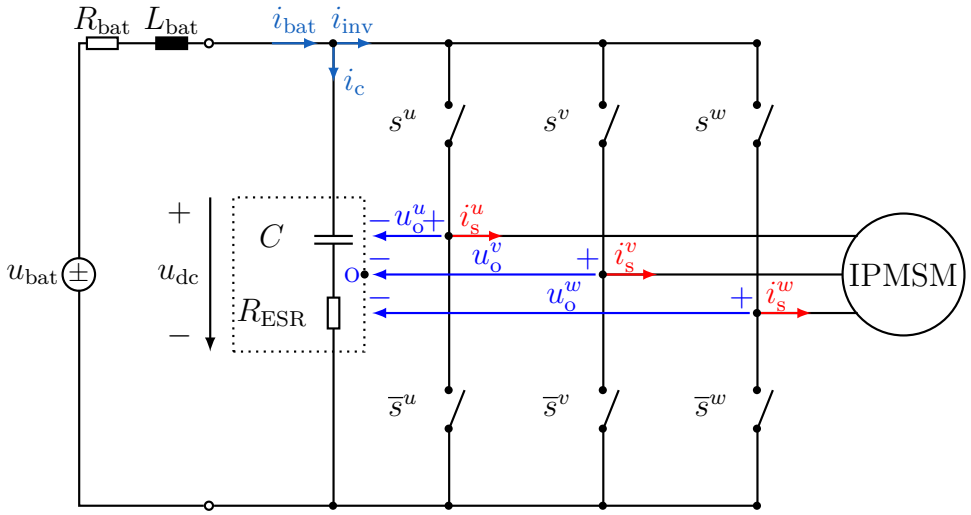

Figure 2.1: *Electrical three-phase drive system.*

where ℓ denotes the number of independent switching angles to be optimized. The harmonic content of each of these electrical quantities can be minimized by using the corresponding objective function in the optimization problem formulation according to the objectives of the application. In this thesis, the enhancement of the machine performance is targeted. The copper losses account for a major portion of the machine losses [16] and are proportional to the square of the RMS value of the current harmonics [50]. Therefore, the harmonic content of the machine phase current is minimized in this thesis. Sec. 2.3 describes the optimization problem formulation and Sec. 2.4 presents the optimization results, which are then evaluated in Sec. 2.5.

2.2.1 Inverter output and machine phase voltages

In this subsection, the analytical expressions of the inverter output and machine phase voltages with respect to the inverter switching angles will be derived imposing the following assumptions:

(A1) The influence of the dc-link voltage ripple on the machine phase voltages and currents is negligible. Thereafter, the equations of $\boldsymbol{u}_{\mathrm{o}}^{uvw}$, $\boldsymbol{u}_{\mathrm{s}}^{uvw}$ and $\boldsymbol{i}_{\mathrm{s}}^{uvw}$ are derived assuming that the impedance of the battery simulator and cable is equal to zero and $u_{\mathrm{dc}} = u_{\mathrm{bat}}$.

(A2) A dead-time free inverter operation with ideal semiconductor switches is assumed, where the switches toggle their ON/OFF state instantly.

Applying the gate signals to the switches of each phase leg $z = \{u, v, w\}$, the desired PWM waveform

$$u_{\mathrm{o}}^z = \begin{cases} \frac{u_{\mathrm{dc}}}{2} & \text{if } s^z = 1 \\ -\frac{u_{\mathrm{dc}}}{2} & \text{if } s^z = 0 \end{cases} \tag{2.18}$$

can be formed (see Fig. 2.2), where the values 0 and 1 denote that the switch is turned OFF and ON, respectively. Fig. 2.2a illustrates a PWM waveform $u_{\mathrm{o}}^u(\boldsymbol{\alpha})$ in which QWS and HWS conditions are imposed, whereas the PWM waveform in Fig. 2.2b possesses only HWS, while the QWS property is dropped. The main advantages of applying symmetry properties to the PWM waveform are the simplification of the optimization procedure and the elimination of the even order harmonics in the machine phase voltages, as will be discussed in the upcoming subsections.

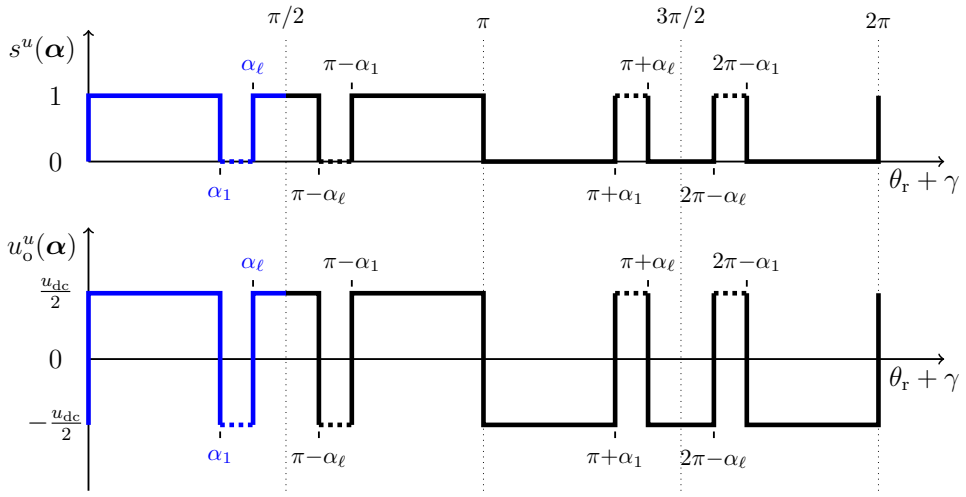

(a) *QWS and HWS.*

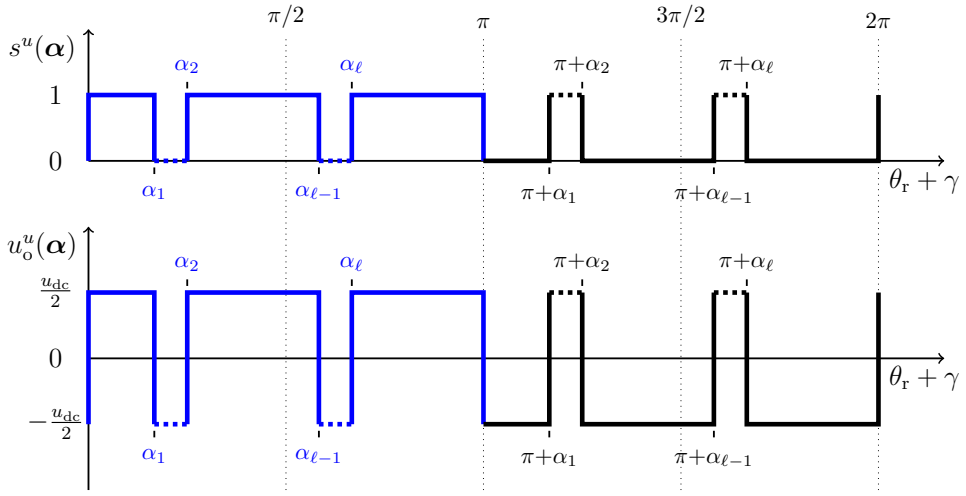

(b) *HWS.*

Figure 2.2: *Gate signal $s^u(\boldsymbol{\alpha})$ and inverter output phase voltage $u_o^u(\boldsymbol{\alpha})$ possessing different symmetry properties.*

The upper switch of each phase leg is usually turned on in the beginning of the positive half cycle of each PWM waveform (see Fig. 2.2) when an even number ℓ of independent switching angles in each quarter cycle is utilized and vice-versa when ℓ is odd [62] [83, p. 396]. This topic is investigated in [65] and the results show that the PWM waveform of Fig. 2.2 leads to improved harmonic current quality in the major part of modulation index range. A pulse number of

$$q = 5 \quad \text{or} \quad q = 9 \tag{2.19}$$

will be investigated in this thesis and, thus, the PWM waveform of Fig. 2.2 is considered here.

The analytical expressions for the phase voltages and currents of a salient pole IPMSM in the time domain with respect to the inverter switching angles are deduced in [33] and [41] using PWM waveforms with both HWS and QWS properties. In this thesis, the more general case of only half-wave symmetric PWM signals is also considered (see Sec. 2.2.1-2.2.2). This work has been partly published in *European Conference on Power Electronics and Applications* [66] and parts have been accepted for publication in *IEEE Transactions on Industrial Electronics* [90].

2.2.1.1 Half- and quarter-wave symmetric PWM

Traditionally, the SOPWM strategy is investigated imposing QWS (i.e. $u_{\mathrm{o}}^{u}(t,\boldsymbol{\alpha}) = u_{\mathrm{o}}^{u}(\frac{\pi}{\omega_{\mathrm{r}}} - t,\boldsymbol{\alpha})$) and HWS (i.e. $u_{\mathrm{o}}^{u}(t,\boldsymbol{\alpha}) = -u_{\mathrm{o}}^{u}(t-\frac{\pi}{\omega_{\mathrm{r}}},\boldsymbol{\alpha})$) conditions in the PWM waveform, as shown in Fig. 2.2a. Two fixed switching events occur at the half cycle points 0 and π rad and the number of independent inverter switching angles to be optimized is

$$\ell := \frac{q-1}{2}, \tag{2.20}$$

where q is as in (1.6). This approach reduces the computational burden of the optimization procedure, since the number of switching angles ℓ to be optimized is reduced. However, the resulting angles must be in the range of $[0,\pi/2]$ rad, which restricts the solution space and suboptimal switching angles may result [61, 62]. Furthermore, all harmonics are either in phase or anti-phase with the fundamental, as discussed in Sec. 2.1.2. Consequently, the phasing of the harmonics cannot be controlled.

The inverter output phase voltages relative to the inverter midpoint o with arbitrary harmonic distortion in the stationary uvw-reference frame can be expressed as a function of the independent inverter switching angles $\boldsymbol{\alpha}$ by

$$\boldsymbol{u}_{\mathrm{o}}^{uvw}(\boldsymbol{\alpha}) \overset{(2.5),\,(2.8)}{=} \sum_{\nu\in\mathcal{I}}^{\infty} \begin{pmatrix} b_\nu(\boldsymbol{\alpha})\sin\left(\nu\left(\theta_{\mathrm{r}}+\gamma\right)\right) \\ b_\nu(\boldsymbol{\alpha})\sin\left(\nu\left(\theta_{\mathrm{r}}+\gamma-\frac{2\pi}{3}\right)\right) \\ b_\nu(\boldsymbol{\alpha})\sin\left(\nu\left(\theta_{\mathrm{r}}+\gamma-\frac{4\pi}{3}\right)\right) \end{pmatrix} \tag{2.21}$$

using Fourier theory, where $b_\nu(\boldsymbol{\alpha})$ is the Fourier coefficient of each harmonic component. Note that $a_\nu = 0$ due to QWS. Furthermore, the dc component and all even order harmonics are eliminated, since the voltage waveforms are half-wave symmetric. Thus, the inverter output voltages contain only odd order harmonics, i.e. $\mathcal{I}{:=}\,\{1,3,5,7,\ldots\}$ [83].

Furthermore, the motor phase voltages are given by

$$\boldsymbol{u}_{\mathrm{s}}^{uvw}(\boldsymbol{\alpha}) = \begin{pmatrix} u_{\mathrm{o}}^{u}(\boldsymbol{\alpha}) + u_{\mathrm{os}}(\boldsymbol{\alpha}) \\ u_{\mathrm{o}}^{v}(\boldsymbol{\alpha}) + u_{\mathrm{os}}(\boldsymbol{\alpha}) \\ u_{\mathrm{o}}^{w}(\boldsymbol{\alpha}) + u_{\mathrm{os}}(\boldsymbol{\alpha}) \end{pmatrix} = \sum_{\nu\in\mathcal{H}}^{\infty} \begin{pmatrix} b_\nu(\boldsymbol{\alpha})\sin\left(\nu\left(\theta_{\mathrm{r}}+\gamma\right)\right) \\ b_\nu(\boldsymbol{\alpha})\sin\left(\nu\left(\theta_{\mathrm{r}}+\gamma-\frac{2\pi}{3}\right)\right) \\ b_\nu(\boldsymbol{\alpha})\sin\left(\nu\left(\theta_{\mathrm{r}}+\gamma-\frac{4\pi}{3}\right)\right) \end{pmatrix}, \tag{2.22}$$

where $u_{\mathrm{os}}(\boldsymbol{\alpha})$ is the voltage between the inverter midpoint o and the machine star point. The motor phase voltages contain only odd order non-triplen harmonics, i.e. $\mathcal{H} := \{1,5,7,\ldots\}$ [83], since triplen harmonics do not exist in a star connected and balanced three-phase system.

The angle $\theta_{\mathrm{r}} := \omega_{\mathrm{r}}t + \phi_0$ represents the electrical rotor position, where ϕ_0 is the initial rotor position, $\omega_{\mathrm{r}} := n_{\mathrm{p}}\omega_{\mathrm{m}}$ is the electrical angular velocity, ω_{m} is the mechanical angular velocity and n_{p} is the pole pair number of the machine. The angles θ_{u} and $\theta := \theta_{\mathrm{r}} + \theta_{\mathrm{u}}$ are the phase angles of the fundamental voltage vector $\boldsymbol{u}_{\mathrm{s},1}^{k}(\boldsymbol{\alpha}) := \left(u_{\mathrm{s},1}^{d}(\boldsymbol{\alpha}),\ u_{\mathrm{s},1}^{q}(\boldsymbol{\alpha})\right)^{\top}$ in the dq- and uvw-reference frame, respectively, as depicted in Fig. 2.3. The angle γ represents the phase angle of the vector $\boldsymbol{b}_1(\boldsymbol{\alpha}) := \left(b_1(\boldsymbol{\alpha})\sin\gamma,\ -b_1(\boldsymbol{\alpha})\cos\gamma\right)^{\top}$ in the dq-reference frame and is equal to

$$\gamma := \theta_{\mathrm{u}} - \frac{3\pi}{2} \tag{2.23}$$

for a quarter- and half-wave symmetric PWM signal, since $a_\nu = 0$ and $\boldsymbol{u}_{\mathrm{s},1}^{k}(\boldsymbol{\alpha}) = \boldsymbol{b}_1(\boldsymbol{\alpha})$ (see Fig. 2.3a).

Based on Fig. 2.2a and applying the Fourier theory (see (2.8)), the Fourier coefficient $b_\nu(\boldsymbol{\alpha})$ can be derived as follows

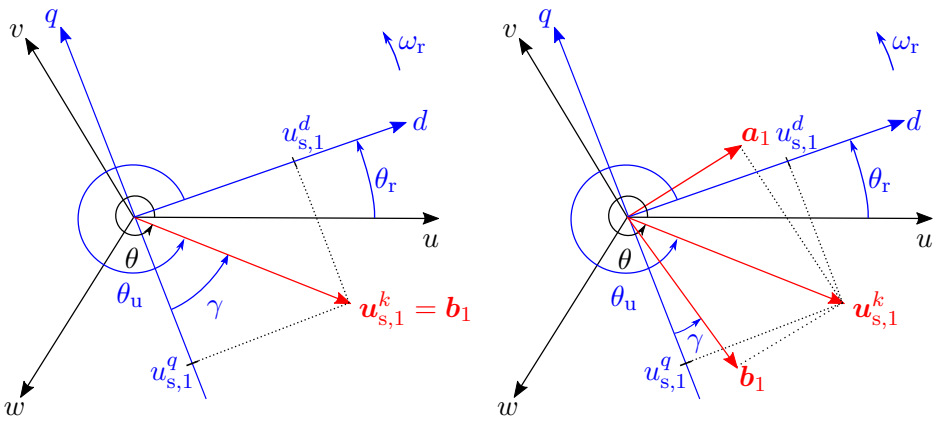

(a) *QWS and HWS.* (b) *HWS.*

Figure 2.3: *Voltage vector representation in the uvw- and dq-reference frame.*

$$
\begin{aligned}
b_\nu(\boldsymbol{\alpha}) \overset{(2.8)}{=} & \frac{4}{\pi}\int_0^{\pi/2} u_{\mathrm{o}}^{u}\left(\theta_{\mathrm{r}}+\gamma\right)\sin\left(\nu\left(\theta_{\mathrm{r}}+\gamma\right)\right)d\left(\theta_{\mathrm{r}}+\gamma\right) \\
= & \frac{4}{\pi}\int_0^{\alpha_1} \frac{u_{\mathrm{dc}}}{2}\sin\left(\nu\left(\theta_{\mathrm{r}}+\gamma\right)\right)d\left(\theta_{\mathrm{r}}+\gamma\right) \\
& -\frac{4}{\pi}\int_{\alpha_1}^{\alpha_\ell} \frac{u_{\mathrm{dc}}}{2}\sin\left(\nu\left(\theta_{\mathrm{r}}+\gamma\right)\right)d\left(\theta_{\mathrm{r}}+\gamma\right) \\
& +\frac{4}{\pi}\int_{\alpha_\ell}^{\pi/2} \frac{u_{\mathrm{dc}}}{2}\sin\left(\nu\left(\theta_{\mathrm{r}}+\gamma\right)\right)d\left(\theta_{\mathrm{r}}+\gamma\right) \\
= & \frac{2u_{\mathrm{dc}}}{\nu\pi}\left(1+2\sum_{i=1}^{\ell}(-1)^i\cos(\nu\alpha_i)\right).
\end{aligned}
\tag{2.24}
$$

2.2.1.2 Half-wave symmetric PWM

Fig. 2.2b depicts a PWM waveform possessing only HWS, while the QWS condition is relaxed. All even harmonic components are still absent but the harmonic phasing is free to vary (see Sec. 2.1.2 and [44]). The advantage of generalizing the problem formulation to not require QWS is that the available solution space is expanded and solutions not obtainable when preserving the QWS condition may be found. While this formulation leads to a more complicated optimization procedure, since the number

$$\ell := q - 1 \tag{2.25}$$

of independent switching angles to be optimized increases (compare (2.25) with (2.20)), improved solutions may be obtained, leading to enhanced electrical drive efficiency.

The inverter output phase voltages relative to the inverter midpoint o with arbitrary harmonic distortion in the stationary *uvw*-reference frame can be expressed as a function of the independent

inverter switching angles $\boldsymbol{\alpha}$ by

$$\boldsymbol{u}_{\mathrm{o}}^{uvw}(\boldsymbol{\alpha}) \overset{(2.5),(2.7)}{=} \sum_{\nu\in\mathcal{I}}^{\infty} \begin{pmatrix} a_\nu(\boldsymbol{\alpha})\cos\left(\nu\left(\theta_{\mathrm{r}}+\gamma(\boldsymbol{\alpha})\right)\right) + b_\nu(\boldsymbol{\alpha})\sin\left(\nu\left(\theta_{\mathrm{r}}+\gamma(\boldsymbol{\alpha})\right)\right) \\ a_\nu(\boldsymbol{\alpha})\cos\left(\nu\left(\theta_{\mathrm{r}}+\gamma(\boldsymbol{\alpha})-\frac{2\pi}{3}\right)\right) + b_\nu(\boldsymbol{\alpha})\sin\left(\nu\left(\theta_{\mathrm{r}}+\gamma(\boldsymbol{\alpha})-\frac{2\pi}{3}\right)\right) \\ a_\nu(\boldsymbol{\alpha})\cos\left(\nu\left(\theta_{\mathrm{r}}+\gamma(\boldsymbol{\alpha})-\frac{4\pi}{3}\right)\right) + b_\nu(\boldsymbol{\alpha})\sin\left(\nu\left(\theta_{\mathrm{r}}+\gamma(\boldsymbol{\alpha})-\frac{4\pi}{3}\right)\right) \end{pmatrix} \tag{2.26}$$

and the machine phase voltages by

$$\boldsymbol{u}_{\mathrm{s}}^{uvw}(\boldsymbol{\alpha}) \overset{(2.5),(2.7)}{=} \sum_{\nu\in\mathcal{H}}^{\infty} \begin{pmatrix} a_\nu(\boldsymbol{\alpha})\cos\left(\nu\left(\theta_{\mathrm{r}}+\gamma(\boldsymbol{\alpha})\right)\right) + b_\nu(\boldsymbol{\alpha})\sin\left(\nu\left(\theta_{\mathrm{r}}+\gamma(\boldsymbol{\alpha})\right)\right) \\ a_\nu(\boldsymbol{\alpha})\cos\left(\nu\left(\theta_{\mathrm{r}}+\gamma(\boldsymbol{\alpha})-\frac{2\pi}{3}\right)\right) + b_\nu(\boldsymbol{\alpha})\sin\left(\nu\left(\theta_{\mathrm{r}}+\gamma(\boldsymbol{\alpha})-\frac{2\pi}{3}\right)\right) \\ a_\nu(\boldsymbol{\alpha})\cos\left(\nu\left(\theta_{\mathrm{r}}+\gamma(\boldsymbol{\alpha})-\frac{4\pi}{3}\right)\right) + b_\nu(\boldsymbol{\alpha})\sin\left(\nu\left(\theta_{\mathrm{r}}+\gamma(\boldsymbol{\alpha})-\frac{4\pi}{3}\right)\right) \end{pmatrix}. \tag{2.27}$$

All even harmonic components are still absent and $\boldsymbol{u}_{\mathrm{o}}^{uvw}(\boldsymbol{\alpha})$ and $\boldsymbol{u}_{\mathrm{s}}^{uvw}(\boldsymbol{\alpha})$ contain the same order harmonic components as in the case of QWS preserved (see (2.21) and (2.22)).

The angle $\gamma(\boldsymbol{\alpha})$ represents the phase angle of the vectors

$$\begin{aligned} \boldsymbol{a}_1(\boldsymbol{\alpha}) &:= \left(a_1(\boldsymbol{\alpha})\cos\gamma(\boldsymbol{\alpha}),\ \ a_1(\boldsymbol{\alpha})\sin\gamma(\boldsymbol{\alpha})\right)^\top \quad \text{and} \\ \boldsymbol{b}_1(\boldsymbol{\alpha}) &:= \left(b_1(\boldsymbol{\alpha})\sin\gamma(\boldsymbol{\alpha}),\ \ -b_1(\boldsymbol{\alpha})\cos\gamma(\boldsymbol{\alpha})\right)^\top \end{aligned} \tag{2.28}$$

in the dq-reference frame and is given by

$$\begin{aligned} &\tan\theta_{\mathrm{u}} = \frac{u_{\mathrm{s},1}^q(\boldsymbol{\alpha})}{u_{\mathrm{s},1}^d(\boldsymbol{\alpha})} \\ &\Rightarrow \frac{\cos\theta_{\mathrm{u}}}{\sin\theta_{\mathrm{u}}} = \frac{a_1(\boldsymbol{\alpha})\sin\gamma(\boldsymbol{\alpha}) - b_1(\boldsymbol{\alpha})\cos\gamma(\boldsymbol{\alpha})}{a_1(\boldsymbol{\alpha})\cos\gamma(\boldsymbol{\alpha}) + b_1(\boldsymbol{\alpha})\sin\gamma(\boldsymbol{\alpha})} \\ &\Rightarrow \left(a_1(\boldsymbol{\alpha})\sin\theta_{\mathrm{u}} + b_1(\boldsymbol{\alpha})\cos\theta_{\mathrm{u}}\right)\cos\gamma(\boldsymbol{\alpha}) = \left(a_1(\boldsymbol{\alpha})\cos\theta_{\mathrm{u}} - b_1(\boldsymbol{\alpha})\sin\theta_{\mathrm{u}}\right)\sin\gamma(\boldsymbol{\alpha}) \\ &\Rightarrow \gamma(\boldsymbol{\alpha}) = \arctan\left(\frac{a_1(\boldsymbol{\alpha})\sin\theta_{\mathrm{u}} + b_1(\boldsymbol{\alpha})\cos\theta_{\mathrm{u}}}{a_1(\boldsymbol{\alpha})\cos\theta_{\mathrm{u}} - b_1(\boldsymbol{\alpha})\sin\theta_{\mathrm{u}}}\right), \end{aligned} \tag{2.29}$$

where $u_{\mathrm{s},1}^d(\boldsymbol{\alpha})$ and $u_{\mathrm{s},1}^q(\boldsymbol{\alpha})$ are the direct and quadrature components of $\boldsymbol{u}_{\mathrm{s},1}^k(\boldsymbol{\alpha})$ in the dq-reference frame. Note that $\gamma(\boldsymbol{\alpha})$ depends on $\boldsymbol{\alpha}$ in contrast to the case when QWS is dropped (see (2.23)), since both Fourier coefficients

$$\begin{aligned} a_\nu(\boldsymbol{\alpha}) \overset{(2.7)}{=} &\frac{2}{\pi}\int_0^{\pi} u_{\mathrm{o}}^u\left(\theta_{\mathrm{r}}+\gamma(\boldsymbol{\alpha})\right)\cos\left(\nu\left(\theta_{\mathrm{r}}+\gamma(\boldsymbol{\alpha})\right)\right) d\left(\theta_{\mathrm{r}}+\gamma(\boldsymbol{\alpha})\right) \\ = &\frac{2}{\pi}\int_0^{\alpha_1} \frac{u_{\mathrm{dc}}}{2}\cos\left(\nu\left(\theta_{\mathrm{r}}+\gamma(\boldsymbol{\alpha})\right)\right) d\left(\theta_{\mathrm{r}}+\gamma(\boldsymbol{\alpha})\right) \\ &-\frac{2}{\pi}\int_{\alpha_1}^{\alpha_2} \frac{u_{\mathrm{dc}}}{2}\cos\left(\nu\left(\theta_{\mathrm{r}}+\gamma(\boldsymbol{\alpha})\right)\right) d\left(\theta_{\mathrm{r}}+\gamma(\boldsymbol{\alpha})\right) \\ &+\frac{2}{\pi}\int_{\alpha_{\ell-1}}^{\alpha_\ell} \frac{u_{\mathrm{dc}}}{2}\cos\left(\nu\left(\theta_{\mathrm{r}}+\gamma(\boldsymbol{\alpha})\right)\right) d\left(\theta_{\mathrm{r}}+\gamma(\boldsymbol{\alpha})\right) \\ &-\frac{2}{\pi}\int_{\alpha_\ell}^{\pi} \frac{u_{\mathrm{dc}}}{2}\cos\left(\nu\left(\theta_{\mathrm{r}}+\gamma(\boldsymbol{\alpha})\right)\right) d\left(\theta_{\mathrm{r}}+\gamma(\boldsymbol{\alpha})\right) \\ = &\frac{2u_{\mathrm{dc}}}{\nu\pi}\sum_{i=1}^{\ell}(-1)^{i+1}\sin(\nu\alpha_i) \end{aligned} \tag{2.30}$$

and

$$
\begin{aligned}
b_\nu(\boldsymbol{\alpha}) \overset{(2.7)}{=} & \frac{2}{\pi}\int_0^{\pi} u_{\mathrm{o}}^{u}\left(\theta_{\mathrm{r}}+\gamma(\boldsymbol{\alpha})\right)\sin\left(\nu\left(\theta_{\mathrm{r}}+\gamma(\boldsymbol{\alpha})\right)\right) d\left(\theta_{\mathrm{r}}+\gamma(\boldsymbol{\alpha})\right) \\
= & \frac{2}{\pi}\int_0^{\alpha_1} \frac{u_{\mathrm{dc}}}{2}\sin\left(\nu\left(\theta_{\mathrm{r}}+\gamma(\boldsymbol{\alpha})\right)\right) d\left(\theta_{\mathrm{r}}+\gamma(\boldsymbol{\alpha})\right) \\
& -\frac{2}{\pi}\int_{\alpha_1}^{\alpha_2} \frac{u_{\mathrm{dc}}}{2}\sin\left(\nu\left(\theta_{\mathrm{r}}+\gamma(\boldsymbol{\alpha})\right)\right) d\left(\theta_{\mathrm{r}}+\gamma(\boldsymbol{\alpha})\right) \\
& +\frac{2}{\pi}\int_{\alpha_{\ell-1}}^{\alpha_\ell} \frac{u_{\mathrm{dc}}}{2}\sin\left(\nu\left(\theta_{\mathrm{r}}+\gamma(\boldsymbol{\alpha})\right)\right) d\left(\theta_{\mathrm{r}}+\gamma(\boldsymbol{\alpha})\right) \\
& -\frac{2}{\pi}\int_{\alpha_\ell}^{\pi} \frac{u_{\mathrm{dc}}}{2}\sin\left(\nu\left(\theta_{\mathrm{r}}+\gamma(\boldsymbol{\alpha})\right)\right) d\left(\theta_{\mathrm{r}}+\gamma(\boldsymbol{\alpha})\right) \\
= & \frac{2u_{\mathrm{dc}}}{\nu\pi}\left(1+\sum_{i=1}^{\ell}(-1)^i\cos(\nu\alpha_i)\right)
\end{aligned}
\tag{2.31}
$$

are not zero.

The different symmetry conditions on the PWM waveform have been thoroughly investigated in [42–47,53–56] when the SHEPWM strategy is employed for inverter control. In [42–45,53,54], the optimized switching angles for SHEPWM are presented, when the PWM waveform possesses only HWS, while QWS is eliminated. In [53], multiple sets of solutions are reported for three-level inverter and classified in terms of harmonic distribution, pulsewidth and total harmonic distortion. Furthermore, different HWS formulations have been considered in [46, 47] and the SHEPWM solutions have been evaluated in terms of harmonic performance. In addition to QWS, HWS is also dropped in [42, 43], [55] and [56] for a two-, three- and five-level inverter, respectively. However, this leads to the presence of undesirable even order harmonics in the PWM waveform.

On the contrary, little research on the PWM waveform symmetry conditions has been conducted for SOPWM [61,62,66,87,88]. The QWS condition is relaxed in [61,62] and in [87,88] for two- and three-level inverter fed induction motor drives, respectively, and improved solutions are obtained. [66] focuses on enhancing the performance of a highly anisotropic PMSM and compares the optimization results with those of an isotropic PMSM. It is concluded, that the differences between the optimization results of an isotropic and anisotropic PMSM are minimal, when the QWS is preserved. However, the opposite is true, when the QWS condition is dropped. Thereupon, only half-wave symmetric PWM waveforms are utilized in this thesis. The content of [66] will be revised and extended in this thesis by using a higher pulse number and by validating the outcomes with experimental results.

The motor phase voltages $\boldsymbol{u}_{\mathrm{s}}^{uvw}(\boldsymbol{\alpha})$ in the three-phase system (see (2.27)) can be transformed into the synchronously rotating dq-coordinate system using the Clarke-Park transformation

$$
\boldsymbol{u}_{\mathrm{s}}^{k}(\boldsymbol{\alpha}) := \begin{pmatrix} u_{\mathrm{s}}^{d}(\boldsymbol{\alpha}) \\ u_{\mathrm{s}}^{q}(\boldsymbol{\alpha}) \end{pmatrix} = \boldsymbol{u}_{\mathrm{s},1}^{k}(\boldsymbol{\alpha}) + \boldsymbol{u}_{\mathrm{s,h}}^{k}(\boldsymbol{\alpha}) = \boldsymbol{T}_{\mathrm{p}}^{-1}(\theta_{\mathrm{r}})\boldsymbol{T}_{\mathrm{c}}\boldsymbol{u}_{\mathrm{s}}^{uvw}(\boldsymbol{\alpha}), \tag{2.32}
$$

where

$$
\boldsymbol{T}_{\mathrm{c}} := \frac{2}{3}\begin{bmatrix} 1 & -\frac{1}{2} & -\frac{1}{2} \\ 0 & \frac{\sqrt{3}}{2} & -\frac{\sqrt{3}}{2} \end{bmatrix} \qquad \text{and} \qquad \boldsymbol{T}_{\mathrm{p}}(\theta_{\mathrm{r}}) := \begin{bmatrix} \cos(\theta_{\mathrm{r}}) & -\sin(\theta_{\mathrm{r}}) \\ \sin(\theta_{\mathrm{r}}) & \cos(\theta_{\mathrm{r}}) \end{bmatrix} \tag{2.33}
$$

are the Clarke-Park transformation matrices [99, Chapter 14], respectively. It should be noted, that a balanced three-phase system is assumed and, thus, no zero components exist in the

Clarke-Park transformation matrices. Solving (2.32), the fundamental voltage component in the dq-reference frame is given by

$$\boldsymbol{u}_{\mathrm{s},1}^{k}(\boldsymbol{\alpha}) \overset{(2.32)}{:=} \begin{pmatrix} u_{\mathrm{s},1}^{d}(\boldsymbol{\alpha}) \\ u_{\mathrm{s},1}^{q}(\boldsymbol{\alpha}) \end{pmatrix} = \begin{pmatrix} a_1(\boldsymbol{\alpha})\cos\gamma(\boldsymbol{\alpha}) + b_1(\boldsymbol{\alpha})\sin\gamma(\boldsymbol{\alpha}) \\ a_1(\boldsymbol{\alpha})\sin\gamma(\boldsymbol{\alpha}) - b_1(\boldsymbol{\alpha})\cos\gamma(\boldsymbol{\alpha}) \end{pmatrix} \tag{2.34}$$

and the voltage harmonic content is expressed by

$$\begin{aligned} \boldsymbol{u}_{\mathrm{s,h}}^{k}(\boldsymbol{\alpha}) \overset{(2.32)}{:=} \sum_{\nu=6i}^{\infty} \boldsymbol{u}_{\mathrm{s},\nu}^{k}(\boldsymbol{\alpha}) &= \sum_{\nu=6i}^{\infty} \begin{pmatrix} u_{\mathrm{s},\nu}^{d}(\boldsymbol{\alpha}) \\ u_{\mathrm{s},\nu}^{q}(\boldsymbol{\alpha}) \end{pmatrix} \\ &= \sum_{\nu=6i}^{\infty} \begin{pmatrix} a_{\nu-1}(\boldsymbol{\alpha})\cos\left(\nu\theta_{\mathrm{r}}+(\nu-1)\gamma(\boldsymbol{\alpha})\right) + a_{\nu+1}(\boldsymbol{\alpha})\cos\left(\nu\theta_{\mathrm{r}}+(\nu+1)\gamma(\boldsymbol{\alpha})\right) \\ -a_{\nu-1}(\boldsymbol{\alpha})\sin\left(\nu\theta_{\mathrm{r}}+(\nu-1)\gamma(\boldsymbol{\alpha})\right) + a_{\nu+1}(\boldsymbol{\alpha})\sin\left(\nu\theta_{\mathrm{r}}+(\nu+1)\gamma(\boldsymbol{\alpha})\right) \end{pmatrix} \\ &+ \sum_{\nu=6i}^{\infty} \begin{pmatrix} b_{\nu-1}(\boldsymbol{\alpha})\sin\left(\nu\theta_{\mathrm{r}}+(\nu-1)\gamma(\boldsymbol{\alpha})\right) + b_{\nu+1}(\boldsymbol{\alpha})\sin\left(\nu\theta_{\mathrm{r}}+(\nu+1)\gamma(\boldsymbol{\alpha})\right) \\ b_{\nu-1}(\boldsymbol{\alpha})\cos\left(\nu\theta_{\mathrm{r}}+(\nu-1)\gamma(\boldsymbol{\alpha})\right) - b_{\nu+1}(\boldsymbol{\alpha})\cos\left(\nu\theta_{\mathrm{r}}+(\nu+1)\gamma(\boldsymbol{\alpha})\right) \end{pmatrix}. \end{aligned} \tag{2.35}$$

It is worth mentioning the fact that the two orthogonal voltage components in the dq-reference frame contain harmonic components of multiples of six, i.e. $\nu = 6i$ in (2.35), while the motor voltages in the uvw-reference frame contain harmonics multiples of $6i\pm1$ (see $\mathcal{H}$ in (2.27)), where $i \in \mathbb{N}$.

Applying the phasor theory (see Sec. 2.1.3), the machine voltage harmonics of (2.35) can be represented in polar form by

$$\begin{aligned} \mathbf{U}_{\mathrm{s,h}}^{k}(\boldsymbol{\alpha}) \overset{(2.35)}{=} &\sum_{\nu=6i}^{\infty} \begin{pmatrix} a_{\nu-1}(\boldsymbol{\alpha})\angle\big(\nu\phi_0 + (\nu-1)\gamma(\boldsymbol{\alpha})\big) + a_{\nu+1}(\boldsymbol{\alpha})\angle\big(\nu\phi_0 + (\nu+1)\gamma(\boldsymbol{\alpha})\big) \\ -a_{\nu-1}(\boldsymbol{\alpha})\angle\big(\nu\phi_0 + (\nu-1)\gamma(\boldsymbol{\alpha}) - \frac{\pi}{2}\big) + a_{\nu+1}(\boldsymbol{\alpha})\angle\big(\nu\phi_0 + (\nu+1)\gamma(\boldsymbol{\alpha}) - \frac{\pi}{2}\big) \end{pmatrix} \\ &+ \sum_{\nu=6i}^{\infty} \begin{pmatrix} b_{\nu-1}(\boldsymbol{\alpha})\angle\big(\nu\phi_0 + (\nu-1)\gamma(\boldsymbol{\alpha}) - \frac{\pi}{2}\big) + b_{\nu+1}(\boldsymbol{\alpha})\angle\big(\nu\phi_0 + (\nu+1)\gamma(\boldsymbol{\alpha}) - \frac{\pi}{2}\big) \\ b_{\nu-1}(\boldsymbol{\alpha})\angle\big(\nu\phi_0 + (\nu-1)\gamma(\boldsymbol{\alpha})\big) - b_{\nu+1}(\boldsymbol{\alpha})\angle\big(\nu\phi_0 + (\nu+1)\gamma(\boldsymbol{\alpha})\big) \end{pmatrix}. \end{aligned} \tag{2.36}$$

This representation will facilitate the derivation of the motor currents expressions, described in the next subsection.

2.2.2 Machine phase currents

In this subsection, the expressions of the machine phase currents with respect to the inverter switching angles are deduced. For this purpose, the voltage equations of an anisotropic IPMSM [22, 100]

$$\boldsymbol{u}_{\mathrm{s}}^{k}(\boldsymbol{\alpha}) = \begin{bmatrix} R_{\mathrm{s}} & -\omega_{\mathrm{r}}L_{\mathrm{s}}^{q} \\ \omega_{\mathrm{r}}L_{\mathrm{s}}^{d} & R_{\mathrm{s}} \end{bmatrix} \boldsymbol{i}_{\mathrm{s}}^{k}(\boldsymbol{\alpha}) + \begin{bmatrix} L_{\mathrm{s}}^{d} & 0 \\ 0 & L_{\mathrm{s}}^{q} \end{bmatrix} \frac{\mathrm{d}}{\mathrm{d}t}\boldsymbol{i}_{\mathrm{s}}^{k}(\boldsymbol{\alpha}) + \begin{pmatrix} 0 \\ \omega_{\mathrm{r}}\psi_{\mathrm{PM}} \end{pmatrix} \tag{2.37}$$

in the dq-reference frame and steady-state operation are used, where R_{s}[1] is the stator resistance, ψ_{PM} is the PM flux linkage, L_{s}^{d}, L_{s}^{q} are the stator self-inductances in the dq-reference frame and

$$\boldsymbol{i}_{\mathrm{s}}^{k}(\boldsymbol{\alpha}) := \boldsymbol{i}_{\mathrm{s},1}^{k}(\boldsymbol{\alpha}) + \sum_{\nu=1}^{\infty} \boldsymbol{i}_{\mathrm{s},\nu}^{k}(\boldsymbol{\alpha}) \tag{2.38}$$

[1] The stator resistance is usually identical for all three windings, i.e. $R_{\mathrm{s}} = R_{\mathrm{s}}^{u} = R_{\mathrm{s}}^{v} = R_{\mathrm{s}}^{w}$.

are the machine phase currents in the dq-reference frame expressed as a function of the fundamental current

$$\boldsymbol{i}^k_{\mathrm{s},1}(\boldsymbol{\alpha}) := \left(i^d_{\mathrm{s},1}(\boldsymbol{\alpha}),\ \ i^q_{\mathrm{s},1}(\boldsymbol{\alpha})\right)^\top \tag{2.39}$$

and the current harmonic components

$$\boldsymbol{i}^k_{\mathrm{s},\nu}(\boldsymbol{\alpha}) := \left(i^d_{\mathrm{s},\nu}(\boldsymbol{\alpha}),\ \ i^q_{\mathrm{s},\nu}(\boldsymbol{\alpha})\right)^\top . \tag{2.40}$$

The expression of the phase voltages $\boldsymbol{u}^k_{\mathrm{s}}(\boldsymbol{\alpha})$ has been derived in the previous subsection (see Sec. 2.2.1) under the assumptions of a constant dc-link voltage u_{dc} (A1) and ideal semiconductor switches (A2). Moreover, the IPMSM model (2.37) is deduced under the following assumptions:

(A3) The cross-coupling (mutual) inductance of the machine is neglected (see (2.37)).

(A4) The harmonic content of ψ_{PM} is neglected in (2.37) for reasons of simplicity and the back-EMF voltages are considered to be sinusoidal.[2]

(A5) The stator self-inductances L^d_{s}, L^q_{s} and PM flux linkage ψ_{PM} depend on the *fundamental* currents $\boldsymbol{i}^k_{\mathrm{s},1}$ and, thus, remain constant in steady-state operation [101].

(A6) The influence of the motor temperature on the parameters L^d_{s}, L^q_{s}, ψ_{PM} and R_{s} is neglected.

The motor fundamental currents in the dq-reference frame are time-invariant assuming steady-state operation and, thus, $\frac{\mathrm{d}}{\mathrm{d}t}\boldsymbol{i}^k_{\mathrm{s},1}(\boldsymbol{\alpha}) = 0$. Consequently, the fundamental voltage component is given by

$$\boldsymbol{u}^k_{\mathrm{s},1}(\boldsymbol{\alpha}) \overset{(2.37)}{=} \begin{bmatrix} R_{\mathrm{s}} & -\omega_{\mathrm{r}} L^q_{\mathrm{s}} \\ \omega_{\mathrm{r}} L^d_{\mathrm{s}} & R_{\mathrm{s}} \end{bmatrix} \boldsymbol{i}^k_{\mathrm{s},1}(\boldsymbol{\alpha}) + \begin{pmatrix} 0 \\ \omega_{\mathrm{r}} \psi_{\mathrm{PM}} \end{pmatrix} \tag{2.41}$$

and the ν-th voltage component by

$$\boldsymbol{u}^k_{\mathrm{s},\nu}(\boldsymbol{\alpha}) \overset{(2.37)}{=} \begin{bmatrix} R_{\mathrm{s}} & -\nu\omega_{\mathrm{r}} L^q_{\mathrm{s}} \\ \nu\omega_{\mathrm{r}} L^d_{\mathrm{s}} & R_{\mathrm{s}} \end{bmatrix} \boldsymbol{i}^k_{\mathrm{s},\nu}(\boldsymbol{\alpha}) + \begin{bmatrix} L^d_{\mathrm{s}} & 0 \\ 0 & L^q_{\mathrm{s}} \end{bmatrix} \frac{\mathrm{d}}{\mathrm{d}t} \boldsymbol{i}^k_{\mathrm{s},\nu}(\boldsymbol{\alpha}). \tag{2.42}$$

Solving (2.41) for the motor fundamental currents, one obtains

$$\boldsymbol{i}^k_{\mathrm{s},1}(\boldsymbol{\alpha}) \overset{(2.41)}{=} \frac{1}{R^2_{\mathrm{s}} + \omega^2_{\mathrm{r}} L^d_{\mathrm{s}} L^q_{\mathrm{s}}} \begin{bmatrix} R_{\mathrm{s}} & \omega_{\mathrm{r}} L^q_{\mathrm{s}} \\ -\omega_{\mathrm{r}} L^d_{\mathrm{s}} & R_{\mathrm{s}} \end{bmatrix} \left(\boldsymbol{u}^k_{\mathrm{s},1}(\boldsymbol{\alpha}) - \begin{pmatrix} 0 \\ \omega_{\mathrm{r}} \psi_{\mathrm{PM}} \end{pmatrix} \right). \tag{2.43}$$

In order to find the respective formulations for the current harmonic components, the phasor theory should be applied. Eq. (2.42) can be written in the phasor domain by

$$\mathbf{U}^k_{\mathrm{s},\nu}(\boldsymbol{\alpha}) = \overbrace{\begin{bmatrix} R_{\mathrm{s}} + j\nu\omega_{\mathrm{r}} L^d_{\mathrm{s}} & -\omega_{\mathrm{r}} L^q_{\mathrm{s}} \\ \omega_{\mathrm{r}} L^d_{\mathrm{s}} & R_{\mathrm{s}} + j\nu\omega_{\mathrm{r}} L^q_{\mathrm{s}} \end{bmatrix}}^{:=\boldsymbol{H}^{-1}_\nu} \mathbf{I}^k_{\mathrm{s},\nu}(\boldsymbol{\alpha}). \tag{2.44}$$

Solving (2.44) for the motor harmonic currents, one obtains

$$\begin{aligned} \mathbf{I}^k_{\mathrm{s},\nu}(\boldsymbol{\alpha}) &= \boldsymbol{H}_\nu \mathbf{U}^k_{\mathrm{s},\nu}(\boldsymbol{\alpha}) \\ &= \frac{1}{R^2_{\mathrm{s}} + (1-\nu^2)\omega^2_{\mathrm{r}} L^d_{\mathrm{s}} L^q_{\mathrm{s}} + j\nu\omega_{\mathrm{r}} R_{\mathrm{s}} (L^d_{\mathrm{s}} + L^q_{\mathrm{s}})} \begin{bmatrix} R_{\mathrm{s}} + j\nu\omega_{\mathrm{r}} L^q_{\mathrm{s}} & \omega_{\mathrm{r}} L^q_{\mathrm{s}} \\ -\omega_{\mathrm{r}} L^d_{\mathrm{s}} & R_{\mathrm{s}} + j\nu\omega_{\mathrm{r}} L^d_{\mathrm{s}} \end{bmatrix} \mathbf{U}^k_{\mathrm{s},\nu}(\boldsymbol{\alpha}) \\ &= \begin{bmatrix} H_{\mathrm{dd},\nu} & H_{\mathrm{dq},\nu} \\ H_{\mathrm{qd},\nu} & H_{\mathrm{qq},\nu} \end{bmatrix} \mathbf{U}^k_{\mathrm{s},\nu}(\boldsymbol{\alpha}) \end{aligned} \tag{2.45}$$

[2] The back-EMF voltage harmonic distortion of the used PMSM is rather small (6.4% at 650Hz and $\boldsymbol{i}^k_{\mathrm{s}}{=}(0,0)^\top$).

with coefficients [33]

$$
\begin{aligned}
H_{\mathrm{dd},\nu} :=& \frac{R_\mathrm{s} + j\nu\omega_\mathrm{r} L_\mathrm{s}^q}{R_\mathrm{s}^2 + (1-\nu^2)\omega_\mathrm{r}^2 L_\mathrm{s}^d L_\mathrm{s}^q + j\nu\omega_\mathrm{r} R_\mathrm{s}(L_\mathrm{s}^d + L_\mathrm{s}^q)} \\
=& \frac{\Big(R_\mathrm{s} + j\nu\omega_\mathrm{r} L_\mathrm{s}^q\Big)\Big(R_\mathrm{s}^2 + (1-\nu^2)\omega_\mathrm{r}^2 L_\mathrm{s}^d L_\mathrm{s}^q - j\nu\omega_\mathrm{r} R_\mathrm{s}(L_\mathrm{s}^d + L_\mathrm{s}^q)\Big)}{\Big(R_\mathrm{s}^2 + (1-\nu^2)\omega_\mathrm{r}^2 L_\mathrm{s}^d L_\mathrm{s}^q + j\nu\omega_\mathrm{r} R_\mathrm{s}(L_\mathrm{s}^d + L_\mathrm{s}^q)\Big)\Big(R_\mathrm{s}^2 + (1-\nu^2)\omega_\mathrm{r}^2 L_\mathrm{s}^d L_\mathrm{s}^q - j\nu\omega_\mathrm{r} R_\mathrm{s}(L_\mathrm{s}^d + L_\mathrm{s}^q)\Big)} \\
=& \frac{R_\mathrm{s}\Big(R_\mathrm{s}^2 + (1-\nu^2)\omega_\mathrm{r}^2 L_\mathrm{s}^d L_\mathrm{s}^q\Big) + \nu^2\omega_\mathrm{r}^2 L_\mathrm{s}^q R_\mathrm{s}(L_\mathrm{s}^d + L_\mathrm{s}^q)}{\Big(R_\mathrm{s} + (1-\nu^2)\omega_\mathrm{r}^2 L_\mathrm{s}^d L_\mathrm{s}^q\Big)^2 + \Big(\nu\omega_\mathrm{r} R_\mathrm{s}(L_\mathrm{s}^d + L_\mathrm{s}^q)\Big)^2} \\
&+ j\frac{\nu\omega_\mathrm{r} L_\mathrm{s}^q\Big(R_\mathrm{s}^2 + (1-\nu^2)\omega_\mathrm{r}^2 L_\mathrm{s}^d L_\mathrm{s}^q\Big) - \nu\omega_\mathrm{r} R_\mathrm{s}^2(L_\mathrm{s}^d + L_\mathrm{s}^q)}{\Big(R_\mathrm{s} + (1-\nu^2)\omega_\mathrm{r}^2 L_\mathrm{s}^d L_\mathrm{s}^q\Big)^2 + \Big(\nu\omega_\mathrm{r} R_\mathrm{s}(L_\mathrm{s}^d + L_\mathrm{s}^q)\Big)^2} \\
=& \underbrace{\frac{R_\mathrm{s}\Big(R_\mathrm{s}^2 + \omega_\mathrm{r}^2 L_\mathrm{s}^d L_\mathrm{s}^q + \nu^2\omega_\mathrm{r}^2 (L_\mathrm{s}^q)^2\Big)}{\Big(R_\mathrm{s}^2 + (1-\nu^2)\omega_\mathrm{r}^2 L_\mathrm{s}^d L_\mathrm{s}^q\Big)^2 + \Big(\nu\omega_\mathrm{r} R_\mathrm{s}(L_\mathrm{s}^d + L_\mathrm{s}^q)\Big)^2}}_{:=K_1} \\
&+ j\underbrace{\frac{\nu\omega_\mathrm{r} L_\mathrm{s}^d\Big(-R_\mathrm{s}^2 + \omega_\mathrm{r}^2 (L_\mathrm{s}^q)^2(1-\nu^2)\Big)}{\Big(R_\mathrm{s}^2 + (1-\nu^2)\omega_\mathrm{r}^2 L_\mathrm{s}^d L_\mathrm{s}^q\Big)^2 + \Big(\nu\omega_\mathrm{r} R_\mathrm{s}(L_\mathrm{s}^d + L_\mathrm{s}^q)\Big)^2}}_{:=K_2} = \sqrt{K_1^2 + K_2^2}\angle \arctan\left(\frac{K_2}{K_1}\right) \\
=& \underbrace{\sqrt{\frac{R_\mathrm{s}^2 + \nu^2\omega_\mathrm{r}^2 (L_\mathrm{s}^q)^2}{A}}}_{:=h_{\mathrm{dd},\nu}} \angle \underbrace{\arctan\left[\frac{\nu\omega_\mathrm{r} L_\mathrm{s}^d(-R_\mathrm{s}^2 + \omega_\mathrm{r}^2 (L_\mathrm{s}^q)^2(1-\nu^2))}{R_\mathrm{s}(R_\mathrm{s}^2 + \omega_\mathrm{r}^2 L_\mathrm{s}^d L_\mathrm{s}^q + \nu^2\omega_\mathrm{r}^2 (L_\mathrm{s}^q)^2)}\right]}_{:=\theta_{\mathrm{dd},\nu}},
\end{aligned}
\tag{2.46}
$$

$$
\begin{aligned}
H_{\mathrm{dq},\nu} :=& \frac{\omega_\mathrm{r} L_\mathrm{s}^q}{R_\mathrm{s}^2 + (1-\nu^2)\omega_\mathrm{r}^2 L_\mathrm{s}^d L_\mathrm{s}^q + j\nu\omega_\mathrm{r} R_\mathrm{s}(L_\mathrm{s}^d + L_\mathrm{s}^q)} \\
=& \frac{\omega_\mathrm{r} L_\mathrm{s}^q\left(R_\mathrm{s}^2 + (1-\nu^2)\omega_\mathrm{r}^2 L_\mathrm{s}^d L_\mathrm{s}^q - j\nu\omega_\mathrm{r} R_\mathrm{s}(L_\mathrm{s}^d + L_\mathrm{s}^q)\right)}{\left(R_\mathrm{s}^2 + (1-\nu^2)\omega_\mathrm{r}^2 L_\mathrm{s}^d L_\mathrm{s}^q + j\nu\omega_\mathrm{r} R_\mathrm{s}(L_\mathrm{s}^d + L_\mathrm{s}^q)\right)\left(R_\mathrm{s}^2 + (1-\nu^2)\omega_\mathrm{r}^2 L_\mathrm{s}^d L_\mathrm{s}^q - j\nu\omega_\mathrm{r} R_\mathrm{s}(L_\mathrm{s}^d + L_\mathrm{s}^q)\right)} \\
=& \underbrace{\frac{\omega_\mathrm{r} L_\mathrm{s}^q\Big(R_\mathrm{s}^2 + (1-\nu^2)\omega_\mathrm{r}^2 L_\mathrm{s}^d L_\mathrm{s}^q\Big)}{\Big(R_\mathrm{s}^2 + (1-\nu^2)\omega_\mathrm{r}^2 L_\mathrm{s}^d L_\mathrm{s}^q\Big)^2 + \Big(\nu\omega_\mathrm{r} R_\mathrm{s}(L_\mathrm{s}^d + L_\mathrm{s}^q)\Big)^2}}_{:=K_3} \\
&+ j\underbrace{\frac{-\nu\omega_\mathrm{r}^2 R_\mathrm{s} L_\mathrm{s}^q(L_\mathrm{s}^d + L_\mathrm{s}^q)}{\Big(R_\mathrm{s}^2 + (1-\nu^2)\omega_\mathrm{r}^2 L_\mathrm{s}^d L_\mathrm{s}^q\Big)^2 + \Big(\nu\omega_\mathrm{r} R_\mathrm{s}(L_\mathrm{s}^d + L_\mathrm{s}^q)\Big)^2}}_{:=K_4} \\
=& \sqrt{K_3^2 + K_4^2}\angle \arctan\left(\frac{K_4}{K_3}\right) = \underbrace{\frac{\omega_\mathrm{r} L_\mathrm{s}^q}{\sqrt{A}}}_{:=h_{\mathrm{dq},\nu}} \angle \underbrace{\arctan\left[\frac{-\nu\omega_\mathrm{r} R_\mathrm{s}(L_\mathrm{s}^d + L_\mathrm{s}^q)}{R_\mathrm{s}^2 + \omega_\mathrm{r}^2 L_\mathrm{s}^d L_\mathrm{s}^q(1-\nu^2)}\right]}_{:=\theta_{\mathrm{dq},\nu}},
\end{aligned}
\tag{2.47}
$$

$$
\begin{aligned}
H_{\mathrm{qd},\nu} :=& \frac{-\omega_\mathrm{r} L_\mathrm{s}^d}{R_\mathrm{s}^2 + (1-\nu^2)\omega_\mathrm{r}^2 L_\mathrm{s}^d L_\mathrm{s}^q + j\nu\omega_\mathrm{r} R_\mathrm{s}(L_\mathrm{s}^d + L_\mathrm{s}^q)} \\
=& \frac{-\omega_\mathrm{r} L_\mathrm{s}^d \left(R_\mathrm{s}^2 + (1-\nu^2)\omega_\mathrm{r}^2 L_\mathrm{s}^d L_\mathrm{s}^q - j\nu\omega_\mathrm{r} R_\mathrm{s}(L_\mathrm{s}^d + L_\mathrm{s}^q)\right)}{\left(R_\mathrm{s}^2 + (1-\nu^2)\omega_\mathrm{r}^2 L_\mathrm{s}^d L_\mathrm{s}^q + j\nu\omega_\mathrm{r} R_\mathrm{s}(L_\mathrm{s}^d + L_\mathrm{s}^q)\right)\left(R_\mathrm{s}^2 + (1-\nu^2)\omega_\mathrm{r}^2 L_\mathrm{s}^d L_\mathrm{s}^q - j\nu\omega_\mathrm{r} R_\mathrm{s}(L_\mathrm{s}^d + L_\mathrm{s}^q)\right)} \\
=& \underbrace{\frac{-\omega_\mathrm{r} L_\mathrm{s}^d \left(R_\mathrm{s}^2 + \omega_\mathrm{r}^2 L_\mathrm{s}^d L_\mathrm{s}^q (1-\nu^2)\right)}{\left(R_\mathrm{s}^2 + (1-\nu^2)\omega_\mathrm{r}^2 L_\mathrm{s}^d L_\mathrm{s}^q\right)^2 + \left(\nu\omega_\mathrm{r} R_\mathrm{s}(L_\mathrm{s}^d + L_\mathrm{s}^q)\right)^2}}_{:=K_5} \\
& + j \underbrace{\frac{\nu\omega_\mathrm{r}^2 R_\mathrm{s} L_\mathrm{s}^d (L_\mathrm{s}^d + L_\mathrm{s}^q)}{\left(R_\mathrm{s}^2 + (1-\nu^2)\omega_\mathrm{r}^2 L_\mathrm{s}^d L_\mathrm{s}^q\right)^2 + \left(\nu\omega_\mathrm{r} R_\mathrm{s}(L_\mathrm{s}^d + L_\mathrm{s}^q)\right)^2}}_{:=K_6} \\
=& \sqrt{K_5^2 + K_6^2} \angle \arctan\left(\frac{K_6}{K_5}\right) = \underbrace{\frac{\omega_\mathrm{r} L_\mathrm{s}^d}{\sqrt{A}}}_{:=h_{\mathrm{qd},\nu}} \angle \underbrace{\arctan\left[\frac{\nu\omega_\mathrm{r} R_\mathrm{s}(L_\mathrm{s}^d + L_\mathrm{s}^q)}{-R_\mathrm{s}^2 + \omega_\mathrm{r}^2 L_\mathrm{s}^d L_\mathrm{s}^q(\nu^2-1)}\right]}_{:=\theta_{\mathrm{qd},\nu} = \theta_{\mathrm{dq},\nu} \pm \pi} \qquad \text{and}
\end{aligned}
\tag{2.48}
$$

$$
\begin{aligned}
H_{\mathrm{qq},\nu} :=& \frac{R_\mathrm{s} + j\nu\omega_\mathrm{r} L_\mathrm{s}^d}{R_\mathrm{s}^2 + (1-\nu^2)\omega_\mathrm{r}^2 L_\mathrm{s}^d L_\mathrm{s}^q + j\nu\omega_\mathrm{r} R_\mathrm{s}(L_\mathrm{s}^d + L_\mathrm{s}^q)} \\
=& \frac{\left(R_\mathrm{s} + j\nu\omega_\mathrm{r} L_\mathrm{s}^d\right)\left(R_\mathrm{s}^2 + (1-\nu^2)\omega_\mathrm{r}^2 L_\mathrm{s}^d L_\mathrm{s}^q - j\nu\omega_\mathrm{r} R_\mathrm{s}(L_\mathrm{s}^d + L_\mathrm{s}^q)\right)}{\left(R_\mathrm{s}^2 + (1-\nu^2)\omega_\mathrm{r}^2 L_\mathrm{s}^d L_\mathrm{s}^q + j\nu\omega_\mathrm{r} R_\mathrm{s}(L_\mathrm{s}^d + L_\mathrm{s}^q)\right)\left(R_\mathrm{s}^2 + (1-\nu^2)\omega_\mathrm{r}^2 L_\mathrm{s}^d L_\mathrm{s}^q - j\nu\omega_\mathrm{r} R_\mathrm{s}(L_\mathrm{s}^d + L_\mathrm{s}^q)\right)} \\
=& \frac{R_\mathrm{s}\left(R_\mathrm{s}^2 + (1-\nu^2)\omega_\mathrm{r}^2 L_\mathrm{s}^d L_\mathrm{s}^q\right) + \nu^2\omega_\mathrm{r}^2 L_\mathrm{s}^d R_\mathrm{s}(L_\mathrm{s}^d + L_\mathrm{s}^q)}{\left(R_\mathrm{s} + (1-\nu^2)\omega_\mathrm{r}^2 L_\mathrm{s}^d L_\mathrm{s}^q\right)^2 + \left(\nu\omega_\mathrm{r} R_\mathrm{s}(L_\mathrm{s}^d + L_\mathrm{s}^q)\right)^2} \\
& + j\frac{\nu\omega_\mathrm{r} L_\mathrm{s}^d\left(R_\mathrm{s}^2 + (1-\nu^2)\omega_\mathrm{r}^2 L_\mathrm{s}^d L_\mathrm{s}^q\right) - \nu\omega_\mathrm{r} R_\mathrm{s}^2(L_\mathrm{s}^d + L_\mathrm{s}^q)}{\left(R_\mathrm{s} + (1-\nu^2)\omega_\mathrm{r}^2 L_\mathrm{s}^d L_\mathrm{s}^q\right)^2 + \left(\nu\omega_\mathrm{r} R_\mathrm{s}(L_\mathrm{s}^d + L_\mathrm{s}^q)\right)^2} \\
=& \underbrace{\frac{R_\mathrm{s}\left(R_\mathrm{s}^2 + \omega_\mathrm{r}^2 L_\mathrm{s}^d L_\mathrm{s}^q + \nu^2\omega_\mathrm{r}^2 (L_\mathrm{s}^d)^2\right)}{\left(R_\mathrm{s}^2 + (1-\nu^2)\omega_\mathrm{r}^2 L_\mathrm{s}^d L_\mathrm{s}^q\right)^2 + \left(\nu\omega_\mathrm{r} R_\mathrm{s}(L_\mathrm{s}^d + L_\mathrm{s}^q)\right)^2}}_{:=K_7} \\
& + j\underbrace{\frac{\nu\omega_\mathrm{r} L_\mathrm{s}^q\left(-R_\mathrm{s}^2 + \omega_\mathrm{r}^2 (L_\mathrm{s}^d)^2(1-\nu^2)\right)}{\left(R_\mathrm{s}^2 + (1-\nu^2)\omega_\mathrm{r}^2 L_\mathrm{s}^d L_\mathrm{s}^q\right)^2 + \left(\nu\omega_\mathrm{r} R_\mathrm{s}(L_\mathrm{s}^d + L_\mathrm{s}^q)\right)^2}}_{:=K_8} = \sqrt{K_7^2 + K_8^2} \angle \arctan\left(\frac{K_8}{K_7}\right) \\
=& \underbrace{\sqrt{\frac{R_\mathrm{s}^2 + \nu^2\omega_\mathrm{r}^2 (L_\mathrm{s}^d)^2}{A}}}_{:=h_{\mathrm{qq},\nu}} \angle \underbrace{\arctan\left[\frac{\nu\omega_\mathrm{r} L_\mathrm{s}^q\left(-R_\mathrm{s}^2 + \omega_\mathrm{r}^2 (L_\mathrm{s}^d)^2(1-\nu^2)\right)}{R_\mathrm{s}\left(R_\mathrm{s}^2 + \omega_\mathrm{r}^2 L_\mathrm{s}^d L_\mathrm{s}^q + \nu^2\omega_\mathrm{r}^2 (L_\mathrm{s}^d)^2\right)}\right]}_{:=\theta_{\mathrm{qq},\nu}},
\end{aligned}
\tag{2.49}
$$

where

$$
A := \left(R_\mathrm{s}^2 + (1-\nu^2) L_\mathrm{s}^d L_\mathrm{s}^q \omega_\mathrm{r}^2\right)^2 + \left(\nu\omega_\mathrm{r} R_\mathrm{s}(L_\mathrm{s}^d + L_\mathrm{s}^q)\right)^2. \tag{2.50}
$$

Eq. (2.45) can now be re-written as follows

$$
\begin{aligned}
\mathbf{I}^{k}_{\mathrm{s},\nu}(\boldsymbol{\alpha}) &= \begin{bmatrix} h_{\mathrm{dd},\nu}\angle\theta_{\mathrm{dd},\nu} & h_{\mathrm{dq},\nu}\angle\theta_{\mathrm{dq},\nu} \\ h_{\mathrm{qd},\nu}\angle\theta_{\mathrm{qd},\nu} & h_{\mathrm{qq},\nu}\angle\theta_{\mathrm{qq},\nu} \end{bmatrix} \begin{pmatrix} \mathrm{U}^{d}_{\mathrm{s},\nu}(\boldsymbol{\alpha}) \\ \mathrm{U}^{q}_{\mathrm{s},\nu}(\boldsymbol{\alpha}) \end{pmatrix} \\
&\overset{(2.36)}{=} \begin{pmatrix} h_{\mathrm{dd},\nu}a_{\nu+1}(\boldsymbol{\alpha})\angle\big(\nu\phi_0+(\nu+1)\gamma(\boldsymbol{\alpha})+\theta_{\mathrm{dd},\nu}\big) \\ h_{\mathrm{qd},\nu}a_{\nu+1}(\boldsymbol{\alpha})\angle\big(\nu\phi_0+(\nu+1)\gamma(\boldsymbol{\alpha})+\theta_{\mathrm{qd},\nu}\big) \end{pmatrix} \\
&\quad + \begin{pmatrix} h_{\mathrm{dd},\nu}a_{\nu-1}(\boldsymbol{\alpha})\angle\big(\nu\phi_0+(\nu-1)\gamma(\boldsymbol{\alpha})+\theta_{\mathrm{dd},\nu}\big) \\ h_{\mathrm{qd},\nu}a_{\nu-1}(\boldsymbol{\alpha})\angle\big(\nu\phi_0+(\nu-1)\gamma(\boldsymbol{\alpha})+\theta_{\mathrm{qd},\nu}\big) \end{pmatrix} \\
&\quad + \begin{pmatrix} h_{\mathrm{dd},\nu}b_{\nu+1}(\boldsymbol{\alpha})\angle\big(\nu\phi_0+(\nu+1)\gamma(\boldsymbol{\alpha})-\frac{\pi}{2}+\theta_{\mathrm{dd},\nu}\big) \\ h_{\mathrm{qd},\nu}b_{\nu+1}(\boldsymbol{\alpha})\angle\big(\nu\phi_0+(\nu+1)\gamma(\boldsymbol{\alpha})-\frac{\pi}{2}+\theta_{\mathrm{qd},\nu}\big) \end{pmatrix} \\
&\quad + \begin{pmatrix} h_{\mathrm{dd},\nu}b_{\nu-1}(\boldsymbol{\alpha})\angle\big(\nu\phi_0+(\nu-1)\gamma(\boldsymbol{\alpha})-\frac{\pi}{2}+\theta_{\mathrm{dd},\nu}\big) \\ h_{\mathrm{qd},\nu}b_{\nu-1}(\boldsymbol{\alpha})\angle\big(\nu\phi_0+(\nu-1)\gamma(\boldsymbol{\alpha})-\frac{\pi}{2}+\theta_{\mathrm{qd},\nu}\big) \end{pmatrix} \\
&\quad + \begin{pmatrix} h_{\mathrm{dq},\nu}a_{\nu+1}(\boldsymbol{\alpha})\angle\big(\nu\phi_0+(\nu+1)\gamma(\boldsymbol{\alpha})-\frac{\pi}{2}+\theta_{\mathrm{dq},\nu}\big) \\ h_{\mathrm{qq},\nu}a_{\nu+1}(\boldsymbol{\alpha})\angle\big(\nu\phi_0+(\nu+1)\gamma(\boldsymbol{\alpha})-\frac{\pi}{2}+\theta_{\mathrm{qq},\nu}\big) \end{pmatrix} \\
&\quad - \begin{pmatrix} h_{\mathrm{dq},\nu}a_{\nu-1}(\boldsymbol{\alpha})\angle\big(\nu\phi_0+(\nu-1)\gamma(\boldsymbol{\alpha})-\frac{\pi}{2}+\theta_{\mathrm{dq},\nu}\big) \\ h_{\mathrm{qq},\nu}a_{\nu-1}(\boldsymbol{\alpha})\angle\big(\nu\phi_0+(\nu-1)\gamma(\boldsymbol{\alpha})-\frac{\pi}{2}+\theta_{\mathrm{qq},\nu}\big) \end{pmatrix} \\
&\quad - \begin{pmatrix} h_{\mathrm{dq},\nu}b_{\nu+1}(\boldsymbol{\alpha})\angle\big(\nu\phi_0+(\nu+1)\gamma(\boldsymbol{\alpha})+\theta_{\mathrm{dq},\nu}\big) \\ h_{\mathrm{qq},\nu}b_{\nu+1}(\boldsymbol{\alpha})\angle\big(\nu\phi_0+(\nu+1)\gamma(\boldsymbol{\alpha})+\theta_{\mathrm{qq},\nu}\big) \end{pmatrix} \\
&\quad + \begin{pmatrix} h_{\mathrm{dq},\nu}b_{\nu-1}(\boldsymbol{\alpha})\angle\big(\nu\phi_0+(\nu-1)\gamma(\boldsymbol{\alpha})+\theta_{\mathrm{dq},\nu}\big) \\ h_{\mathrm{qq},\nu}b_{\nu-1}(\boldsymbol{\alpha})\angle\big(\nu\phi_0+(\nu-1)\gamma(\boldsymbol{\alpha})+\theta_{\mathrm{qq},\nu}\big) \end{pmatrix}.
\end{aligned}
\tag{2.51}
$$

Applying the phasor theory to (2.51), the motor harmonic current can be transformed into the time domain

$$
\begin{aligned}
\boldsymbol{i}^{k}_{\mathrm{s,h}}(\boldsymbol{\alpha}) := \sum_{\nu=6i}^{\infty} \boldsymbol{i}^{k}_{\mathrm{s},\nu}(\boldsymbol{\alpha}) &= \sum_{\nu=6i}^{\infty} \begin{pmatrix} h_{\mathrm{dd},\nu}a_{\nu+1}(\boldsymbol{\alpha})\cos\big(\nu\theta_{\mathrm{r}}+(\nu+1)\gamma(\boldsymbol{\alpha})+\theta_{\mathrm{dd},\nu}\big) \\ h_{\mathrm{qd},\nu}a_{\nu+1}(\boldsymbol{\alpha})\cos\big(\nu\theta_{\mathrm{r}}+(\nu+1)\gamma(\boldsymbol{\alpha})+\theta_{\mathrm{qd},\nu}\big) \end{pmatrix} \\
&\quad + \sum_{\nu=6i}^{\infty} \begin{pmatrix} h_{\mathrm{dd},\nu}a_{\nu-1}(\boldsymbol{\alpha})\cos\big(\nu\theta_{\mathrm{r}}+(\nu-1)\gamma(\boldsymbol{\alpha})+\theta_{\mathrm{dd},\nu}\big) \\ h_{\mathrm{qd},\nu}a_{\nu-1}(\boldsymbol{\alpha})\cos\big(\nu\theta_{\mathrm{r}}+(\nu-1)\gamma(\boldsymbol{\alpha})+\theta_{\mathrm{qd},\nu}\big) \end{pmatrix} \\
&\quad + \sum_{\nu=6i}^{+\infty} \begin{pmatrix} h_{\mathrm{dq},\nu}a_{\nu+1}(\boldsymbol{\alpha})\cos\big(\nu\theta_{\mathrm{r}}+(\nu+1)\gamma(\boldsymbol{\alpha})-\frac{\pi}{2}+\theta_{\mathrm{dq},\nu}\big) \\ h_{\mathrm{qq},\nu}a_{\nu+1}(\boldsymbol{\alpha})\cos\big(\nu\theta_{\mathrm{r}}+(\nu+1)\gamma(\boldsymbol{\alpha})-\frac{\pi}{2}+\theta_{\mathrm{qq},\nu}\big) \end{pmatrix} \\
&\quad - \sum_{\nu=6i}^{+\infty} \begin{pmatrix} h_{\mathrm{dq},\nu}a_{\nu-1}(\boldsymbol{\alpha})\cos\big(\nu\theta_{\mathrm{r}}+(\nu-1)\gamma(\boldsymbol{\alpha})-\frac{\pi}{2}+\theta_{\mathrm{dq},\nu}\big) \\ h_{\mathrm{qq},\nu}a_{\nu-1}(\boldsymbol{\alpha})\cos\big(\nu\theta_{\mathrm{r}}+(\nu-1)\gamma(\boldsymbol{\alpha})-\frac{\pi}{2}+\theta_{\mathrm{qq},\nu}\big) \end{pmatrix} \\
&\quad + \sum_{\nu=6i}^{+\infty} \begin{pmatrix} h_{\mathrm{dd},\nu}b_{\nu+1}(\boldsymbol{\alpha})\cos\big(\nu\theta_{\mathrm{r}}+(\nu+1)\gamma(\boldsymbol{\alpha})-\frac{\pi}{2}+\theta_{\mathrm{dd},\nu}\big) \\ h_{\mathrm{qd},\nu}b_{\nu+1}(\boldsymbol{\alpha})\cos\big(\nu\theta_{\mathrm{r}}+(\nu+1)\gamma(\boldsymbol{\alpha})-\frac{\pi}{2}+\theta_{\mathrm{qd},\nu}\big) \end{pmatrix} \\
&\quad + \sum_{\nu=6i}^{+\infty} \begin{pmatrix} h_{\mathrm{dd},\nu}b_{\nu-1}(\boldsymbol{\alpha})\cos\big(\nu\theta_{\mathrm{r}}+(\nu-1)\gamma(\boldsymbol{\alpha})-\frac{\pi}{2}+\theta_{\mathrm{dd},\nu}\big) \\ h_{\mathrm{qd},\nu}b_{\nu-1}(\boldsymbol{\alpha})\cos\big(\nu\theta_{\mathrm{r}}+(\nu-1)\gamma(\boldsymbol{\alpha})-\frac{\pi}{2}+\theta_{\mathrm{qd},\nu}\big) \end{pmatrix} \\
&\quad - \sum_{\nu=6i}^{+\infty} \begin{pmatrix} h_{\mathrm{dq},\nu}b_{\nu+1}(\boldsymbol{\alpha})\cos\big(\nu\theta_{\mathrm{r}}+(\nu+1)\gamma(\boldsymbol{\alpha})+\theta_{\mathrm{dq},\nu}\big) \\ h_{\mathrm{qq},\nu}b_{\nu+1}(\boldsymbol{\alpha})\cos\big(\nu\theta_{\mathrm{r}}+(\nu+1)\gamma(\boldsymbol{\alpha})+\theta_{\mathrm{qq},\nu}\big) \end{pmatrix} \\
&\quad + \sum_{\nu=6i}^{+\infty} \begin{pmatrix} h_{\mathrm{dq},\nu}b_{\nu-1}(\boldsymbol{\alpha})\cos\big(\nu\theta_{\mathrm{r}}+(\nu-1)\gamma(\boldsymbol{\alpha})+\theta_{\mathrm{dq},\nu}\big) \\ h_{\mathrm{qq},\nu}b_{\nu-1}(\boldsymbol{\alpha})\cos\big(\nu\theta_{\mathrm{r}}+(\nu-1)\gamma(\boldsymbol{\alpha})+\theta_{\mathrm{qq},\nu}\big) \end{pmatrix}.
\end{aligned}
\tag{2.52}
$$

Since the objective of this thesis is to minimize the harmonic distortion of the machine phase current, the formulation of the phase current as function of the inverter switching angles has to be derived. Hence, the inverse Clarke-Park transformation is applied to $\boldsymbol{i}_{\mathrm{s}}^{k}(\boldsymbol{\alpha})$ as follows

$$\begin{aligned}\boldsymbol{i}_{\mathrm{s}}^{uvw}(\boldsymbol{\alpha}) :=&(i_{\mathrm{s}}^{u}(\boldsymbol{\alpha}), i_{\mathrm{s}}^{v}(\boldsymbol{\alpha}), i_{\mathrm{s}}^{w}(\boldsymbol{\alpha}))^{\top} = (i_{\mathrm{s,1}}^{u}(\boldsymbol{\alpha}), i_{\mathrm{s,1}}^{v}(\boldsymbol{\alpha}), i_{\mathrm{s,1}}^{w}(\boldsymbol{\alpha}))^{\top} + (i_{\mathrm{s,h}}^{u}(\boldsymbol{\alpha}), i_{\mathrm{s,h}}^{v}(\boldsymbol{\alpha}), i_{\mathrm{s,h}}^{w}(\boldsymbol{\alpha}))^{\top} \\ =&\boldsymbol{T}_{\mathrm{c}}^{-1}\boldsymbol{T}_{\mathrm{p}}(\theta_{\mathrm{r}})\boldsymbol{i}_{\mathrm{s}}^{k}(\boldsymbol{\alpha}) = \begin{bmatrix} \cos(\theta_{\mathrm{r}}) & -\sin(\theta_{\mathrm{r}}) \\ -\frac{1}{2}\cos(\theta_{\mathrm{r}}) + \frac{\sqrt{3}}{2}\sin(\theta_{\mathrm{r}}) & \frac{1}{2}\sin(\theta_{\mathrm{r}}) + \frac{\sqrt{3}}{2}\cos(\theta_{\mathrm{r}}) \\ -\frac{1}{2}\cos(\theta_{\mathrm{r}}) - \frac{\sqrt{3}}{2}\sin(\theta_{\mathrm{r}}) & \frac{1}{2}\sin(\theta_{\mathrm{r}}) - \frac{\sqrt{3}}{2}\cos(\theta_{\mathrm{r}}) \end{bmatrix} \boldsymbol{i}_{\mathrm{s}}^{k}(\boldsymbol{\alpha}).\end{aligned} \tag{2.53}$$

For instance, the fundamental and harmonic currents of phase u are, respectively, given by

$$\begin{aligned} i_{\mathrm{s,1}}^{u}(\boldsymbol{\alpha}) &\overset{(2.53)}{=} \begin{pmatrix} \cos(\theta_{\mathrm{r}}) \\ -\sin(\theta_{\mathrm{r}}) \end{pmatrix}^{\top} \boldsymbol{i}_{\mathrm{s,1}}^{k}(\boldsymbol{\alpha}) \\ &\overset{(2.34),\,(2.43)}{=} \begin{pmatrix} \cos(\theta_{\mathrm{r}}) \\ -\sin(\theta_{\mathrm{r}}) \end{pmatrix}^{\top} \\ &\qquad \frac{1}{R_{\mathrm{s}}^2+\omega_{\mathrm{r}}^2 L_{\mathrm{s}}^{d} L_{\mathrm{s}}^{q}} \begin{bmatrix} R_{\mathrm{s}} & \omega_{\mathrm{r}} L_{\mathrm{s}}^{q} \\ -\omega_{\mathrm{r}} L_{\mathrm{s}}^{d} & R_{\mathrm{s}} \end{bmatrix} \begin{pmatrix} a_1(\boldsymbol{\alpha})\cos\gamma(\boldsymbol{\alpha}) + b_1(\boldsymbol{\alpha})\sin\gamma(\boldsymbol{\alpha}) \\ a_1(\boldsymbol{\alpha})\sin\gamma(\boldsymbol{\alpha}) - b_1(\boldsymbol{\alpha})\cos\gamma(\boldsymbol{\alpha}) - \omega_{\mathrm{r}}\psi_{\mathrm{PM}} \end{pmatrix} \end{aligned} \tag{2.54}$$

and

$$\begin{aligned} i_{\mathrm{s,h}}^{u}(\boldsymbol{\alpha}) &\overset{(2.53)}{=} \begin{pmatrix} \cos(\theta_{\mathrm{r}}) \\ -\sin(\theta_{\mathrm{r}}) \end{pmatrix}^{\top} \boldsymbol{i}_{\mathrm{s,h}}^{k}(\boldsymbol{\alpha}) \\ &\overset{(2.52)}{=} \frac{1}{2}\sum_{\nu=6i}^{\infty}\sum_{k=-1,1}\Big[h_{\mathrm{dd},\nu}a_{\nu+k}(\boldsymbol{\alpha})\cos\big((\nu{-}1)\theta_{\mathrm{r}} + (\nu{+}k)\gamma(\boldsymbol{\alpha}) + \theta_{\mathrm{dd},\nu}\big) \\ &\qquad + kh_{\mathrm{dq},\nu}a_{\nu+k}(\boldsymbol{\alpha})\cos\big((\nu{-}1)\theta_{\mathrm{r}} + (\nu{+}k)\gamma(\boldsymbol{\alpha}) + \theta_{\mathrm{dq},\nu} - \frac{\pi}{2}\big) \\ &\qquad - h_{\mathrm{qd},\nu}a_{\nu+k}(\boldsymbol{\alpha})\cos\big((\nu{-}1)\theta_{\mathrm{r}} + (\nu{+}k)\gamma(\boldsymbol{\alpha}) + \theta_{\mathrm{qd},\nu} + \frac{\pi}{2}\big) \\ &\qquad - kh_{\mathrm{qq},\nu}a_{\nu+k}(\boldsymbol{\alpha})\cos\big((\nu{-}1)\theta_{\mathrm{r}} + (\nu{+}k)\gamma(\boldsymbol{\alpha}) + \theta_{\mathrm{qq},\nu}\big) \\ &\qquad + h_{\mathrm{dd},\nu}b_{\nu+k}(\boldsymbol{\alpha})\cos\big((\nu{-}1)\theta_{\mathrm{r}} + (\nu{+}k)\gamma(\boldsymbol{\alpha}) + \theta_{\mathrm{dd},\nu} - \frac{\pi}{2}\big) \\ &\qquad - kh_{\mathrm{dq},\nu}b_{\nu+k}(\boldsymbol{\alpha})\cos\big((\nu{-}1)\theta_{\mathrm{r}} + (\nu{+}k)\gamma(\boldsymbol{\alpha}) + \theta_{\mathrm{dq},\nu}\big) \\ &\qquad - h_{\mathrm{qd},\nu}b_{\nu+k}(\boldsymbol{\alpha})\cos\big((\nu{-}1)\theta_{\mathrm{r}} + (\nu{+}k)\gamma(\boldsymbol{\alpha}) + \theta_{\mathrm{qd},\nu}\big) \\ &\qquad + kh_{\mathrm{qq},\nu}b_{\nu+k}(\boldsymbol{\alpha})\cos\big((\nu{-}1)\theta_{\mathrm{r}} + (\nu{+}k)\gamma(\boldsymbol{\alpha}) + \theta_{\mathrm{qq},\nu} + \frac{\pi}{2}\big) \\ &\qquad + h_{\mathrm{dd},\nu}a_{\nu+k}(\boldsymbol{\alpha})\cos\big((\nu{+}1)\theta_{\mathrm{r}} + (\nu{+}k)\gamma(\boldsymbol{\alpha}) + \theta_{\mathrm{dd},\nu}\big) \\ &\qquad + kh_{\mathrm{dq},\nu}a_{\nu+k}(\boldsymbol{\alpha})\cos\big((\nu{+}1)\theta_{\mathrm{r}} + (\nu{+}k)\gamma(\boldsymbol{\alpha}) + \theta_{\mathrm{dq},\nu} - \frac{\pi}{2}\big) \\ &\qquad + h_{\mathrm{qd},\nu}a_{\nu+k}(\boldsymbol{\alpha})\cos\big((\nu{+}1)\theta_{\mathrm{r}} + (\nu{+}k)\gamma(\boldsymbol{\alpha}) + \theta_{\mathrm{qd},\nu} + \frac{\pi}{2}\big) \\ &\qquad + kh_{\mathrm{qq},\nu}a_{\nu+k}(\boldsymbol{\alpha})\cos\big((\nu{+}1)\theta_{\mathrm{r}} + (\nu{+}k)\gamma(\boldsymbol{\alpha}) + \theta_{\mathrm{qq},\nu}\big) \\ &\qquad + h_{\mathrm{dd},\nu}b_{\nu+k}(\boldsymbol{\alpha})\cos\big((\nu{+}1)\theta_{\mathrm{r}} + (\nu{+}k)\gamma(\boldsymbol{\alpha}) + \theta_{\mathrm{dd},\nu} - \frac{\pi}{2}\big) \\ &\qquad - kh_{\mathrm{dq},\nu}b_{\nu+k}\nu\cos\big((\nu{+}1)\theta_{\mathrm{r}} + (\nu{+}k)\gamma(\boldsymbol{\alpha}) + \theta_{\mathrm{dq},\nu}\big) \\ &\qquad + h_{\mathrm{qd},\nu}b_{\nu+k}(\boldsymbol{\alpha})\cos\big((\nu{+}1)\theta_{\mathrm{r}} + (\nu{+}k)\gamma(\boldsymbol{\alpha}) + \theta_{\mathrm{qd},\nu}\big) \\ &\qquad - kh_{\mathrm{qq},\nu}b_{\nu+k}(\boldsymbol{\alpha})\cos\big((\nu{+}1)\theta_{\mathrm{r}} + (\nu{+}k)\gamma(\boldsymbol{\alpha}) + \theta_{\mathrm{qq},\nu} + \frac{\pi}{2}\big)\Big]. \end{aligned} \tag{2.55}$$

Eq. (2.55) represents the harmonic content of the motor current as a function of the inverter switching angles $\boldsymbol{\alpha}$. This equation can be simplified assuming that the influence of the stator resistance R_s on the phase harmonic current $i^u_{\mathrm{s,h}}(\boldsymbol{\alpha})$ is small.

Setting $R_\mathrm{s} = 0$ in (2.46) - (2.48) yields the simplified coefficients

$$\begin{aligned}
\mathrm{H}_{\mathrm{dd},\nu}\Big|_{R_\mathrm{s}=0} &= h_{\mathrm{dd},\nu}\Big|_{R_\mathrm{s}=0}\angle\theta_{\mathrm{dd},\nu}\Big|_{R_\mathrm{s}=0} = \frac{\nu}{(\nu^2-1)\omega_\mathrm{r}L_\mathrm{s}^d}\angle -\pi/2\\
\mathrm{H}_{\mathrm{dq},\nu}\Big|_{R_\mathrm{s}=0} &= h_{\mathrm{dq},\nu}\Big|_{R_\mathrm{s}=0}\angle\theta_{\mathrm{dq},\nu}\Big|_{R_\mathrm{s}=0} = \frac{1}{(\nu^2-1)\omega_\mathrm{r}L_\mathrm{s}^d}\angle\pi\\
\mathrm{H}_{\mathrm{qd},\nu}\Big|_{R_\mathrm{s}=0} &= h_{\mathrm{qd},\nu}\Big|_{R_\mathrm{s}=0}\angle\theta_{\mathrm{qd},\nu}\Big|_{R_\mathrm{s}=0} = \frac{1}{(\nu^2-1)\omega_\mathrm{r}L_\mathrm{s}^q}\angle 0 \qquad \text{and}\\
\mathrm{H}_{\mathrm{qq},\nu}\Big|_{R_\mathrm{s}=0} &= h_{\mathrm{qq},\nu}\Big|_{R_\mathrm{s}=0}\angle\theta_{\mathrm{qq},\nu}\Big|_{R_\mathrm{s}=0} = \frac{\nu}{(\nu^2-1)\omega_\mathrm{r}L_\mathrm{s}^q}\angle -\pi/2.
\end{aligned} \tag{2.56}$$

Based on (2.56), the current harmonic component of phase u, expressed by (2.55), can be reformulated as follows

$$\begin{aligned}
i^u_{\mathrm{s,h}}(\boldsymbol{\alpha})\Big|_{R_\mathrm{s}=0} \overset{(2.55)}{=}\ & \frac{1}{2\omega_\mathrm{r}L_\mathrm{s}^q}\sum_{\nu=6i}^{\infty}\Bigg[\frac{a_{\nu-1}(\boldsymbol{\alpha})}{\nu-1}(\lambda+1)\cos\Big((\nu-1)\theta_\mathrm{r}+(\nu-1)\gamma(\boldsymbol{\alpha})-\frac{\pi}{2}\Big)\\
&+\frac{a_{\nu+1}(\boldsymbol{\alpha})}{\nu+1}(\lambda-1)\cos\Big((\nu-1)\theta_\mathrm{r}+(\nu+1)\gamma(\boldsymbol{\alpha})-\frac{\pi}{2}\Big)\\
&-\frac{b_{\nu-1}(\boldsymbol{\alpha})}{\nu-1}(\lambda+1)\cos\Big((\nu-1)\theta_\mathrm{r}+(\nu-1)\gamma(\boldsymbol{\alpha})\Big)\\
&-\frac{b_{\nu+1}(\boldsymbol{\alpha})}{\nu+1}(\lambda-1)\cos\Big((\nu-1)\theta_\mathrm{r}+(\nu+1)\gamma(\boldsymbol{\alpha})\Big)\\
&+\frac{a_{\nu-1}(\boldsymbol{\alpha})}{\nu-1}(\lambda-1)\cos\Big((\nu+1)\theta_\mathrm{r}+(\nu-1)\gamma(\boldsymbol{\alpha})-\frac{\pi}{2}\Big)\\
&+\frac{a_{\nu+1}(\boldsymbol{\alpha})}{\nu+1}(\lambda+1)\cos\Big((\nu+1)\theta_\mathrm{r}+(\nu+1)\gamma(\boldsymbol{\alpha})-\frac{\pi}{2}\Big)\\
&-\frac{b_{\nu-1}(\boldsymbol{\alpha})}{\nu-1}(\lambda-1)\cos\Big((\nu+1)\theta_\mathrm{r}+(\nu-1)\gamma(\boldsymbol{\alpha})\Big)\\
&-\frac{b_{\nu+1}(\boldsymbol{\alpha})}{\nu+1}(\lambda+1)\cos\Big((\nu+1)\theta_\mathrm{r}+(\nu+1)\gamma(\boldsymbol{\alpha})\Big)\Bigg]\\
\overset{(2.1),(2.2)}{=}\ & \frac{1}{2\omega_\mathrm{r}L_\mathrm{s}^q}\sum_{\nu=6i}^{\infty}\Bigg[H_{1,\nu}(\boldsymbol{\alpha})\sin\Big((\nu-1)(\theta_\mathrm{r}+\gamma(\boldsymbol{\alpha})\Big)\\
&+H_{2,\nu}(\boldsymbol{\alpha})\cos\Big((\nu-1)(\theta_\mathrm{r}+\gamma(\boldsymbol{\alpha})\Big)\\
&+H_{3,\nu}(\boldsymbol{\alpha})\sin\Big((\nu+1)(\theta_\mathrm{r}+\gamma(\boldsymbol{\alpha})\Big)\\
&+H_{4,\nu}(\boldsymbol{\alpha})\cos\Big((\nu+1)(\theta_\mathrm{r}+\gamma(\boldsymbol{\alpha})\Big)\Bigg],
\end{aligned} \tag{2.57}$$

where

$$\lambda := \frac{L_\mathrm{s}^q}{L_\mathrm{s}^d} \tag{2.58}$$

is the anisotropic factor or saliency ratio of the machine and

$$H_{1,\nu}(\boldsymbol{\alpha}) := \frac{a_{\nu+1}(\boldsymbol{\alpha})}{\nu+1}(\lambda-1)\cos\left(2\gamma(\boldsymbol{\alpha})\right) + \frac{a_{\nu-1}(\boldsymbol{\alpha})}{\nu-1}(\lambda+1) + \frac{b_{\nu+1}(\boldsymbol{\alpha})}{\nu+1}(\lambda-1)\sin\left(2\gamma(\boldsymbol{\alpha})\right)$$

$$
\begin{aligned}
H_{2,\nu}(\boldsymbol{\alpha}) :=& \frac{a_{\nu+1}(\boldsymbol{\alpha})}{\nu+1}(\lambda-1)\sin\left(2\gamma(\boldsymbol{\alpha})\right) - \frac{b_{\nu-1}(\boldsymbol{\alpha})}{\nu-1}(\lambda+1) - \frac{b_{\nu+1}(\boldsymbol{\alpha})}{\nu+1}(\lambda-1)\cos\left(2\gamma(\boldsymbol{\alpha})\right) \\
H_{3,\nu}(\boldsymbol{\alpha}) :=& \frac{a_{\nu-1}(\boldsymbol{\alpha})}{\nu-1}(\lambda-1)\cos\left(2\gamma(\boldsymbol{\alpha})\right) + \frac{a_{\nu+1}(\boldsymbol{\alpha})}{\nu+1}(\lambda+1) - \frac{b_{\nu-1}(\boldsymbol{\alpha})}{\nu-1}(\lambda-1)\sin\left(2\gamma(\boldsymbol{\alpha})\right) \\
H_{4,\nu}(\boldsymbol{\alpha}) :=& -\frac{a_{\nu-1}(\boldsymbol{\alpha})}{\nu-1}(\lambda-1)\sin\left(2\gamma(\boldsymbol{\alpha})\right) - \frac{b_{\nu+1}(\boldsymbol{\alpha})}{\nu+1}(\lambda+1) - \frac{b_{\nu-1}(\boldsymbol{\alpha})}{\nu-1}(\lambda-1)\cos\left(2\gamma(\boldsymbol{\alpha})\right).
\end{aligned}
\tag{2.59}
$$

Concluding, the machine current of each phase can be expressed by

$$
\begin{aligned}
i_{\mathrm{s}}^{u}(\boldsymbol{\alpha}) = \begin{pmatrix} \cos(\theta_{\mathrm{r}}) \\ -\sin(\theta_{\mathrm{r}}) \end{pmatrix}^{\top} \boldsymbol{i}_{\mathrm{s},1}^{k}(\boldsymbol{\alpha}) \Bigg\} &= i_{\mathrm{s},1}^{u}(\boldsymbol{\alpha}) \\
+\tfrac{1}{2\omega_{\mathrm{r}} L_{\mathrm{s}}^{q}} \sum_{\nu=6i}^{\infty} H_{1,\nu}(\boldsymbol{\alpha}) \sin\Big((\nu-1)\big(\theta_{\mathrm{r}}+\gamma(\boldsymbol{\alpha})\big)\Big) & \\
+H_{2,\nu}(\boldsymbol{\alpha}) \cos\Big((\nu-1)\big(\theta_{\mathrm{r}}+\gamma(\boldsymbol{\alpha})\big)\Big) & \\
+H_{3,\nu}(\boldsymbol{\alpha}) \sin\Big((\nu+1)\big(\theta_{\mathrm{r}}+\gamma(\boldsymbol{\alpha})\big)\Big) & \\
+H_{4,\nu}(\boldsymbol{\alpha}) \cos\Big((\nu+1)\big(\theta_{\mathrm{r}}+\gamma(\boldsymbol{\alpha})\big)\Big) \Bigg\} &= i_{\mathrm{s,h}}^{u}(\boldsymbol{\alpha}),
\end{aligned}
\tag{2.60}
$$

$$
\begin{aligned}
i_{\mathrm{s}}^{v}(\boldsymbol{\alpha}) = \begin{pmatrix} \cos(\theta_{\mathrm{r}}-\frac{2\pi}{3}) \\ -\sin(\theta_{\mathrm{r}}-\frac{2\pi}{3}) \end{pmatrix}^{\top} \boldsymbol{i}_{\mathrm{s},1}^{k}(\boldsymbol{\alpha}) \Bigg\} &= i_{\mathrm{s},1}^{v}(\boldsymbol{\alpha}) \\
+\tfrac{1}{2\omega_{\mathrm{r}} L_{\mathrm{s}}^{q}} \sum_{\nu=6i}^{\infty} H_{1,\nu}(\boldsymbol{\alpha}) \sin\Big((\nu-1)\big(\theta_{\mathrm{r}}+\gamma(\boldsymbol{\alpha})-\tfrac{2\pi}{3}\big)\Big) & \\
+H_{2,\nu}(\boldsymbol{\alpha}) \cos\Big((\nu-1)\big(\theta_{\mathrm{r}}+\gamma(\boldsymbol{\alpha})-\tfrac{2\pi}{3}\big)\Big) & \\
+H_{3,\nu}(\boldsymbol{\alpha}) \sin\Big((\nu+1)\big(\theta_{\mathrm{r}}+\gamma(\boldsymbol{\alpha})-\tfrac{2\pi}{3}\big)\Big) & \\
+H_{4,\nu}(\boldsymbol{\alpha}) \cos\Big((\nu+1)\big(\theta_{\mathrm{r}}+\gamma(\boldsymbol{\alpha})-\tfrac{2\pi}{3}\big)\Big) \Bigg\} &= i_{\mathrm{s,h}}^{v}(\boldsymbol{\alpha})
\end{aligned}
\tag{2.61}
$$

and

$$
\begin{aligned}
i_{\mathrm{s}}^{w}(\boldsymbol{\alpha}) = \begin{pmatrix} \cos(\theta_{\mathrm{r}}-\frac{4\pi}{3}) \\ -\sin(\theta_{\mathrm{r}}-\frac{4\pi}{3}) \end{pmatrix}^{\top} \boldsymbol{i}_{\mathrm{s},1}^{k}(\boldsymbol{\alpha}) \Bigg\} &= i_{\mathrm{s},1}^{w}(\boldsymbol{\alpha}) \\
+\tfrac{1}{2\omega_{\mathrm{r}} L_{\mathrm{s}}^{q}} \sum_{\nu=6i}^{\infty} H_{1,\nu}(\boldsymbol{\alpha}) \sin\Big((\nu-1)\big(\theta_{\mathrm{r}}+\gamma(\boldsymbol{\alpha})-\tfrac{4\pi}{3}\big)\Big) & \\
+H_{2,\nu}(\boldsymbol{\alpha}) \cos\Big((\nu-1)\big(\theta_{\mathrm{r}}+\gamma(\boldsymbol{\alpha})-\tfrac{4\pi}{3}\big)\Big) & \\
+H_{3,\nu}(\boldsymbol{\alpha}) \sin\Big((\nu+1)\big(\theta_{\mathrm{r}}+\gamma(\boldsymbol{\alpha})-\tfrac{4\pi}{3}\big)\Big) & \\
+H_{4,\nu}(\boldsymbol{\alpha}) \cos\Big((\nu+1)\big(\theta_{\mathrm{r}}+\gamma(\boldsymbol{\alpha})-\tfrac{4\pi}{3}\big)\Big) \Bigg\} &= i_{\mathrm{s,h}}^{w}(\boldsymbol{\alpha}),
\end{aligned}
\tag{2.62}
$$

where $\boldsymbol{i}_{\mathrm{s},1}^{k}(\boldsymbol{\alpha})$ is given by (2.43) and $H_{1\ldots4,\nu}(\boldsymbol{\alpha})$ by (2.59).

2.2.3 Inverter current and dc-link capacitor current

The design of the dc-link capacitor is mainly influenced by its operational lifetime. The ambient temperature as well as the capacitor's internal self-heating caused by the dc-link current ripple are the main contributors to the temperature rise of the capacitor, which accelerates its wear-out process [102]. In case of high current harmonic content in the dc-link, the use of several capacitors connected in parallel is necessary. This leads to increased space and cost. For these reasons, the analysis of the dc-link harmonic current is of significant importance for the accurate capacitor scaling [103].

Conventionally, the RMS value of the capacitor current is used for scaling the dc-link capacitor. Analytical expressions for the capacitor RMS current with respect to the modulation index and the magnitude and phase angle of the load current are presented in [104] and [105] for space vector modulation and in [106] for sine triangular modulation. Apart from the RMS value, the identification of the dc-link current in the time and frequency domain can provide a more accurate VSI design. A general formulation for the dc-link inverter current in the time domain is introduced in [107] without considering a specific modulation scheme or load. Furthermore, the harmonic spectrum of the dc-link current is calculated in [108] and [109] for continuous and discontinuous carrier-based PWM. Lastly, the dc-link inverter current is analytically identified in [110] using a wound-rotor synchronous starter generator as load and SHEPWM is employed to eliminate predefined dc-link current harmonics.

In this subsection, the dc-link analysis of [107] and [110] is extended for the case of a salient pole IPMSM driven by SOPWM. The analytical expressions of the dc-link capacitor and inverter currents are deduced in the time and frequency domain with respect to the switching angles when the SOPWM is employed for the control of a salient pole IPMSM drive. In the following analysis, the magnetic anisotropic properties of the machine are taken into account and half-wave symmetric PWM waveforms are used. Furthermore, not only the fundamental component but also the harmonics of the load currents are considered. Although the harmonic content of the load currents produced by carrier-based modulation is rather low and affects only marginally the dc-link capacitor current [104–106, 109], this assumption may not be applicable for low switching frequency PWM strategies like the SOPWM. The low switching frequencies employed by SOPWM may lead to increased harmonic currents in the machine, which cannot be ignored in the formulation of the dc-link capacitor current. The content of this subsection was developed as part of the supervised master's thesis [91] and was submitted to *IEEE Transactions on Industrial Electronics* [92] for publication.

The equation of the inverter current $i_{\mathrm{inv}}(\boldsymbol{\alpha})$ (see Fig. 2.1) in time domain with respect to the inverter switching angles can be derived by applying Kirchhoff's law [111, Ch. 3] as follows

$$\begin{aligned} i_{\mathrm{inv}}(\boldsymbol{\alpha}) &:= \boldsymbol{s}^{uvw}(\boldsymbol{\alpha})^{\top} \boldsymbol{i}_{\mathrm{s}}^{uvw}(\boldsymbol{\alpha}) \\ &= s^{u}(\boldsymbol{\alpha}) i_{\mathrm{s}}^{u}(\boldsymbol{\alpha}) + s^{v}(\boldsymbol{\alpha}) i_{\mathrm{s}}^{v}(\boldsymbol{\alpha}) + s^{w}(\boldsymbol{\alpha}) i_{\mathrm{s}}^{w}(\boldsymbol{\alpha}) \\ &= i_{\mathrm{inv,dc}}(\boldsymbol{\alpha}) + i_{\mathrm{inv,ac}}(\boldsymbol{\alpha}) \\ &= i_{\mathrm{inv,dc}}(\boldsymbol{\alpha}) + i_{\mathrm{inv,ac_1}}(\boldsymbol{\alpha}) + i_{\mathrm{inv,ac_2}}(\boldsymbol{\alpha}) + i_{\mathrm{inv,ac_3}}(\boldsymbol{\alpha}). \end{aligned} \tag{2.63}$$

The motor phase currents $\boldsymbol{i}_{\mathrm{s}}^{uvw}(\boldsymbol{\alpha})$ are given by (2.60) - (2.62) while the gate signals $\boldsymbol{s}^{uvw}(\boldsymbol{\alpha})$ can be expressed by [99, Chapter 14]

$$\boldsymbol{s}^{uvw}(\boldsymbol{\alpha}) = \begin{pmatrix} 0.5 \\ 0.5 \\ 0.5 \end{pmatrix} + \frac{1}{u_{\mathrm{dc}}} \begin{pmatrix} u_{\mathrm{o}}^{u}(\boldsymbol{\alpha}) \\ u_{\mathrm{o}}^{v}(\boldsymbol{\alpha}) \\ u_{\mathrm{o}}^{w}(\boldsymbol{\alpha}) \end{pmatrix} \tag{2.64}$$

$$
\begin{aligned}
&\overset{(2.26)}{=} \begin{pmatrix} 0.5 \\ 0.5 \\ 0.5 \end{pmatrix} + \frac{1}{u_{\mathrm{dc}}} \sum_{\nu \in \mathcal{I}}^{\infty} \begin{pmatrix} a_\nu(\boldsymbol{\alpha}) \cos\left(\nu\left(\theta_{\mathrm{r}}+\gamma(\boldsymbol{\alpha})\right)\right) + b_\nu(\boldsymbol{\alpha}) \sin\left(\nu\left(\theta_{\mathrm{r}}+\gamma(\boldsymbol{\alpha})\right)\right) \\ a_\nu(\boldsymbol{\alpha}) \cos\left(\nu\left(\theta_{\mathrm{r}}+\gamma(\boldsymbol{\alpha})-\frac{2\pi}{3}\right)\right) + b_\nu(\boldsymbol{\alpha}) \sin\left(\nu\left(\theta_{\mathrm{r}}+\gamma(\boldsymbol{\alpha})-\frac{2\pi}{3}\right)\right) \\ a_\nu(\boldsymbol{\alpha}) \cos\left(\nu\left(\theta_{\mathrm{r}}+\gamma(\boldsymbol{\alpha})-\frac{4\pi}{3}\right)\right) + b_\nu(\boldsymbol{\alpha}) \sin\left(\nu\left(\theta_{\mathrm{r}}+\gamma(\boldsymbol{\alpha})-\frac{4\pi}{3}\right)\right) \end{pmatrix} \\
&= \begin{pmatrix} 0.5 \\ 0.5 \\ 0.5 \end{pmatrix} + \sum_{\nu \in \mathcal{I}}^{\infty} \begin{pmatrix} \widetilde{a}_\nu(\boldsymbol{\alpha}) \cos\left(\nu\left(\theta_{\mathrm{r}}+\gamma(\boldsymbol{\alpha})\right)\right) + \widetilde{b}_\nu(\boldsymbol{\alpha}) \sin\left(\nu\left(\theta_{\mathrm{r}}+\gamma(\boldsymbol{\alpha})\right)\right) \\ \widetilde{a}_\nu(\boldsymbol{\alpha}) \cos\left(\nu\left(\theta_{\mathrm{r}}+\gamma(\boldsymbol{\alpha})-\frac{2\pi}{3}\right)\right) + \widetilde{b}_\nu(\boldsymbol{\alpha}) \sin\left(\nu\left(\theta_{\mathrm{r}}+\gamma(\boldsymbol{\alpha})-\frac{2\pi}{3}\right)\right) \\ \widetilde{a}_\nu(\boldsymbol{\alpha}) \cos\left(\nu\left(\theta_{\mathrm{r}}+\gamma(\boldsymbol{\alpha})-\frac{4\pi}{3}\right)\right) + \widetilde{b}_\nu(\boldsymbol{\alpha}) \sin\left(\nu\left(\theta_{\mathrm{r}}+\gamma(\boldsymbol{\alpha})-\frac{4\pi}{3}\right)\right) \end{pmatrix},
\end{aligned}
$$

based on (2.18) and Fig. 2.1, where the Fourier coefficients

$$
\widetilde{a}_\nu(\boldsymbol{\alpha}) := a_\nu(\boldsymbol{\alpha})/u_{\mathrm{dc}} \qquad \text{and} \qquad \widetilde{b}_\nu(\boldsymbol{\alpha}) := b_\nu(\boldsymbol{\alpha})/u_{\mathrm{dc}} \tag{2.65}
$$

are normalized by the factor u_{dc}.

Eq. (2.63) indicates that $i_{\mathrm{inv}}(\boldsymbol{\alpha})$ consists of a major dc component $i_{\mathrm{inv,dc}}(\boldsymbol{\alpha})$ and harmonics $i_{\mathrm{inv,ac}}(\boldsymbol{\alpha})$, which can be split into the three groups $i_{\mathrm{inv,ac_1}}(\boldsymbol{\alpha})$, $i_{\mathrm{inv,ac_2}}(\boldsymbol{\alpha})$ and $i_{\mathrm{inv,ac_3}}(\boldsymbol{\alpha})$. This representation has no physical interpretation but facilitates the derivation of $i_{\mathrm{inv}}(\boldsymbol{\alpha})$. The dc component $i_{\mathrm{inv,dc}}(\boldsymbol{\alpha})$ is formed by the signals $\boldsymbol{s}_\nu^{uvw}(\boldsymbol{\alpha})$ and $\boldsymbol{i}_{\mathrm{s},\nu}^{uvw}(\boldsymbol{\alpha})$ of the same order $\nu \in \mathcal{H}$, i.e.

$$
\begin{aligned}
i_{\mathrm{inv,dc}}(\boldsymbol{\alpha}) :=& \sum_{\nu \in \mathcal{H}} \boldsymbol{s}_\nu^{uvw}(\boldsymbol{\alpha})^\top \boldsymbol{i}_{\mathrm{s},\nu}^{uvw}(\boldsymbol{\alpha}) \\
=& \boldsymbol{s}_1^{uvw}(\boldsymbol{\alpha})^\top \boldsymbol{i}_{\mathrm{s},1}^{uvw}(\boldsymbol{\alpha}) + \boldsymbol{s}_5^{uvw}(\boldsymbol{\alpha})^\top \boldsymbol{i}_{\mathrm{s},5}^{uvw}(\boldsymbol{\alpha}) + \boldsymbol{s}_7^{uvw}(\boldsymbol{\alpha})^\top \boldsymbol{i}_{\mathrm{s},7}^{uvw}(\boldsymbol{\alpha}) + \ldots \\
\overset{\substack{(2.60)-(2.62),\\(2.64)}}{=}& \frac{3}{2} \Bigg(\left(\widetilde{a}_1(\boldsymbol{\alpha}) i_{\mathrm{s},1}^d(\boldsymbol{\alpha}) - \widetilde{b}_1(\boldsymbol{\alpha}) i_{\mathrm{s},1}^q(\boldsymbol{\alpha}) \right) \cos\gamma(\boldsymbol{\alpha}) \\
& + \left(\widetilde{a}_1(\boldsymbol{\alpha}) i_{\mathrm{s},1}^q(\boldsymbol{\alpha}) + \widetilde{b}_1(\boldsymbol{\alpha}) i_{\mathrm{s},1}^d(\boldsymbol{\alpha}) \right) \sin\gamma(\boldsymbol{\alpha}) \Bigg) \\
& + \frac{3}{2} \frac{1}{2\omega_{\mathrm{r}} L_{\mathrm{s}}^q} \sum_{\nu=6i}^{\infty} \Big(H_{1,\nu}(\boldsymbol{\alpha}) \widetilde{b}_{\nu-1}(\boldsymbol{\alpha}) + H_{2,\nu}(\boldsymbol{\alpha}) \widetilde{a}_{\nu-1}(\boldsymbol{\alpha}) \\
& \qquad + H_{3,\nu}(\boldsymbol{\alpha}) \widetilde{b}_{\nu+1}(\boldsymbol{\alpha}) + H_{4,\nu}(\boldsymbol{\alpha}) \widetilde{a}_{\nu+1}(\boldsymbol{\alpha}) \Big),
\end{aligned} \tag{2.66}
$$

where $i \in \mathbb{N}$ in all equations in this subsection. The first ac group $i_{\mathrm{inv,ac_1}}(\boldsymbol{\alpha})$ is formed by multiplying the fundamental component $\nu = 1$ of the one phase signal is multiplied with all harmonics $\nu = 6i \pm 1$ of the other phase signal, i.e.

$$
\begin{aligned}
i_{\mathrm{inv,ac_1}}(\boldsymbol{\alpha}) :=& \boldsymbol{s}_1^{uvw}(\boldsymbol{\alpha})^\top \sum_{\nu=6i\pm1}^{\infty} \boldsymbol{i}_{\mathrm{s},\nu}^{uvw}(\boldsymbol{\alpha}) + \sum_{\nu=6i\pm1}^{\infty} \boldsymbol{s}_\nu^{uvw}(\boldsymbol{\alpha})^\top \boldsymbol{i}_{\mathrm{s},1}^{uvw}(\boldsymbol{\alpha}) \\
=& \boldsymbol{s}_1^{uvw}(\boldsymbol{\alpha})^\top \boldsymbol{i}_{\mathrm{s},5}^{uvw}(\boldsymbol{\alpha}) + \boldsymbol{s}_1^{uvw}(\boldsymbol{\alpha})^\top \boldsymbol{i}_{\mathrm{s},7}^{uvw}(\boldsymbol{\alpha}) + \ldots \\
& + \boldsymbol{s}_5^{uvw}(\boldsymbol{\alpha})^\top \boldsymbol{i}_{\mathrm{s},1}^{uvw}(\boldsymbol{\alpha}) + \boldsymbol{s}_7^{uvw}(\boldsymbol{\alpha})^\top \boldsymbol{i}_{\mathrm{s},1}^{uvw}(\boldsymbol{\alpha}) + \ldots \\
\overset{\substack{(2.60)-(2.62),\\(2.64)}}{=}& \frac{3}{2} \sum_{\nu=6i}^{\infty} \Bigg(\left(i_{\mathrm{s},1}^d(\boldsymbol{\alpha}) \cos\gamma(\boldsymbol{\alpha}) + i_{\mathrm{s},1}^q(\boldsymbol{\alpha}) \sin\gamma(\boldsymbol{\alpha}) \right) \left(\widetilde{a}_{\nu-1}(\boldsymbol{\alpha}) + \widetilde{a}_{\nu+1}(\boldsymbol{\alpha}) \right) \\
& + \left(-i_{\mathrm{s},1}^d(\boldsymbol{\alpha}) \sin\gamma(\boldsymbol{\alpha}) + i_{\mathrm{s},1}^q(\boldsymbol{\alpha}) \cos\gamma(\boldsymbol{\alpha}) \right) \left(\widetilde{b}_{\nu-1}(\boldsymbol{\alpha}) - \widetilde{b}_{\nu+1}(\boldsymbol{\alpha}) \right) \\
& + \frac{1}{2\omega_{\mathrm{r}} L_{\mathrm{s}}^q} \Big(- H_{1,\nu}(\boldsymbol{\alpha}) \widetilde{b}_1(\boldsymbol{\alpha}) + H_{2,\nu}(\boldsymbol{\alpha}) \widetilde{a}_1(\boldsymbol{\alpha}) \\
& \qquad + H_{3,\nu}(\boldsymbol{\alpha}) \widetilde{b}_1(\boldsymbol{\alpha}) + H_{4,\nu}(\boldsymbol{\alpha}) \widetilde{a}_1(\boldsymbol{\alpha}) \Big) \Bigg) \cos(\nu(\theta_{\mathrm{r}} + \gamma(\boldsymbol{\alpha})))
\end{aligned} \tag{2.67}
$$

$$
\begin{aligned}
&+\frac{3}{2}\sum_{\nu=6i}^{\infty}\Bigg(\Big(i_{\mathrm{s},1}^{d}(\boldsymbol{\alpha})\sin\gamma(\boldsymbol{\alpha})-i_{\mathrm{s},1}^{q}(\boldsymbol{\alpha})\cos\gamma(\boldsymbol{\alpha})\Big)\left(\widetilde{a}_{\nu-1}(\boldsymbol{\alpha})-\widetilde{a}_{\nu+1}(\boldsymbol{\alpha})\right)\\
&\qquad+\Big(i_{\mathrm{s},1}^{d}(\boldsymbol{\alpha})\cos\gamma(\boldsymbol{\alpha})+i_{\mathrm{s},1}^{q}(\boldsymbol{\alpha})\sin\gamma(\boldsymbol{\alpha})\Big)\left(\widetilde{b}_{\nu-1}(\boldsymbol{\alpha})+\widetilde{b}_{\nu+1}(\boldsymbol{\alpha})\right)\\
&\qquad+\frac{1}{2\omega_{\mathrm{r}}L_{\mathrm{s}}^{q}}\Big(H_{1,\nu}(\boldsymbol{\alpha})\widetilde{a}_1(\boldsymbol{\alpha})+H_{2,\nu}(\boldsymbol{\alpha})\widetilde{b}_1(\boldsymbol{\alpha})\\
&\qquad\qquad+H_{3,\nu}(\boldsymbol{\alpha})\widetilde{a}_1(\boldsymbol{\alpha})-H_{4,\nu}(\boldsymbol{\alpha})\widetilde{b}_1(\boldsymbol{\alpha})\Big)\Bigg)\sin(\nu(\theta_{\mathrm{r}}+\gamma(\boldsymbol{\alpha}))).
\end{aligned}
$$

The second ac group $i_{\mathrm{inv,ac_2}}(\boldsymbol{\alpha})$ is defined by the signals $\boldsymbol{s}_{\nu_1}^{uvw}(\boldsymbol{\alpha})$ and $\boldsymbol{i}_{\mathrm{s},\nu_2}^{uvw}(\boldsymbol{\alpha})$, where $\nu_1+\nu_2=6i$ and $\nu_1,\nu_2\neq 1$, i.e.

$$
\begin{aligned}
i_{\mathrm{inv,ac_2}}(\boldsymbol{\alpha}) &:= \sum_{\nu=6i}^{\infty}\sum_{k=6i}^{\nu-6}\boldsymbol{s}_{k+1}^{uvw}(\boldsymbol{\alpha})^{\top}\boldsymbol{i}_{\mathrm{s},\nu-k-1}^{uvw}(\boldsymbol{\alpha})+\boldsymbol{s}_{k-1}^{uvw}(\boldsymbol{\alpha})^{\top}\boldsymbol{i}_{\mathrm{s},\nu-k+1}^{uvw}(\boldsymbol{\alpha})\\
&=\boldsymbol{s}_{7}^{uvw}(\boldsymbol{\alpha})^{\top}\boldsymbol{i}_{\mathrm{s},5}^{uvw}(\boldsymbol{\alpha})+\boldsymbol{s}_{5}^{uvw}(\boldsymbol{\alpha})^{\top}\boldsymbol{i}_{\mathrm{s},7}^{uvw}(\boldsymbol{\alpha})+\boldsymbol{s}_{7}^{uvw}(\boldsymbol{\alpha})^{\top}\boldsymbol{i}_{\mathrm{s},11}^{uvw}(\boldsymbol{\alpha})\\
&\quad+\boldsymbol{s}_{5}^{uvw}(\boldsymbol{\alpha})^{\top}\boldsymbol{i}_{\mathrm{s},13}^{uvw}(\boldsymbol{\alpha})+\boldsymbol{s}_{13}^{uvw}(\boldsymbol{\alpha})^{\top}\boldsymbol{i}_{\mathrm{s},5}^{uvw}(\boldsymbol{\alpha})+\boldsymbol{s}_{11}^{uvw}(\boldsymbol{\alpha})^{\top}\boldsymbol{i}_{\mathrm{s},7}^{uvw}(\boldsymbol{\alpha})+\dots\\
&\overset{\substack{(2.60)-(2.62),\\(2.64)}}{=}\frac{3}{2}\frac{1}{2\omega_{\mathrm{r}}L_{\mathrm{s}}^{q}}\sum_{\nu=6i}^{\infty}\sum_{k=6i}^{\nu-6}\Big(-\widetilde{b}_{k+1}(\boldsymbol{\alpha})H_{1,\nu-k}(\boldsymbol{\alpha})-\widetilde{a}_{k+1}(\boldsymbol{\alpha})H_{2,\nu-k}(\boldsymbol{\alpha})\\
&\qquad\qquad+\widetilde{b}_{k-1}(\boldsymbol{\alpha})H_{3,\nu-k}(\boldsymbol{\alpha})-\widetilde{a}_{k-1}(\boldsymbol{\alpha})H_{4,\nu-k}(\boldsymbol{\alpha})\Big)\cos(\nu(\theta_{\mathrm{r}}+\gamma(\boldsymbol{\alpha})))\\
&\quad+\frac{3}{2}\frac{1}{2\omega_{\mathrm{r}}L_{\mathrm{s}}^{q}}\sum_{\nu=6i}^{\infty}\sum_{k=6i}^{\nu-6}\Big(\widetilde{a}_{k+1}(\boldsymbol{\alpha})H_{1,\nu-k}(\boldsymbol{\alpha})+\widetilde{b}_{k+1}(\boldsymbol{\alpha})H_{2,\nu-k}(\boldsymbol{\alpha})\\
&\qquad\qquad+\widetilde{a}_{k-1}(\boldsymbol{\alpha})H_{3,\nu-k}(\boldsymbol{\alpha})+\widetilde{b}_{k-1}(\boldsymbol{\alpha})H_{4,\nu-k}(\boldsymbol{\alpha})\Big)\sin(\nu(\theta_{\mathrm{r}}+\gamma(\boldsymbol{\alpha})))
\end{aligned}
\tag{2.68}
$$

Lastly, $i_{\mathrm{inv,ac_3}}(\boldsymbol{\alpha})$ is defined by $\boldsymbol{s}_{\nu_1}^{uvw}(\boldsymbol{\alpha})$ and $\boldsymbol{i}_{\mathrm{s},\nu_2}^{uvw}(\boldsymbol{\alpha})$, where $|\nu_1-\nu_2|=6i$ and $\nu_1,\nu_2\neq 1$, i.e.

$$
\begin{aligned}
i_{\mathrm{inv,ac_3}}(\boldsymbol{\alpha}) &:= \sum_{\nu=6i}^{\infty}\sum_{k=6i}^{\infty}\Big(\boldsymbol{s}_{k-1}^{uvw}(\boldsymbol{\alpha})^{\top}\boldsymbol{i}_{\mathrm{s},\nu+k-1}^{uvw}(\boldsymbol{\alpha})+\boldsymbol{s}_{\nu+k-1}^{uvw}(\boldsymbol{\alpha})^{\top}\boldsymbol{i}_{\mathrm{s},k-1}^{uvw}(\boldsymbol{\alpha})\\
&\qquad+\boldsymbol{s}_{k+1}^{uvw}(\boldsymbol{\alpha})^{\top}\boldsymbol{i}_{\mathrm{s},\nu+k+1}^{uvw}(\boldsymbol{\alpha})+\boldsymbol{s}_{\nu+k+1}^{uvw}(\boldsymbol{\alpha})^{\top}\boldsymbol{i}_{\mathrm{s},k+1}^{uvw}(\boldsymbol{\alpha})\Big)\\
&=\boldsymbol{s}_{5}^{uvw}(\boldsymbol{\alpha})^{\top}\boldsymbol{i}_{\mathrm{s},11}^{uvw}(\boldsymbol{\alpha})+\boldsymbol{s}_{11}^{uvw}(\boldsymbol{\alpha})^{\top}\boldsymbol{i}_{\mathrm{s},5}^{uvw}(\boldsymbol{\alpha})+\boldsymbol{s}_{7}^{uvw}(\boldsymbol{\alpha})^{\top}\boldsymbol{i}_{\mathrm{s},13}^{uvw}(\boldsymbol{\alpha})+\boldsymbol{s}_{13}^{uvw}(\boldsymbol{\alpha})^{\top}\boldsymbol{i}_{\mathrm{s},7}^{uvw}(\boldsymbol{\alpha})+\dots\\
&\quad+\boldsymbol{s}_{5}^{uvw}(\boldsymbol{\alpha})^{\top}\boldsymbol{i}_{\mathrm{s},17}^{uvw}(\boldsymbol{\alpha})+\boldsymbol{s}_{17}^{uvw}(\boldsymbol{\alpha})^{\top}\boldsymbol{i}_{\mathrm{s},5}^{uvw}(\boldsymbol{\alpha})+\boldsymbol{s}_{7}^{uvw}(\boldsymbol{\alpha})^{\top}\boldsymbol{i}_{\mathrm{s},19}^{uvw}(\boldsymbol{\alpha})+\boldsymbol{s}_{19}^{uvw}(\boldsymbol{\alpha})^{\top}\boldsymbol{i}_{\mathrm{s},7}^{uvw}(\boldsymbol{\alpha})+\dots\\
&\overset{\substack{(2.60)-(2.62),\\(2.64)}}{=}\frac{3}{2}\frac{1}{2\omega_{\mathrm{r}}L_{\mathrm{s}}^{q}}\sum_{\nu=6i}^{\infty}\sum_{k=6i}^{\infty}\Big(\widetilde{b}_{k-1}(\boldsymbol{\alpha})H_{1,\nu+k}(\boldsymbol{\alpha})+\widetilde{a}_{k-1}(\boldsymbol{\alpha})H_{2,\nu+k}(\boldsymbol{\alpha})\\
&\qquad\qquad+\widetilde{b}_{\nu+k-1}(\boldsymbol{\alpha})H_{1,k}(\boldsymbol{\alpha})+\widetilde{a}_{\nu+k-1}(\boldsymbol{\alpha})H_{2,k}(\boldsymbol{\alpha})\\
&\qquad\qquad+\widetilde{b}_{k+1}(\boldsymbol{\alpha})H_{3,\nu+k}(\boldsymbol{\alpha})+\widetilde{a}_{k+1}(\boldsymbol{\alpha})H_{4,\nu+k}(\boldsymbol{\alpha})\\
&\qquad\qquad+\widetilde{b}_{\nu+k+1}(\boldsymbol{\alpha})H_{3,k}(\boldsymbol{\alpha})+\widetilde{a}_{\nu+k+1}(\boldsymbol{\alpha})H_{4,k}(\boldsymbol{\alpha})\Big)\cos\left(\nu(\theta_{\mathrm{r}}+\gamma(\boldsymbol{\alpha}))\right)
\end{aligned}
\tag{2.69}
$$

$$
\begin{aligned}
&+\frac{3}{2}\frac{1}{2\omega_{\mathrm{r}}L_{\mathrm{s}}^{q}}\sum_{\nu=6i}^{\infty}\sum_{k=6i}^{\infty}\Big(\widetilde{a}_{k-1}(\boldsymbol{\alpha})H_{1,\nu+k}(\boldsymbol{\alpha})-\widetilde{b}_{k-1}(\boldsymbol{\alpha})H_{2,\nu+k}(\boldsymbol{\alpha})\\
&\qquad\qquad-\widetilde{a}_{\nu+k-1}(\boldsymbol{\alpha})H_{1,k}(\boldsymbol{\alpha})+\widetilde{b}_{\nu+k-1}(\boldsymbol{\alpha})H_{2,k}(\boldsymbol{\alpha})\\
&\qquad\qquad+\widetilde{a}_{k+1}(\boldsymbol{\alpha})H_{3,\nu+k}(\boldsymbol{\alpha})-\widetilde{b}_{k+1}(\boldsymbol{\alpha})H_{4,\nu+k}(\boldsymbol{\alpha})\\
&\qquad\qquad-\widetilde{a}_{\nu+k+1}(\boldsymbol{\alpha})H_{3,k}(\boldsymbol{\alpha})+\widetilde{b}_{\nu+k+1}(\boldsymbol{\alpha})H_{4,k}(\boldsymbol{\alpha})\Big)\sin\left(\nu(\theta_{\mathrm{r}}+\gamma(\boldsymbol{\alpha}))\right)
\end{aligned}
$$

The products $\boldsymbol{s}_{\nu_1}^{uvw}(\boldsymbol{\alpha})^{\top}\boldsymbol{i}_{\mathrm{s},\nu_2}^{uvw}(\boldsymbol{\alpha})$ of all other combinations of harmonic components $\nu_1\in\mathcal{I}$ and $\nu_2\in\mathcal{H}$ are zero. Eq. (2.67) - (2.69) show that only ac harmonics multiples of six exist in $i_{\mathrm{inv}}(\boldsymbol{\alpha})$, whereas the odd triplen harmonics of $\boldsymbol{s}^{uvw}(\boldsymbol{\alpha})$ do not produce ripple in $i_{\mathrm{inv}}(\boldsymbol{\alpha})$. Subsequently, the inverter current $i_{\mathrm{inv}}(\boldsymbol{\alpha})$ can be written in the following form

$$
i_{\mathrm{inv}}(\boldsymbol{\alpha})\overset{(2.63)}{=}i_{\mathrm{inv,dc}}(\boldsymbol{\alpha})+\sum_{\nu=6i}^{\infty}i_{\mathrm{inv,COS},\nu}(\boldsymbol{\alpha})\cos(\nu(\theta_{\mathrm{r}}+\gamma(\boldsymbol{\alpha})))+i_{\mathrm{inv,SIN},\nu}(\boldsymbol{\alpha})\sin(\nu(\theta_{\mathrm{r}}+\gamma(\boldsymbol{\alpha}))),
\tag{2.70}
$$

where $i_{\mathrm{inv,COS},\nu}(\boldsymbol{\alpha})$ is composed of the cosine components of $i_{\mathrm{inv}}(\boldsymbol{\alpha})$, i.e.

$$
\begin{aligned}
i_{\mathrm{inv,COS},\nu}(\boldsymbol{\alpha}):=&\frac{3}{2}\left(i_{\mathrm{s},1}^{d}(\boldsymbol{\alpha})\cos\gamma(\boldsymbol{\alpha})+i_{\mathrm{s},1}^{q}(\boldsymbol{\alpha})\sin\gamma(\boldsymbol{\alpha})\right)\left(\widetilde{a}_{\nu-1}(\boldsymbol{\alpha})+\widetilde{a}_{\nu+1}(\boldsymbol{\alpha})\right)\\
&+\frac{3}{2}\left(-i_{\mathrm{s},1}^{d}(\boldsymbol{\alpha})\sin\gamma(\boldsymbol{\alpha})+i_{\mathrm{s},1}^{q}(\boldsymbol{\alpha})\cos\gamma(\boldsymbol{\alpha})\right)\left(\widetilde{b}_{\nu-1}(\boldsymbol{\alpha})-\widetilde{b}_{\nu+1}(\boldsymbol{\alpha})\right)\\
&+\frac{3}{2}\frac{1}{2\omega_{\mathrm{r}}L_{\mathrm{s}}^{q}}\Big(-H_{1,\nu}(\boldsymbol{\alpha})\widetilde{b}_1(\boldsymbol{\alpha})+H_{2,\nu}(\boldsymbol{\alpha})\widetilde{a}_1(\boldsymbol{\alpha})+H_{3,\nu}(\boldsymbol{\alpha})\widetilde{b}_1(\boldsymbol{\alpha})+H_{4,\nu}(\boldsymbol{\alpha})\widetilde{a}_1(\boldsymbol{\alpha})\Big)\\
&+\frac{3}{2}\frac{1}{2\omega_{\mathrm{r}}L_{\mathrm{s}}^{q}}\sum_{k=6i}^{\nu-6}-\widetilde{b}_{k+1}(\boldsymbol{\alpha})H_{1,\nu-k}(\boldsymbol{\alpha})-\widetilde{a}_{k+1}(\boldsymbol{\alpha})H_{2,\nu-k}(\boldsymbol{\alpha})\\
&\qquad+\widetilde{b}_{k-1}(\boldsymbol{\alpha})H_{3,\nu-k}(\boldsymbol{\alpha})-\widetilde{a}_{k-1}(\boldsymbol{\alpha})H_{4,\nu-k}(\boldsymbol{\alpha})\\
&+\frac{3}{2}\frac{1}{2\omega_{\mathrm{r}}L_{\mathrm{s}}^{q}}\sum_{k=6i}^{\infty}\widetilde{b}_{k-1}(\boldsymbol{\alpha})H_{1,\nu+k}(\boldsymbol{\alpha})+\widetilde{a}_{k-1}(\boldsymbol{\alpha})H_{2,\nu+k}(\boldsymbol{\alpha})\\
&\qquad+\widetilde{b}_{\nu+k-1}(\boldsymbol{\alpha})H_{1,k}(\boldsymbol{\alpha})+\widetilde{a}_{\nu+k-1}(\boldsymbol{\alpha})H_{2,k}(\boldsymbol{\alpha})\\
&\qquad+\widetilde{b}_{k+1}(\boldsymbol{\alpha})H_{3,\nu+k}(\boldsymbol{\alpha})+\widetilde{a}_{k+1}(\boldsymbol{\alpha})H_{4,\nu+k}(\boldsymbol{\alpha})\\
&\qquad+\widetilde{b}_{\nu+k+1}(\boldsymbol{\alpha})H_{3,k}(\boldsymbol{\alpha})+\widetilde{a}_{\nu+k+1}(\boldsymbol{\alpha})H_{4,k}(\boldsymbol{\alpha}),
\end{aligned}
\tag{2.71}
$$

and $i_{\mathrm{inv,SIN},\nu}(\boldsymbol{\alpha})$ is formed of the sine components of $i_{\mathrm{inv}}(\boldsymbol{\alpha})$, i.e.

$$
\begin{aligned}
i_{\mathrm{inv,SIN},\nu}(\boldsymbol{\alpha}):=&\frac{3}{2}\left(i_{\mathrm{s},1}^{d}(\boldsymbol{\alpha})\sin\gamma(\boldsymbol{\alpha})-i_{\mathrm{s},1}^{q}(\boldsymbol{\alpha})\cos\gamma(\boldsymbol{\alpha})\right)\left(\widetilde{a}_{\nu-1}(\boldsymbol{\alpha})-\widetilde{a}_{\nu+1}(\boldsymbol{\alpha})\right)\\
&+\frac{3}{2}\left(i_{\mathrm{s},1}^{d}(\boldsymbol{\alpha})\cos\gamma(\boldsymbol{\alpha})+i_{\mathrm{s},1}^{q}(\boldsymbol{\alpha})\sin\gamma(\boldsymbol{\alpha})\right)\left(\widetilde{b}_{\nu-1}(\boldsymbol{\alpha})+\widetilde{b}_{\nu+1}(\boldsymbol{\alpha})\right)\\
&+\frac{3}{2}\frac{1}{2\omega_{\mathrm{r}}L_{\mathrm{s}}^{q}}\Big(H_{1,\nu}(\boldsymbol{\alpha})\widetilde{a}_1(\boldsymbol{\alpha})+H_{2,\nu}(\boldsymbol{\alpha})\widetilde{b}_1(\boldsymbol{\alpha})+H_{3,\nu}(\boldsymbol{\alpha})\widetilde{a}_1(\boldsymbol{\alpha})-H_{4,\nu}(\boldsymbol{\alpha})\widetilde{b}_1(\boldsymbol{\alpha})\Big)\Big)\\
&+\frac{3}{2}\frac{1}{2\omega_{\mathrm{r}}L_{\mathrm{s}}^{q}}\sum_{k=6i}^{\nu-6}\widetilde{a}_{k+1}(\boldsymbol{\alpha})H_{1,\nu-k}(\boldsymbol{\alpha})+\widetilde{b}_{k+1}(\boldsymbol{\alpha})H_{2,\nu-k}(\boldsymbol{\alpha})\\
&\qquad+\widetilde{a}_{k-1}(\boldsymbol{\alpha})H_{3,\nu-k}(\boldsymbol{\alpha})+\widetilde{b}_{k-1}(\boldsymbol{\alpha})H_{4,\nu-k}(\boldsymbol{\alpha})
\end{aligned}
\tag{2.72}
$$

$$
\begin{aligned}
+\frac{3}{2}\frac{1}{2\omega_\mathrm{r} L_\mathrm{s}^q}\sum_{k=6i}^{\infty} & \widetilde{a}_{k-1}(\boldsymbol{\alpha})H_{1,\nu+k}(\boldsymbol{\alpha}) - \widetilde{b}_{k-1}(\boldsymbol{\alpha})H_{2,\nu+k}(\boldsymbol{\alpha}) \\
& -\widetilde{a}_{\nu+k-1}(\boldsymbol{\alpha})H_{1,k}(\boldsymbol{\alpha}) + \widetilde{b}_{\nu+k-1}(\boldsymbol{\alpha})H_{2,k}(\boldsymbol{\alpha}) \\
& +\widetilde{a}_{k+1}(\boldsymbol{\alpha})H_{3,\nu+k}(\boldsymbol{\alpha}) - \widetilde{b}_{k+1}(\boldsymbol{\alpha})H_{4,\nu+k}(\boldsymbol{\alpha}) \\
& -\widetilde{a}_{\nu+k+1}(\boldsymbol{\alpha})H_{3,k}(\boldsymbol{\alpha}) + \widetilde{b}_{\nu+k+1}(\boldsymbol{\alpha})H_{4,k}(\boldsymbol{\alpha}).
\end{aligned}
$$

For the derivation of all of the equations above, the ripple in the dc-link voltage u_dc was neglected (see (A1)). However, a small impedance in the battery simulator and cable Z_bat always exists. Assuming that the current of Eq. (2.70) flows in the inverter, the expression of the dc-link capacitor current $i_\mathrm{c}(\boldsymbol{\alpha})$ can be derived applying the Kirchhoff's voltage and current law [111, Ch. 3] in the electrical circuit of Fig. 2.1 as follows

$$
\begin{aligned}
u_\mathrm{bat} &= Z_\mathrm{bat} i_\mathrm{bat}(\boldsymbol{\alpha}) + Z_\mathrm{c} i_\mathrm{c}(\boldsymbol{\alpha}) \\
i_\mathrm{bat}(\boldsymbol{\alpha}) &= i_\mathrm{c}(\boldsymbol{\alpha}) + i_\mathrm{inv}(\boldsymbol{\alpha}).
\end{aligned}
\tag{2.73}
$$

The impedances of the battery stack Z_bat and the capacitor Z_c are given in rectangular form by

$$
Z_\mathrm{bat} = R_\mathrm{bat} + j\nu\omega_\mathrm{r} L_\mathrm{bat} \tag{2.74}
$$

and

$$
Z_\mathrm{c} = R_\mathrm{ESR} + \frac{1}{j\nu\omega_\mathrm{r} C}, \tag{2.75}
$$

respectively. The inverter dc component

$$
i_\mathrm{inv,dc} \overset{(2.73)}{=} i_\mathrm{bat,dc} = \frac{u_\mathrm{bat}}{Z_\mathrm{bat}} = \frac{u_\mathrm{bat}}{R_\mathrm{bat}} \tag{2.76}
$$

is drawn from the battery; consequently, the dc-link capacitor current can be calculated as follows

$$
\begin{aligned}
i_\mathrm{c}(\boldsymbol{\alpha}) &\overset{(2.73)}{=} \frac{u_\mathrm{bat}}{Z_\mathrm{bat}+Z_\mathrm{c}} - \frac{Z_\mathrm{bat}}{Z_\mathrm{bat}+Z_\mathrm{c}} i_\mathrm{inv}(\boldsymbol{\alpha}) \\
&= \frac{u_\mathrm{bat}}{Z_\mathrm{bat}+Z_\mathrm{c}} - \frac{Z_\mathrm{bat}}{Z_\mathrm{bat}+Z_\mathrm{c}} \left(i_\mathrm{inv,dc}(\boldsymbol{\alpha}) + i_\mathrm{inv,ac}(\boldsymbol{\alpha})\right) \\
&\overset{(2.76)}{=} \underbrace{-\frac{Z_\mathrm{bat}}{Z_\mathrm{bat}+Z_\mathrm{c}}}_{:=H_{\mathrm{c},\nu}\in\mathbb{C}} i_\mathrm{inv,ac}(\boldsymbol{\alpha}).
\end{aligned}
\tag{2.77}
$$

Based on (2.74) and (2.75), the coefficient $H_{c,\nu}$ is given in rectangular form by

$$
\begin{aligned}
H_{\mathrm{c},\nu} &= \frac{Z_\mathrm{bat}}{Z_\mathrm{bat}+Z_\mathrm{c}} = \frac{R_\mathrm{bat} + j\nu\omega_\mathrm{r} L_\mathrm{bat}}{R_\mathrm{bat} + R_\mathrm{ESR} + j\left(\nu\omega_\mathrm{r} L_\mathrm{bat} - \frac{1}{\nu\omega_\mathrm{r} C}\right)} \\
&= \frac{(R_\mathrm{bat} + j\nu\omega_\mathrm{r} L_\mathrm{bat})\left(R_\mathrm{bat} + R_\mathrm{ESR} - j\left(\nu\omega_\mathrm{r} L_\mathrm{bat} - \frac{1}{\nu\omega_\mathrm{r} C}\right)\right)}{\left(R_\mathrm{bat} + R_\mathrm{ESR} + j\left(\nu\omega_\mathrm{r} L_\mathrm{bat} - \frac{1}{\nu\omega_\mathrm{r} C}\right)\right)\left(R_\mathrm{bat} + R_\mathrm{ESR} - j\left(\nu\omega_\mathrm{r} L_\mathrm{bat} - \frac{1}{\nu\omega_\mathrm{r} C}\right)\right)} \\
&= \frac{R_\mathrm{bat}(R_\mathrm{bat} + R_\mathrm{ESR}) + \nu^2\omega_\mathrm{r}^2 L_\mathrm{bat}^2 - \frac{L_\mathrm{bat}}{C}}{(R_\mathrm{bat} + R_\mathrm{ESR})^2 + \left(\nu\omega_\mathrm{r} L_\mathrm{bat} - \frac{1}{\nu\omega_\mathrm{r} C}\right)^2} + j\frac{\nu\omega_\mathrm{r} L_\mathrm{bat}(R_\mathrm{bat} + R_\mathrm{ESR}) - R_\mathrm{bat}\left(\nu\omega_\mathrm{r} L_\mathrm{bat} - \frac{1}{\nu\omega_\mathrm{r} C}\right)}{(R_\mathrm{bat} + R_\mathrm{ESR})^2 + \left(\nu\omega_\mathrm{r} L_\mathrm{bat} - \frac{1}{\nu\omega_\mathrm{r} C}\right)^2}
\end{aligned}
\tag{2.78}
$$

$$= \underbrace{\frac{R_{\text{bat}}(R_{\text{bat}}+R_{\text{ESR}})+\nu^2\omega_{\text{r}}^2L_{\text{bat}}^2-\frac{L_{\text{bat}}}{C}}{(R_{\text{bat}}+R_{\text{ESR}})^2+\left(\nu\omega_{\text{r}}L_{\text{bat}}-\frac{1}{\nu\omega_{\text{r}}C}\right)^2}}_{:=K_9}$$
$$+ j\underbrace{\frac{\nu\omega_{\text{r}}L_{\text{bat}}(R_{\text{bat}}+R_{\text{ESR}})-R_{\text{bat}}\left(\nu\omega_{\text{r}}L_{\text{bat}}-\frac{1}{\nu\omega_{\text{r}}C}\right)}{(R_{\text{bat}}+R_{\text{ESR}})^2+\left(\nu\omega_{\text{r}}L_{\text{bat}}-\frac{1}{\nu\omega_{\text{r}}C}\right)^2}}_{:=K_{10}}$$

or in polar form by

$$H_{\text{c},\nu} = h_{\text{c},\nu}\angle\theta_{\text{c},\nu}, \tag{2.79}$$

where

$$\theta_{\text{c},\nu} = \arctan\left(\frac{K_{10}}{K_9}\right) = \arctan\left(\frac{\nu\omega_{\text{r}}L_{\text{bat}}(R_{\text{bat}}+R_{\text{ESR}})-R_{\text{bat}}\left(\nu\omega_{\text{r}}L_{\text{bat}}-\frac{1}{\nu\omega_{\text{r}}C}\right)}{R_{\text{bat}}(R_{\text{bat}}+R_{\text{ESR}})+\nu^2\omega_{\text{r}}^2L_{\text{bat}}^2-\frac{L_{\text{bat}}}{C}}\right) \tag{2.80}$$

and

$$h_{\text{c},\nu} = \sqrt{K_9^2+K_{10}^2}$$
$$= \frac{\sqrt{\left(R_{\text{bat}}(R_{\text{bat}}+R_{\text{ESR}})+\nu^2\omega_{\text{r}}^2L_{\text{bat}}^2-\frac{L_{\text{bat}}}{C}\right)^2+\left(\nu\omega_{\text{r}}L_{\text{bat}}(R_{\text{bat}}+R_{\text{ESR}})-R_{\text{bat}}\left(\nu\omega_{\text{r}}L_{\text{bat}}-\frac{1}{\nu\omega_{\text{r}}C}\right)\right)^2}}{(R_{\text{bat}}+R_{\text{ESR}})^2+\left(\nu\omega_{\text{r}}L_{\text{bat}}-\frac{1}{\nu\omega_{\text{r}}C}\right)^2}. \tag{2.81}$$

Eq. (2.77) can be written in polar form as follows

$$\begin{aligned}\text{I}_{\text{c}}(\boldsymbol{\alpha}) &= -\sum_{\nu=6i}^{\infty} h_{\text{c},\nu}\angle\theta_{\text{c},\nu}\left(i_{\text{inv,COS},\nu}(\boldsymbol{\alpha})\angle(\nu\phi_0+\nu\gamma(\boldsymbol{\alpha}))+i_{\text{inv,SIN},\nu}(\boldsymbol{\alpha})\angle\left(\nu\phi_0+\nu\gamma(\boldsymbol{\alpha})-\frac{\pi}{2}\right)\right)\\ &= -\sum_{\nu=6i}^{\infty} h_{\text{c},\nu}i_{\text{inv,COS},\nu}(\boldsymbol{\alpha})\angle(\nu\phi_0+\nu\gamma(\boldsymbol{\alpha})+\theta_{\text{c},\nu})+h_{\text{c},\nu}i_{\text{inv,SIN},\nu}(\boldsymbol{\alpha})\angle\left(\nu\phi_0+\nu\gamma(\boldsymbol{\alpha})-\frac{\pi}{2}+\theta_{\text{c},\nu}\right).\end{aligned} \tag{2.82}$$

Applying the phasor theory, the dc-link capacitor current is given in the time domain by

$$\begin{aligned}i_{\text{c}}(\boldsymbol{\alpha}) = -\sum_{\nu=6i}^{\infty} &h_{\text{c},\nu}i_{\text{inv,COS},\nu}(\boldsymbol{\alpha})\cos\left(\nu(\theta_{\text{r}}+\gamma(\boldsymbol{\alpha}))+\theta_{\text{c},\nu}\right)\\ &+h_{\text{c},\nu}i_{\text{inv,SIN},\nu}(\boldsymbol{\alpha})\sin\left(\nu(\theta_{\text{r}}+\gamma(\boldsymbol{\alpha}))+\theta_{\text{c},\nu}\right)\end{aligned} \tag{2.83}$$

and its RMS value is

$$I_{\text{c,RMS}}(\boldsymbol{\alpha}) := \sqrt{\frac{1}{2}\sum_{\nu=6i}^{\infty}(h_{\text{c},\nu}i_{\text{inv,COS},\nu}(\boldsymbol{\alpha}))^2+(h_{\text{c},\nu}i_{\text{inv,SIN},\nu}(\boldsymbol{\alpha}))^2}. \tag{2.84}$$

2.3 Optimization problem

The SOPWM scheme has been extensively investigated over the last years for optimizing the performance of induction motor drives. To this end, the drive system power losses [48, 49, 86], the torque ripple [23, 24, 63], the WTHD factor [61, 62, 65, 83] and the current harmonic distortion [32, 50, 64, 74–81, 84] have been used as optimization objectives to be minimized. On the contrary, the research activity in the control of synchronous motor drives with SOPWM is limited [7, 35–41, 66] and has been focused on optimizing the current harmonic quality. A new current harmonic evaluation index is proposed in [41] for a salient pole PMSM considering PWM waveforms with HWS and QWS properties. Optimization results are presented using a PMSM with constant saliency ratio as load.

This thesis aims at minimizing the current harmonic distortion of a salient pole IPMSM, where anisotropic properties vary due to magnetic saturation and cross-saturation effects and depend on the operating point. The analysis of [41] is extended in this section for the case of only half-wave symmetric PWM waveforms and optimization results are presented considering also the varying machine saliency ratio. In this way, the influence of the motor magnetic saliency and voltage phase angle on the optimization outcomes is evaluated. In this section, the optimization problem is formulated for an isotropic and anisotropic motor and the optimization results are discussed in Sec. 2.4. The outcomes of this section are covered in [90], which is accepted for publication in *IEEE Transactions on Industrial Electronics*.

The choice of the current harmonic distortion as performance index is due to the fact that the motor copper losses are proportional to the square of the RMS value of the current harmonics [50]. Consequently, an improvement in the current harmonic quality leads to reduced losses in the copper windings. Furthermore, the torque ripple can be approximately estimated by the current harmonics [32].

It should be noted, that the dc-link capacitor current ripple (see (2.84)) is also a very attractive choice of objective function to be minimized, since the size and cost of the dc-link capacitor can be reduced in this way. SOPWM to minimize (2.84) is investigated in [91].

2.3.1 Anisotropic PMSM

The RMS value of the harmonic currents $\boldsymbol{i}_{\mathrm{s,h}}^{uvw}(\boldsymbol{\alpha})$ (see (2.60) - (2.62)) can be written as follows

$$
\begin{aligned}
I_{\mathrm{s,h,RMS}}(\boldsymbol{\alpha}) &= \frac{1}{2\sqrt{2}\omega_{\mathrm{r}} L_{\mathrm{s}}^{q}} \sqrt{\sum_{\nu=6i}^{\infty} \left(H_{1,\nu}(\boldsymbol{\alpha})\right)^2 + \left(H_{2,\nu}(\boldsymbol{\alpha})\right)^2 + \left(H_{3,\nu}(\boldsymbol{\alpha})\right)^2 + \left(H_{4,\nu}(\boldsymbol{\alpha})\right)^2} \\
&= \frac{1}{\omega_{\mathrm{r}} L_{\mathrm{s}}^{q}} \Bigg[\sum_{\nu=6i}^{\infty} \left(\left(\frac{a_{\nu-1}(\boldsymbol{\alpha})}{\nu-1} \right)^2 + \left(\frac{a_{\nu+1}(\boldsymbol{\alpha})}{\nu+1} \right)^2 + \left(\frac{b_{\nu-1}(\boldsymbol{\alpha})}{\nu-1} \right)^2 + \left(\frac{b_{\nu+1}(\boldsymbol{\alpha})}{\nu+1} \right)^2 \right) \frac{\lambda^2+1}{4} \\
&\quad + 2 \left(\frac{a_{\nu-1}(\boldsymbol{\alpha})}{\nu-1} \frac{a_{\nu+1}(\boldsymbol{\alpha})}{\nu+1} + \frac{b_{\nu-1}(\boldsymbol{\alpha})}{\nu-1} \frac{b_{\nu+1}(\boldsymbol{\alpha})}{\nu+1} \right) \left(\frac{\lambda^2-1}{4} \right) \cos(2\gamma(\boldsymbol{\alpha})) \\
&\quad + 2 \left(\frac{a_{\nu-1}(\boldsymbol{\alpha})}{\nu-1} \frac{b_{\nu+1}(\boldsymbol{\alpha})}{\nu+1} - \frac{a_{\nu+1}(\boldsymbol{\alpha})}{\nu+1} \frac{b_{\nu-1}(\boldsymbol{\alpha})}{\nu-1} \right) \left(\frac{\lambda^2-1}{4} \right) \sin(2\gamma(\boldsymbol{\alpha})) \Bigg]^{\frac{1}{2}} \\
&= K \sigma_{\mathrm{aniso}}(\boldsymbol{\alpha}),
\end{aligned}
\tag{2.85}
$$

where

$$
K := \frac{u_{\mathrm{dc}}}{\omega_{\mathrm{r}} L_{\mathrm{s}}^{q}} \tag{2.86}
$$

and

$$\begin{aligned}\sigma_{\text{aniso}}(\boldsymbol{\alpha}) &:= \sigma_{\text{aniso}}(\boldsymbol{\alpha}, \theta_{\text{u}}, \lambda) \\ &= \Bigg[\sum_{\nu=6i}^{\infty} \left(\left(\frac{\widetilde{a}_{\nu-1}(\boldsymbol{\alpha})}{\nu-1}\right)^2 + \left(\frac{\widetilde{a}_{\nu+1}(\boldsymbol{\alpha})}{\nu+1}\right)^2 + \left(\frac{\widetilde{b}_{\nu-1}(\boldsymbol{\alpha})}{\nu-1}\right)^2 + \left(\frac{\widetilde{b}_{\nu+1}(\boldsymbol{\alpha})}{\nu+1}\right)^2\right)\left(\frac{\lambda^2+1}{4}\right) \\ &\quad +2\left(\frac{\widetilde{a}_{\nu-1}(\boldsymbol{\alpha})}{\nu-1}\frac{\widetilde{a}_{\nu+1}(\boldsymbol{\alpha})}{\nu+1} + \frac{\widetilde{b}_{\nu-1}(\boldsymbol{\alpha})}{\nu-1}\frac{\widetilde{b}_{\nu+1}(\boldsymbol{\alpha})}{\nu+1}\right)\left(\frac{\lambda^2-1}{4}\right)\cos(2\gamma(\boldsymbol{\alpha})) \\ &\quad +2\left(\frac{\widetilde{a}_{\nu-1}(\boldsymbol{\alpha})}{\nu-1}\frac{\widetilde{b}_{\nu+1}(\boldsymbol{\alpha})}{\nu+1} - \frac{\widetilde{a}_{\nu+1}(\boldsymbol{\alpha})}{\nu+1}\frac{\widetilde{b}_{\nu-1}(\boldsymbol{\alpha})}{\nu-1}\right)\left(\frac{\lambda^2-1}{4}\right)\sin(2\gamma(\boldsymbol{\alpha}))\Bigg]^{\frac{1}{2}}.\end{aligned} \tag{2.87}$$

The variable $\sigma_{\text{aniso}}(\boldsymbol{\alpha}) := \sigma_{\text{aniso}}(\boldsymbol{\alpha}, \theta_{\text{u}}, \lambda)$ depends on the optimized switching angle vector $\boldsymbol{\alpha}$ as in (2.17), the saliency ratio λ as in (2.58) and the angle $\gamma = \gamma(\boldsymbol{\alpha}, \theta_{\text{u}})$, i.e. the voltage phase angle θ_{u}, as in (2.29). Moreover, $\sigma_{\text{aniso}}(\boldsymbol{\alpha})$ has no unit, since the Fourier coefficients $\widetilde{a}_{\nu}(\boldsymbol{\alpha})$ and $\widetilde{b}_{\nu}(\boldsymbol{\alpha})$ are normalized by the factor u_{dc} (see (2.30), (2.31) and (2.65)). The analytical expressions of the harmonic currents are derived under the assumption (A1) that the dc-link voltage u_{dc} has no ripple and the assumption (A5) that the machine magnetic properties are constant in steady-state operation. As a consequence, the factor K remains constant in steady-state operation and influences the amplitude of each current harmonic component equally. For that reason, it does not affect the optimization results and can be ignored in the optimization procedure. Thereupon, the minimization of $I_{\text{s,h,RMS}}(\boldsymbol{\alpha})$ coincides with that of $\sigma_{\text{aniso}}(\boldsymbol{\alpha})$.

The same feature applies also for the total harmonic distortion (THD) of the phase current [83]

$$I_{\text{s,THD}}(\boldsymbol{\alpha}) := 100\frac{I_{\text{s,h,RMS}}(\boldsymbol{\alpha})}{I_{\text{s,1,RMS}}(\boldsymbol{\alpha})} \overset{(2.85)}{=} 100\frac{K\sigma_{\text{aniso}}(\boldsymbol{\alpha})}{I_{\text{s,1,RMS}}(\boldsymbol{\alpha})}, \tag{2.88}$$

since K and the RMS value of the fundamental current $I_{\text{s,1,RMS}}(\boldsymbol{\alpha})$ remain constant in steady-state operation. Therefore, the minimization of $I_{\text{s,THD}}(\boldsymbol{\alpha})$ coincides also with that of $\sigma_{\text{aniso}}(\boldsymbol{\alpha})$.

In this thesis, the factor $\sigma_{\text{aniso}}(\boldsymbol{\alpha})$ is used as performance index in the optimization procedure. The optimization problem can be formulated as

$$\begin{aligned} &\min_{\boldsymbol{\alpha}\in[0,\pi]} \sigma_{\text{aniso}}(\boldsymbol{\alpha})\Big|_{\theta_{\text{u}},\lambda} \\ &\text{s.t} \qquad \sqrt{a_1^2(\boldsymbol{\alpha}) + b_1^2(\boldsymbol{\alpha})} = m\frac{u_{\text{dc}}}{2} \\ &\qquad\quad 0 \le \alpha_1 \le \alpha_2 \le \cdots \le \alpha_\ell \le \pi, \end{aligned} \tag{2.89}$$

where $m \in [0, \frac{4}{\pi}]$ represents the modulation index defined by (1.1). Two constraints are imposed in the optimization problem formulation as indicated by (2.89).

1. The equality constraint guarantees that the amplitude of the fundamental voltage component is preserved.

2. The inequality constraints assure that the optimized angles are in the right order within the interval $[0, \pi]$ due to the half-wave symmetric properties of the voltage waveform.

The optimization problem depends on the modulation index as indicated by the equality constraint in (2.89). Since $\sigma_{\text{aniso}}(\boldsymbol{\alpha}) := \sigma_{\text{aniso}}(\boldsymbol{\alpha}, \theta_{\text{u}}, \lambda)$ is affected also by θ_{u} and λ (see (2.87)), the optimization procedure is repeated for each triple $(m, \theta_{\text{u}}, \lambda)$ and the resulting optimized

switching angles $\boldsymbol{\alpha}_{\text{aniso}}$ are stored in three-dimensional LUTs (see Fig. 2.4a). It should be noted, that the optimized angles are symmetrical at $\theta_{\text{u}} = \pi$, i.e.

$$\boldsymbol{\alpha}|_{\theta_{\text{u}}+\pi} = \boldsymbol{\alpha}|_{\theta_{\text{u}}},$$

since

$$\gamma|_{\theta_{\text{u}}+\pi} \overset{(2.29)}{=} \gamma|_{\theta_{\text{u}}} + \pi \quad \text{and} \quad \sigma_{\text{aniso}}|_{\theta_{\text{u}}+\pi,\lambda} \overset{(2.87)}{=} \sigma_{\text{aniso}}|_{\theta_{\text{u}},\lambda}.$$

For that reason, the optimization is repeated only for $\theta_{\text{u}} \in [0, \pi)$.

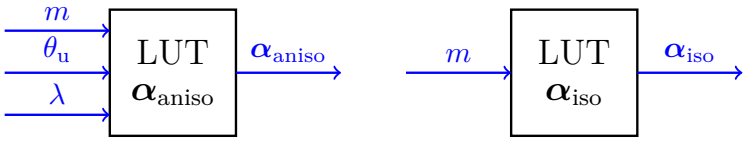

(a) *anisotropic PMSM.* (b) *isotropic PMSM.*

Figure 2.4: *LUTs for the optimized inverter switching angles of an (a) anisotropic and (b) isotropic PMSM.*

In [41], the SOPWM strategy is also investigated for a salient pole PMSM imposing QWS and HWS conditions on the PWM waveform, i.e. $a_\nu = 0$ in (2.85). Moreover, the used PMSM has a constant saliency ratio of $\lambda = 2.5$. In [39] and [40], the SOPWM is applied to an electrically excited synchronous motor considering its salient pole properties and assuming that the load angle is zero. In that case, the RMS value of the harmonic current is given by (2.85) for $a_\nu = 0$ and $\theta_{\text{u}} = \pi/2$, i.e. $\gamma = \pi$ (see (2.23)). However, the voltage phase angle θ_{u} influences the motor harmonic content, as discussed previously, and must be considered in the optimization procedure.

2.3.2 Isotropic PMSM

The objective function for an isotropic PMSM can be derived by replacing $\lambda = L_{\text{s}}^q / L_{\text{s}}^d = 1$ in (2.87) which yields

$$\sigma_{\text{iso}}(\boldsymbol{\alpha}) := \sigma_{\text{aniso}}(\boldsymbol{\alpha})\Big|_{\lambda=1} = \sqrt{\frac{1}{2} \sum_{\nu=6i\pm1}^{\infty} \frac{(\widetilde{a}_\nu(\boldsymbol{\alpha}))^2 + (\widetilde{b}_\nu(\boldsymbol{\alpha}))^2}{\nu^2}}. \tag{2.90}$$

The optimization problem for an isotropic motor can be formulated as

$$\begin{aligned} &\min_{\boldsymbol{\alpha}\in[0,\pi]} \ \sigma_{\text{iso}}(\boldsymbol{\alpha}) \\ &\text{s.t} \quad \sqrt{a_1^2(\boldsymbol{\alpha}) + b_1^2(\boldsymbol{\alpha})} = m\frac{u_{\text{dc}}}{2} \\ &\qquad 0 \le \alpha_1 \le \alpha_2 \le \cdots \le \alpha_\ell \le \pi. \end{aligned} \tag{2.91}$$

It is apparent from (2.90) and (2.91), that the optimization procedure is independent of the motor parameters and voltage phase angle. Only the modulation index m influences the optimization results. Therefore, the optimized inverter switching angles are derived only with respect to m and are stored in one-dimensional LUTs (see Fig. 2.4b). For that reason, the hardware memory requirements are reduced when the angles $\boldsymbol{\alpha}_{\textbf{iso}}$ are utilized instead of $\boldsymbol{\alpha}_{\textbf{aniso}}$.

The RMS value of the isotropic PMSM current harmonics is given by (2.85) for $L = L_{\text{s}}^d = L_{\text{s}}^q$

and $\lambda = 1$ as follows

$$I_{\mathrm{s},\nu,\mathrm{RMS}}\Big|_{L=L_\mathrm{s}^d=L_\mathrm{s}^q} = \frac{1}{\omega_\mathrm{r} L}\sqrt{\frac{1}{2}\frac{a_\nu^2+b_\nu^2}{\nu^2}} = \frac{U_{\mathrm{s},\nu,\mathrm{RMS}}}{\nu\omega_\mathrm{r} L}. \tag{2.92}$$

The same equation describes the current harmonics of an induction motor (see (1.2)). Hence, the current harmonic content optimization of an isotropic PMSM and that of an induction motor yield the same results.

2.4 Optimization results

In this section, the optimization results for an isotropic and anisotropic PMSM will be presented and compared. The optimization method employed is the Quasi-Newton method for constrained optimization problems [112].

The SOPWM is a synchronous modulation strategy and the switching frequency of the inverter is proportional to the electrical frequency for a given pulse number q (see (1.6)). The motor of electric vehicles is operated in a wide frequency range, as depicted in Fig. 2.5, and the switching frequency may drop to undesired low levels if a constant pulse number is used over an electrical period. For that reason, the pulse number must increase with reducing electrical frequencies, i.e. $f_\mathrm{r} \searrow \Rightarrow q \nearrow$, as can be seen in Fig. 2.5.

Moreover, a high pulse number entails the use of more LUTs for the optimized inverter switching angles to be stored. This may not be feasible due the limited resource capabilities of the processors used in electric vehicles. Furthermore, the computation time of the optimization procedure increases with q. Thereafter, the performance of SOPWM degrades and it is more advantageous to use SVM in the lower electrical frequency range.

In this thesis, the asynchronous SVM scheme is used for electrical frequencies $f_\mathrm{r} < 400\,\mathrm{Hz}$, whereas the SOPWM scheme with a pulse number of $q = 9$ and $q = 5$ is employed for $f_\mathrm{r} \in [400, 900)\mathrm{Hz}$ and $f_\mathrm{r} \in [900, 1200]\mathrm{Hz}$, respectively. The inverter switching frequency in the case of SOPWM is reduced in comparison to asynchronous SVM, as can be seen in Fig. 2.5. This is done in order to investigate the SOPWM performance at highly reduced switching frequencies (between 4 kHz and 8 kHz) aiming at reducing the inverter switching losses.

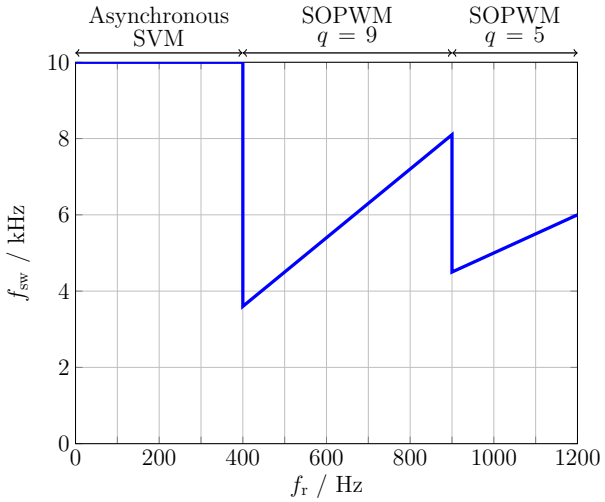

Figure 2.5: *Inverter switching frequency versus electrical frequency of the motor.*

2.4.1 Isotropic PMSM

Fig. 2.6a and Fig. 2.6b depict the optimal switching angles $\boldsymbol{\alpha}_{\text{opt}}$ for an isotropic PMSM depending on the modulation index m, when nine and five pulses are used over an electrical period, respectively. Angle discontinuities, i.e. large differencies between consecutive optimal switching angles, can be observed in $\boldsymbol{\alpha}_{\text{opt}}$. These discontinuities cause transients in machine currents and, thus, their usage is prohibited. For that reason, the angles must be postoptimized compromising current harmonic distortion. The postoptimization procedure is described in detail in [74, 76, 77]. The suboptimal postoptimized switching angles $\boldsymbol{\alpha}_{\text{iso}}$ are illustrated with continuous lines in Fig. 2.6a and Fig. 2.6b and the resulting values of $\sigma_{\text{iso}}(\boldsymbol{\alpha})$ are depicted in Fig. 2.7, which shows that $\sigma_{\text{iso}}(\boldsymbol{\alpha}_{\text{opt}}) \leq \sigma_{\text{iso}}(\boldsymbol{\alpha}_{\text{iso}})$. It should be noted, that the SOPWM with $q = 5$ is activated at high frequencies (see Fig. 2.5) where the values of m are also high. For that reason, the switching angles are postoptimized using $\boldsymbol{\alpha}_{\text{opt}}$ for $m \in [1.03, 1.2]$ as reference values. The SOPWM with $q = 9$ is employed in the middle electrical frequency range and, hence, the postoptimization is conducted based on $\boldsymbol{\alpha}_{\text{opt}}$ for $m \in [0.59, 1.01]$.

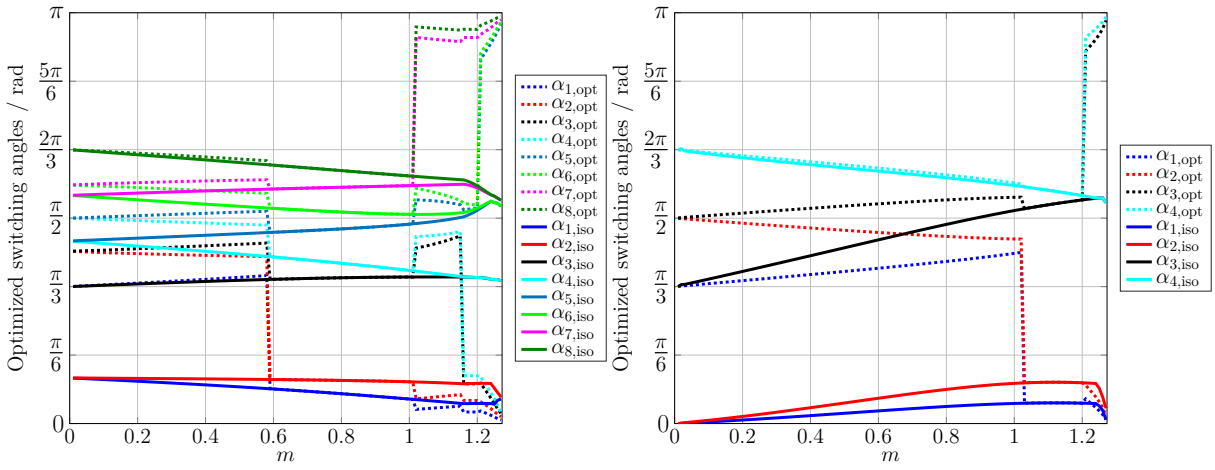

(a) $q = 9$. (b) $q = 5$.

Figure 2.6: *Optimized inverter switching angles for an isotropic PMSM when (a) $q = 9$ and (b) $q = 5$ pulses are used over an electrical period.*

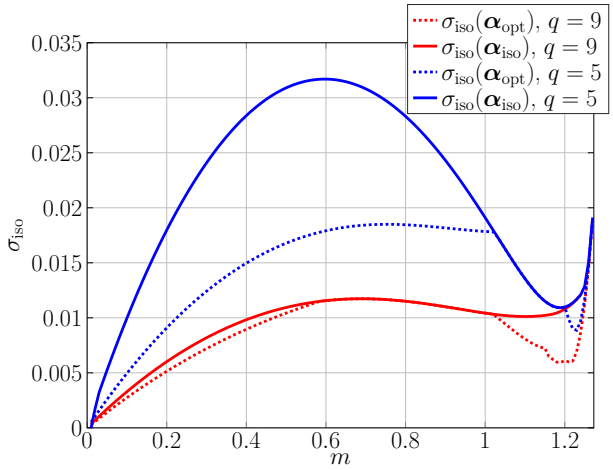

Figure 2.7: *Distortion factor when the optimal $\boldsymbol{\alpha}_{\text{opt}}$ and suboptimal $\boldsymbol{\alpha}_{\text{iso}}$ switching angles are utilized.*

2.4.2 Anisotropic PMSM

In this section, the optimized switching angles for an anisotropic PMSM will be presented, which do not depend solely on the magnitude of the fundamental voltage component, i.e. the modulation index m, but also on the voltage phase angle θ_u and the anisotropic factor λ.

The motor is operated according to the maximum torque per ampere (MTPA) and maximum torque per voltage (MTPV) operation strategies for optimal feedforward torque control for minimal motor losses [22, 113]. The optimal reference currents $\boldsymbol{i}^k_{\mathrm{s,ref}}$ and voltages $\boldsymbol{u}^k_{\mathrm{s,ref}}$ with respect to the motor torque and speed are presented in Fig. 2.8. The magnetic anisotropic properties of the machine depend on the motor currents, as depicted in Fig. 2.9a. Thereafter, the machine anisotropic factor λ varies over the motor operation range (see Fig. 2.9b) and lies within $\lambda \in [2.5, 3.2]$ when the SOPWM strategy is utilized, i.e. for $n_\mathrm{m} \geq 4\,000\,\mathrm{rpm}$ or $f_\mathrm{r} = n_\mathrm{m} n_\mathrm{p}/60 \geq 400\,\mathrm{Hz}$. Based on that, the optimization procedure is repeated for each $m \in [0, 4/\pi]$, $\theta_\mathrm{u} \in [0, \pi)$ and $\lambda \in [2.5, 3.2]$ with a step of 0.01, $\pi/180$ rad and 0.35, respectively. A small step is utilized for m, since the equality constraint in (2.89) must be kept to assure a stable current control. On the contrary, θ_u and λ do not affect the performance of the current control. They only contribute to an optimal current quality. Thus, bigger steps are used for θ_u and λ, in order to decrease the size of the LUTs and the memory needed. The optimization is performed using the fmincon algorithm [112] with the optimized angles $\boldsymbol{\alpha}_\mathrm{iso}$ of an isotropic PMSM as initial values (see Fig. 2.6).

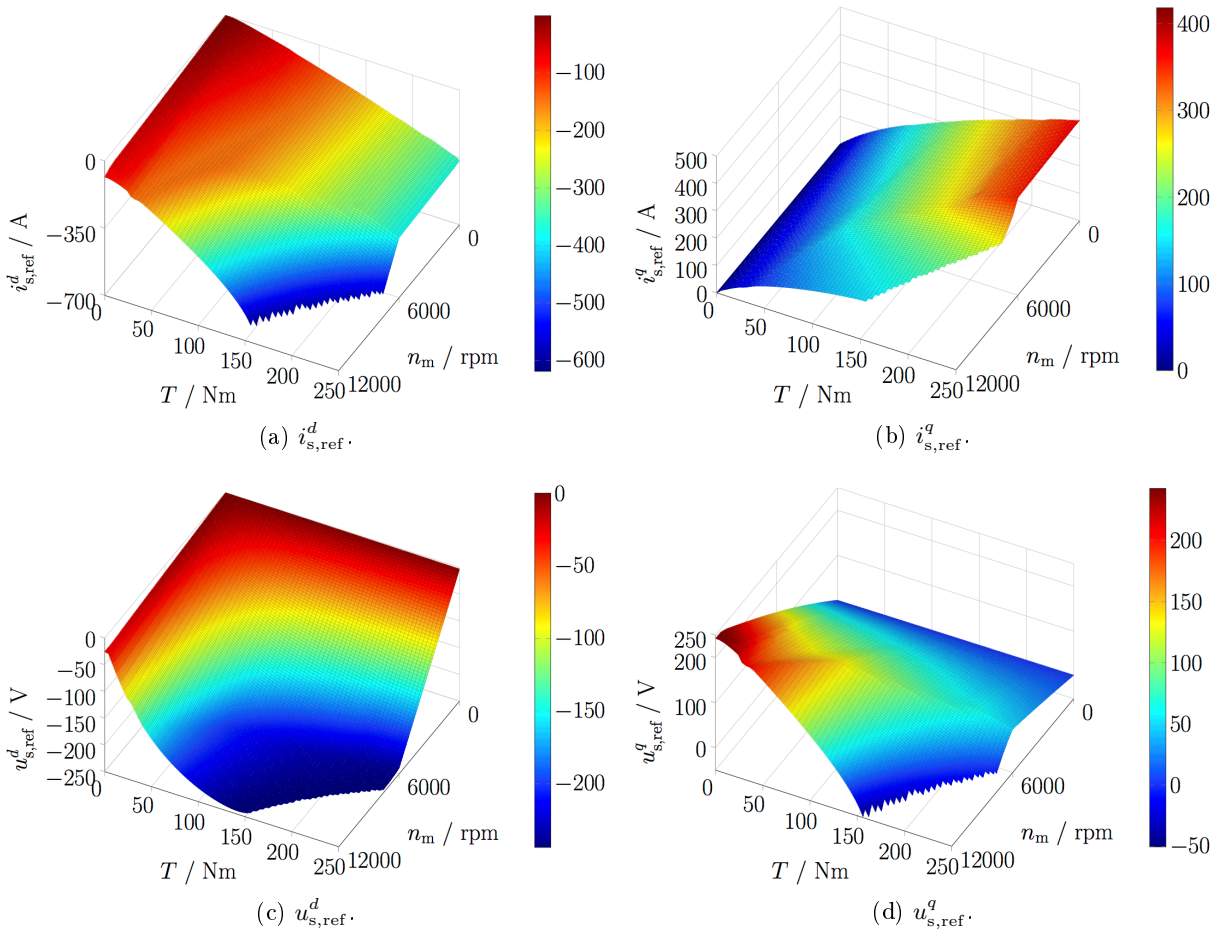

(a) $i^d_{\mathrm{s,ref}}$. (b) $i^q_{\mathrm{s,ref}}$. (c) $u^d_{\mathrm{s,ref}}$. (d) $u^q_{\mathrm{s,ref}}$.

Figure 2.8: *Reference currents and voltages in the dq-frame over motor torque and speed. The data was obtained by finite element analysis based on the MTPA and MTPV operation strategies.*

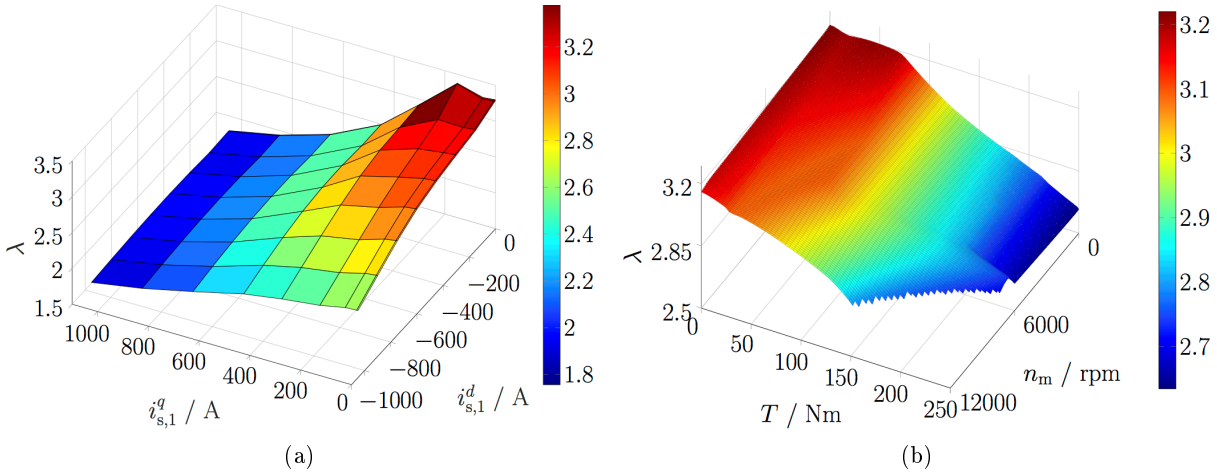

Figure 2.9: *Anisotropic factor λ (a) over the fundamental current components in the dq-frame and (b) over motor torque and speed. The data was obtained by finite element analysis.*

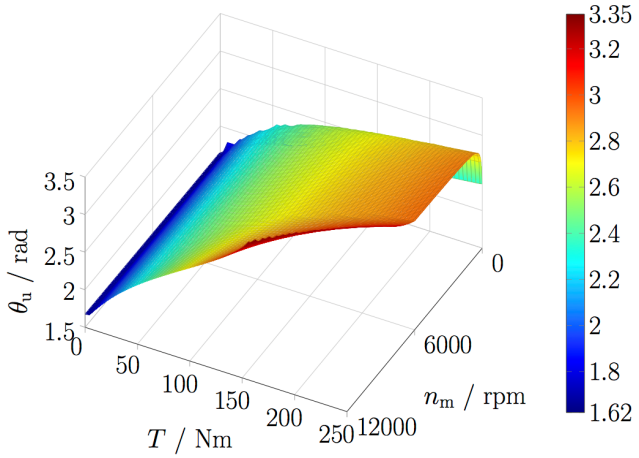

Figure 2.10: *Voltage phase angle θ_u over motor torque and speed.*

The optimized inverter switching angles for an anisotropic motor with respect to (m, θ_u, λ), which are used in this thesis, are included in Appendix B. Fig. 2.11 presents part of the optimization results for different values of m, θ_u and λ when $q = 5$ pulses are utilized. As expected, $\boldsymbol{\alpha}_{\text{aniso}}$ depends not solely on m but also on θ_u and λ. On the contrary, the voltage phase angle does not affect the optimization results of an isotropic motor (see optimized angles for $\lambda = 1$ in Fig. 2.11).

Furthermore, angle discontinuities can be observed for α_3 and α_4 in Fig. 2.11 at $\theta_u \approx \pi/2$ and $\theta_u \approx 3\pi/2$ rad. However, the motor is operated within the range of $\theta_u \in [1.62, 3.35]$ rad (see Fig. 2.10) and does not pass a point of discontinuity. The values of θ_u in Fig. 2.10 are calculated by

$$\theta_u = \arctan\left(\frac{u^q_{s,\text{ref}}}{u^d_{s,\text{ref}}}\right), \tag{2.93}$$

where $u^d_{s,\text{ref}}$ and $u^q_{s,\text{ref}}$ are given in Fig. 2.8.

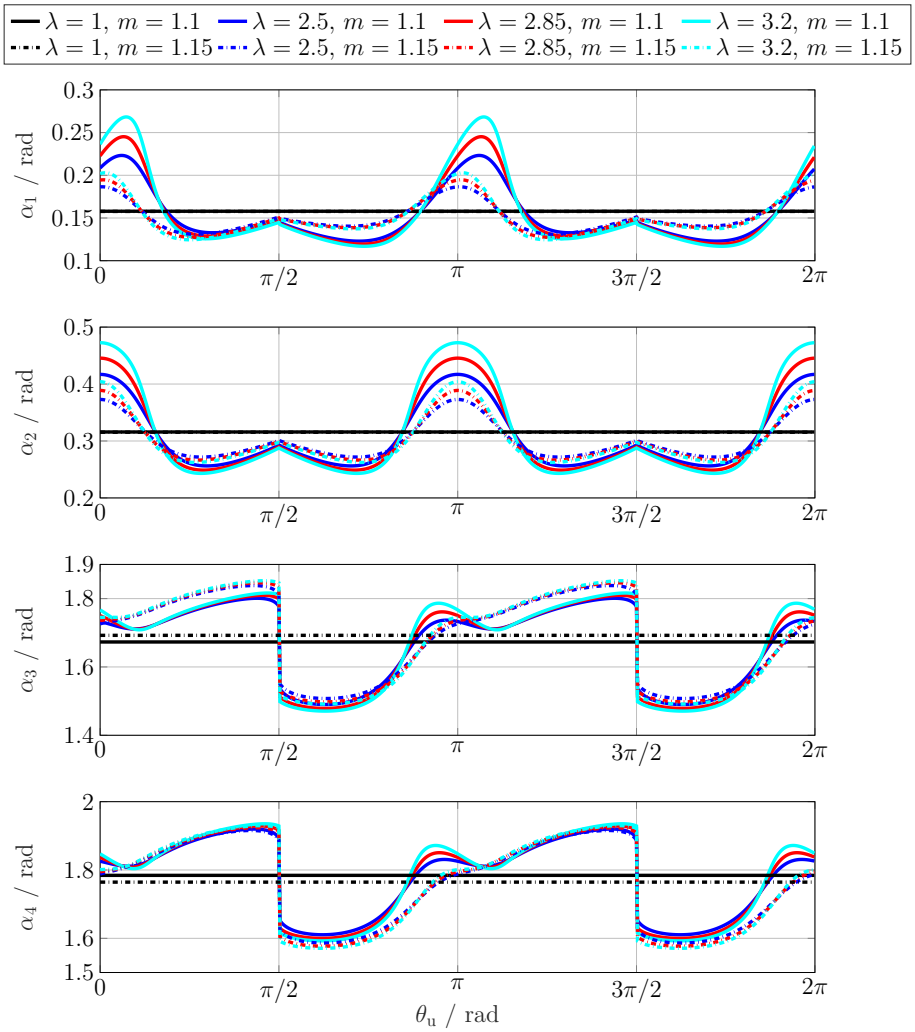

Figure 2.11: *Optimized inverter switching angles for different values of* m, θ_u *and* λ *when* $q = 5$.

2.5 Validation of the derived equations via simulation

In order to validate the derived equations of Sec. 2.2.1-2.2.3 and verify the optimization results of Fig. 2.11, a simulation model is build in MATLAB Simulink. The IPMSM is modelled using the PLECS simulation software [114, pp. 507-510]. The IPMSM is driven in steady-state operation at $T = 20$ Nm and $n_\mathrm{m} = 10200$ rpm. The machine anisotropic properties in this operating point as well as the inverter and dc-link parameters are summarized in Table 2.1. The pulse patterns $\boldsymbol{\alpha}_\mathrm{iso}$ and $\boldsymbol{\alpha}_\mathrm{aniso}$ can also be seen in Fig. 2.11 for $(m, \theta_\mathrm{u}, \lambda) = (1.1, 1.940, 1)$ and $(m, \theta_\mathrm{u}, \lambda) = (1.1, 1.940, 3.139)$, respectively. This operating point has been chosen, so that the difference between the two pulse patterns is visible.

Fig. 2.12 to Fig. 2.16 depict the simulated and calculated waveforms of the inverter output voltage u_o^u, the motor phase voltage u_s^u, the motor phase current i_s^u, the inverter current i_inv and the dc-link capacitor current i_c, respectively, in time and frequency domain using the pulse patterns $\boldsymbol{\alpha}_\mathrm{iso}$ and $\boldsymbol{\alpha}_\mathrm{aniso}$. Equations (2.26), (2.27), (2.60), (2.70) and (2.83) have been used for the calculations, respectively. The deviation between calculated and simulated signals is minimal. This proves the validity of the derived equations even though the assumption of a constant dc-link voltage has been made (see (A1)).

The differences in the two pulse patterns can be seen in Fig. 2.12a and Fig. 2.12b, where

Table 2.1: *Operating point parameters.*

Parameter	**Value**	**Parameter**	**Value**
m, θ_u / rad, λ	1.1, 1.940, 3.139	C / µF	320
L_s^d / µH, L_s^q / µH	89.044, 279.506	R_ESR / mΩ	0.4
ψ_PM / mWb	39.495	u_bat / V	400
$\boldsymbol{\alpha}_\mathrm{iso}$ / rad	$(0.158, 0.316, 1.673, 1.784)^\top$	R_bat / mΩ	10
$\boldsymbol{\alpha}_\mathrm{aniso}$ / rad	$(0.126, 0.257, 1.472, 1.594)^\top$	L_bat / µH	7.3

the pulse number and switching frequency is the same and only the locations of the switching instants change. The resulting phase voltages and currents are illustrated in Fig. 2.13 and Fig. 2.14, respectively. As expected, the current harmonic distortions produced by the two pulse patterns differ. The suboptimal $\boldsymbol{\alpha}_\mathrm{iso}$ deteriorate the current harmonic quality by $I_\mathrm{s,THD}(\boldsymbol{\alpha}_\mathrm{iso}) - I_\mathrm{s,THD}(\boldsymbol{\alpha}_\mathrm{aniso}) = 1.939$ %. Thereafter, it may be concluded that improved solutions are obtained when the machine anisotropic properties are considered in the optimization procedure. This comes with the drawback that the memory requirements of the hardware are in this case increased, since the LUTs of $\boldsymbol{\alpha}_\mathrm{aniso}$ are three-dimensional whereas those of $\boldsymbol{\alpha}_\mathrm{iso}$ only one-dimensional.

Fig. 2.16 illustrates the dc-link capacitor currents. The RMS value of i_c is reduced when the inverter is driven with $\boldsymbol{\alpha}_\mathrm{aniso}$. However, this cannot be guaranteed for all operating points, since the harmonic distortion of the machine current and not the dc-link capacitor current is subject of minimization by the optimization problem.

The harmonic content of the machine phase current and dc-link capacitor current resulting by the two groups of optimized pulse patterns will be evaluated in Sec. 3.4 in the whole torque/speed motor operating range and the outcomes will be validated with experimental results.

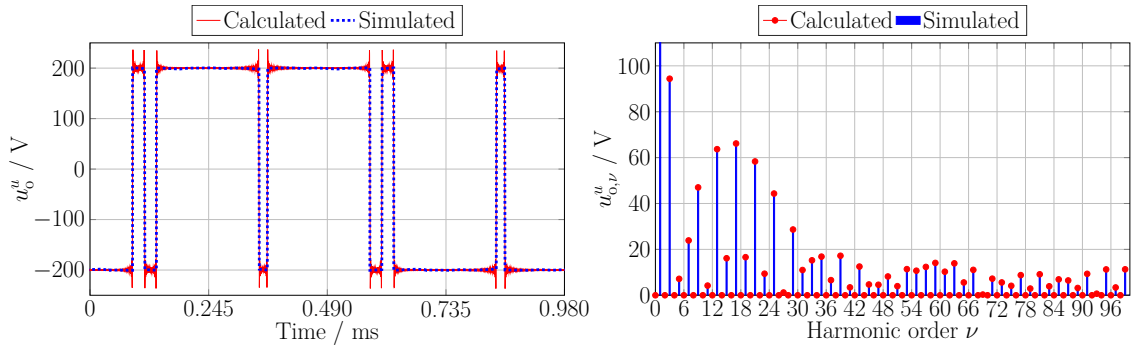

(a) $\boldsymbol{\alpha}_\mathrm{iso}$.

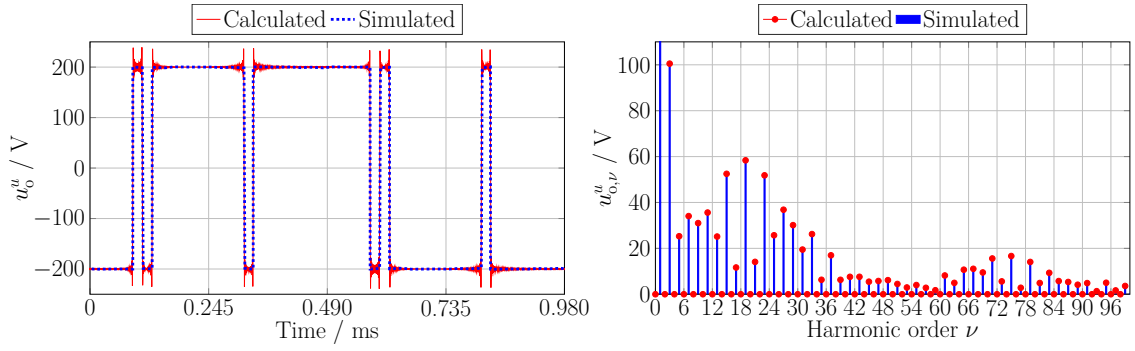

(b) $\boldsymbol{\alpha}_\mathrm{aniso}$.

Figure 2.12: *Inverter output voltage in time and frequency domain.*

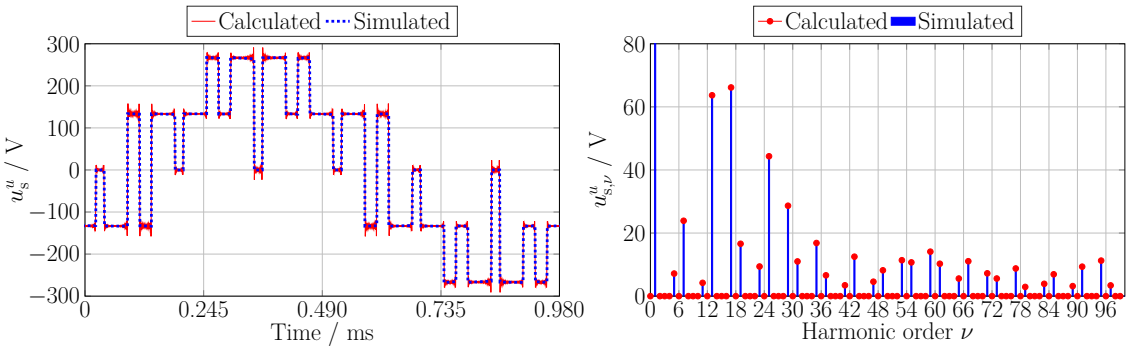

(a) $\boldsymbol{\alpha}_{\text{iso}}$.

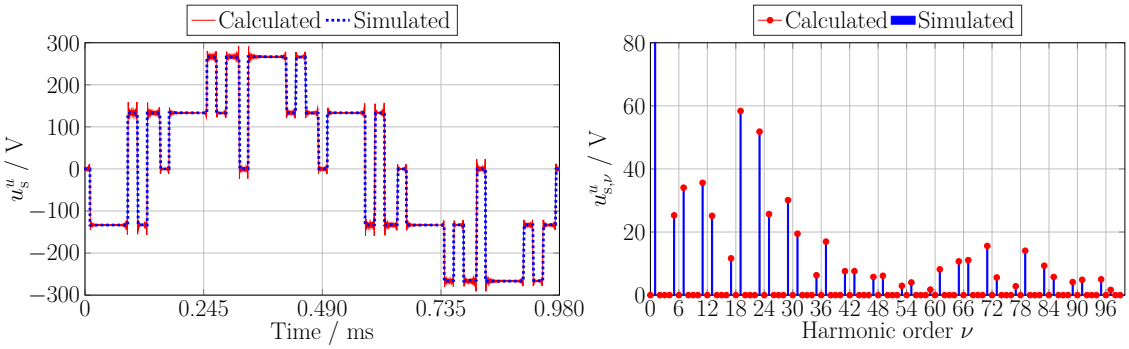

(b) $\boldsymbol{\alpha}_{\text{aniso}}$.

Figure 2.13: *Machine phase voltage in time and frequency domain.*

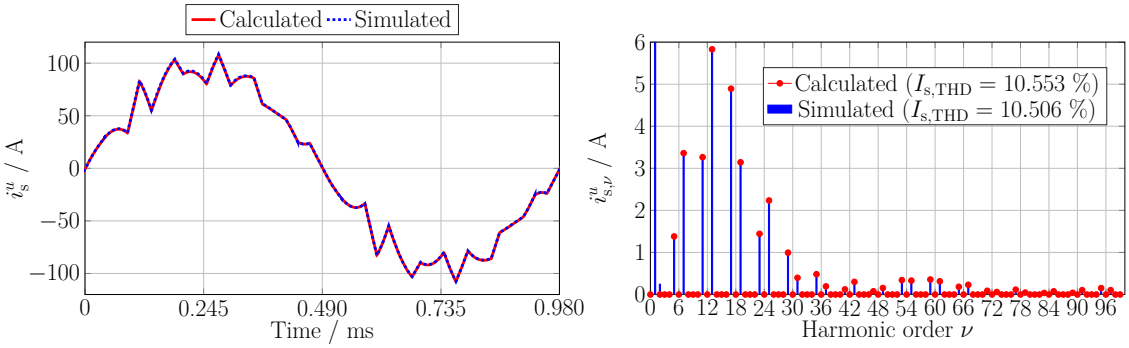

(a) $\boldsymbol{\alpha}_{\text{iso}}$.

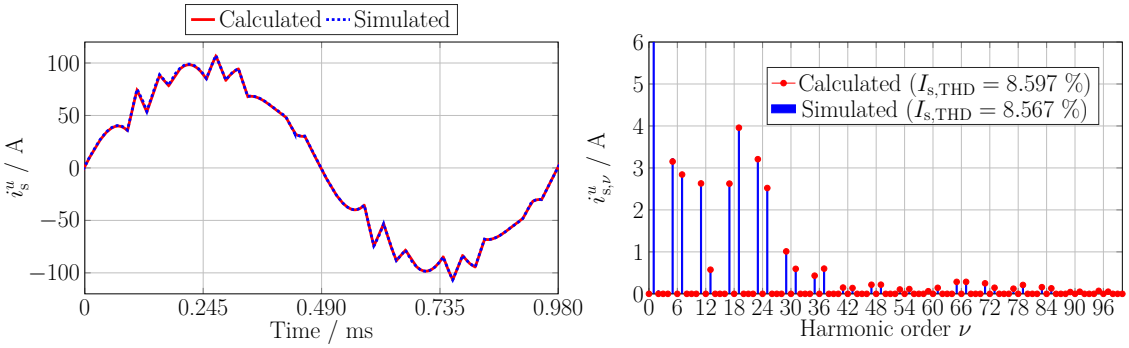

(b) $\boldsymbol{\alpha}_{\text{aniso}}$.

Figure 2.14: *Machine phase current in time and frequency domain.*

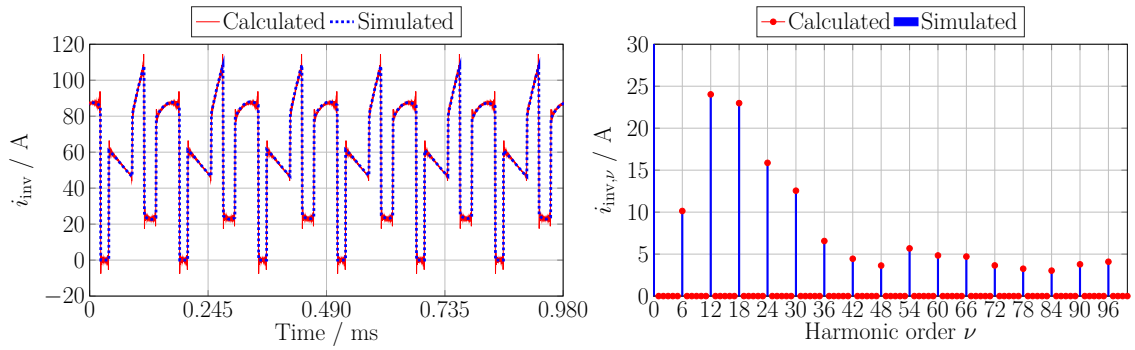

(a) $\boldsymbol{\alpha}_{\mathrm{iso}}$.

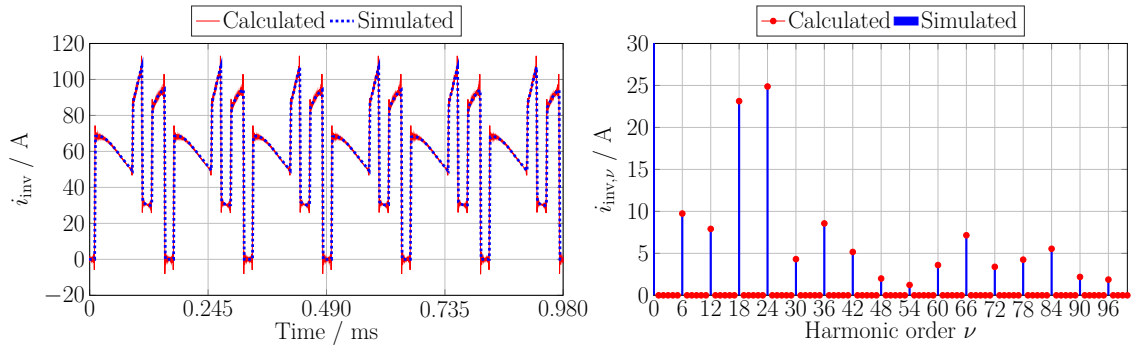

(b) $\boldsymbol{\alpha}_{\mathrm{aniso}}$.

Figure 2.15: *Inverter current in time and frequency domain.*

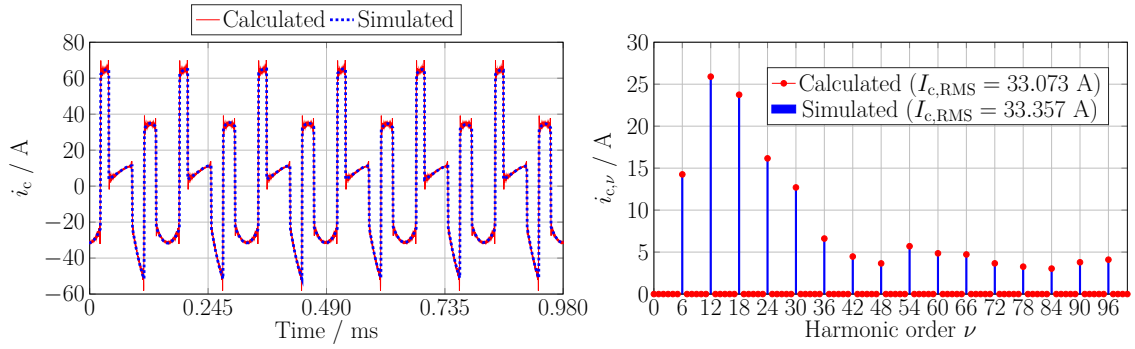

(a) $\boldsymbol{\alpha}_{\mathrm{iso}}$.

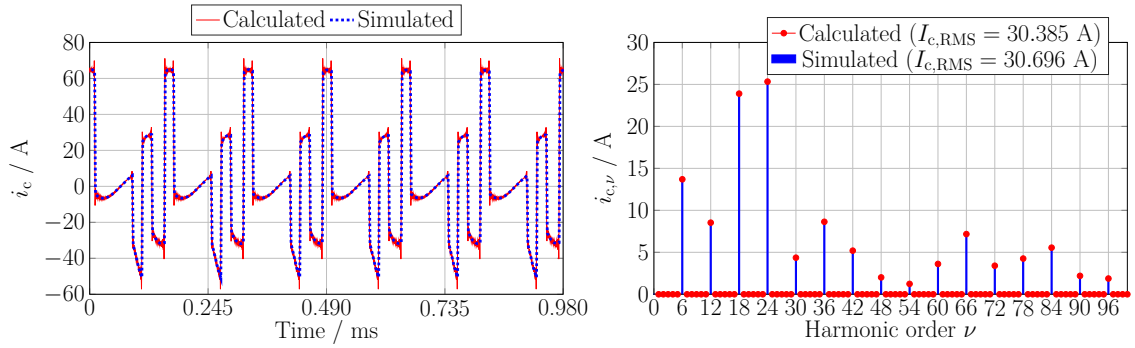

(b) $\boldsymbol{\alpha}_{\mathrm{aniso}}$.

Figure 2.16: *Dc-link capacitor current in time and frequency domain.*

Chapter 3

Implementation and experimental results

In this chapter, the implementation of the SOPWM scheme will be described and its performance will be evaluated with experimental results. Sec. 3.1 describes the control system and modulator. In Sec. 3.2, a simple fundamental current estimation method is presented, which facilitates the integration of the SOPWM scheme into a FOC scheme. Furthermore, a switching transition strategy between different pulse patterns is proposed in Sec. 3.3, which avoids major disturbances in the current control. The main principles of the proposed fundamental current estimation method and switching transition method were published in *IEEE Transactions on Industrial Electronics* [94] and their performance was demonstrated using a three-phase inductive load. However, these methods are applicable also to synchronous motor drives, as will be shown in the following sections. Finally, the theoretical analysis and optimization results, presented in the previous chapter, are validated by experimental results in Sec. 3.4.

3.1 Overview

The block diagram of the control system and modulator is depicted in Fig. 3.1. The control system is implemented on the DS1007 processor board, whereas the modulator is implemented on the DS5203 FPGA board of a dSpace AutoBox. The same modulator is used for both SVM and SOPWM schemes. The FPGA clock frequency is $f_{\mathrm{FPGA}} = 100\,\mathrm{MHz}$.

In the FPGA, an up-counting timer with a frequency of $f_{\mathrm{FPGA}}/(c_{\max}+1)$ Hz, starting from zero and counting to $c_{\max}$ ticks, is included. When the counter signal equals zero (see trigger instant p in Fig. 3.1), the FPGA receives

(a) the four switching time counters $c^z_{i,j}$ (expressed in ticks), with $j \in \{1,\ldots,4\}$ and $i \in \{\mathrm{H},\mathrm{L}\}$ for the high (H) and low (L) side switch of each phase leg $z \in \{u,v,w\}$, and

(b) the upper counter limit $c_{\max}$ of the current counter period.

The modulator compares $c^z_{i,j}$ with the actual counter value and applies the gate signals s^z_i with $i \in \{\mathrm{H},\mathrm{L}\}$ and $z \in \{u,v,w\}$ to each switch.

The measured phase currents $\boldsymbol{i}^{uvw}_{\mathrm{s,SP_1}}$ and $\boldsymbol{i}^{uvw}_{\mathrm{s,SP_2}}$ and mechanical angles $\theta_{\mathrm{m,SP_1}}$ and $\theta_{\mathrm{m,SP_2}}$ are sampled twice at each counter period and passed to the processor, when triggered. The first sampling point ($\mathrm{SP_1}$) is located at the beginning whereas the second point ($\mathrm{SP_2}$) is at the center of each counter period. By controlling the upper counter limit $c_{\max}$, the location of the sampling points can be changed.

The FOC scheme is implemented on the processor model (see Fig. 3.1), i.e. the model running on the DS1007 processor board. For a stable and accurate current control, the fundamental current components are needed for feedback. To this end, a simple fundamental current estimation method is presented in Sec. 3.2, which estimates the fundamental current components $\hat{\boldsymbol{i}}^k_{\mathrm{s},1}$ using the sampled currents $\boldsymbol{i}^{uvw}_{\mathrm{s,SP}_1}$ and $\boldsymbol{i}^{uvw}_{\mathrm{s,SP}_2}$ (see block *"Fundamental current estimation"*).

The values of the stator self-inductances $\boldsymbol{L}^k_{\mathrm{s}} := (L^d_{\mathrm{s}}, L^q_{\mathrm{s}})^\top$ and PM flux linkage ψ_{PM} are stored in LUTs depending on $\boldsymbol{i}^k_{\mathrm{s,ref}}$. PI controllers with feedforward control are utilized for current control. The feedforward (FF) voltages

$$\boldsymbol{u}^k_{\mathrm{s,FF}} := \begin{pmatrix} -\omega_{\mathrm{r}} L^q_{\mathrm{s}} i^q_{\mathrm{s,ref}} \\ \omega_{\mathrm{r}} L^d_{\mathrm{s}} i^d_{\mathrm{s,ref}} + \omega_{\mathrm{r}} \psi_{\mathrm{PM}} \end{pmatrix} \tag{3.1}$$

are determined using the reference currents $\boldsymbol{i}^k_{\mathrm{s,ref}}$ and are then added to the PI controller output voltages $\boldsymbol{u}^k_{\mathrm{s,PI}}$. This feature acts as a feedforward control mechanism and enables a fast current control also during transient conditions. The resulting voltage vector $\boldsymbol{u}^k_{\mathrm{s},1} := \boldsymbol{u}^k_{\mathrm{s,PI}} + \boldsymbol{u}^k_{\mathrm{s,FF}}$ defines the new operating point of the load with modulation index m and voltage phase angle θ_{u}. For the fundamental current estimation method to work, the currents must be sampled at specific points, which can be controlled by $c_{\max}$. In other words, $c_{\max}$ is specified according to the desired locations of the current sampling points (SP_1&SP_2). The calculation of $c_{\max}$ is implemented in the block *"$c_{\max}$ Calculation"* and is explained in Sec. 3.2.2. The optimized inverter switching angles $\boldsymbol{\alpha}$ and the angle γ are stored in LUTs. During real time operation, the optimized values of $\boldsymbol{\alpha}$ and γ are selected from the LUTs according to m, $\theta_{\mathrm{u,FF}}$ and λ. It should be noted, that $\theta_{\mathrm{u,FF}}$ and λ are specified using the reference currents $\boldsymbol{i}^k_{\mathrm{s,ref}}$ (see Fig. 2.8) and not the estimated feedback currents $\hat{\boldsymbol{i}}^k_{\mathrm{s},1}$, as indicated in (3.1) and Fig. 3.1. This is done, in order to avoid any additional oscillations in $\boldsymbol{\alpha}$. The variables $\theta_{\mathrm{u,FF}}$ and λ contribute to an optimal current quality in steady-state operation and do not affect the performance of the current control. Using $c_{\max}$ and the current control outputs, the switching time counters $c^z_{i,j}$ can then be specified (see block *"$c^z_{i,j}$ Calculation SOPWM"*), as will be discussed in Sec. 3.2.3.

3.2 Fundamental current estimation method

Fast current control at reduced switching frequency requires closed-loop control methods, where the fundamental component must be fed back. The fundamental component of the feedback current is inherently obtained when the SVM is used, by sampling the measured currents at the center of the zero vector time interval [16]. In contrast to SVM, the SOPWM strategy does not offer this feature, since the measured and sampled current contains a significant harmonic content [71]. Fig. 3.2 illustrates the motor output currents $\boldsymbol{i}^k_{\mathrm{s}}$ in the synchronously rotating dq-frame as well as their first four harmonic components when the SOPWM scheme is used. It can be clearly seen that there is no sampling position where all current harmonics are simultaneously zero. Thus, the fundamental component of the motor current cannot be inherently obtained, when the SOPWM scheme is employed.

A variety of methods have been proposed to estimate the fundamental component of the measured currents when SOPWM is utilized. One possibility is to filter out the harmonics of the measured currents [35, 36]. Nevertheless, the harmonic filtering is not the appropriate method when high dynamic performance is required. In [67–71, 89], an observer is used to identify the fundamental components of stator current and flux linkage vectors. While this method provides high control dynamic, the implementation of an observer is rather complex. Lastly, SOPWM is combined with MPC in [72, 73]. This seems to be a very effective but computationally expensive

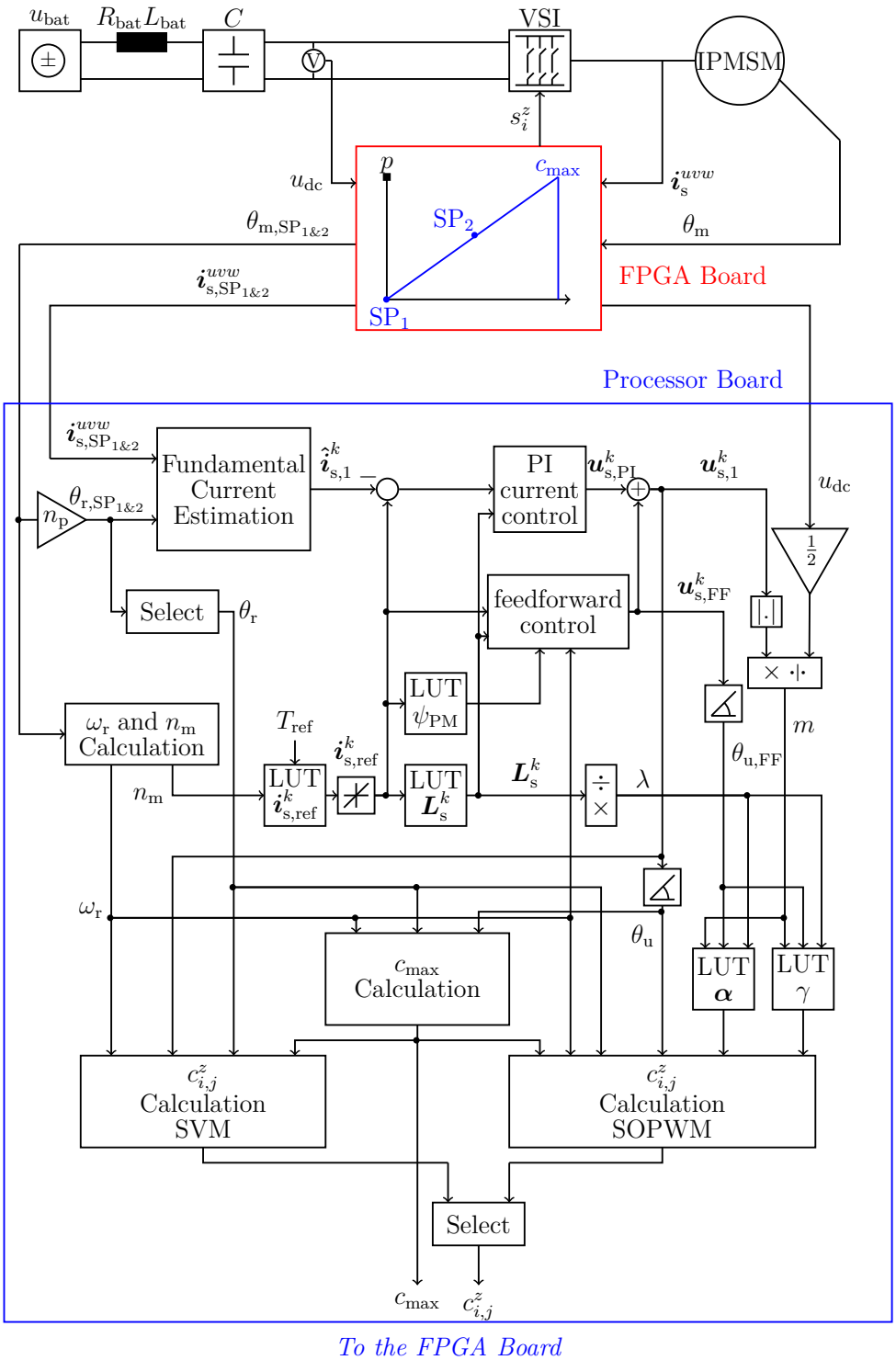

Figure 3.1: *Block diagram of the control system and modulator.*

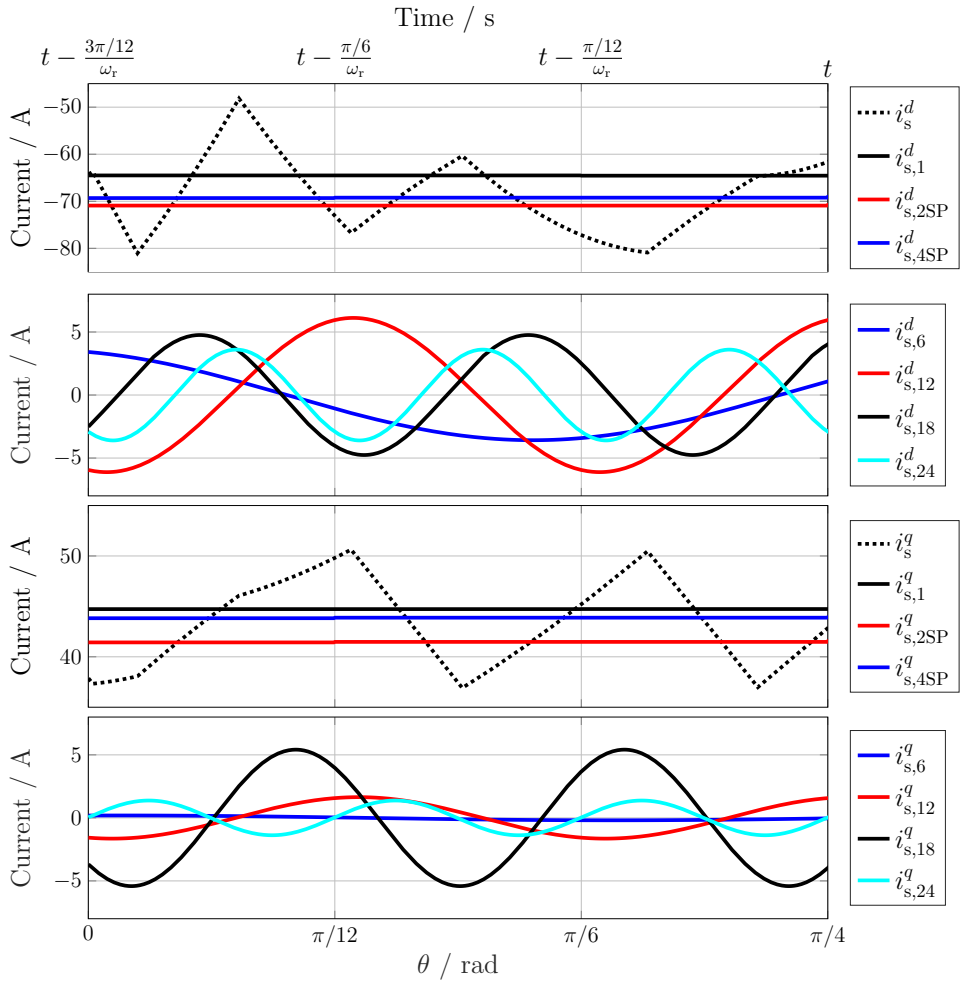

Figure 3.2: *Principle of the proposed fundamental current estimation method.*

method, which enables a very fast dynamic response.

In this section, a simple yet very effective fundamental current estimation method is proposed, which eliminates the undesired harmonics in the measured currents by sampling at specific points in time and allows for the integration of the SOPWM into a conventional FOC scheme without the need of an observer. The main feature of this method is its implementation simplicity, since the computational effort required is within the capability of a standard industrial DSP system. Furthermore, it is independent of the load parameters. These features make the proposed method an attractive alternative to a complex observer or MPC for industrial applications (e.g. electric vehicles), where implementation simplicity is of outmost importance. The results of an initial investigation have been published in [94] using an inductive load. In this thesis, the proposed method will be employed for the control of an IPMSM drive.

3.2.1 Main principle

In Sec. 2.2.2, the equations of the motor phase currents in the *dq*-frame with respect to the inverter switching angles have been derived. As indicated in (2.52), the two orthogonal current components in the *dq*-frame contain harmonics of an order of multiples of six. In steady-state, all the parameters in (2.52) remain constant, except from the electrical angle $\theta_r = \omega_r t + \phi_0$. In other words, the amplitude and phase shift of each current harmonic component remain constant in

steady-state operation. Consequently, for $i \in \mathbb{N}$, the $\nu = 12i - 6$ current harmonic components have opposite values at each multiple of $\pi/6$ rad (see $\boldsymbol{i}^k_{\mathrm{s},6}$ and $\boldsymbol{i}^k_{\mathrm{s},18}$ in Fig. 3.2), i.e.

$$\begin{aligned} \boldsymbol{i}^k_{\mathrm{s},12i-6}(t) + \boldsymbol{i}^k_{\mathrm{s},12i-6}\left(t - \frac{\pi/6}{\omega_\mathrm{r}}\right) &= 0 \\ \boldsymbol{i}^k_{\mathrm{s},12i-6}\left(t - \frac{\pi/12}{\omega_\mathrm{r}}\right) + \boldsymbol{i}^k_{\mathrm{s},12i-6}\left(t - \frac{\pi/12}{\omega_\mathrm{r}} - \frac{\pi/6}{\omega_\mathrm{r}}\right) &= 0. \end{aligned} \tag{3.2}$$

Moreover, the $\nu = 24i - 12$ harmonics have equal values at each multiple of $\pi/6$ rad and opposite values at each multiple of $\pi/12$ rad (see $\boldsymbol{i}^k_{\mathrm{s},12}$ in Fig. 3.2), i.e.

$$\begin{aligned} \boldsymbol{i}^k_{\mathrm{s},24i-12}(t) + \boldsymbol{i}^k_{\mathrm{s},24i-12}\left(t - \frac{\pi/12}{\omega_\mathrm{r}}\right) &= 0 \\ \boldsymbol{i}^k_{\mathrm{s},24i-12}\left(t - \frac{\pi/6}{\omega_\mathrm{r}}\right) + \boldsymbol{i}^k_{\mathrm{s},24i-12}\left(t - \frac{\pi/6}{\omega_\mathrm{r}} - \frac{\pi/12}{\omega_\mathrm{r}}\right) &= 0 \end{aligned} \tag{3.3}$$

and the remaining harmonics $\nu = 24i$ have equal values at each multiple of $\pi/12$ rad (see $\boldsymbol{i}^k_{\mathrm{s},24}$ in Fig. 3.2), i.e.

$$\boldsymbol{i}^k_{\mathrm{s},24i}(t) = \boldsymbol{i}^k_{\mathrm{s},24i}\left(t - \frac{\pi/12}{\omega_\mathrm{r}}\right) = \boldsymbol{i}^k_{\mathrm{s},24i}\left(t - \frac{\pi/6}{\omega_\mathrm{r}}\right) = \boldsymbol{i}^k_{\mathrm{s},24i}\left(t - \frac{3\pi/12}{\omega_\mathrm{r}}\right). \tag{3.4}$$

Consequently, if the harmonic currents are sampled at each $\pi/6$ rad rotation of the voltage vector (i.e. at t and $t - \frac{\pi/6}{\omega_\mathrm{r}}$) and the mean values

$$\boldsymbol{i}^k_{\mathrm{s,2SP}}(t) := \frac{\boldsymbol{i}^k_\mathrm{s}(t) + \boldsymbol{i}^k_\mathrm{s}\left(t - \frac{\pi/6}{\omega_\mathrm{r}}\right)}{2} = \boldsymbol{i}^k_{\mathrm{s},1} + \sum_{\nu=12i}^{+\infty} \boldsymbol{i}^k_{\mathrm{s},\nu}(t) \tag{3.5}$$

of these two sampling points (2SP) are computed, then they only contain the dc and the $\nu = 12i$ harmonic components. Moreover, if four sampling points (4SP) at each $\pi/12$ rad rotation (i.e. at t, $t - \frac{\pi/12}{\omega_\mathrm{r}}$, $t - \frac{\pi/6}{\omega_\mathrm{r}}$ and $t - \frac{3\pi/12}{\omega_\mathrm{r}}$) are used, then the mean value becomes

$$\boldsymbol{i}^k_{\mathrm{s,4SP}}(t) := \frac{\boldsymbol{i}^k_\mathrm{s}(t) + \boldsymbol{i}^k_\mathrm{s}\left(t - \frac{\pi/12}{\omega_\mathrm{r}}\right) + \boldsymbol{i}^k_\mathrm{s}\left(t - \frac{\pi/6}{\omega_\mathrm{r}}\right) + \boldsymbol{i}^k_\mathrm{s}\left(t - \frac{3\pi/12}{\omega_\mathrm{r}}\right)}{4} = \boldsymbol{i}^k_{\mathrm{s},1} + \sum_{\nu=24i}^{+\infty} \boldsymbol{i}^k_{\mathrm{s},\nu}(t), \tag{3.6}$$

and only the dc and the $\nu = 24i$ harmonic components remain, while all other harmonics are eliminated. As a result, the sampled and averaged currents $\boldsymbol{i}^k_{\mathrm{s,4SP}}$ are very close to the dc components $\boldsymbol{i}^k_{\mathrm{s},1}$, since the remaining $\nu = 24i$ harmonics have small amplitudes at the sampling points (see Fig. 3.2). If more sampling points are used, more harmonics can be eliminated. However then, also more delay is induced into the current control system and its dynamic performance degrades.

The main feature of the proposed fundamental current estimation method is its implementation simplicity, since the computational effort required is within the capability of a standard industrial DSP system, as will be described in the next subsection. Furthermore, the proposed method is based only on the symmetry properties of the current harmonic components and, therefore, is independent of the load parameters. Lastly, it is applicable not only to synchronous but also to asynchronous electrical drives, since the only requirement is that the load voltage and current waveforms in the uvw-frame contain only odd-order non-triplen harmonics. Although this method

is analytically derived in steady-state operation, experimental results will confirm its applicability during transients with relatively high dynamic performance requirements.

3.2.2 Implementation

The signal flow diagram of the proposed fundamental current estimation method is illustrated in Fig. 3.3. The motor currents must be sampled at specific points ($SP_{1\&2}$) according to the used modulation scheme and passed to the processor model when triggered. Since SP_1 is located at the beginning, whereas SP_2 at the center, of each counter period, the location of the sampling points can be controlled by adjusting the upper counter limit c_{max}. Hence, the upper counter limit and the processor model trigger instants are specified for each modulation scheme considering

- the desired location of the current sampling points,
- the processor model turnaround time (TAT) and
- the processor model trigger rate, i.e. the desired current controller activation rate.

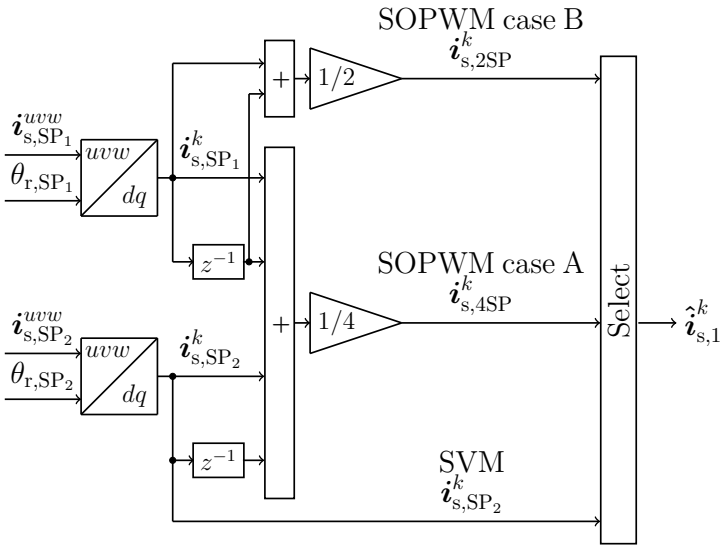

Figure 3.3: *Signal flow diagram of the fundamental current estimation method (see block "Fundamental current estimation" in Fig. 3.1).*

3.2.2.1 SVM

When the SVM strategy is utilized, the measured currents must be sampled at the center of the switching period, i.e. at the center of the zero switching vector time interval, where the current harmonic content is zero. For this purpose, the frequency of the counter signal must be equal to the SVM switching frequency $f_{sw,SVM} = 10\,\text{kHz}$, as depicted in Fig. 3.4, and the upper counter limit, specified at the n-th processor model trigger instant, is given by

$$c_{max}[n] := \frac{f_{FPGA}}{f_{sw,SVM}} - 1. \tag{3.7}$$

In this way, the currents $\boldsymbol{i}^{uvw}_{s,SP_2}$ are sampled at the center of the switching period and their dq-components $\boldsymbol{i}^k_{s,SP_2}$ correspond to the estimated fundamental current components $\hat{\boldsymbol{i}}^k_{s,1}$. These are used for feedback current control, as depicted in Fig. 3.1 and 3.3.

The processor model is triggered at the center of each counter period, so that it receives $\boldsymbol{i}^{uvw}_{\mathrm{s,SP_2}}$ as inputs. Its turnaround time is $t_{\mathrm{TAT,SVM}}$=70 µs, when the SVM scheme is used. The arrows in Fig. 3.4 indicate the processor model trigger instants $n-1,\ldots,n+2$ while the squares represent the trigger instants $p-3,\ldots,p+1$ for the FPGA inputs. Since $t[p-1]-t[n] = 1/(2f_{\mathrm{sw,SVM}}) < t_{\mathrm{TAT,SVM}}$, the processor model outputs of the n-th trigger instant have not yet been specified when the $p-1$-th instant occurs. Therefore, the processor model outputs are determined for the next but one counter period, indicated with blue color in Fig. 3.4, and the modulator receives them at instant p, as shown in Fig. 3.4. In this way, there is enough time ($t[n+1]-t[n] = 1/f_{\mathrm{sw,SVM}} > t_{\mathrm{TAT,SVM}}$) for all the calculations to be conducted, until the processor model is triggered again.

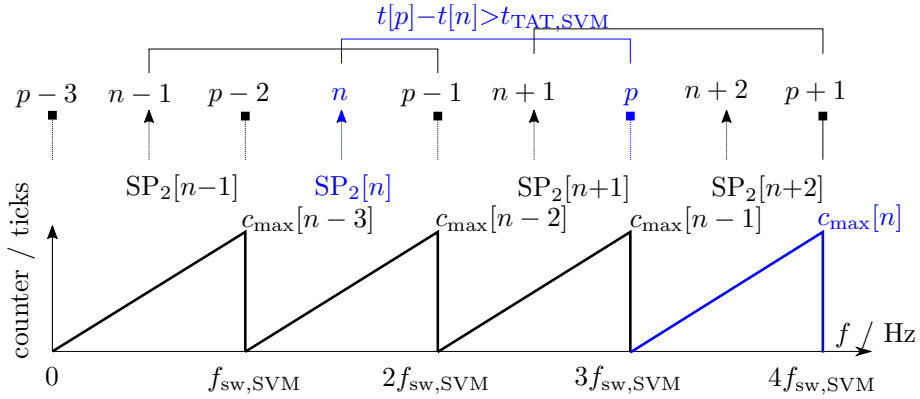

Figure 3.4: *Implementation principle of SVM (arrows: processor model trigger instants, squares: trigger instants for the FPGA inputs).*

3.2.2.2 SOPWM

When the SOPWM strategy is used, the phase currents must be sampled at each $\pi/12$ rad rotation of the voltage vector, so that (3.5) or (3.6) can be used for the fundamental current estimation. For this purpose, the counter signal must be synchronized with the angle $\theta = \theta_{\mathrm{r}} + \theta_{\mathrm{u}}$ and its period must be equal to a $\pi/6$ rad rotation of the voltage vector (i.e. $\theta[p+1]-\theta[p] = \pi/6$ rad), as shown in Fig. 3.5.

The processor turnaround time is $t_{\mathrm{TAT,SOPWM}}$=60 µs[1], when the electrical system is controlled based on the SOPWM. Taking that into consideration, the SOPWM implementation is split into two cases:

- **Case A**: For low electrical frequencies ($f_{\mathrm{r}} < 600$ Hz), the processor model is triggered at the center of each counter period (see Fig. 3.5a) since $t[p]-t[n] = 1/(24f_{\mathrm{r}}) > t_{\mathrm{TAT,SOPWM}}$ for $f_{\mathrm{r}} < 600$ Hz. The dc current components are estimated by the mean value $\boldsymbol{i}^{k}_{\mathrm{s,4SP}}[n]$ of the last four transformed sampled currents ($\boldsymbol{i}^{k}_{\mathrm{s,SP_2}}[n]$, $\boldsymbol{i}^{k}_{\mathrm{s,SP_1}}[n]$, $\boldsymbol{i}^{k}_{\mathrm{s,SP_2}}[n-1]$, $\boldsymbol{i}^{k}_{\mathrm{s,SP_1}}[n-1]$) using (3.6), as can be observed in Fig. 3.3. The processor outputs at the n-th trigger instant are determined for the next counter period and the modulator receives them at instant p. This implementation strategy is referred to case A.

- **Case B**: At high electrical frequencies ($f_{\mathrm{r}} \geq 600$ Hz), $t[p]-t[n] < t_{\mathrm{TAT,SOPWM}}$ would hold for case A. For that reason, the implementation of case B is introduced, where the processor

[1]Only the algorithm of the modulation method in use is active, i.e. either the SVM or the SOPWM algorithm. For that reason, $t_{\mathrm{TAT,SVM}} \neq t_{\mathrm{TAT,SOPWM}}$.

model is triggered at the beginning of each counter period (see Fig. 3.5b), such that $t[p] - t[n] = 1/(12 f_\mathrm{r}) > t_\mathrm{TAT,SOPWM}$. Furthermore, the dc current components are estimated by the mean values $\boldsymbol{i}^k_\mathrm{s,2SP}[n]$ of two sampled currents ($\boldsymbol{i}^k_\mathrm{s,SP_1}[n]$ and $\boldsymbol{i}^k_\mathrm{s,SP_1}[n-1]$) using (3.5), so that the delay in the current control does not increase relatively to case A. Note that case B could also be used for f_r<600 Hz. However, case A at low f_r is preferred over B, since

(a) the trigger instant n is closer to p, i.e. the dead time between the current controller trigger instant and the application of the gate signals is smaller, and

(b) more sampling points are used for the estimation of the fundamental current and more current harmonics can be eliminated from the measured and sampled currents (see Sec. 3.2.1).

These features contribute to a faster and more accurate current control when SOPWM with case A is employed.

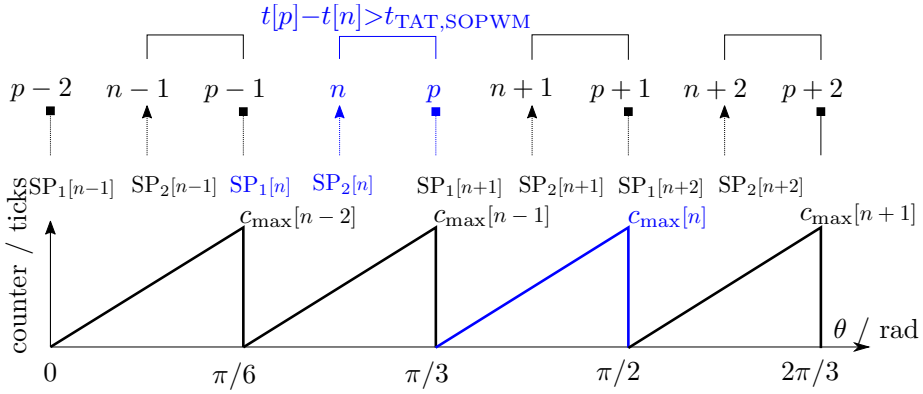

(a) *SOPWM case A.*

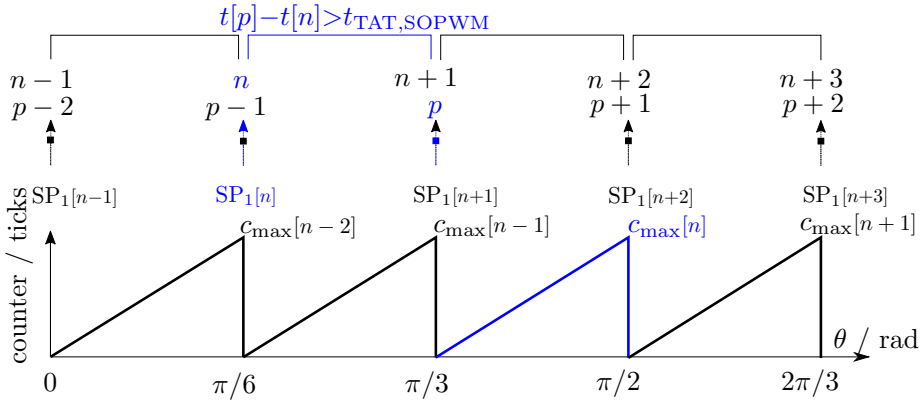

(b) *SOPWM case B.*

Figure 3.5: *Implementation principle of SOPWM using the same modulator as in SVM (arrows: processor model trigger instants, squares: trigger instants for the FPGA inputs).*

For both SOPWM implementation cases, the counter signal must be synchronized with the voltage vector rotation and its period must correspond to a $\pi/6$ rad rotation of the voltage vector not only in steady-state operation but also in transient conditions. To this end, two mechanisms are employed. A phase-locked loop (PLL) and a feedforward (FF) phase control function, which modify c_max by the factors c_PLL and c_FF, respectively, so that the counter signal

remains synchronized with $\theta = \theta_\mathrm{r} + \theta_\mathrm{u}$ also during transients. The resulting upper limit at the next counter period, indicated with blue color in Fig. 3.5, is given by

$$c_\mathrm{max}[n] := c_{\pi/6}[n] + g_\mathrm{PLL} c_\mathrm{PLL}[n] + c_\mathrm{FF}[n] - 1 \tag{3.8}$$

(see Fig. 3.6), where

$$c_{\pi/6}[n] := \frac{\pi/6}{\omega_\mathrm{r}[n]} f_\mathrm{FPGA} \tag{3.9}$$

is the equivalent counter value for a $\pi/6$ rad rotation in steady-state operation, g_PLL is the PLL gain, c_PLL is the PLL counter and c_FF is the FF counter.

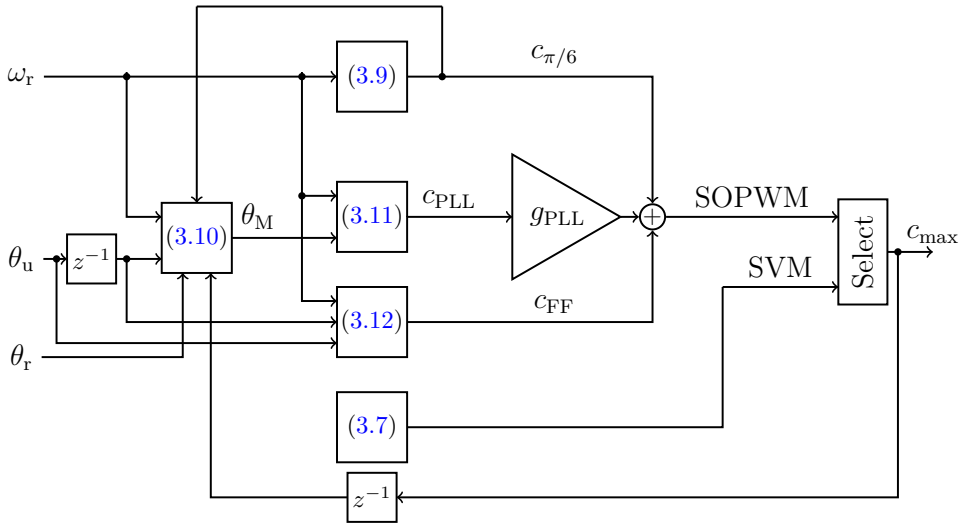

Figure 3.6: *Signal flow diagram of the upper counter limit calculation (see block "c_max Calculation" in Fig. 3.1).*

Phase-locked loop (PLL): The PLL mechanism adjusts c_max, such that the counter signal is not only synchronized with the electrical frequency but also with the voltage vector rotation $\theta = \theta_\mathrm{r} + \theta_\mathrm{u}$. In other words, each counter period must fit exactly into each voltage hexagon subsector SS (see Fig. 3.7).

If $c_\mathrm{max}[n] = c_{\pi/6}[n] - 1$, i.e. $c_\mathrm{PLL} = c_\mathrm{FF} = 0$ in (3.8), the voltage phase angle $\theta_\mathrm{M}[n]$ at the middle of the next counter period (see Fig. 3.8) is given by

$$\begin{aligned} \theta_\mathrm{M}[n] :=& \theta[n] + \omega_\mathrm{r}[n]\,(t_\mathrm{M}[n] - t[n]) \\ =& \theta[n] + \omega_\mathrm{r}[n] \begin{cases} \frac{c_\mathrm{max}[n-1]+1+c_{\pi/6}[n]}{2 f_\mathrm{FPGA}} & \text{for case A} \\ \frac{2(c_\mathrm{max}[n-1]+1)+c_{\pi/6}[n]}{2 f_\mathrm{FPGA}} & \text{for case B.} \end{cases} \end{aligned} \tag{3.10}$$

The desired phase angle $\theta_\mathrm{M,target}[n]$ is the one at the center of each voltage hexagon subsector. If $\theta_\mathrm{M}[n] = \theta_\mathrm{M,target}[n]$, the counter is synchronized with θ. Therefore, the difference between $\theta_\mathrm{M}[n]$ and $\theta_\mathrm{M,target}[n]$ is used for the derivation of the PLL counter

$$c_\mathrm{PLL}[n] := 2\frac{f_\mathrm{FPGA}}{\omega_\mathrm{r}[n]} \left(\overbrace{\frac{\pi}{6}\mathtt{fix}\left(\frac{\theta_\mathrm{M}[n]}{\pi/6}\right) + \frac{\pi}{12}}^{\theta_\mathrm{M,target}[n]} - \theta_\mathrm{M}[n] \right). \tag{3.11}$$

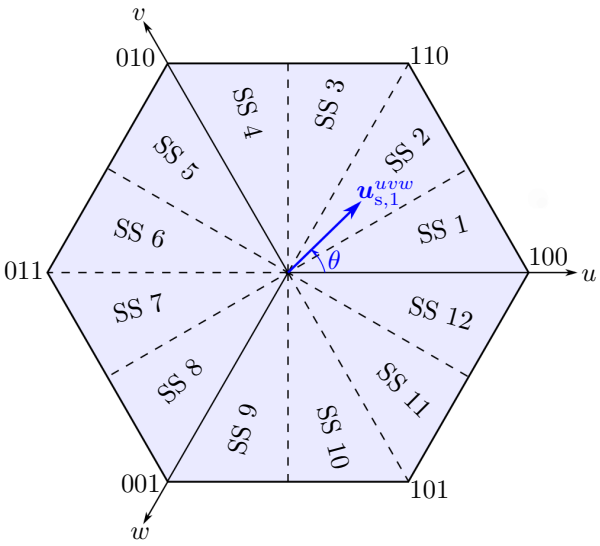

Figure 3.7: *Voltage hexagon.*

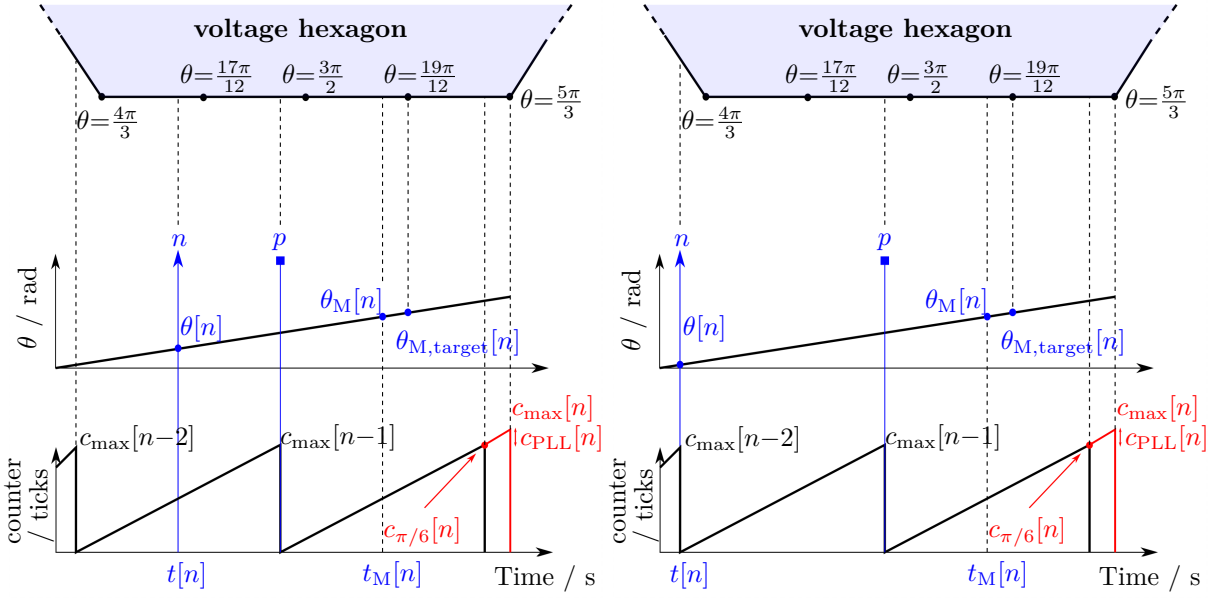

(a) *SOPWM case A.* (b) *SOPWM case B.*

Figure 3.8: *Illustration of the principal idea of the PLL mechanism for* $g_{\mathrm{PLL}} = 1$.

The Matlab function `fix(x)` rounds the element `x` to the nearest integer towards zero and is used in (3.11) to determine in which subsector of the hexagon the voltage vector is located (see Fig. 3.7). Since large changes in the upper counter limit are not desired, a small gain of $g_{\mathrm{PLL}} = 0.2$ in (3.8) is chosen, which is empirically found.

The principal idea of the PLL mechanism is illustrated in Fig. 3.8. The angle $\theta_{\mathrm{M}}[n]$ does not coincide with $\theta_{\mathrm{M,target}}[n]$ ($\theta_{\mathrm{M,target}}[n] = 19\pi/12$ rad in this example) and the counter signal does not fit in the voltage hexagon subsector. For this reason, the PLL adjusts $c_{\mathrm{max}}[n]$, so that the end of the next counter period is located at the edge of the voltage hexagon subsector ($\theta = 5\pi/3$ rad in this example).

Feedforward (FF) phase control function: During transient conditions, the angle θ_u experiences sudden changes, i.e.

$$\Delta\theta_\mathrm{u}[n] := \theta_\mathrm{u}[n-1] - \theta_\mathrm{u}[n] \neq 0,$$

and the PLL function cannot synchronize the counter signal fast enough. To overcome this, a FF phase control mechanism is implemented, which adjusts the upper counter limit in (3.8) by

$$c_\mathrm{FF}[n] := \frac{\Delta\theta_\mathrm{u}[n]}{\omega_\mathrm{r}[n]} f_\mathrm{FPGA} \tag{3.12}$$

to enable a faster synchronization during transients.

The basic principle of the FF mechanism is illustrated in Fig. 3.9. If a negative change in the voltage phase angle is imposed by the current controller ($\Delta\theta_\mathrm{u}[n] < 0$) at the time instant $t[n]$, the upper counter limit of the next counter period is increased by $c_\mathrm{FF}[n]$, such that the voltage vector at the end of the next counter period is located at the edge of the voltage hexagon subsector ($\theta = 5\pi/3$ rad in this example).

The proposed fundamental current estimation method would also work, if the counter signal was synchronized with θ_r. However, the synchronization with the voltage vector rotation facilitates the switching transition between the SVM and SOPWM schemes, as will be described in Sec. 3.3.

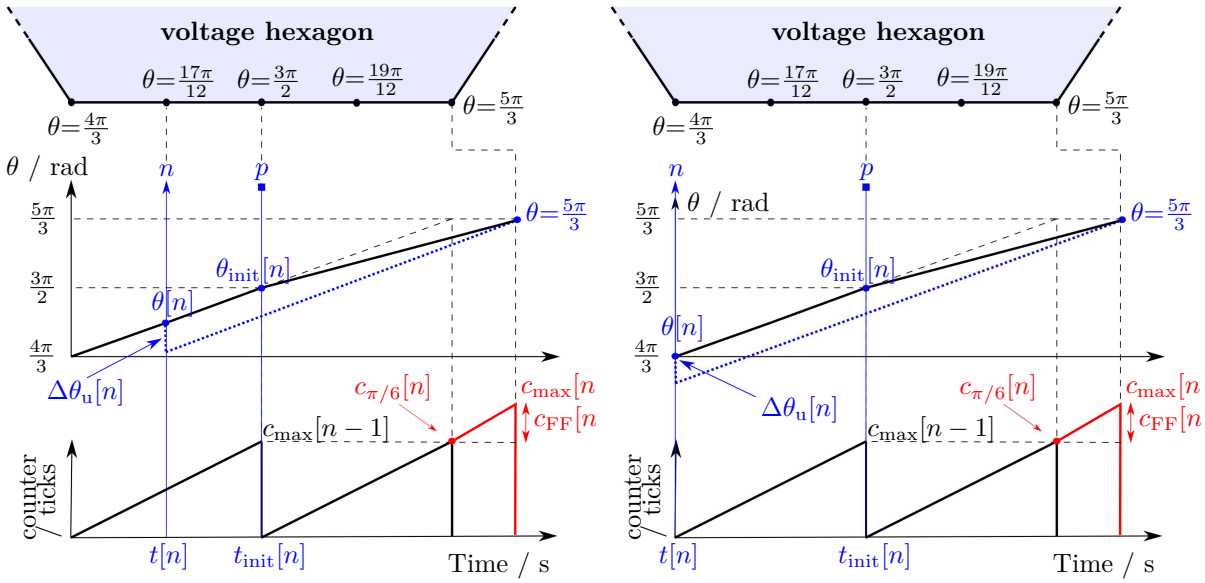

(a) *SOPWM case A.* (b) *SOPWM case B.*

Figure 3.9: *Illustration of the principal idea of the FF phase control mechanism.*

3.2.3 Calculation of the inverter switching times

Since the modulator consists of a counter signal, the inverter switching angles must be transformed to switching time counters. In that way, the same modulator can be used for both SVM and SOPWM schemes. The transformation procedure will be described in this subsection.

The voltage phase angle at the beginning of the next counter period $\theta_\mathrm{init}[n]$ (see Fig. 3.9 and 3.10) is given by

$$\begin{aligned}\theta_{\text{init}}[n] &:= \theta[n] + \omega_{\text{r}}[n]\,(t_{\text{init}}[n] - t[n]) \\ &= \theta[n] + \omega_{\text{r}}[n] \begin{cases} \frac{c_{\max}[n-1]+1}{2f_{\text{FPGA}}} & \text{for case A} \\ \frac{c_{\max}[n-1]+1}{f_{\text{FPGA}}} & \text{for case B.} \end{cases}\end{aligned} \tag{3.13}$$

Moreover, the angular velocity of the voltage vector is

$$\omega_{\text{u}}[n] := \omega_{\text{r}}[n] - \frac{f_{\text{FPGA}}}{c_{\max}[n]+1}\Delta\theta_{\text{u}}[n]. \tag{3.14}$$

In steady-state operation $\Delta\theta_{\text{u}}[n]{=}0$ and the voltage vector rotates with the electrical angular velocity, i.e. $\omega_{\text{u}}[n] = \omega_{\text{r}}[n]$. Nevertheless, during transients the angular velocity of θ is smoothly adjusted (see Fig. 3.9), such that no sudden changes in the voltage vector rotation occur.

The phase voltages depend on γ, as indicated in (2.27). Since the angle $\theta = \theta_{\text{r}} + \theta_{\text{u}}$ and not $\theta_{\text{r}} + \gamma$ is used for the determination of the inverter switching times, each switching angle α_i over an electrical period (i.e. for $i = \{1, \ldots, 2q\}$) must be corrected by the factor $\theta_{\text{u}} - \gamma$ (see Fig. 3.10) as follows

$$\alpha_{\text{cor},i}[n] := \alpha_i[n] + \theta_{\text{u}}[n] - \gamma[n]. \tag{3.15}$$

Each corrected angle $\alpha_{\text{cor},i}[n]$ can then be transformed into a switching time counter

$$c^z_{\alpha_{\text{cor},i}}[n]{:=}\frac{f_{\text{FPGA}}}{\omega_{\text{u}}[n]}\left(\alpha_{\text{cor},i}[n] + l\frac{2\pi}{3} - \theta_{\text{init}}[n]\right) \tag{3.16}$$

for each phase $z \in \{u, v, w\}$, where $l \in \{0, 1, 2\}$, respectively. If $c^z_{\alpha_{\text{cor},i}}[n]$ lies within the interval $[0, c_{\max}[n]]$, it will be used in the next counter period. Otherwise, this switching transition will not take place in the next counter period. The results are stored in the four switching time counter registers $c^z_{i,j}[n]$ ($j \in \{1, \ldots, 4\}$) for each high (H) or low (L) side switch ($i \in \{\text{H}, \text{L}\}$) of each phase leg ($z \in \{u, v, w\}$), considering also the switch dead times t_{DT}. If the number of switching transitions of a switch in the next counter period is less than four, the remaining registers take the value $c_{\max}[n]{+}1$. On the contrary, if more switching transitions take place over one counter period, more registers have to be used.

The modulator reads the register values at the beginning of the next counter period (i.e. at the trigger instant p), compares them with the actual counter value and generates the gate signals s^z_i for each switch, as illustrated in Fig. 3.10.

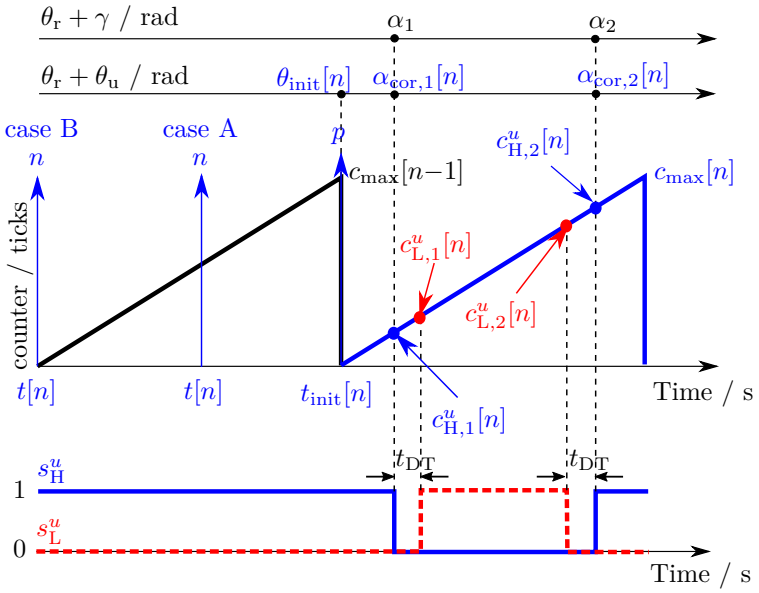

Figure 3.10: *Illustration of the principal idea of the switching time counter determination for phase u.*

3.2.4 Experimental verification

In this subsection, experimental results are presented, in order to verify the performance of the proposed fundamental current estimation method not only in steady-state operation but also during transient conditions. The laboratory setup is presented in Appendix A.

Fig. 3.11 depicts the current waveforms in the *dq*-frame in steady-state operation over one electrical period. In Fig. 3.11a, the SOPWM case A is utilized, since $f_r < 600\,\text{Hz}$. The measured motor currents are sampled at each $\pi/12$ rad rotation of the voltage vector, i.e. twice per counter period, and transformed to the *dq*-frame, as illustrated by $\boldsymbol{i}^k_{s,SP_{1\&2}}$ in Fig. 3.11a. The fundamental current components $\hat{\boldsymbol{i}}^k_{s,1}$ are estimated by the mean values $\boldsymbol{i}^k_{s,4SP}$ of the last four sampling points using (3.6). In Fig. 3.11b, the measured currents are sampled at each $\pi/6$ rad rotation of the voltage vector, i.e. once per counter period, since the SOPWM case B is employed for $f_r \geq 600$ Hz. The fundamental current components $\hat{\boldsymbol{i}}^k_{s,1}$ are estimated by the mean values $\boldsymbol{i}^k_{s,2SP}$ of the last two transformed sampled currents $\boldsymbol{i}^k_{s,SP_1}$ using (3.5) (see also Fig. 3.3). The sampled measured currents still contain some harmonic content in both operating points. Nevertheless, the most dominant harmonic components of the sampled currents are eliminated by the proposed fundamental current estimation method. Hence, the estimated fundamental current components $\hat{\boldsymbol{i}}^k_{s,1}$ can be used for feedback for a stable and accurate closed-loop current control.

The dynamic performance of the proposed fundamental current estimation method is illustrated in Fig. 3.12 and Fig. 3.13 for a torque change of 100 Nm and 50 Nm, while f_r remains constant at 450 Hz and 800 Hz, respectively. The change rate of the reference currents is limited to 3 500 A/s. This is a common strategy in automotive applications, where very fast control dynamics of the drive system are not required. In Fig. 3.12a and Fig. 3.13a, the SVM scheme is utilized with a constant switching frequency of 10 kHz, while in Fig. 3.12b and Fig. 3.13b the inverter control is based on the SOPWM scheme with $q = 9$ pulses over an electrical period. The current control response is sufficiently fast for both modulation schemes. For SOPWM, the current controller is triggered only with a frequency of $12 f_r$ (5.4 kHz in Fig. 3.12b and 9.6 kHz in Fig. 3.13b), i.e. at each $\pi/6$ rad of the voltage vector, and the switching frequency is low

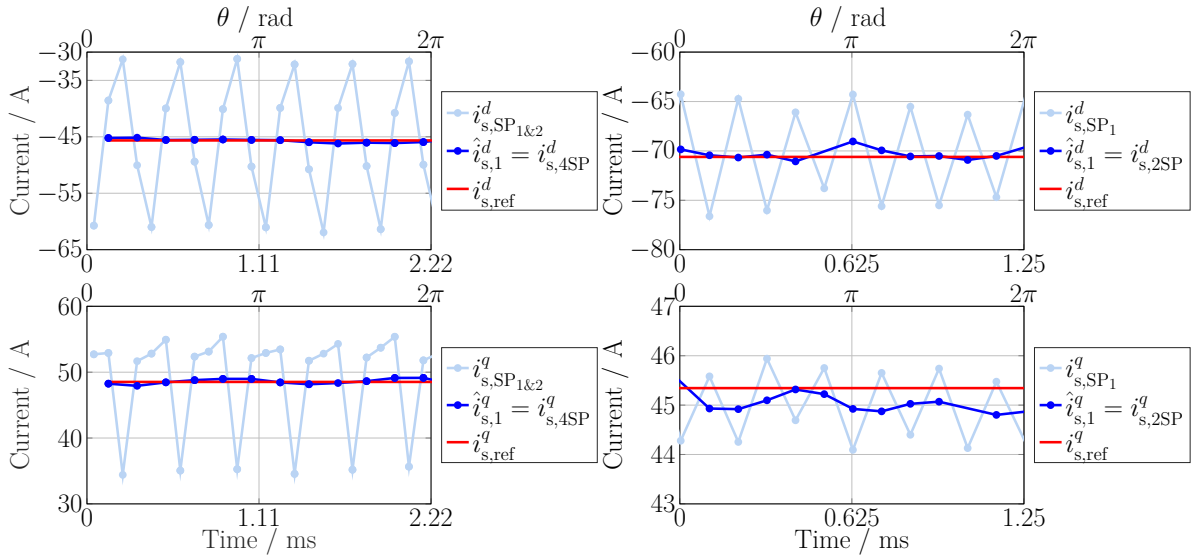

(a) *SOPWM Case A:* $T_{ref} = 20\,\text{Nm}$, $f_r = 450\,\text{Hz}$. (b) *SOPWM Case B:* $T_{ref} = 20\,\text{Nm}$, $f_r = 800\,\text{Hz}$.

Figure 3.11: *Fundamental current estimation in steady-state operation.*

(qf_r=4.05 kHz in Fig. 3.12b and qf_r=7.2 kHz in Fig. 3.13b). For SVM, the controller trigger rate and switching frequency are higher (10 kHz). Nonetheless, no major differences are detected in the current controller performance.

Fig. 3.14 illustrates the performance of the proposed fundamental current estimation method when a change of 100 Hz in f_r and of 40 Nm in T_{ref} are applied simultaneously. The acceleration is limited to 2 000 rpm/s, i.e. $2000 n_p/60 = 200\,\text{Hz/s}$. Disturbances can be observed in the current control system at the beginning and end of the acceleration, regardless of whether SVM (see Fig. 3.14a) or SOPWM (see Fig. 3.14b) are utilized. These disturbances are mainly present due to the rotor position tracking error of the resolver during accelerations. In the experimental setup, the AD2S1210 tracking resolver-to-digital converter (RDC) [115] is used to measure the rotor angular position. The RDC uses a Type-II tracking loop to perform position calculations. The advantage of Type-II tracking loops over Type-I loops is that no positional errors occur at constant velocity. However, acceleration phases impose a tracking error between the converter output angle and the real rotor position [116]. Due to this error, the Clarke-Park transformation of the measured currents $\boldsymbol{i}^{uvw}_{s,SP_{1\&2}}$ to the synchronous reference frame is not correct during accelerations. Consequently, oscillations occur as depicted in Fig. 3.14. These oscillations occur despite the used modulation scheme and are not due to the proposed fundamental current estimation method.

The experimental results confirm the accurate performance of the proposed fundamental current estimation method not only in steady-state operation but also during transient conditions.

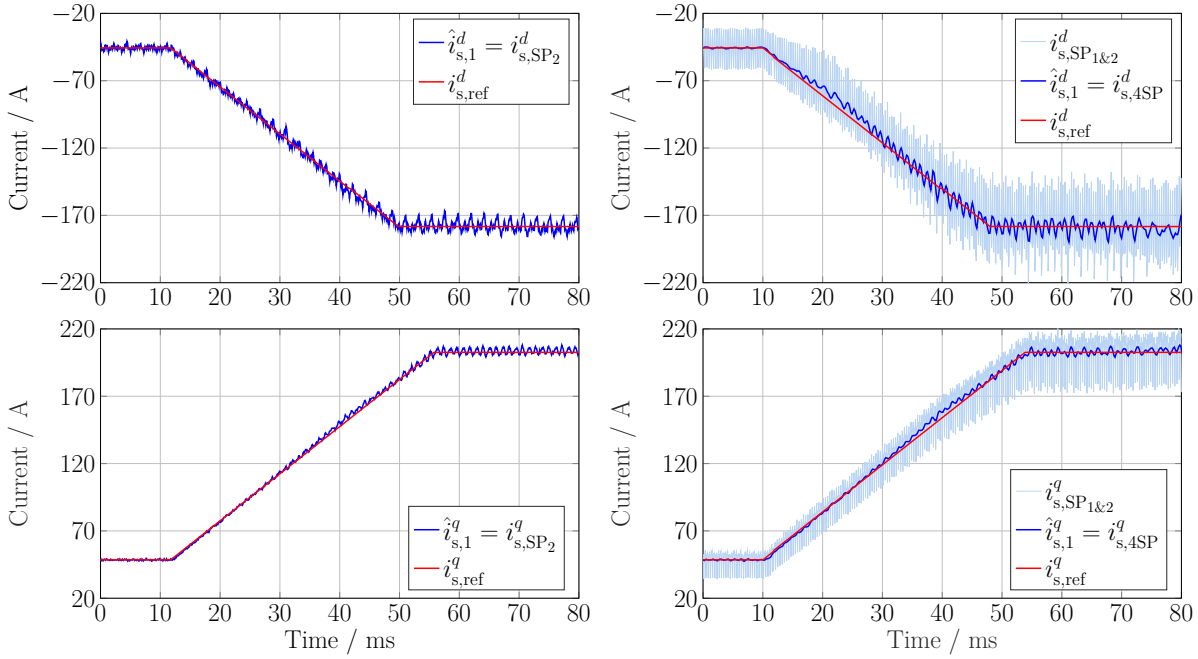

(a) *SVM.* (b) *SOPWM case A.*

Figure 3.12: *Motor current response to a torque change from* 20 Nm *to* 120 Nm *($f_r = 450$ Hz).*

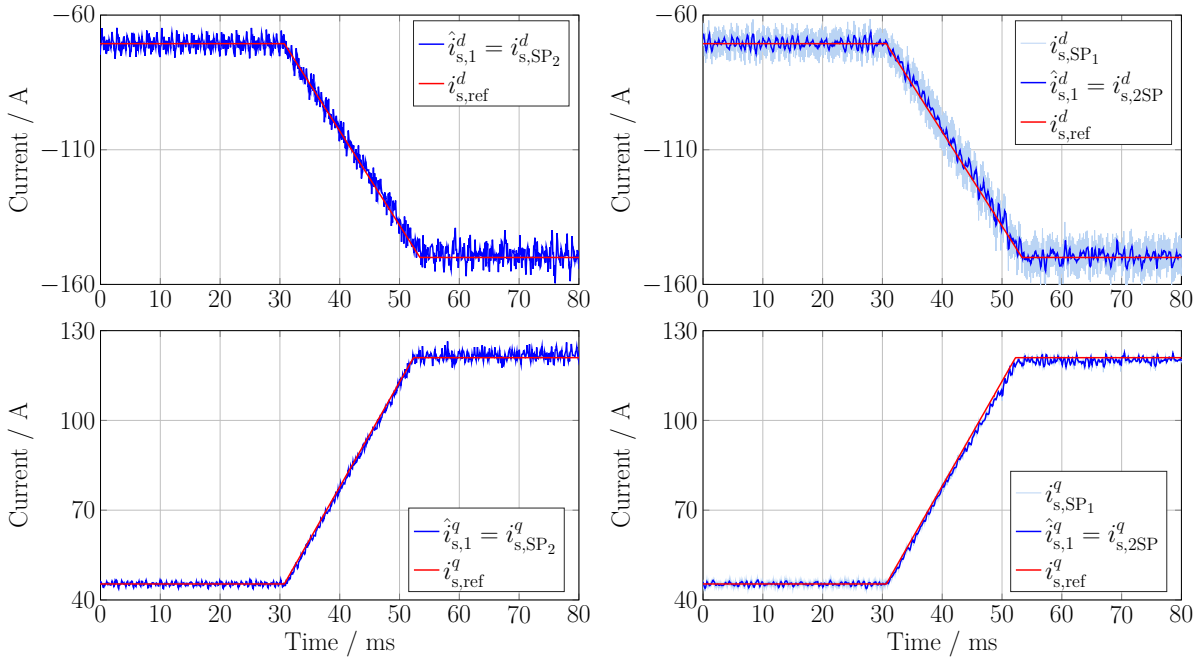

(a) *SVM.* (b) *SOPWM case B.*

Figure 3.13: *Motor current response to a torque change from* 20 Nm *to* 70 Nm *($f_r = 800$ Hz).*

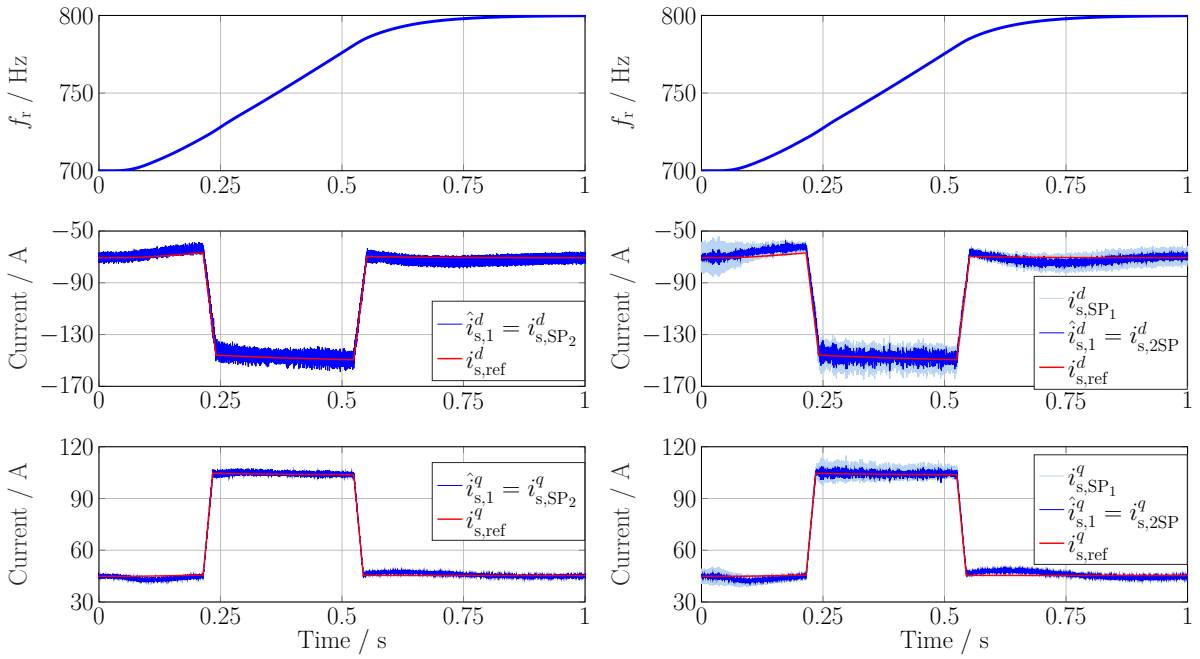

(a) *SVM.* (b) *SOPWM.*

Figure 3.14: *Motor current response to a rotor frequency change of* 100 Hz *and torque change from* 20 Nm *to* 60 Nm.

3.3 Switching transition between different pulse patterns

Another important aspect, concerning the implementation of the SOPWM, involves the transition between different pulse patterns. For this thesis, the asynchronous SVM scheme is used for $f_r < 400\,\text{Hz}$ whereas the SOPWM scheme with a pulse number of $q = 9$ and $q = 5$ is employed for $f_r \in [400, 900)\text{Hz}$ and $f_r \in [900, 1200]\text{Hz}$, respectively, as depicted in Fig. 2.5. A hard switching transition between different modulation modes may cause current and torque transients and even overcurrent conditions. In this section, simple and effective methods to address this problem are proposed.

3.3.1 Switching transition between SVM and SOPWM

In this subsection, the switching between SVM and SOPWM will be investigated. In [58], the switching transition is enabled at a fixed vector angle, while in [59] the switching is optimized, such that no more than one switching state changes during transition. However, these methods do not consider a switching between SVM and SOPWM with highly different switching frequencies. In this subsection, a strategy is proposed, which transforms the asynchronous SVM into a frequency- and phase-synchronous SVM scheme before the switching takes place. When both modulation strategies are synchronized with the voltage vector rotation, the transition between both does not cause disturbances in the current control any more, as will be illustrated by experimental results later.

3.3.1.1 Main principle

In this project, the switching transition between the asynchronous SVM and the SOPWM with $q = 9$ pulses over an electrical period takes place at 400 Hz. Thereafter, the switching

frequency of SOPWM is $f_{\mathrm{sw,SOPWM}} = q f_{\mathrm{r}} \approx 3.6\,\mathrm{kHz}$, while that of SVM is considerably higher with $f_{\mathrm{sw,SVM}} = 10\,\mathrm{kHz}$. In order to achieve a smooth switching between these strategies, despite their highly different switching frequencies, the following issues must be considered:

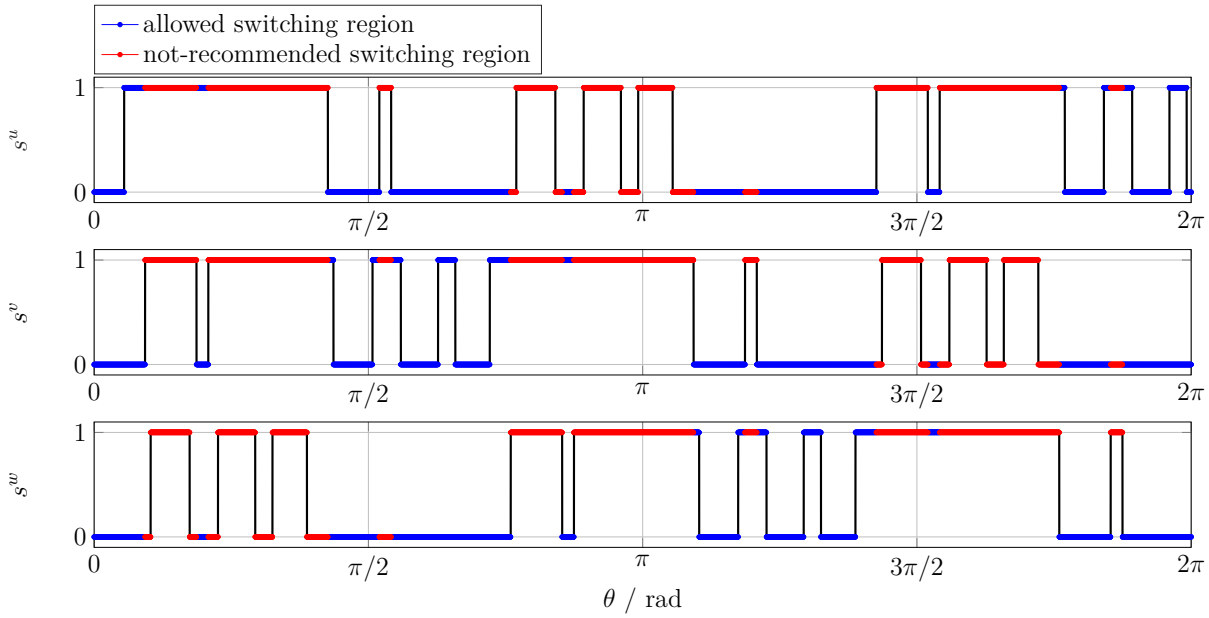

Figure 3.15: *PWM waveforms over an electrical period using SOPWM with $q = 9$ pulses ($T_{\mathrm{ref}} = 20\,\mathrm{N\,m}$, $f_{\mathrm{r}} = 400\,\mathrm{Hz}$, $m = 0.484$, $\theta_{\mathrm{u}} = 1.945\,\mathrm{rad}$, $\lambda = 3.17$).*

1. The number of changing switching states should be zero or one, so that the same or adjacent voltage vectors are utilized before and after the transition [59]. Hence, the switching transition can take place only at specific locations. The first and last voltage vector used by the SVM within each counter period is always the zero vector 000. Consequently, the switching transition should take place when the active vectors 100, 010 and 001 or the zero vector 000 are utilized by the SOPWM. Fig. 3.15 depicts the general form of the PWM phase signals generated by the SOPWM scheme using nine pulses over an electrical period. Although the inverter switching angles depend on m, θ_{u} and λ, angle discontinuities are not allowed, as discussed in Sec. 2.4. Thus, the general structure of the PWM waveforms does not change at different motor operating points. Only the application time of each space vector, i.e. the width of the PWM pulses, differs. The blue color in Fig. 3.15 indicates the allowed switching locations, i.e. the locations where zero or one switching state changes compared to the zero switching vector 000, while the red color implies that switching in this region is not recommended. Although more than one allowed switching locations exist, in this work, the switching is restricted to the regions around $\theta \approx 0$ and $\theta \approx \pi/2$. This is done, firstly, for implementation simplicity, since the activation of both SVM and SOPWM scheme in the same counter period will result in an increased turn-around time of the processor model. Consequently, only one scheme is activated in each counter period and the switching is restricted at the edges of the voltage hexagon subsectors. Secondly, the restriction of the switching process to a specific point makes the switching transition more reliable.

2. The current sampling should be synchronized with the voltage vector rotation *before* the switching takes place. Otherwise, the fundamental current component may not be correctly estimated by the method proposed in Sec. 3.2.

3. A hard switching between highly different switching frequencies is not advisable due to highly different current ripple.

Taking these issues into consideration, the transformation of the asynchronous SVM into a frequency- and phase-synchronous SVM is recommended before the switching to SOPWM takes place. In this way, a smooth transition between the two modulation schemes can be realized. The switching procedure from SVM to SOPWM can be described by the following steps (see Fig. 3.16):

1. For $f_\mathrm{r} \geq 400\,\mathrm{Hz}$, the transition from asynchronous SVM to SOPWM is activated. The upper counter limit c_max is adjusted by a step of c_step ticks at each counter period n, i.e.

$$c_\mathrm{max}[n] = c_\mathrm{max}[n-1] + c_\mathrm{step},$$

   until the value of $c_{\pi/6}[n] - 1$ is reached. At this point, the SVM strategy is synchronized with the electrical rotor frequency, since the switching frequency equals $12 f_\mathrm{r}$. The smaller c_step is chosen, the smoother but slower the synchronization process will be.

2. After synchronization with the electrical rotor frequency, PLL and FF functions are activated. At the end of this step, the SVM strategy is also synchronized with the voltage vector rotation.

3. When the synchronization process of the SVM is completed, i.e. $\theta_\mathrm{M,target} - \theta_\mathrm{M} \approx 0$, the SOPWM strategy can be activated. The switching takes place for $\theta \approx 0$ rad in the beginning of the next counter period. In this way, it is ensured that the number of changing switching states is either zero or one and the transition between the two schemes does not cause major overshoots in the current control system [59].

As can be seen in Fig. 3.16, the PLL and FF mechanisms manage to synchronize the SVM strategy in less than 2.5 ms and the total SVM synchronization process takes approximately 6.25 ms, which is sufficiently fast for the considered application in electric vehicles.

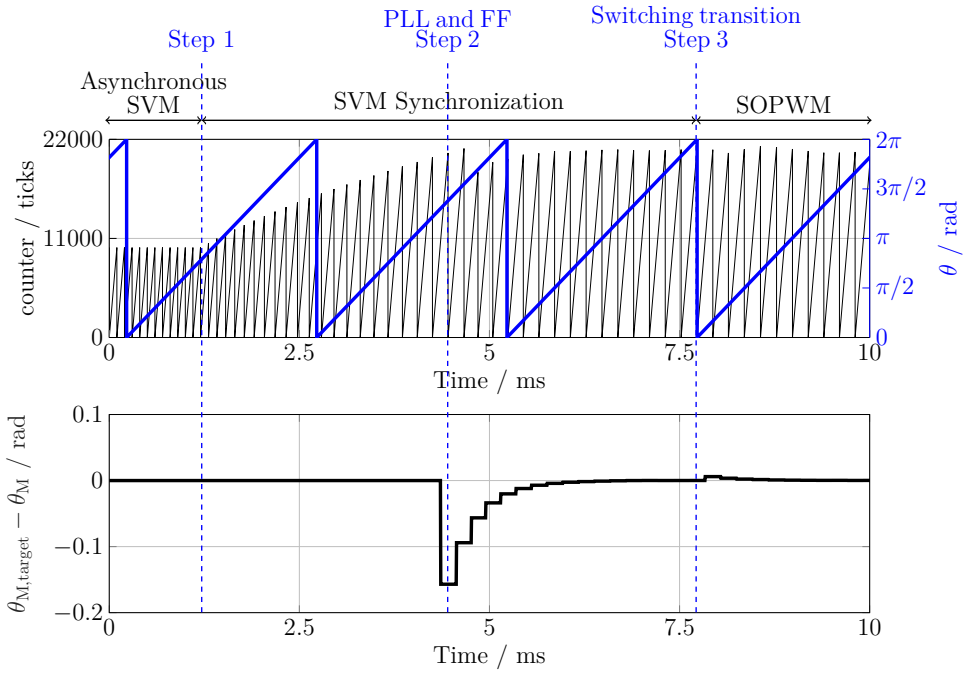

Figure 3.16: *Illustration of the principal idea of the switching transition from SVM to SOPWM.*

The inverse transition procedure from SOPWM to SVM can be described by the following steps (see Fig. 3.17):

1. For $f_\mathrm{r} < 400\,\mathrm{Hz}$ and $\theta \approx \pi/2$ rad, the switching transition from SOPWM to synchronous SVM occurs. The PLL and FF mechanisms are then deactivated (i.e. $c_\mathrm{max}[n] = c_{\pi/6}[n] - 1$ in (3.8)).

2. The upper counter limit is decreased by a step of c_step ticks at each counter period n, i.e.

$$c_\mathrm{max}[n] = c_\mathrm{max}[n-1] - c_\mathrm{step},$$

until the constant switching frequency of $f_\mathrm{sw,SVM}$ is reached. At this point, the asynchronous SVM is employed.

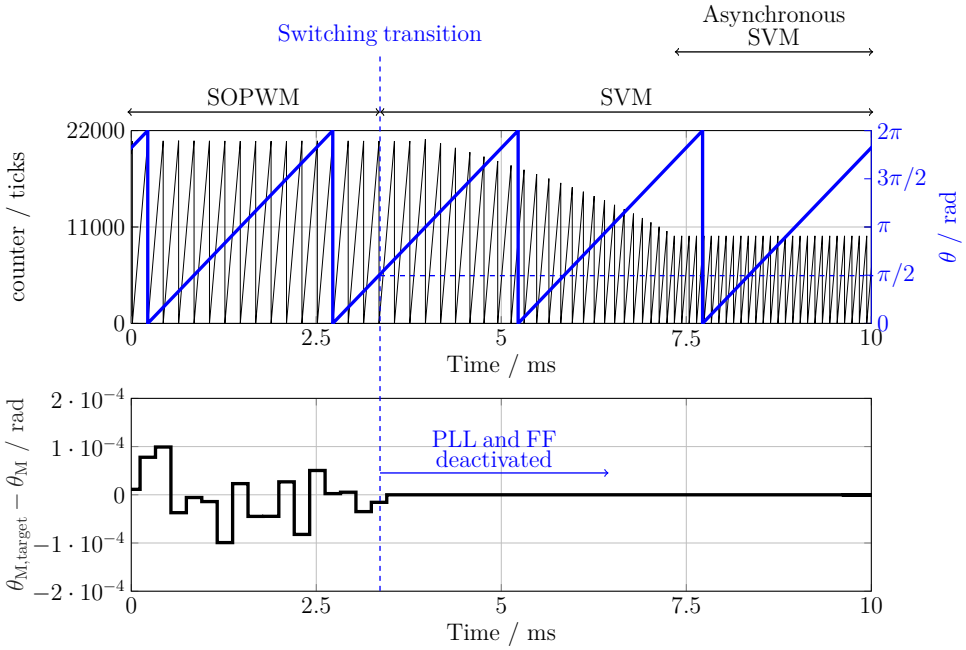

Figure 3.17: *Illustration of the principal idea of the switching transition from SOPWM to SVM.*

3.3.1.2 Experimental verification

The transition between SVM and SOPWM is investigated in Fig. 3.18 - 3.21, which depict the motor phase currents and the voltages $\boldsymbol{u}_{\mathrm{dc}-}^{uvw}$ over the lower half inverter leg of each phase. Changes in the electrical frequency from 380 Hz to 420 Hz and backwards are applied with a rate of 200 Hz/s, while the torque remains constant at 20 Nm and 120 Nm. The transitions take place during these dynamic conditions.

In Fig. 3.18 - 3.21, the fundamental components of the machine phase currents $\boldsymbol{i}_{\mathrm{s},1}^{uvw}$ are illustrated with dotted black lines. Current overshoots take place during the switching transitions between different pulse trains and can be measured by the current percentage overshoot (PO) factor

$$I_{\mathrm{s},1,\mathrm{PO}}^{z} := 100\frac{i_{\mathrm{s},1}^{z}\big|_{\mathrm{transition}} - i_{\mathrm{s},1}^{z}}{i_{\mathrm{s},1}^{z}} \tag{3.17}$$

defined as the percentage deviation of the maximum amplitude of the fundamental current during the transition $i^z_{\mathrm{s},1}\big|_{\text{transition}}$ to the one in normal motor operation $i^z_{\mathrm{s},1}$, where $z = \{u, v, w\}$. Large current overshoots lead to torque transients and, thus, an unpleasant driving behavior. Moreover, overcurrent tripping may be the result of a large current overshoot, especially at high loads. For these reasons, large values of $I^z_{\mathrm{s},1,\mathrm{PO}}$ must be prohibited. The amount of current percentage overshoot, defined by (3.17), determines the performance of the switching transition. Table 3.1 summarizes the values of the current percentage overshoot during the switching transitions between SVM and SOPWM.

Table 3.1: *Current percentage overshoot during the switching transitions between SVM and SOPWM.*

Figure	3.18a	3.19a	3.18c	3.19c	3.20a	3.21a	3.20c	3.21c
$I^u_{\mathrm{s},1,\mathrm{PO}}$ (in %)	24.14	14.32	28.32	4.34	13.40	18.10	2.23	4.09
$I^v_{\mathrm{s},1,\mathrm{PO}}$ (in %)	54.30	3.90	18.85	1.09	21.05	7.78	10.21	6.79
$I^w_{\mathrm{s},1,\mathrm{PO}}$ (in %)	62.22	2.75	13.85	2.09	51.05	11.93	3.81	3.25

Fig. 3.18 depicts the switching transition performance from asynchronous SVM to SOPWM without the proposed transition strategy from Sec. 3.3.1. The percentage overshoots of the phase currents are relatively high in this case (see Table 3.1) and occur due to the following reasons:

- More than one switching states change during the transition. For instance, in Fig. 3.18c the zero vector 000 is used before the transition and the active vector 011 afterwards.
- The PLL and FF mechanisms are activated only after the switching. Consequently, the fundamental current is not correctly estimated until the current sampling frequency is synchronized with the voltage vector rotation.
- A hard switching between two highly different switching frequencies (10 kHz for SVM and $qf_{\mathrm{r}} \approx 3.6$ kHz for SOPWM) occurs, which is not desired due to the highly different current ripple.

On the contrary, the switching transition is smooth when the proposed strategy is employed. Fig. 3.19 depicts the transition process from asynchronous SVM to SOPWM. The asynchronous SVM is transformed into a synchronous SVM before the switching takes place. The SVM switching frequency decreases from 10 kHz to $12f_{\mathrm{r}} \approx 4.8$ kHz and, thus, the current harmonic content increases. Finally, the transition takes place at $\theta \approx 0$ rad, which ensures that no switching state changes occur during the transition, as depicted in Fig. 3.19b and 3.19d. The SVM synchronization process lasts about 5 ms, which empirically makes the proposed strategy sufficiently fast. The phase current overshoots are lower in Fig. 3.19 than in Fig. 3.18, which indicates that the performance of the switching transition is significantly improved by the proposed method.

Fig. 3.20 illustrates the motor phase currents when a hart switching transition from the low-switching frequency SOPWM directly to asynchronous SVM takes place. While the switching transition in Fig. 3.20c is smooth, this is not the case in Fig. 3.20a despite the fact that only one switching state changes (see Fig. 3.20b).

Fig. 3.21 demonstrates the performance of the switching transition from SOPWM to asynchronous SVM when the proposed method is employed. The transition takes place when both strategies are synchronized with the voltage vector rotation and $\theta \approx \pi/2$ rad. The SVM switching frequency increases afterwards until the value of 10 kHz is reached. Thus, no major current overshoots occur (see Table 3.1).

The experimental results prove the satisfactory performance of the proposed switching transition strategy, even when the switching frequencies of the two modulation schemes are highly different (10 kHz for SVM and $qf_{\mathrm{r}} \approx 3.6$ kHz for SOPWM).

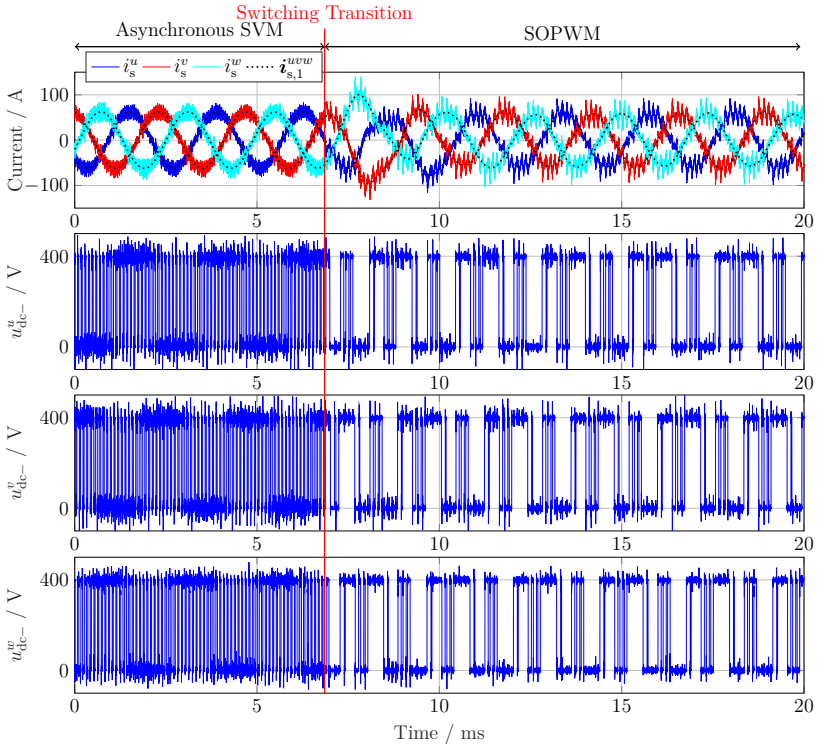

(a) $T_{\mathrm{ref}} = 20\,\mathrm{Nm},\ f_{\mathrm{r}} \in [380, 420]$ Hz.

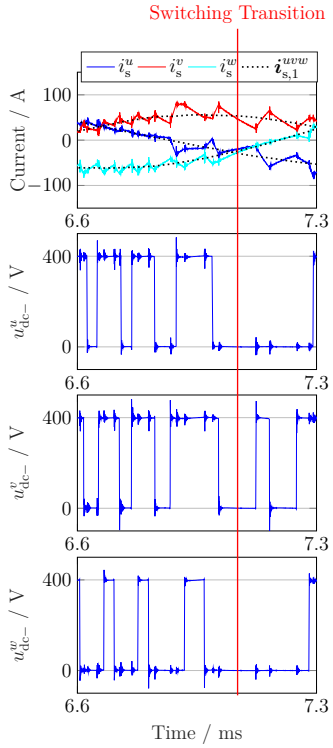

(b) *Zoom in time domain of Fig. 3.18a.*

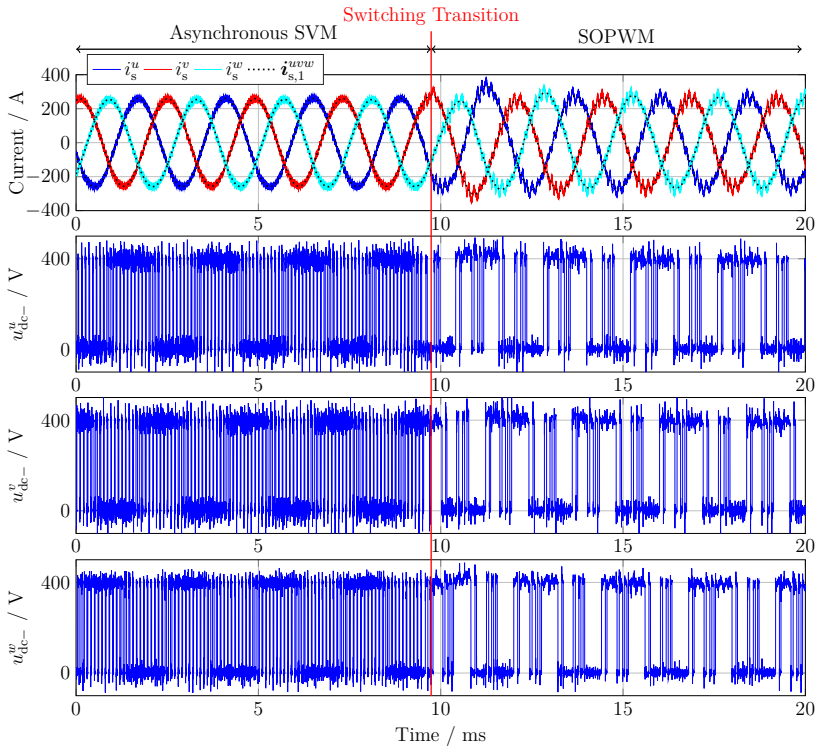

(c) $T_{\mathrm{ref}} = 120\,\mathrm{Nm},\ f_{\mathrm{r}} \in [380, 420]$ Hz.

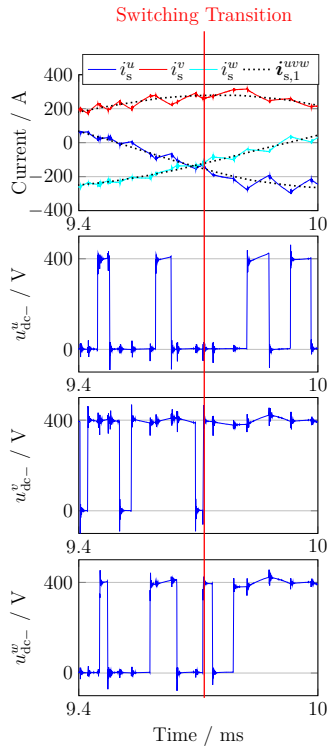

(d) *Zoom in time domain of Fig. 3.18c.*

Figure 3.18: *Switching transition from SVM to SOPWM* ***without*** *the proposed method.*

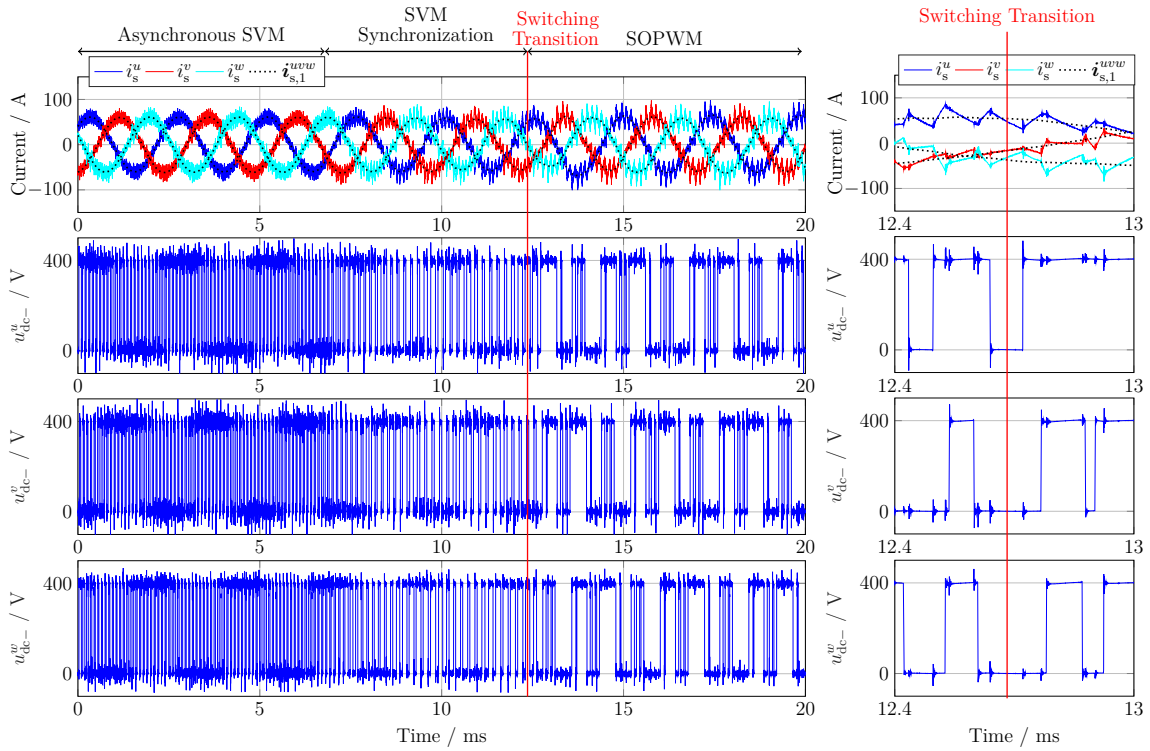

(a) $T_{\text{ref}} = 20\,\text{Nm},\ f_{\text{r}} \in [380, 420]$ Hz.

(b) *Zoom in time domain of Fig. 3.19a.*

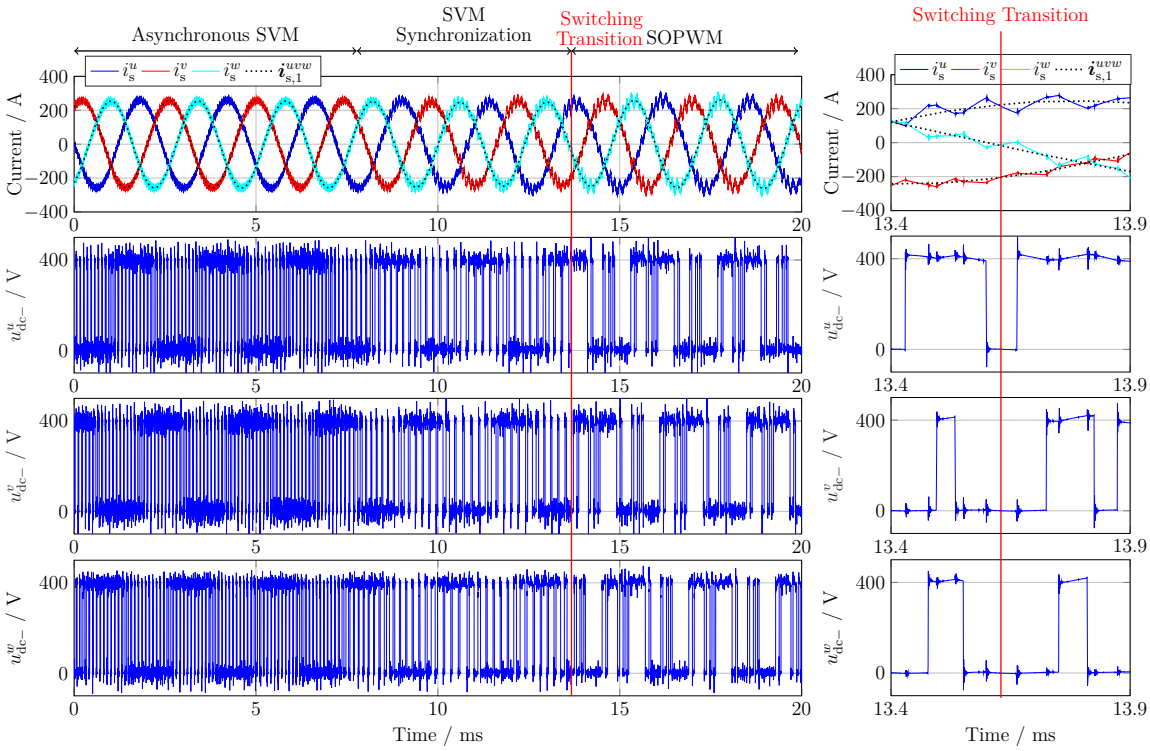

(c) $T_{\text{ref}} = 120\,\text{Nm},\ f_{\text{r}} \in [380, 420]$ Hz.

(d) *Zoom in time domain of Fig. 3.19c.*

Figure 3.19: *Switching transition from SVM to SOPWM* ***with*** *the proposed method.*

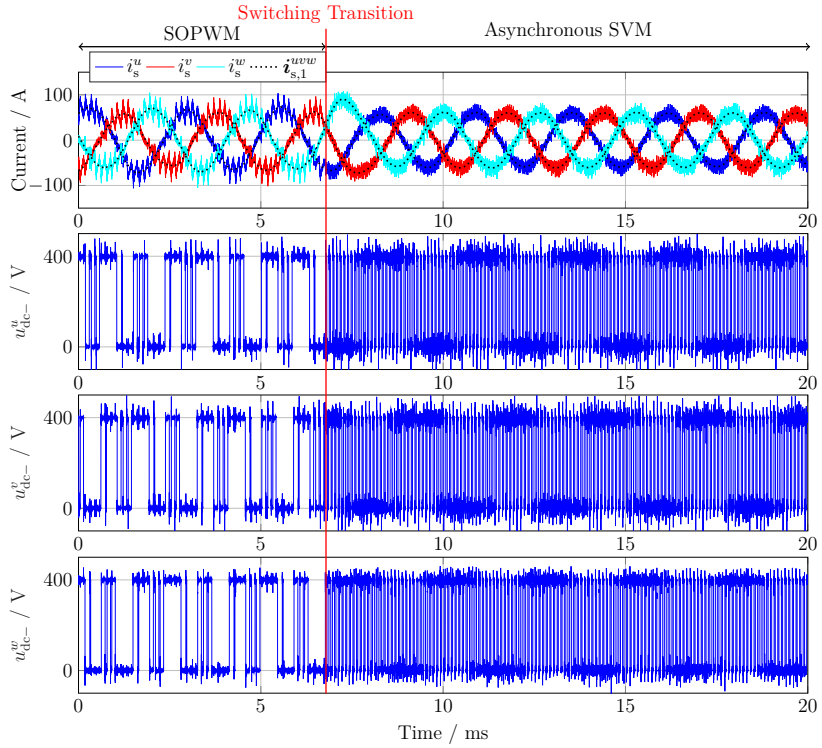

(a) $T_{\mathrm{ref}} = 20\,\mathrm{Nm},\ f_{\mathrm{r}} \in [380, 420]$ Hz.

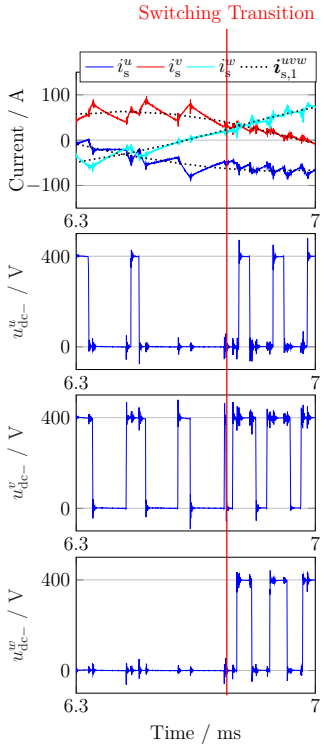

(b) *Zoom in time domain of Fig. 3.20a.*

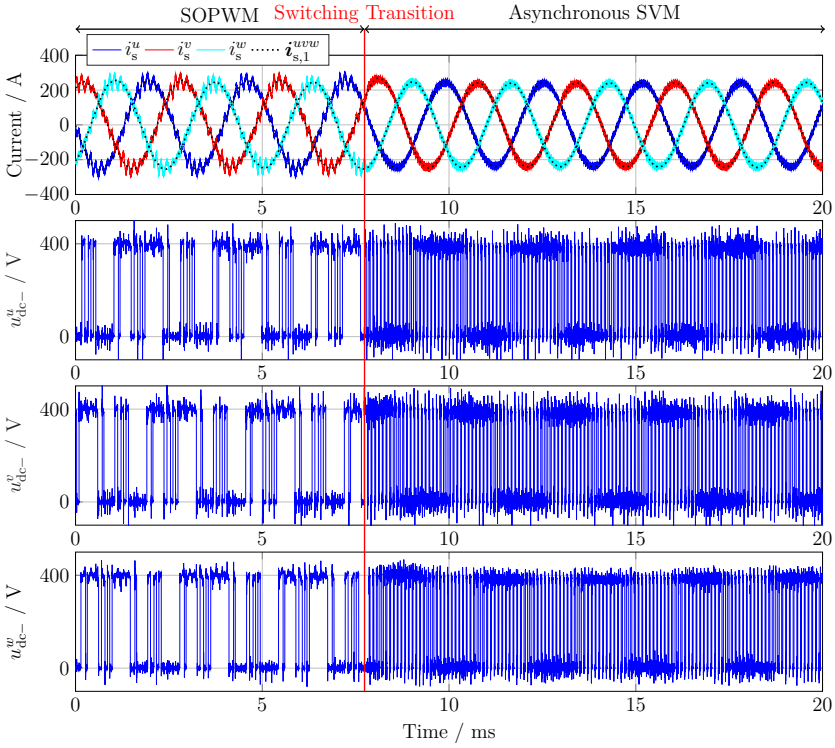

(c) $T_{\mathrm{ref}} = 120\,\mathrm{Nm},\ f_{\mathrm{r}} \in [380, 420]$ Hz.

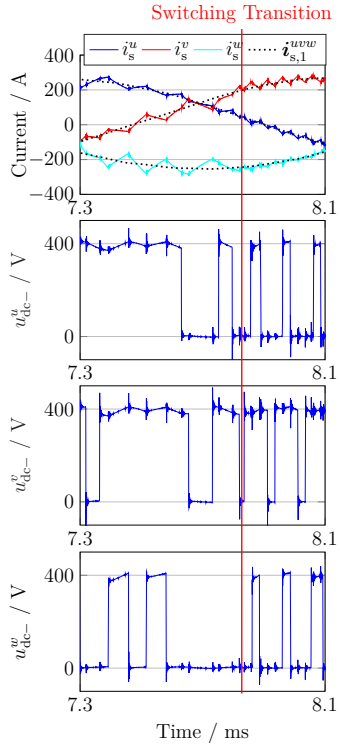

(d) *Zoom in time domain of Fig. 3.20c.*

Figure 3.20: *Switching transition from SOPWM to SVM* ***without*** *the proposed method.*

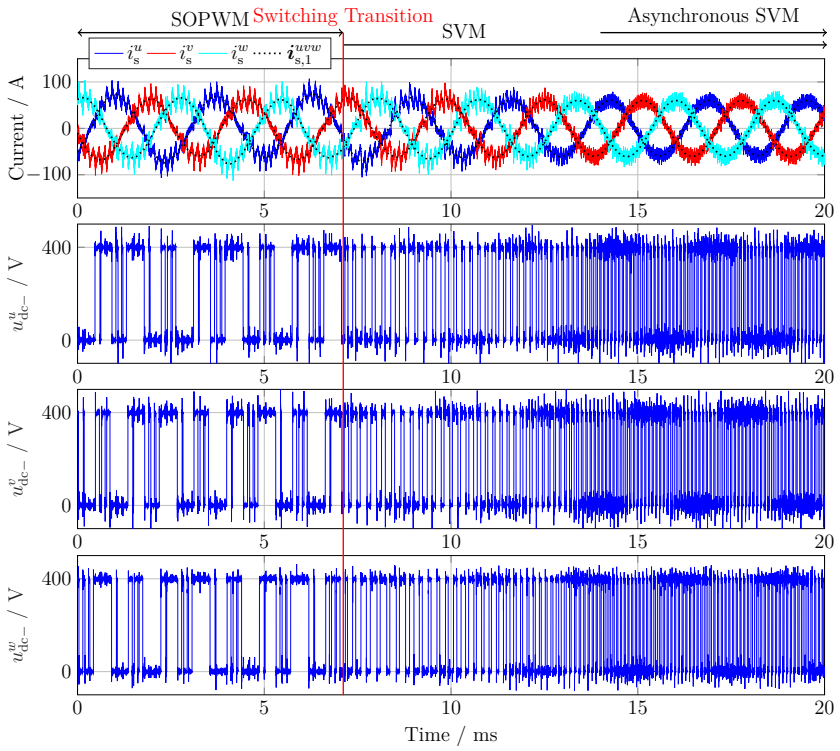

(a) $T_{\text{ref}} = 20\,\text{Nm},\ f_r \in [380, 420]$ Hz.

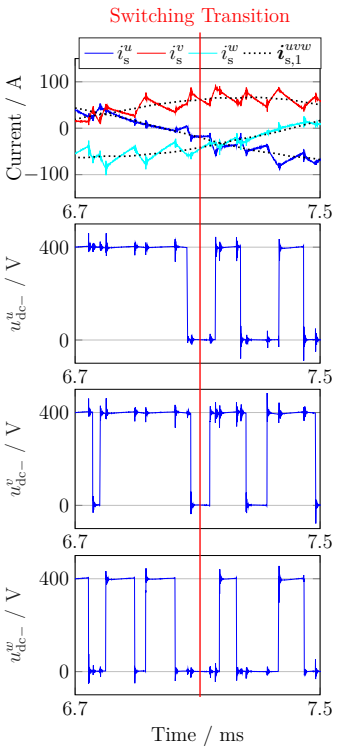

(b) *Zoom in time domain of Fig. 3.21a.*

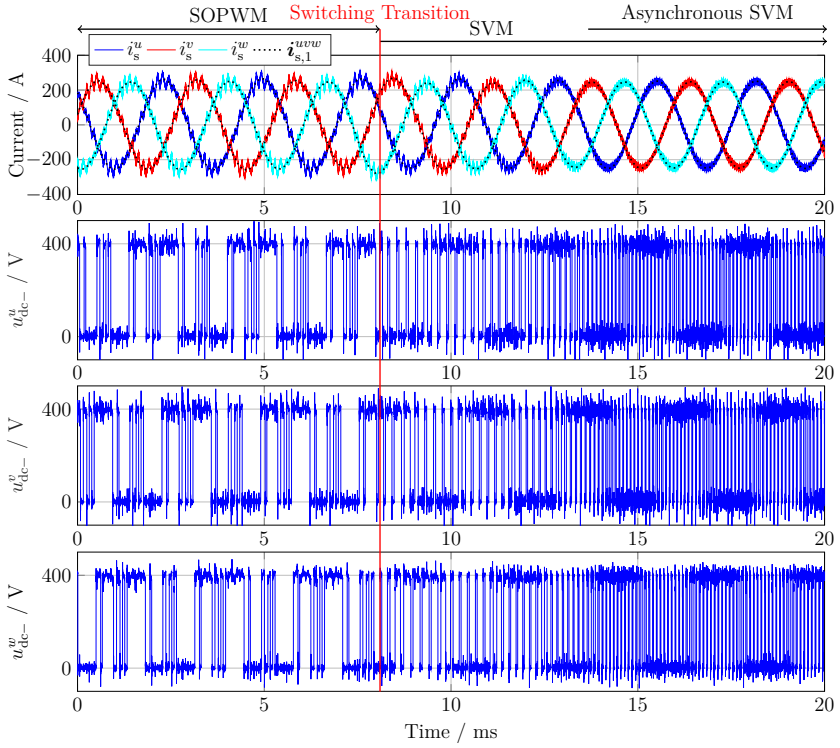

(c) $T_{\text{ref}} = 120\,\text{Nm},\ f_r \in [380, 420]$ Hz.

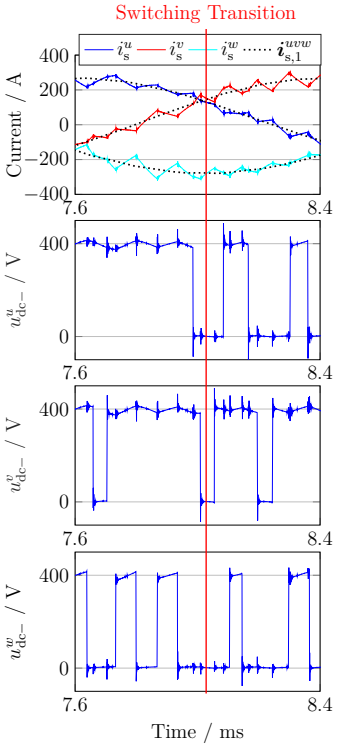

(d) *Zoom in time domain of Fig. 3.21c.*

Figure 3.21: *Switching transition from SOPWM to SVM* ***with*** *the proposed method.*

3.3.2 Switching transition between $q = 9$ and $q = 5$

The pulse number q must decrease with increasing electrical frequencies in order to keep the switching frequency and inverter power losses at a desired low level. In this thesis, the transition between $q = 9$ and $q = 5$ occurs at $f_\mathrm{r} = 900\,\mathrm{Hz}$ (see Fig. 2.5 in Sec. 2.4). The main principle of the switching transition is presented in this subsection.

3.3.2.1 Main principle

Fig. 3.22a and 3.22b demonstrate the inverter gate signals $\boldsymbol{s}^{uvw}$ for $T_\mathrm{ref} = 50\,\mathrm{Nm}$ and $f_\mathrm{r} = 900\,\mathrm{Hz}$, using a pulse number of $q = 9$ and $q = 5$, respectively. Comparing the two pulse patterns, it can be seen that they are very similar. The most important difference is that each pulse corresponding to a zero vector (000 or 111) for $q = 5$ is split into three pulses when $q = 9$. Consequently, a smooth transition between these pulse patterns is expected.

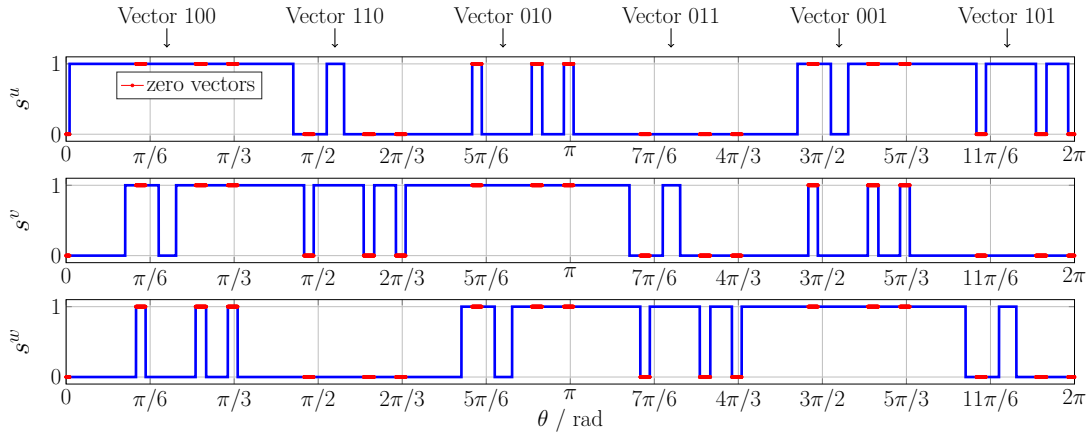

(a) $q = 9$.

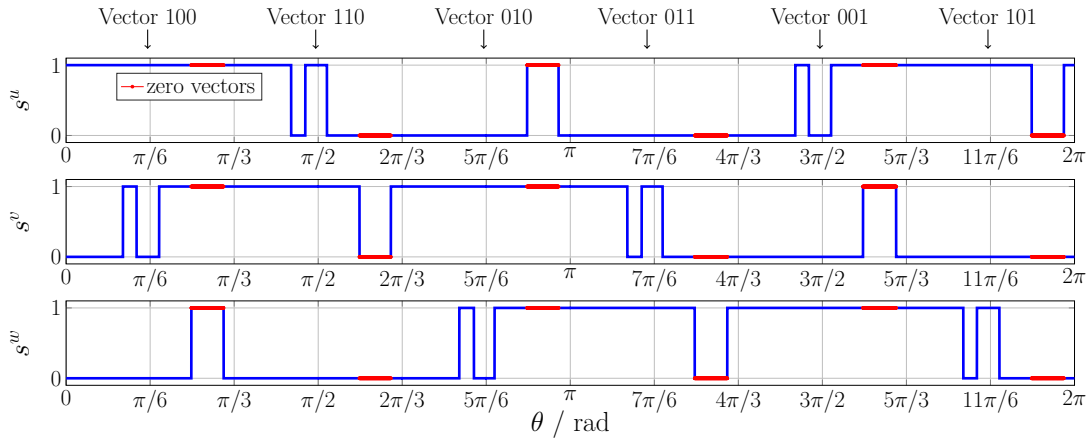

(b) $q = 5$.

Figure 3.22: *PWM waveforms over an electrical period using SOPWM* ($T_\mathrm{ref} = 50\,\mathrm{Nm}$, $f_\mathrm{r} = 900\,\mathrm{Hz}$, $m = 1.02$, $\lambda = 3.09$, $\theta_\mathrm{u} = 2.304\,\mathrm{rad}$).

Selecting the locations of $\theta \approx i\pi/3 + \pi/6$ rad ($i = \{0, \ldots, 5\}$) for the switching transition is not advisable, since the location of the active vectors 100, 110, 010, 011, 001 and 101 is different in both pulse patterns (see Fig. 3.22). For instance, switching from $q = 5$ to $q = 9$ at $\theta \approx 3\pi/2\,\mathrm{rad}$ will result in a very long application time for the active vector 001, while the opposite is true when the transition from $q = 9$ to $q = 5$ occurs.

On the contrary, applying the switching transition at $\theta \approx i\pi/3$ rad ($i = \{0, \ldots, 5\}$) is recommended. To this recommendation leads the fact that the zero vectors have been already used *before* the switching takes place. Furthermore, the total application time of the zero vectors is approximately the same for both pulse patterns. Consequently, no major disturbances in the current control system are to be expected. In this thesis, the transition from $q = 9$ to $q = 5$ (or vice versa) is restricted to the region around $\theta \approx 0$ rad.

3.3.2.2 Experimental verification

The transition between $q = 5$ and $q = 9$ is investigated in Fig. 3.23 and Fig. 3.24, which depict the motor phase currents $\boldsymbol{i}_{\mathrm{s}}^{uvw}$, the voltages $\boldsymbol{u}_{\mathrm{dc-}}^{uvw}$ over the lower half inverter leg of each phase and the dc-link current i_{bat}. Changes in the electrical frequency from 850 Hz to 950 Hz and backwards are applied with a rate of 200 Hz/s, while the torque remains constant at 50 Nm. Again, the transitions take place during dynamic conditions. Table 3.2 summarizes the values of the current percentage overshoot during the switching transitions.

Table 3.2: *Current percentage overshoot during the switching transitions between $q = 9$ and $q = 5$.*

Figure	3.23a	3.24a	3.24c
$I^{u}_{\mathrm{s,1,PO}}$ (in %)	19.94	5.37	13.24
$I^{v}_{\mathrm{s,1,PO}}$ (in %)	8.68	5.63	14.66
$I^{w}_{\mathrm{s,1,PO}}$ (in %)	14.71	5.10	8.26

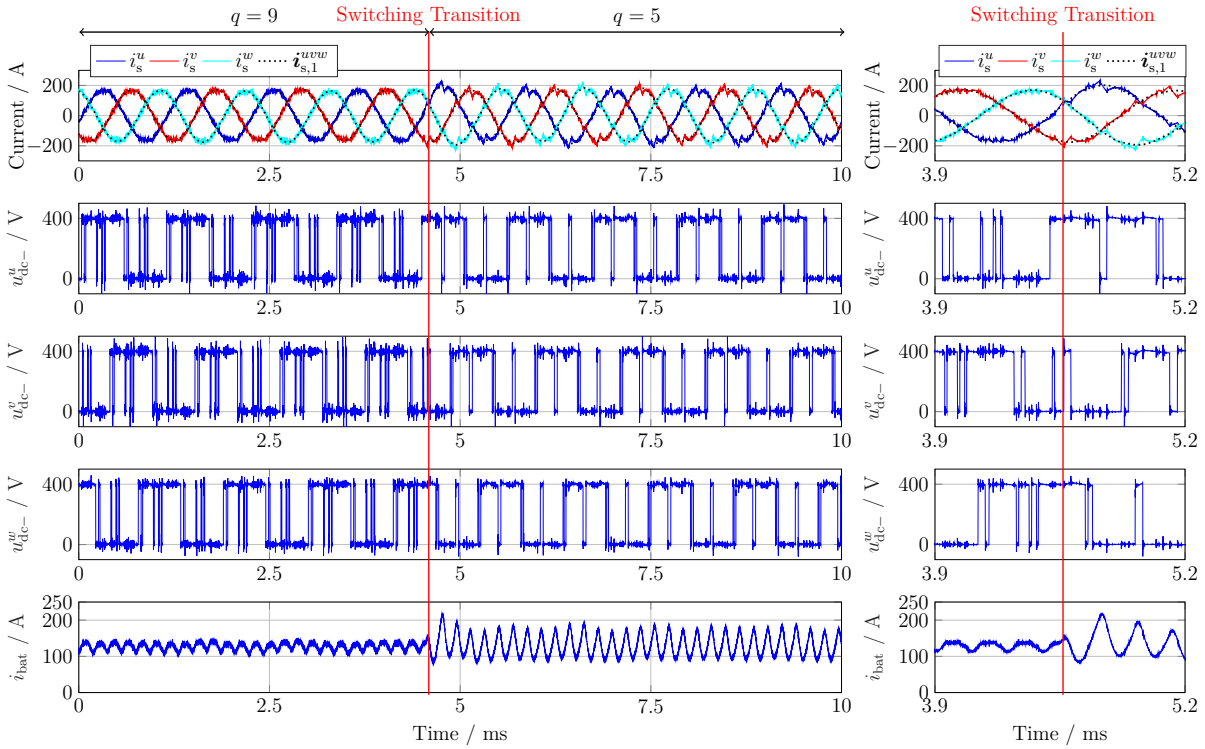

(a) *Switching transition from $f_{\mathrm{r}} = 850$ Hz and $q = 9$ to $f_{\mathrm{r}} = 950$ Hz and $q = 5$.* (b) *Zoom in time domain of Fig. 3.23a.*

Figure 3.23: *Switching transitions from q=9 to q=5 at $\theta \approx 3\pi/2$ rad ($T_{\mathrm{ref}} = 50$ Nm, $f_{\mathrm{r}} \in [850, 950]$ Hz).*

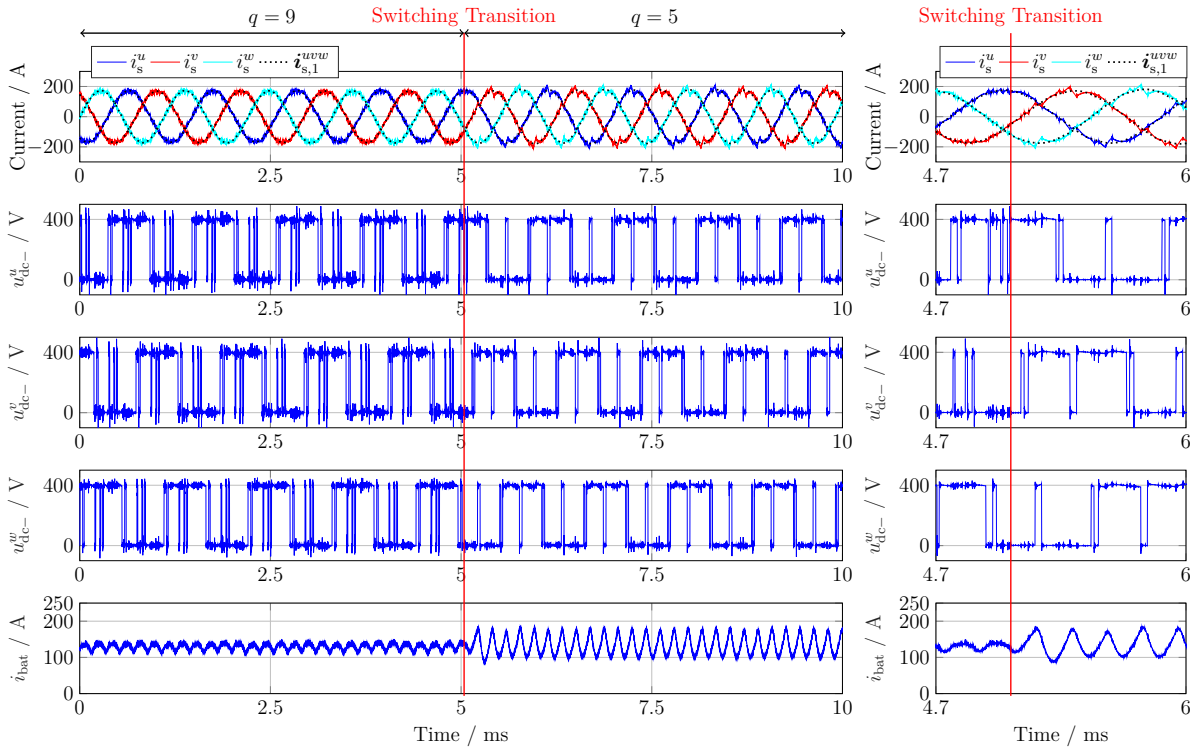

(a) *Switching transition from* $f_\mathrm{r} = 850\,\mathrm{Hz}$ *and* $q = 9$ *to* $f_\mathrm{r} = 950\,\mathrm{Hz}$ *and* $q = 5$. (b) *Zoom in time domain of Fig. 3.24a.*

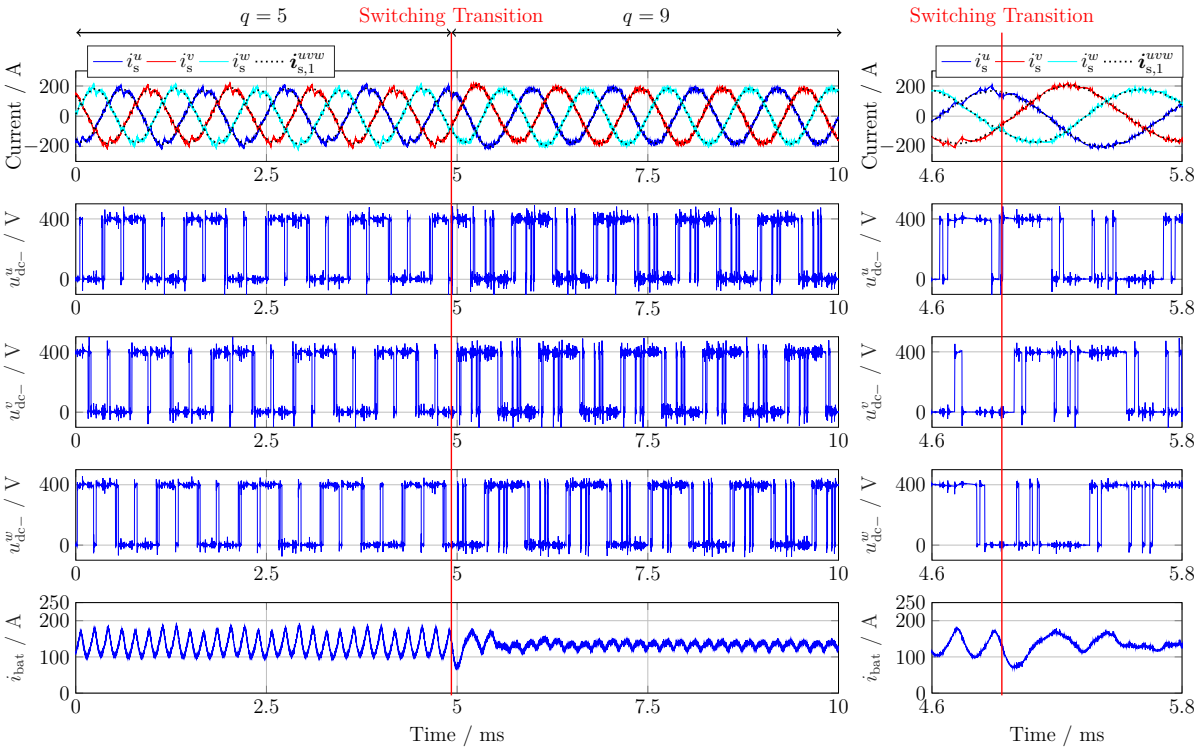

(c) *Switching transition from* $f_\mathrm{r} = 950\,\mathrm{Hz}$ *and* $q = 5$ *to* $f_\mathrm{r} = 850\,\mathrm{Hz}$ *and* $q = 9$. (d) *Zoom in time domain of Fig. 3.24c.*

Figure 3.24: *Switching transitions between* $q = 9$ *and* $q = 5$ *at* $\theta \approx 0\,\mathrm{rad}$ *(*$T_\mathrm{ref} = 50\,\mathrm{Nm}$, $f_\mathrm{r} \in [850, 950]$ Hz*).*

Fig. 3.23 depicts the switching transition performance from $q = 9$ to $q = 5$ at $\theta \approx 3\pi/2\,\mathrm{rad}$. Comparing the signals $\boldsymbol{u}_{\mathrm{dc}-}^{uvw}$ in Fig. 3.23b with the gate signals $\boldsymbol{s}^{uvw}$ of Fig. 3.22, it can be seen that the active vector 001 is missing in Fig. 3.23b. The reason for that lies in the fact, that the vector 001 is located before the switching transition when $q = 5$ pulses are used. As a consequence, the absence of this vector leads to a disturbance in the current control. On the contrary, the switching transition is smooth when it is located at $\theta \approx 0\,\mathrm{rad}$, as illustrated in Fig. 3.24a, since the overshoots in the current waveforms are significantly lower in Fig. 3.24a than in Fig. 3.23a (see Table 3.2). As far as the transition from $q = 5$ to $q = 9$ is concerned, a current oscillation can be observed in Fig. 3.24c. Nevertheless, the performance of the switching transition is still acceptable.

3.4 Experimental verification of the optimization results

The main objective of this project is to investigate the influence of the motor magnetic anisotropy on the optimized inverter switching angles. To this end, the equations of the PMSM phase currents with respect to the inverter switching angles have been derived in Sec. 2 and their RMS value has been used as objective function in the optimization problem. The resulting optimized inverter switching angles of an anisotropic motor are different from those of an isotropic motor, as illustrated in Fig. 2.11, since they depend not only on the modulation index m but also on the anisotropic factor λ and the voltage phase angle θ_{u}. Consequently, the optimization results depend on the motor magnetic properties. In this way, the influence of the magnetic anisotropy on the optimized inverter switching angles has been mathematically validated. The question that arises now is how big this influence is considering a PMSM with operating point dependent magnetic anisotropy (see Fig. 2.9). This question will be answered in Sec. 3.4.1; while in Sec. 3.4.2, the optimization outcomes will be validated by experimental results. The content of this section has been partly presented in [90, 92].

3.4.1 Numerical performance evaluation of the optimized inverter switching angles

In this subsection, the performance of the pulse patterns $\boldsymbol{\alpha}_{\mathrm{iso}}$ and $\boldsymbol{\alpha}_{\mathrm{aniso}}$ will be numerically evaluated in the whole motor operating range considering the motor phase current and dc-link capacitor current harmonic quality. The current harmonic distortion $I_{\mathrm{s,THD}}(\boldsymbol{\alpha})$ in (2.88) will be specified for each motor operating point using $\boldsymbol{\alpha}_{\mathrm{iso}}$ and $\boldsymbol{\alpha}_{\mathrm{aniso}}$. The same procedure is repeated for $I_{\mathrm{c/4,RMS}}(\boldsymbol{\alpha}) := I_{\mathrm{c,RMS}}(\boldsymbol{\alpha})/4$ using (2.84), since four capacitors connected in parallel are used in the test bench (see Appendix A). The performance of the two pulse patterns will be compared by the following measures

$$\begin{aligned} I_{\mathrm{s,THD,dif}} &:= I_{\mathrm{s,THD}}(\boldsymbol{\alpha}_{\mathrm{iso}}) - I_{\mathrm{s,THD}}(\boldsymbol{\alpha}_{\mathrm{aniso}}) \\ I_{\mathrm{s,THD,dev}} &:= 100\frac{I_{\mathrm{s,THD}}(\boldsymbol{\alpha}_{\mathrm{iso}}) - I_{\mathrm{s,THD}}(\boldsymbol{\alpha}_{\mathrm{aniso}})}{I_{\mathrm{s,THD}}(\boldsymbol{\alpha}_{\mathrm{aniso}})} \end{aligned} \tag{3.18}$$

and

$$\begin{aligned} I_{\mathrm{c/4,RMS,dif}} &:= I_{\mathrm{c/4,RMS}}(\boldsymbol{\alpha}_{\mathrm{iso}}) - I_{\mathrm{c/4,RMS}}(\boldsymbol{\alpha}_{\mathrm{aniso}}) \\ I_{\mathrm{c/4,RMS,dev}} &:= 100\frac{I_{\mathrm{c/4,RMS}}(\boldsymbol{\alpha}_{\mathrm{iso}}) - I_{\mathrm{c/4,RMS}}(\boldsymbol{\alpha}_{\mathrm{aniso}})}{I_{\mathrm{c/4,RMS}}(\boldsymbol{\alpha}_{\mathrm{aniso}})} \end{aligned} \tag{3.19}$$

considering the motor phase current and capacitor current harmonic quality, respectively.

Fig. 3.25 illustrates the signal flow diagram of the calculation of $I_{\mathrm{s,THD,dif}}$, $I_{\mathrm{s,THD,dev}}$, $I_{\mathrm{c/4,RMS,dif}}$ and $I_{\mathrm{c/4,RMS,dev}}$. The motor reference currents $\boldsymbol{i}^k_{\mathrm{s,ref}}$ are chosen from LUTs according to the motor operating point (T, n_{m}) (see Fig. 2.8). The motor magnetic characteristics, i.e. $\boldsymbol{L}^k_{\mathrm{s}}$, ψ_{PM} and λ, depend on the motor phase currents $\boldsymbol{i}^k_{\mathrm{s,ref}}$ in the dq-frame. The phase voltages can then be determined using the PMSM voltage equations in steady-state operation, i.e.

$$\boldsymbol{u}^k_{\mathrm{s,ref}} = \begin{bmatrix} R_{\mathrm{s}} & -\omega_{\mathrm{r}} L^q_{\mathrm{s}} \\ \omega_{\mathrm{r}} L^d_{\mathrm{s}} & R_{\mathrm{s}} \end{bmatrix} \boldsymbol{i}^k_{\mathrm{s,ref}} + \begin{pmatrix} 0 \\ \omega_{\mathrm{r}} \psi_{\mathrm{PM}} \end{pmatrix}. \tag{3.20}$$

The optimized inverter switching angles are chosen based on the values of m, θ_{u} and λ. The motor phase current harmonic distortion factors can then be calculated using (2.88) and (3.18), while (2.84) and (3.19) are used for the computation of $I_{\mathrm{c/4,RMS,dif}}$ and $I_{\mathrm{c/4,RMS,dev}}$. This procedure is repeated for each motor torque $T \in [0, 250]$ Nm and speed $n_{\mathrm{m}} \in [4000, 12000]$ rpm (since the SVM scheme is employed for $n_{\mathrm{m}} < 4\,000$ rpm) with a step of 2 Nm and 100 rpm, respectively.

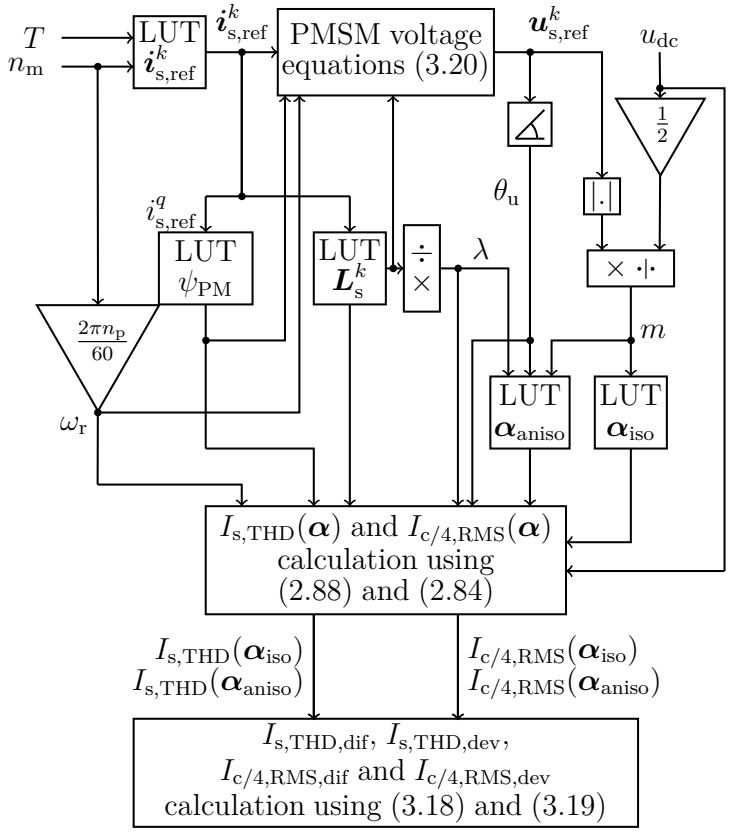

Figure 3.25: *Signal flow diagram of the calculation of* $I_{\mathrm{s,THD,dif}}$, $I_{\mathrm{s,THD,dev}}$, $I_{\mathrm{c/4,RMS,dif}}$ *and* $I_{\mathrm{c/4,RMS,dev}}$.

Fig. 3.26a and Fig. 3.26b depict the resulting $I_{\mathrm{s,THD}}(\boldsymbol{\alpha}_{\mathrm{iso}})$ and $I_{\mathrm{s,THD}}(\boldsymbol{\alpha}_{\mathrm{aniso}})$ when the optimized angles of an isotropic and anisotropic motor are utilized for an anisotropic machine, while Fig. 3.26c and Fig. 3.26d illustrate the resulting difference $I_{\mathrm{s,THD,dif}}$ and percentage deviation $I_{\mathrm{s,THD,dev}}$, respectively. A discontinuity can be observed at $n_{\mathrm{m}} = 9\,000$ rpm, since the pulse number changes at this location from $q = 9$ to $q = 5$ (see Fig. 2.5). The most important observation, when looking at Fig. 3.26c and Fig. 3.26d, is that $I_{\mathrm{s,THD,dif}} > 0$ and $I_{\mathrm{s,THD,dev}} > 0$, i.e. $I_{\mathrm{s,THD}}(\boldsymbol{\alpha}_{\mathrm{aniso}}) < I_{\mathrm{s,THD}}(\boldsymbol{\alpha}_{\mathrm{iso}})$, in the whole operating range. In other words, the performance of $\boldsymbol{\alpha}_{\mathrm{aniso}}$ is superior to that of $\boldsymbol{\alpha}_{\mathrm{iso}}$, considering the motor current harmonic quality. This is expected, since the current harmonic content is subject of minimization and the used motor is

anisotropic. The relative deviation between $I_{\mathrm{s,THD}}(\boldsymbol{\alpha}_{\mathrm{aniso}})$ and $I_{\mathrm{s,THD}}(\boldsymbol{\alpha}_{\mathrm{iso}})$ can reach values of 26% and their maximum difference can be up to 2.94% in some operating points.

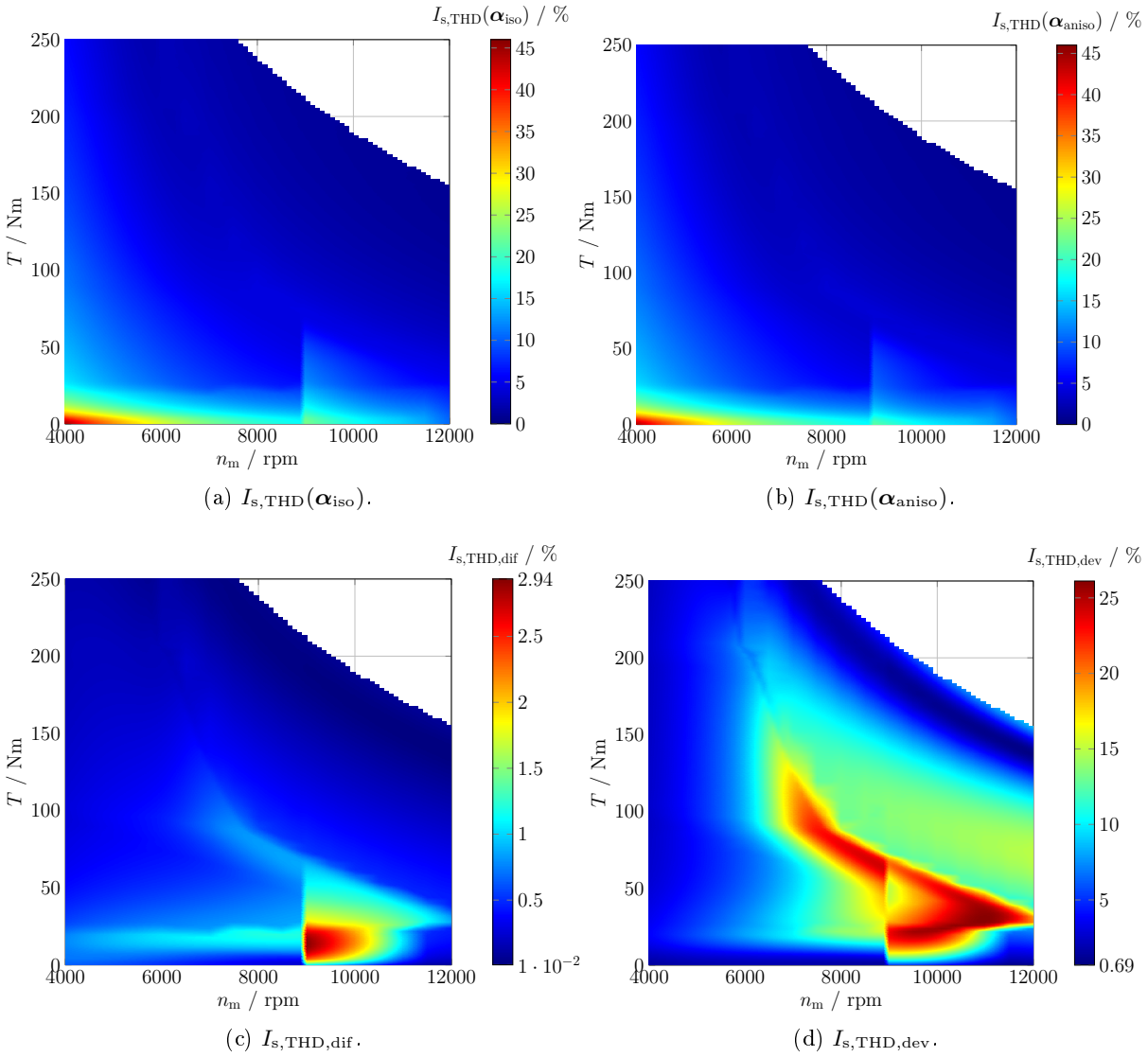

(a) $I_{\mathrm{s,THD}}(\boldsymbol{\alpha}_{\mathrm{iso}})$.

(b) $I_{\mathrm{s,THD}}(\boldsymbol{\alpha}_{\mathrm{aniso}})$.

(c) $I_{\mathrm{s,THD,dif}}$.

(d) $I_{\mathrm{s,THD,dev}}$.

Figure 3.26: *Evaluation of the optimization results considering the motor current harmonic distortion.*

Fig. 3.27 depicts the dc-link capacitor current harmonic distortion factors $I_{\mathrm{c/4,RMS}}(\boldsymbol{\alpha}_{\mathrm{iso}})$, $I_{\mathrm{c/4,RMS}}(\boldsymbol{\alpha}_{\mathrm{aniso}})$, $I_{\mathrm{c/4,RMS,dif}}$ and $I_{\mathrm{c/4,RMS,dev}}$. It can be seen that the angles $\boldsymbol{\alpha}_{\mathrm{iso}}$ outperform $\boldsymbol{\alpha}_{\mathrm{aniso}}$ in some operating regions. Neither $\boldsymbol{\alpha}_{\mathrm{aniso}}$ nor $\boldsymbol{\alpha}_{\mathrm{iso}}$ are the optimal ones in the whole operating range as far as the dc-link capacitor current ripple is concerned. This is expected, since the optimization algorithm seeks to find the optimal pulse pattern which minimizes the harmonic content of the machine current and not of the dc-link capacitor current. The deviation between $I_{\mathrm{c/4,RMS}}(\boldsymbol{\alpha}_{\mathrm{aniso}})$ and $I_{\mathrm{c/4,RMS}}(\boldsymbol{\alpha}_{\mathrm{iso}})$ can reach values of more than $\pm 15\%$ in some OPs. This feature indicates that the pulse pattern $\boldsymbol{\alpha}_{\mathrm{aniso}}$, although optimal regarding the IPMSM current harmonic content, may cause increased current stress in the dc-link. Hence, a careful choice of the objective function in SOPWM is of outmost importance.

The above outcomes will be validated by experimental results presented in the next subsection (see Sec. 3.4.2).

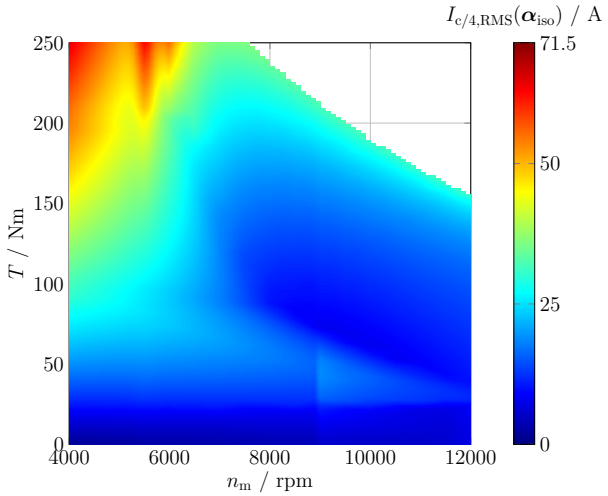

(a) $I_{c/4,RMS}(\boldsymbol{\alpha}_{iso})$.

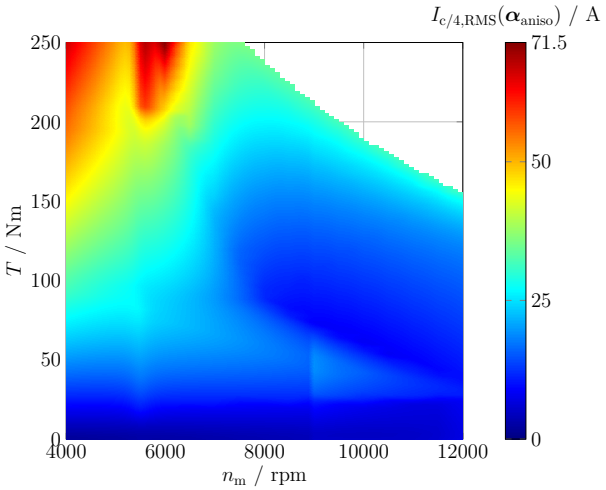

(b) $I_{c/4,RMS}(\boldsymbol{\alpha}_{aniso})$.

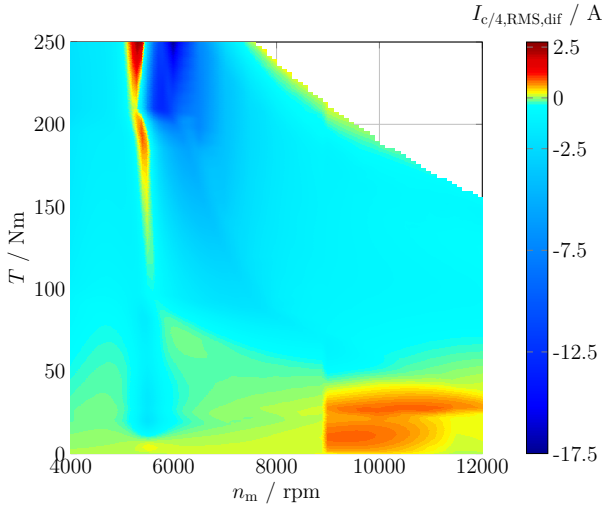

(c) $I_{c/4,RMS,dif}$.

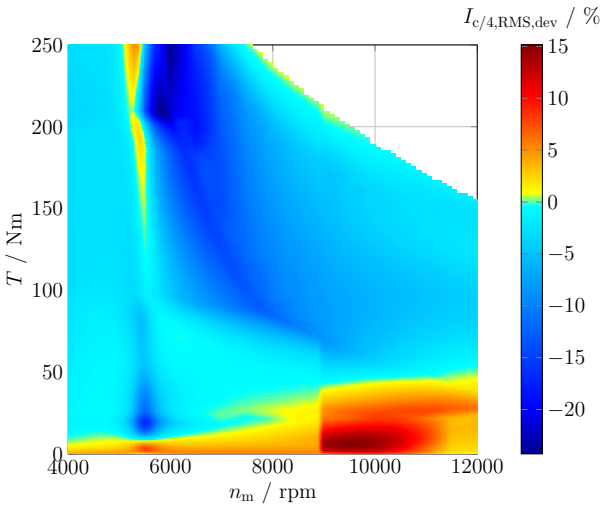

(d) $I_{c/4,RMS,dev}$.

Figure 3.27: *Evaluation of the optimization results considering the RMS value of the dc-link capacitor current.*

3.4.2 Experimental verification

In Sec. 3.4.1, the harmonic distortions of the machine phase current and dc-link capacitor current have been numerically determined for each motor operating point using the optimized pulse patterns of an isotropic and anisotropic motor. The conclusion has been drawn, that the motor current quality can be improved by up to 26 % when taking the motor anisotropic properties into account in the optimization of the inverter pulse patterns. As far as the dc-link capacitor harmonic content is concerned, operating points exist where the isotropic angles outperform the anisotropic ones. In this subsection, experimental results of eight motor operating points (OPs) will be presented in order to validate the above statements.

It should be noted, that the modulation index m and the voltage phase angle θ_u of the theoretical analysis (see Fig. 3.25) have been specified using the reference voltages $\boldsymbol{u}^k_{\mathrm{s,ref}}$ (see (3.20)). However, the actual voltages $\boldsymbol{u}^k_{\mathrm{s,1}} = \boldsymbol{u}^k_{\mathrm{s,PI}} + \boldsymbol{u}^k_{\mathrm{s,FF}}$ (see Fig. 3.1) of the experimental analysis may differ from $\boldsymbol{u}^k_{\mathrm{s,ref}}$ at each OP due to possible inaccuracies in the LUTs of $\boldsymbol{i}^k_{\mathrm{s,ref}}$, ψ_PM and $\boldsymbol{L}^k_\mathrm{s}$. For instance, the PM flux linkage ψ_PM and the stator resistance R_s are temperature dependent, whereas the used LUT for ψ_PM contains the results of the finite element analysis for a constant PM temperature of 20°C. Furthermore, a constant $R_\mathrm{s} = 5\,\mathrm{m\Omega}$ is utilized, specified at 20°C operational temperature of stator winding. These inaccuracies are corrected in the closed-loop control scheme by the PI current controllers, whose outputs $\boldsymbol{u}^k_{\mathrm{s,PI}}$ are added to $\boldsymbol{u}^k_{\mathrm{s,FF}}$. As a consequence, the used optimized switching angles of the theoretical and experimental analysis may differ in each motor operating point. For this reason, experiments have been performed and the parameters $\boldsymbol{\alpha}$, m and θ_u of each OP have been saved. Using these parameters, the machine phase and dc-link capacitor current have been again numerically determined in time and frequency domain. The results are presented in this subsection.

Table 3.3 summarizes the parameters of each OP. The choice of each OP has been done considering the following facts:

- The factors $I_\mathrm{s,THD,dif}$ and $I_\mathrm{s,THD,dev}$ are considerably high in the low torque - high speed operating region (see Fig. 3.26), which implies that the optimized angles of an anisotropic motor lead to a significantly improved motor current quality in this region compared to those of an isotropic motor.

- An electric vehicle is usually operated in the low torque region, while it is driven at higher torques only during de- or acceleration. The maximum rated power of the motor is 74 kW at 6 000 rpm and lower at different speeds. Hence, this project focuses on optimizing the vehicle performance in the low torque region.

- Operating points with similar modulation indices but different anisotropic factors have been chosen, so that the influence of the motor magnetic anisotropy on the optimization results can be evaluated.

Fig. 3.28 to Fig. 3.35 present the measured and calculated motor phase current i^u_s, while Fig. 3.36 to Fig. 3.43 depict the measured and calculated current in one of the four dc-link capacitors $i_{\mathrm{c}/4}$ in time and frequency domain in each OP. The inverter is operated using both pulse patterns $\boldsymbol{\alpha}_\mathrm{iso}$ and $\boldsymbol{\alpha}_\mathrm{aniso}$. Equations (2.60) and (2.83) are employed for the calculation of i^u_s and $i_{\mathrm{c}/4} := i_\mathrm{c}/4$, respectively, by summing the first 600 harmonics of each signal. The difference between the measured and calculated harmonic magnitudes of the motor phase current

$$i^u_{\mathrm{s},\nu,\mathrm{dif}} := i^u_{\mathrm{s},\nu}\big|_\mathrm{measured} - i^u_{\mathrm{s},\nu}\big|_\mathrm{calculated} \tag{3.21}$$

for $\nu = 6i \pm 1$ ($i \in \mathbb{N}$) and capacitor current

$$i_{\mathrm{c}/4,\nu,\mathrm{dif}} = i_{\mathrm{c}/4,\nu}\big|_{\mathrm{measured}} - i_{\mathrm{c}/4,\nu}\big|_{\mathrm{calculated}} \tag{3.22}$$

for $\nu = 6i$ ($i \in \mathbb{N}$) can also be seen in the subplots below. Table 3.4 summarizes the calculated and measured motor current harmonic distortion and dc-link capacitor RMS current in each motor operating point. These values have been specified considering the first 600 harmonic components of each signal.

As shown in Fig. 3.26, the optimized angles $\boldsymbol{\alpha}_{\mathrm{aniso}}$ are superior to $\boldsymbol{\alpha}_{\mathrm{iso}}$ in the low torque motor operating range considering the machine current harmonic distortion. In order to verify these theoretical results, experiments have been conducted in OP1 (20 Nm, 4 500 rpm), OP2 (20 Nm, 6 400 rpm), OP4 (20 Nm, 8 500 rpm) and OP7 (20 Nm, 10 850 rpm). The machine phase currents are depicted in Fig. 3.28, Fig. 3.29, Fig. 3.31 and Fig. 3.34, respectively. Observing the measures $I_{\mathrm{s,THD,dif}}$ and $I_{\mathrm{s,THD,dev}}$ in these OPs (see Table 3.4), it can be concluded, that the motor harmonic content has been significantly decreased by the operation of the inverter with the angles $\boldsymbol{\alpha}_{\mathrm{aniso}}$. Especially in OP7, we have $I_{\mathrm{s,THD,dif}} = 2.482\%$ and $I_{\mathrm{s,THD,dev}} = 26.668\%$.

Operating points with similar modulation indices but different anisotropic factors have also been chosen, so that the influence of the motor magnetic anisotropy on the optimization results can be evaluated. The modulation index has similar values in OP2-OP3 and OP4-OP6, as can be seen in Table 3.3. Since the optimized switching angles of an isotropic motor depend solely on the modulation index, they are similar in these OPs. On the contrary, the optimized angles of an anisotropic motor depend also on θ_{u} and λ and, thus, are different in all OPs. The motor phase current harmonic distortion is decreased in all OPs when the angles $\boldsymbol{\alpha}_{\mathrm{aniso}}$ are utilized (see Table 3.4). Moreover, the relative percentage deviation $I_{\mathrm{s,THD,dev}}$ is not the same in OP2 and OP3 (i.e. in OP4, OP5 and OP6), since the values of θ_{u} and λ change. This feature indicates that the expected improvement in the current quality using $\boldsymbol{\alpha}_{\mathrm{aniso}}$ and not $\boldsymbol{\alpha}_{\mathrm{iso}}$ depends on the machine magnetic properties in the selected OPs.

Fig. 3.36 to Fig. 3.43 illustrate the dc-link capacitor current in the different OPs. The main observation is, that the dc-link capacitor current quality is improved by using $\boldsymbol{\alpha}_{\mathrm{aniso}}$ in the low torque - high speed region and, especially, in the region where $q = 5$ pulses are utilized over an electrical period (see $I_{\mathrm{c}/4,\mathrm{RMS,dif}} = 0.642\,\mathrm{A}$ and $I_{\mathrm{c}/4,\mathrm{RMS,dev}} = 8.768\%$ in OP7). On the contrary, the opposite is true for higher torques (see $I_{\mathrm{c}/4,\mathrm{RMS,dif}} = -1.314\,\mathrm{A}$ and $I_{\mathrm{c}/4,\mathrm{RMS,dev}} = -12.993\%$ in OP8). The same conclusion can be drawn by the theoretical analysis presented in Fig. 3.27. This feature implies that minimizing the harmonic content of the motor phase current may lead to increased dc-link capacitor current ripple. For this reason, the objective function in SOPWM must be chosen carefully. If the improvement of the overall drive system's performance is desired, the thermal stress on both VSI and IPMSM must be considered.

In OP8, the inverter is operated in the overmodulation region, since $m = 1.2$. This operating point cannot be reached with SVM, since the maximum modulation index is equal to 1.155 in SVM [3]. This proves the better dc-link voltage utilization capability of SOPWM in contrast to SVM.

Lastly, the Fourier spectra of the calculated and measured signals have been included in order to validate the correctness of (2.60) and (2.83). It should be mentioned, that a comparison between the harmonic spectra of the measured and calculated signals is preferred over a comparison of the resulting harmonic distortion factors. This is due to the significant amount of noise contained in the measured signals which is not present in the calculated ones. The distortion factors of the measured signals are specified considering the first 600 harmonics including noise. For this reason, they are higher than the calculated ones in most OPs. Nevertheless, comparing the measured signals in both time and frequency domain with the calculated ones, the conclusion can be made,

that the error between them is rather small in all OPs. The deviations between the theoretical and experimental analysis are due to the following reasons:

- The assumptions (A1) to (A6) have been made in the derivation of (2.60) and (2.83).
- Inaccuracies may occur in the measurement of very low current harmonic amplitudes due to the limited capabilities of the current measurement system (see Table A.4).
- The exact magnetic properties of the PMSM are not known. For instance, the influence of the temperature on the PMSM magnetic properties is not considered in the calculations. The same applies also for the impedance of the test bench architecture, which is very difficult to be specified.

Table 3.3: *Parameters of each motor operating point.*

	OP1		**OP2**		**OP3**		**OP4**	
T_{ref} (in Nm)	20	20	20	20	80	80	20	20
n_{m} (in rpm)	4500	4500	6400	6400	5000	5000	8500	8500
m	0.502	0.503	0.700	0.699	0.699	0.699	0.896	0.899
θ_{u} (in rad)	1.961	1.958	2.033	2.006	2.565	2.555	2.044	2.043
$\theta_{\mathrm{u,FF}}$ (in rad)	1.944	1.944	1.939	1.939	2.499	2.499	1.939	1.939
λ	3.167	3.167	3.155	3.155	3.096	3.096	3.146	3.146
	$\boldsymbol{\alpha}_{\mathrm{iso}}$	$\boldsymbol{\alpha}_{\mathrm{aniso}}$	$\boldsymbol{\alpha}_{\mathrm{iso}}$	$\boldsymbol{\alpha}_{\mathrm{aniso}}$	$\boldsymbol{\alpha}_{\mathrm{iso}}$	$\boldsymbol{\alpha}_{\mathrm{aniso}}$	$\boldsymbol{\alpha}_{\mathrm{iso}}$	$\boldsymbol{\alpha}_{\mathrm{aniso}}$
α_1 (in rad)	0.280	0.292	0.247	0.260	0.247	0.263	0.210	0.224
α_2 (in rad)	0.339	0.362	0.334	0.353	0.334	0.385	0.326	0.333
α_3 (in rad)	1.095	1.080	1.110	1.090	1.109	1.097	1.118	1.102
α_4 (in rad)	1.296	1.298	1.251	1.251	1.251	1.254	1.201	1.202
α_5 (in rad)	1.451	1.467	1.475	1.482	1.475	1.512	1.504	1.485
α_6 (in rad)	1.661	1.675	1.631	1.636	1.631	1.659	1.607	1.584
α_7 (in rad)	1.787	1.776	1.800	1.758	1.800	1.803	1.813	1.702
α_8 (in rad)	1.996	1.969	1.955	1.896	1.955	1.946	1.915	1.790
γ (in rad)	3.685	3.746	3.679	3.727	4.240	4.311	3.677	3.700
	OP5		**OP6**		**OP7**		**OP8**	
T_{ref} (in Nm)	80	80	147	147	20	20	70	70
n_{m} (in rpm)	6400	6400	5000	5000	10850	10850	9100	9100
m	0.899	0.9	0.898	0.904	1.098	1.103	1.200	1.200
θ_{u} (in rad)	2.591	2.575	2.798	2.816	2.043	2.041	2.544	2.556
$\theta_{\mathrm{u,FF}}$ (in rad)	2.492	2.492	2.741	2.741	1.940	1.940	2.528	2.528
λ	3.090	3.090	2.923	2.923	3.136	3.136	3.088	3.088
	$\boldsymbol{\alpha}_{\mathrm{iso}}$	$\boldsymbol{\alpha}_{\mathrm{aniso}}$	$\boldsymbol{\alpha}_{\mathrm{iso}}$	$\boldsymbol{\alpha}_{\mathrm{aniso}}$	$\boldsymbol{\alpha}_{\mathrm{iso}}$	$\boldsymbol{\alpha}_{\mathrm{aniso}}$	$\boldsymbol{\alpha}_{\mathrm{iso}}$	$\boldsymbol{\alpha}_{\mathrm{aniso}}$
α_1 (in rad)	0.209	0.233	0.209	0.239	0.163	0.126	0.156	0.167
α_2 (in rad)	0.325	0.359	0.325	0.384	0.316	0.258	0.312	0.287
α_3 (in rad)	1.119	1.105	1.118	1.117	1.672	1.473	1.710	1.535
α_4 (in rad)	1.200	1.201	1.200	1.212	1.785	1.593	1.743	1.573
α_5 (in rad)	1.504	1.519	1.504	1.546	-	-	-	-
α_6 (in rad)	1.607	1.615	1.606	1.639	-	-	-	-
α_7 (in rad)	1.813	1.778	1.813	1.816	-	-	-	-
α_8 (in rad)	1.914	1.868	1.914	1.905	-	-	-	-
γ (in rad)	4.230	4.259	4.479	4.518	3.669	3.666	4.165	4.134

Table 3.4: *Motor current harmonic distortion and dc-link capacitor RMS current in each motor operating point.*

		OP1		**OP2**		**OP3**		**OP4**	
		$\boldsymbol{\alpha}_{\text{iso}}$	$\boldsymbol{\alpha}_{\text{aniso}}$	$\boldsymbol{\alpha}_{\text{iso}}$	$\boldsymbol{\alpha}_{\text{aniso}}$	$\boldsymbol{\alpha}_{\text{iso}}$	$\boldsymbol{\alpha}_{\text{aniso}}$	$\boldsymbol{\alpha}_{\text{iso}}$	$\boldsymbol{\alpha}_{\text{aniso}}$
Measured	$I_{\text{s,THD}}$ (in %)	20.298	19.554	14.129	13.066	10.649	10.511	10.588	9.218
	$I_{\text{s,THD,dif}}$ (in %)	0.744		1.063		0.138		1.370	
	$I_{\text{s,THD,dev}}$ (in %)	3.805		8.136		1.313		14.862	
	$I_{\text{c/4,RMS}}$ (in A)	8.602	8.568	9.637	9.491	25.269	25.585	9.340	9.225
	$I_{\text{c/4,RMS,dif}}$ (in A)	0.034		0.146		-0.316		0.115	
	$I_{\text{c/4,RMS,dev}}$ (in %)	0.397		1.538		-1.235		1.247	
Calculated	$I_{\text{s,THD}}$ (in %)	19.080	18.338	13.196	12.138	10.140	9.805	10.084	8.735
	$I_{\text{s,THD,dif}}$ (in %)	0.742		1.058		0.335		1.349	
	$I_{\text{s,THD,dev}}$ (in %)	4.046		8.716		3.417		15.444	
	$I_{\text{c/4,RMS}}$ (in A)	8.056	8.104	9.281	9.375	24.339	24.622	8.988	8.883
	$I_{\text{c/4,RMS,dif}}$ (in A)	-0.048		-0.094		-0.283		0.105	
	$I_{\text{c/4,RMS,dev}}$ (in %)	-0.592		-1.003		-1.149		1.182	
		OP5		**OP6**		**OP7**		**OP8**	
		$\boldsymbol{\alpha}_{\text{iso}}$	$\boldsymbol{\alpha}_{\text{aniso}}$	$\boldsymbol{\alpha}_{\text{iso}}$	$\boldsymbol{\alpha}_{\text{aniso}}$	$\boldsymbol{\alpha}_{\text{iso}}$	$\boldsymbol{\alpha}_{\text{aniso}}$	$\boldsymbol{\alpha}_{\text{iso}}$	$\boldsymbol{\alpha}_{\text{aniso}}$
Measured	$I_{\text{s,THD}}$ (in %)	6.878	6.715	6.932	6.798	11.789	9.307	4.782	4.461
	$I_{\text{s,THD,dif}}$ (in %)	0.163		0.134		2.482		0.321	
	$I_{\text{s,THD,dev}}$ (in %)	2.427		1.971		26.668		7.196	
	$I_{\text{c/4,RMS}}$ (in A)	22.188	22.579	35.280	36.033	7.964	7.322	8.799	10.113
	$I_{\text{c/4,RMS,dif}}$ (in A)	-0.391		-0.753		0.642		-1.314	
	$I_{\text{c/4,RMS,dev}}$ (in %)	-1.732		-2.090		8.768		-12.993	
Calculated	$I_{\text{s,THD}}$ (in %)	6.336	5.919	6.256	5.868	11.25	9.073	4.654	4.328
	$I_{\text{s,THD,dif}}$ (in %)	0.417		0.388		2.177		0.326	
	$I_{\text{s,THD,dev}}$ (in %)	7.045		6.612		23.994		7.532	
	$I_{\text{c/4,RMS}}$ (in A)	21.749	22.131	33.931	34.989	7.649	7.121	8.895	9.902
	$I_{\text{c/4,RMS,dif}}$ (in A)	-0.382		-1.058		0.528		-1.007	
	$I_{\text{c/4,RMS,dev}}$ (in %)	-1.726		-3.024		7.415		-10.170	

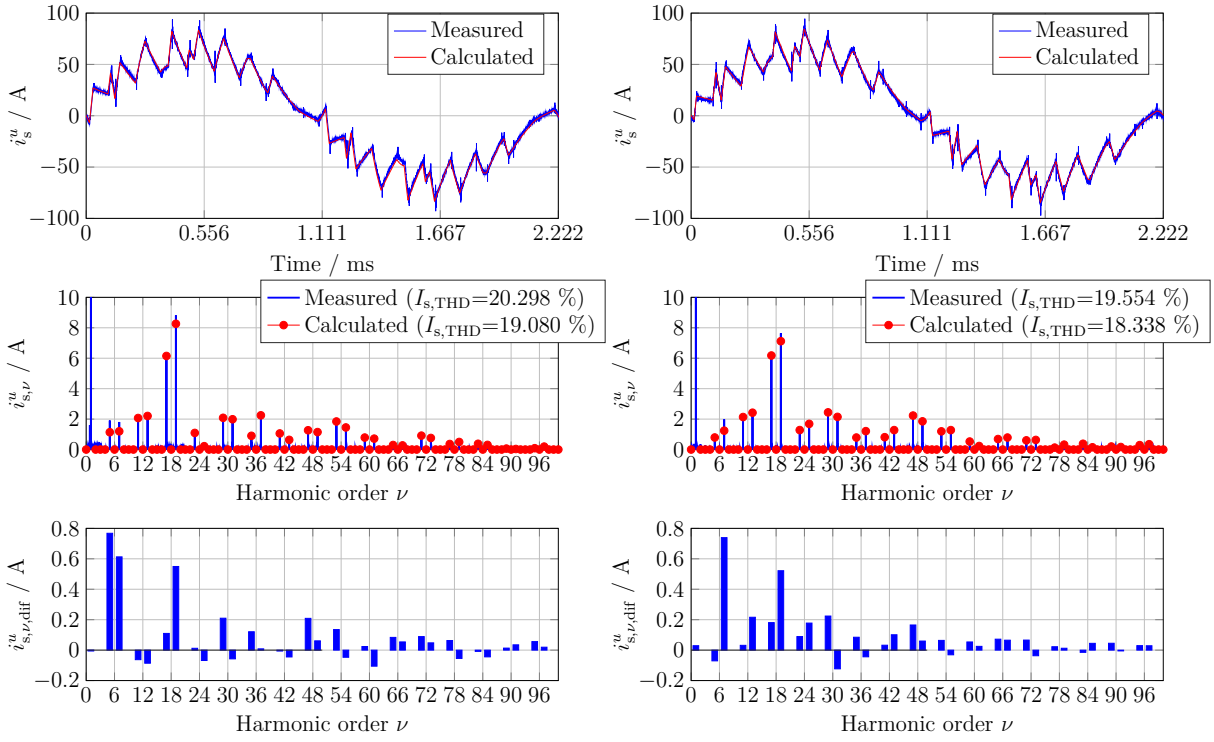

(a) $\boldsymbol{\alpha}_{\text{iso}}$. (b) $\boldsymbol{\alpha}_{\text{aniso}}$.

Figure 3.28: *Motor phase current in OP1 using the optimized switching angles (a)* $\boldsymbol{\alpha}_{\text{iso}}$ *and (b)* $\boldsymbol{\alpha}_{\text{aniso}}$.

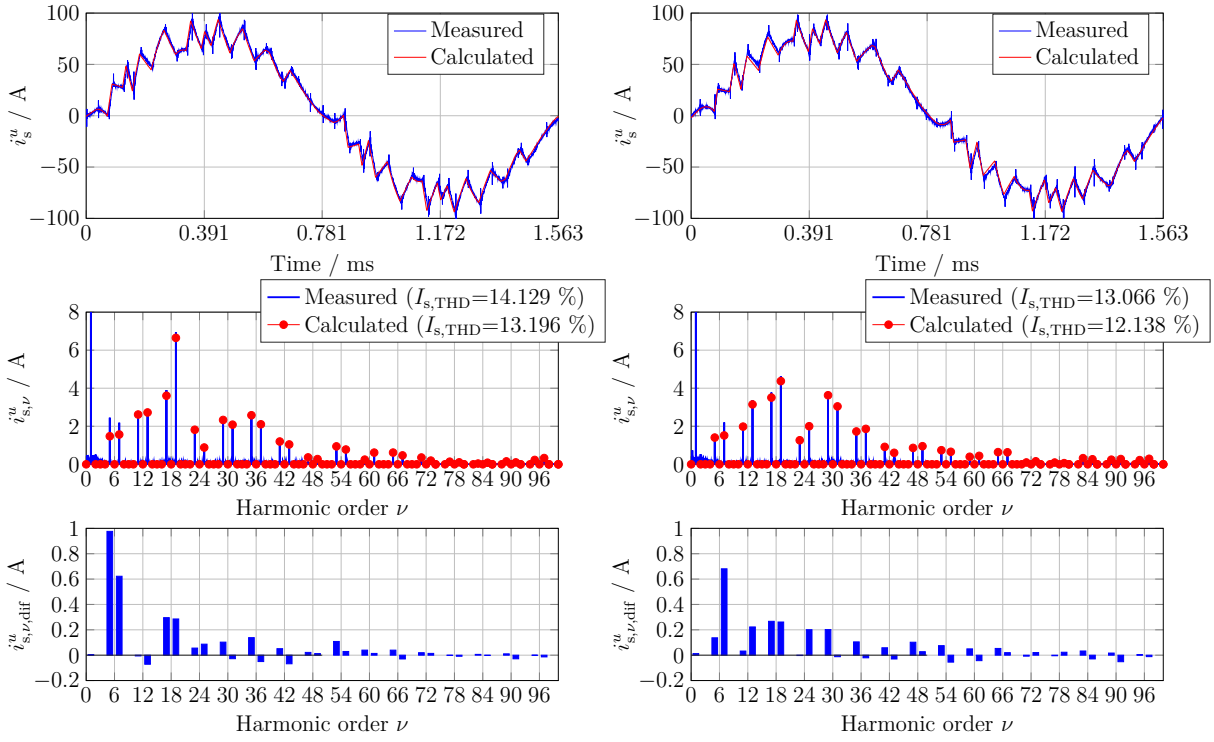

(a) $\boldsymbol{\alpha}_{\text{iso}}$. (b) $\boldsymbol{\alpha}_{\text{aniso}}$.

Figure 3.29: *Motor phase current in OP2 using the optimized switching angles (a)* $\boldsymbol{\alpha}_{\text{iso}}$ *and (b)* $\boldsymbol{\alpha}_{\text{aniso}}$.

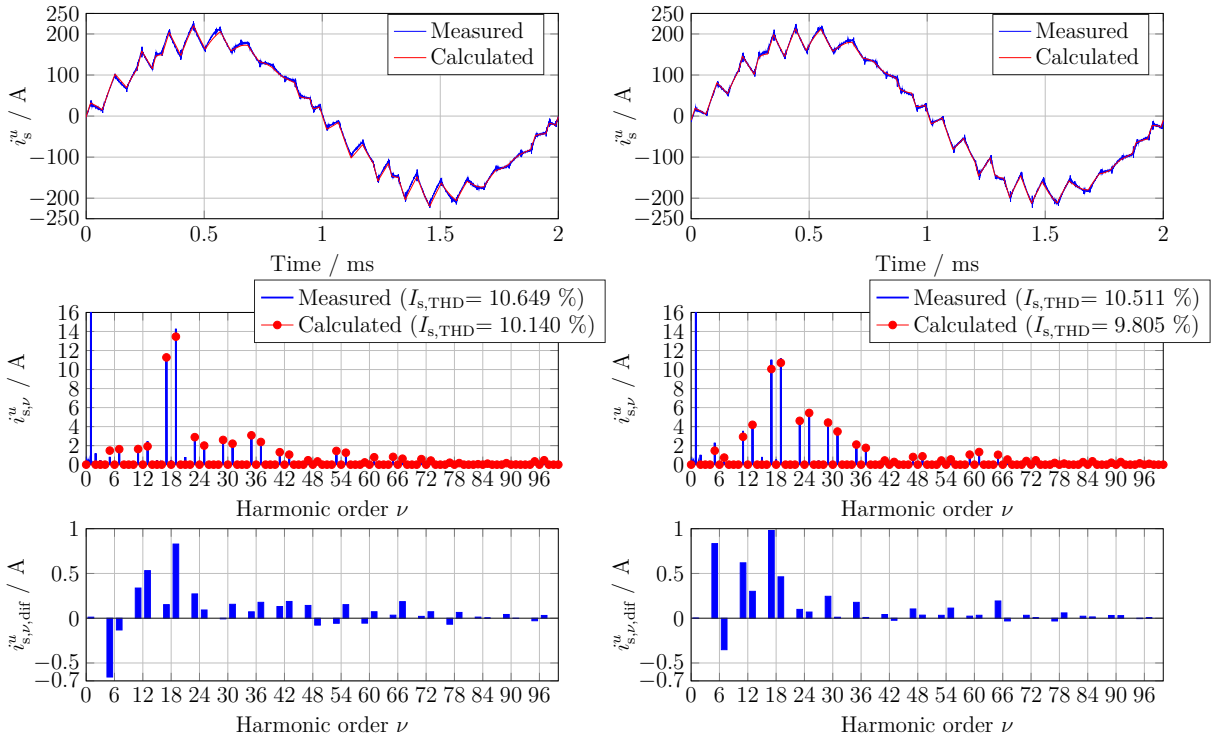

(a) $\boldsymbol{\alpha}_{\text{iso}}$. (b) $\boldsymbol{\alpha}_{\text{aniso}}$.

Figure 3.30: *Motor phase current in OP3 using the optimized switching angles (a)* $\boldsymbol{\alpha}_{\text{iso}}$ *and (b)* $\boldsymbol{\alpha}_{\text{aniso}}$.

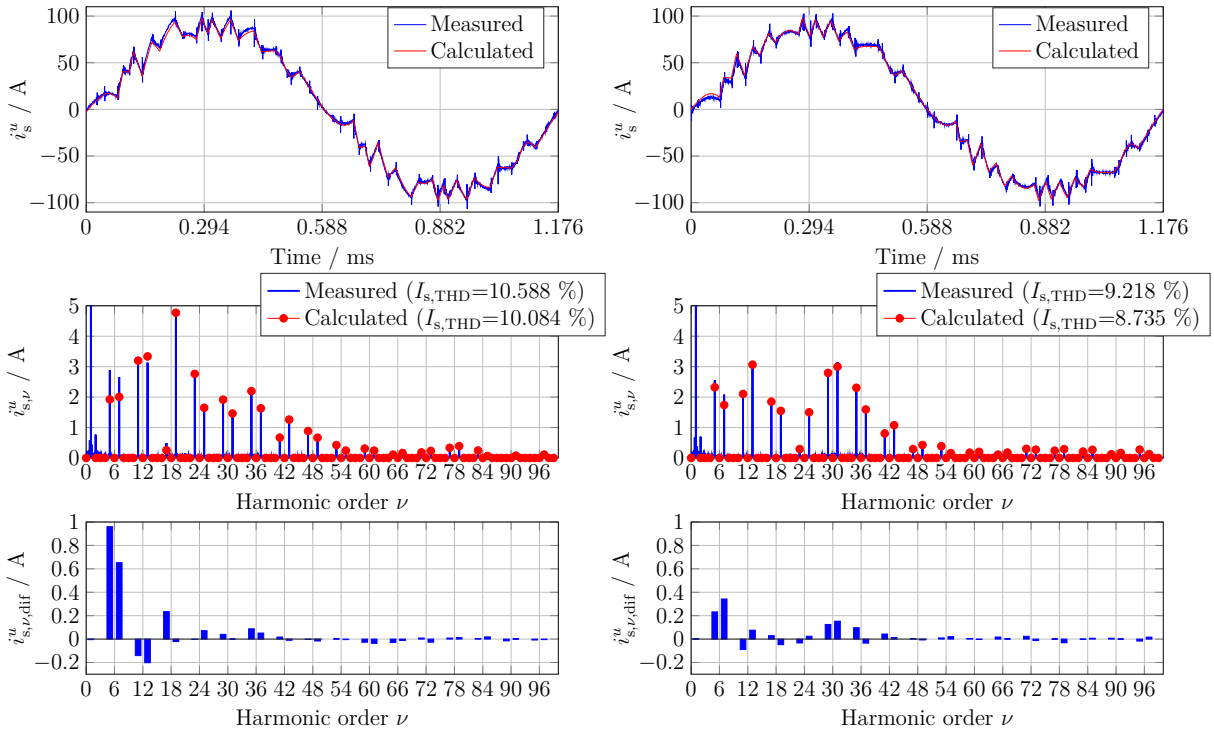

(a) $\boldsymbol{\alpha}_{\text{iso}}$. (b) $\boldsymbol{\alpha}_{\text{aniso}}$.

Figure 3.31: *Motor phase current in OP4 using the optimized switching angles (a)* $\boldsymbol{\alpha}_{\text{iso}}$ *and (b)* $\boldsymbol{\alpha}_{\text{aniso}}$.

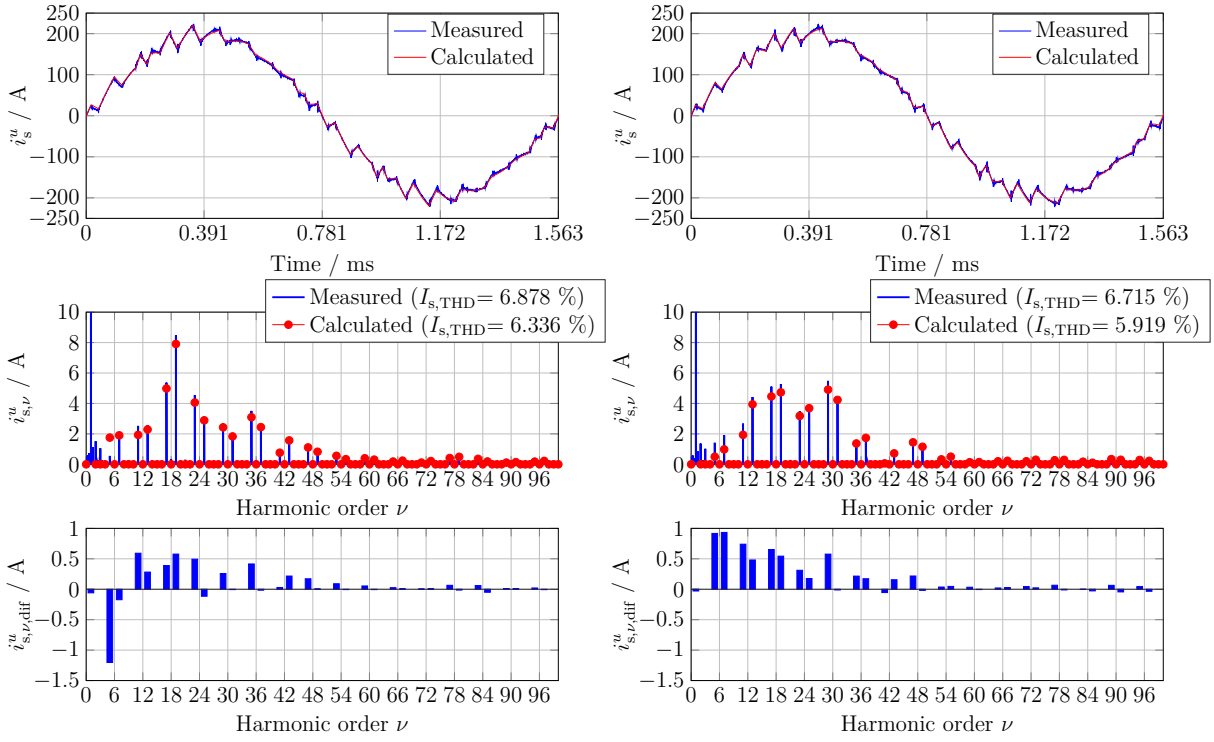

(a) $\boldsymbol{\alpha}_{\text{iso}}$. (b) $\boldsymbol{\alpha}_{\text{aniso}}$.

Figure 3.32: *Motor phase current in OP5 using the optimized switching angles (a)* $\boldsymbol{\alpha}_{\text{iso}}$ *and (b)* $\boldsymbol{\alpha}_{\text{aniso}}$.

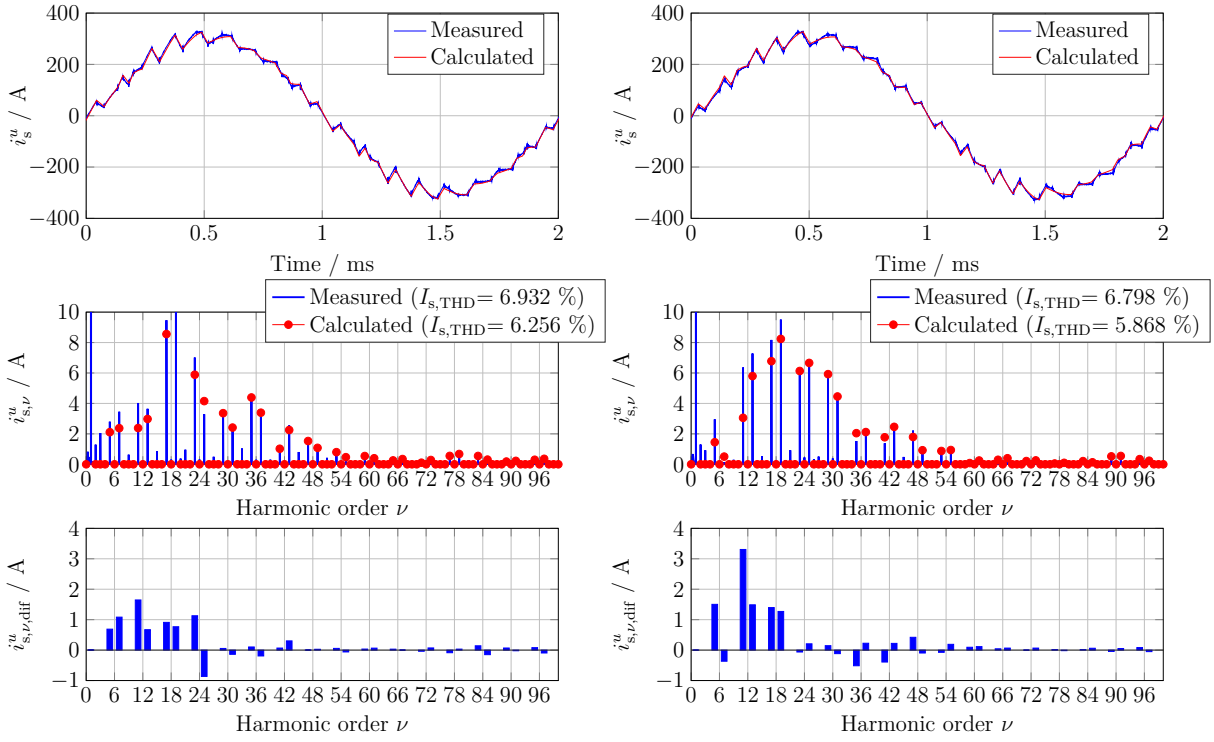

(a) $\boldsymbol{\alpha}_{\text{iso}}$. (b) $\boldsymbol{\alpha}_{\text{aniso}}$.

Figure 3.33: *Motor phase current in OP6 using the optimized switching angles (a)* $\boldsymbol{\alpha}_{\text{iso}}$ *and (b)* $\boldsymbol{\alpha}_{\text{aniso}}$.

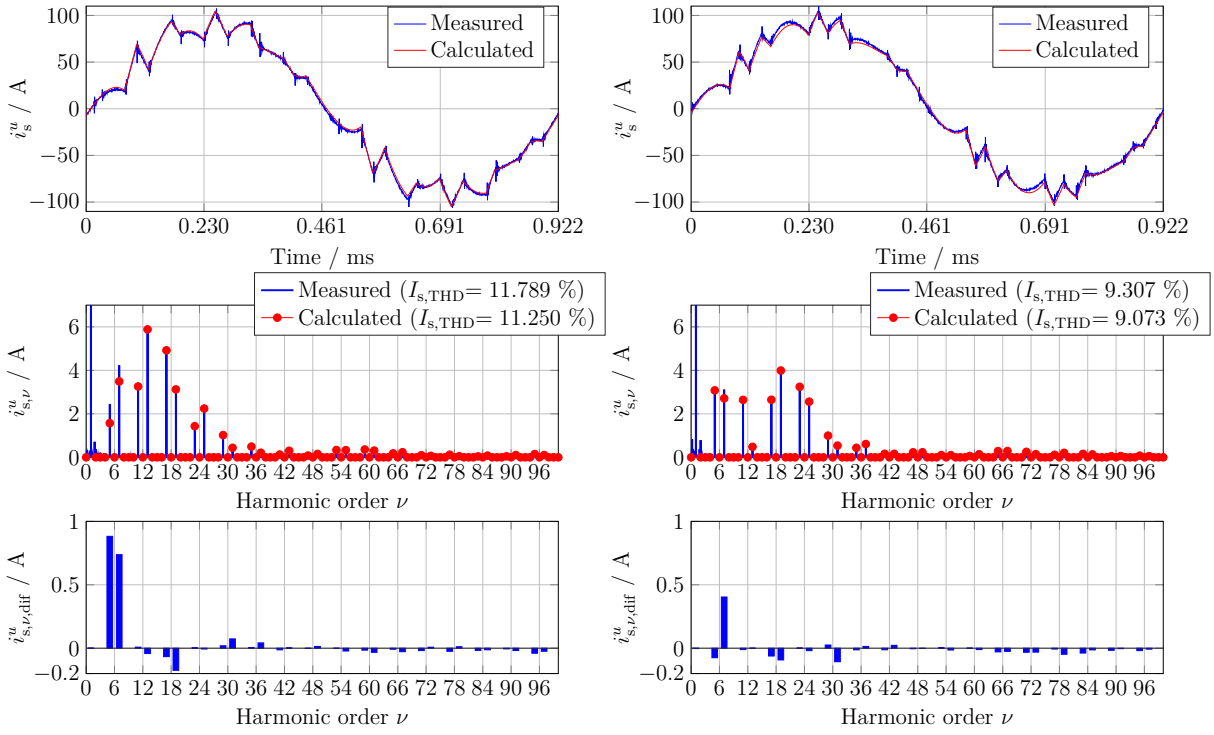

(a) $\boldsymbol{\alpha}_{\text{iso}}$. (b) $\boldsymbol{\alpha}_{\text{aniso}}$.

Figure 3.34: *Motor phase current in OP7 using the optimized switching angles (a)* $\boldsymbol{\alpha}_{\text{iso}}$ *and (b)* $\boldsymbol{\alpha}_{\text{aniso}}$.

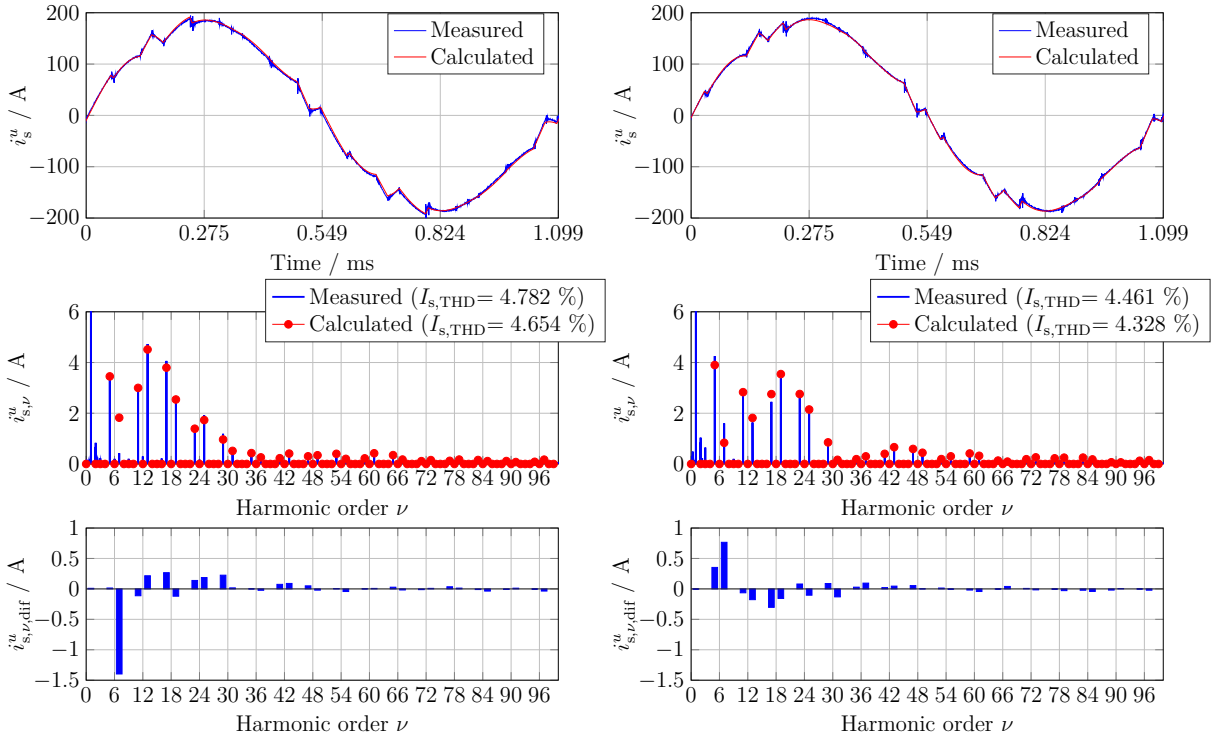

(a) $\boldsymbol{\alpha}_{\text{iso}}$. (b) $\boldsymbol{\alpha}_{\text{aniso}}$.

Figure 3.35: *Motor phase current in OP8 using the optimized switching angles (a)* $\boldsymbol{\alpha}_{\text{iso}}$ *and (b)* $\boldsymbol{\alpha}_{\text{aniso}}$.

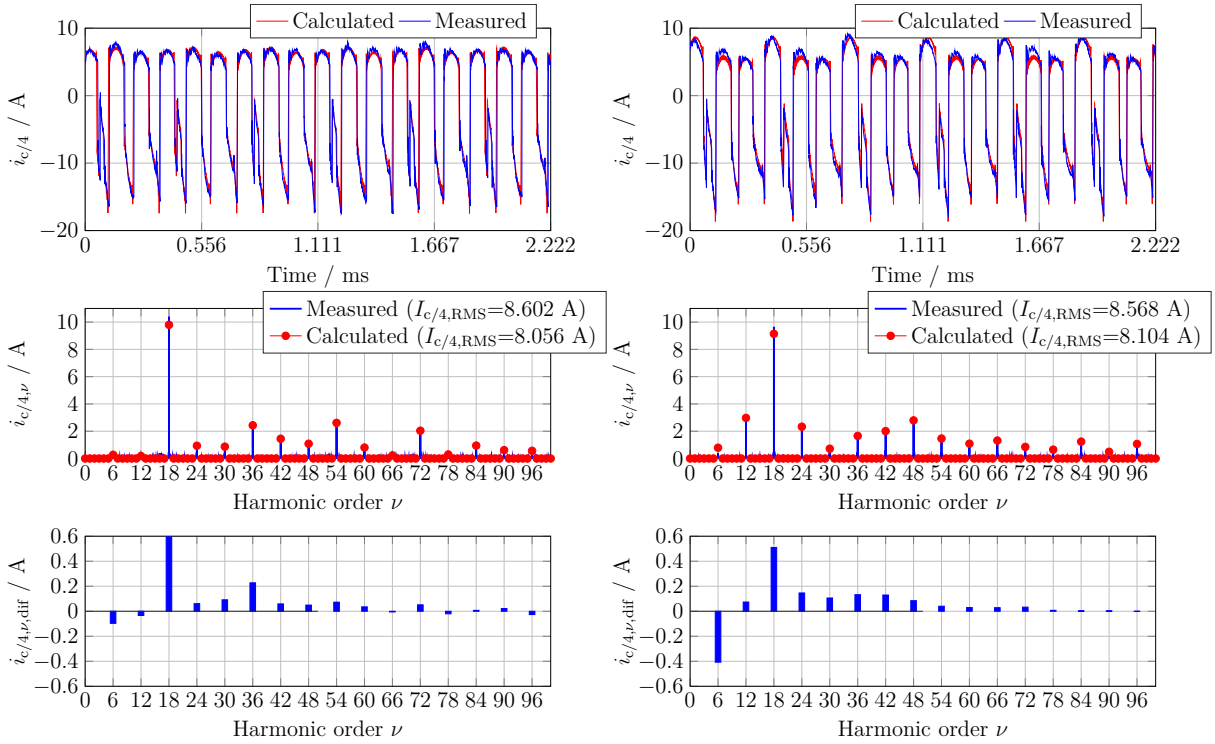

(a) $\boldsymbol{\alpha}_{\text{iso}}$. (b) $\boldsymbol{\alpha}_{\text{aniso}}$.

Figure 3.36: *Capacitor current in OP1 using the optimized switching angles (a)* $\boldsymbol{\alpha}_{\text{iso}}$ *and (b)* $\boldsymbol{\alpha}_{\text{aniso}}$.

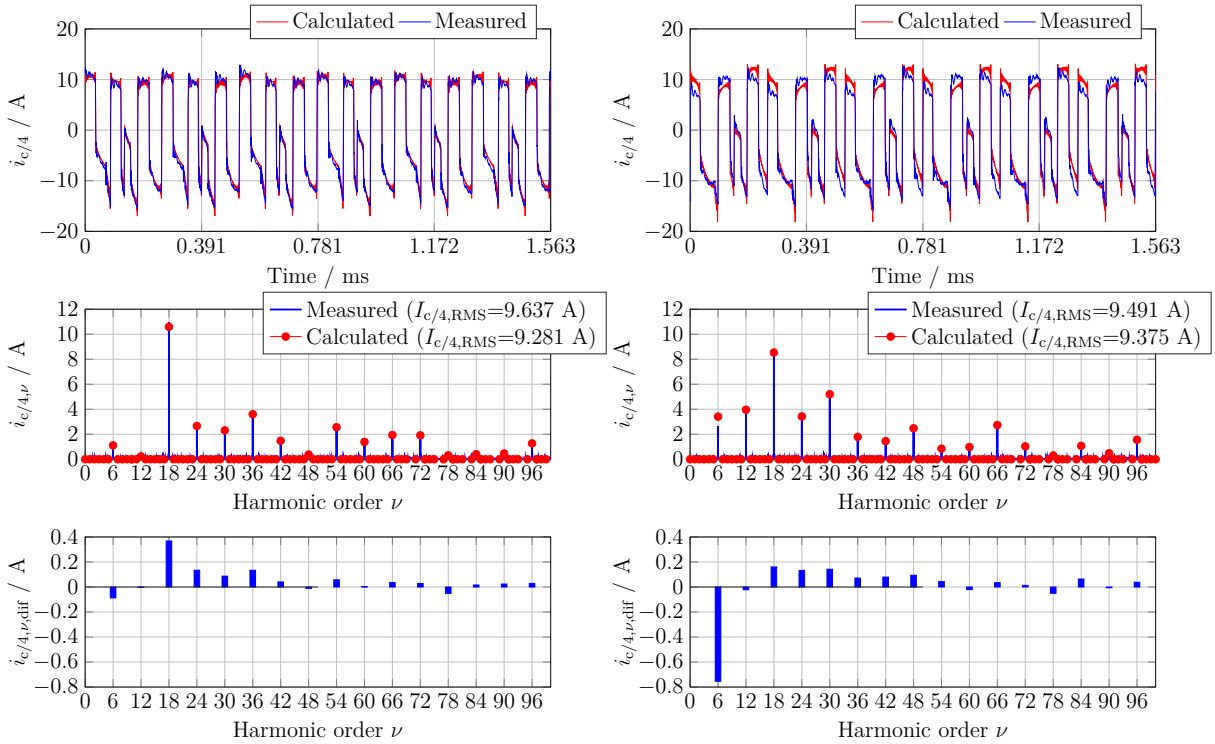

(a) $\boldsymbol{\alpha}_{\text{iso}}$. (b) $\boldsymbol{\alpha}_{\text{aniso}}$.

Figure 3.37: *Capacitor current in OP2 using the optimized switching angles (a)* $\boldsymbol{\alpha}_{\text{iso}}$ *and (b)* $\boldsymbol{\alpha}_{\text{aniso}}$.

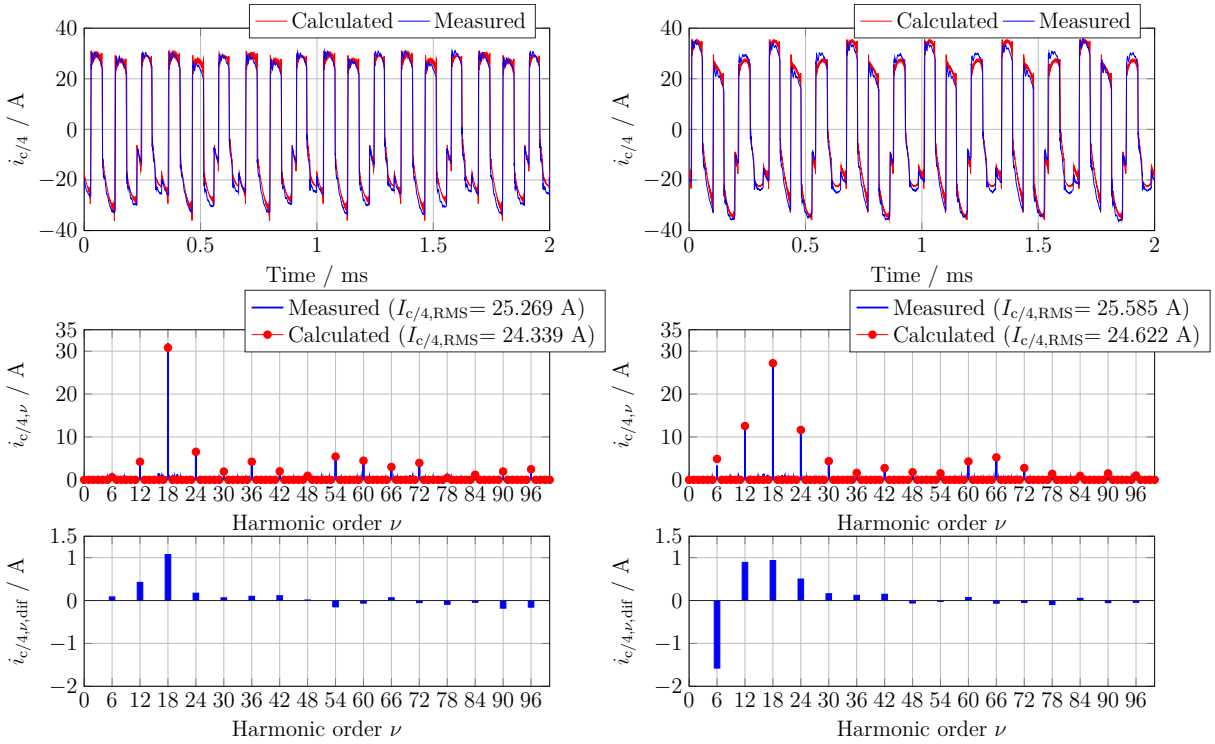

(a) $\boldsymbol{\alpha}_{\text{iso}}$. (b) $\boldsymbol{\alpha}_{\text{aniso}}$.

Figure 3.38: *Capacitor current in OP3 using the optimized switching angles (a)* $\boldsymbol{\alpha}_{\text{iso}}$ *and (b)* $\boldsymbol{\alpha}_{\text{aniso}}$.

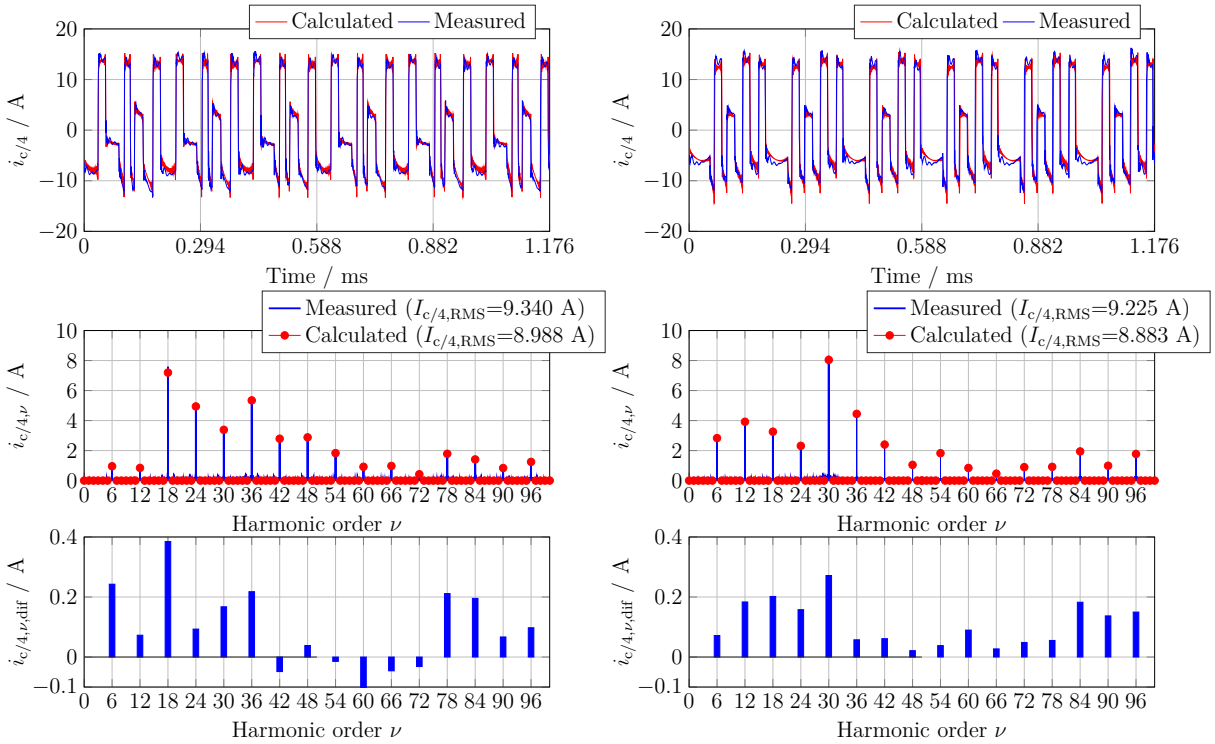

(a) $\boldsymbol{\alpha}_{\text{iso}}$. (b) $\boldsymbol{\alpha}_{\text{aniso}}$.

Figure 3.39: *Capacitor current in OP4 using the optimized switching angles (a)* $\boldsymbol{\alpha}_{\text{iso}}$ *and (b)* $\boldsymbol{\alpha}_{\text{aniso}}$.

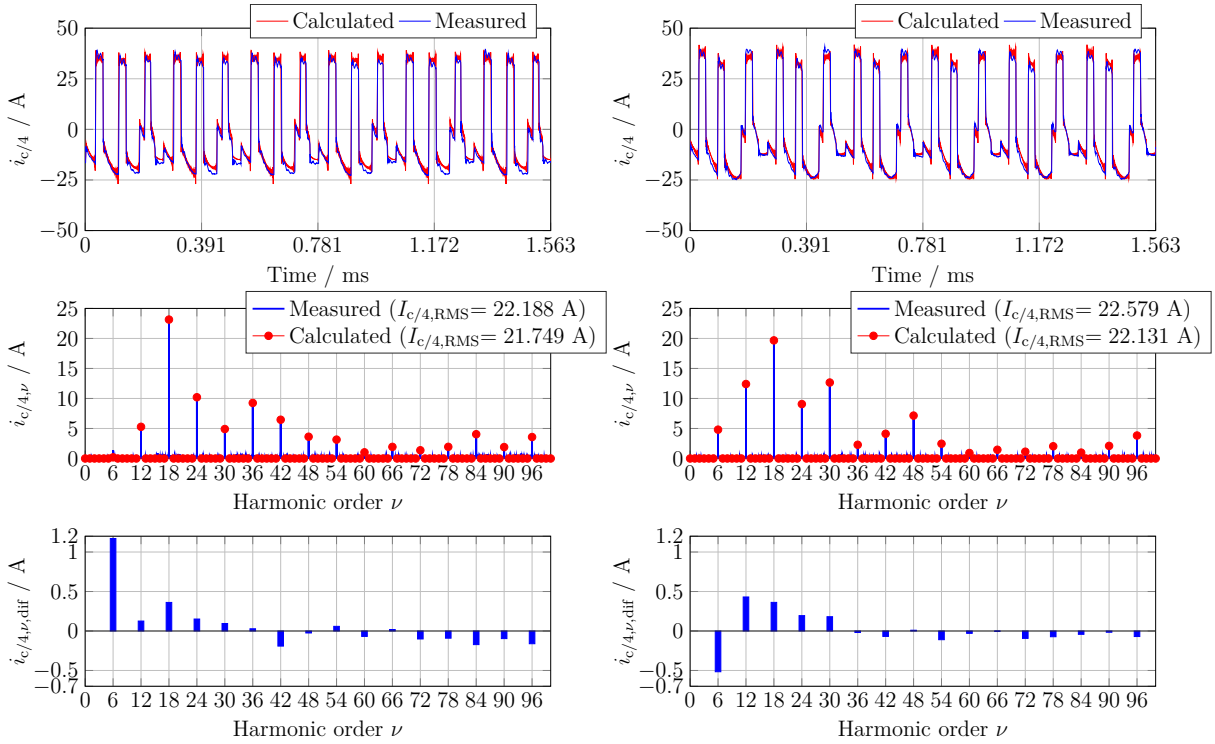

(a) $\boldsymbol{\alpha}_{\text{iso}}$. (b) $\boldsymbol{\alpha}_{\text{aniso}}$.

Figure 3.40: *Capacitor current in OP5 using the optimized switching angles (a)* $\boldsymbol{\alpha}_{\text{iso}}$ *and (b)* $\boldsymbol{\alpha}_{\text{aniso}}$.

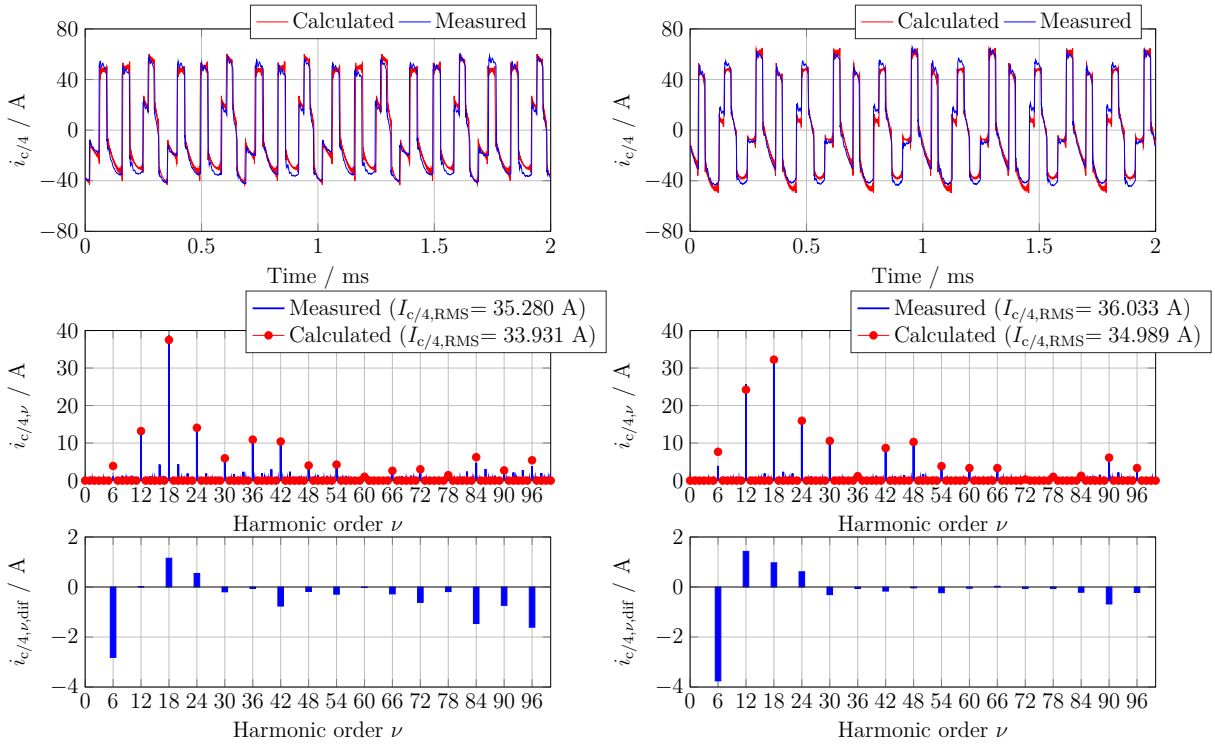

(a) $\boldsymbol{\alpha}_{\text{iso}}$. (b) $\boldsymbol{\alpha}_{\text{aniso}}$.

Figure 3.41: *Capacitor current in OP6 using the optimized switching angles (a)* $\boldsymbol{\alpha}_{\text{iso}}$ *and (b)* $\boldsymbol{\alpha}_{\text{aniso}}$.

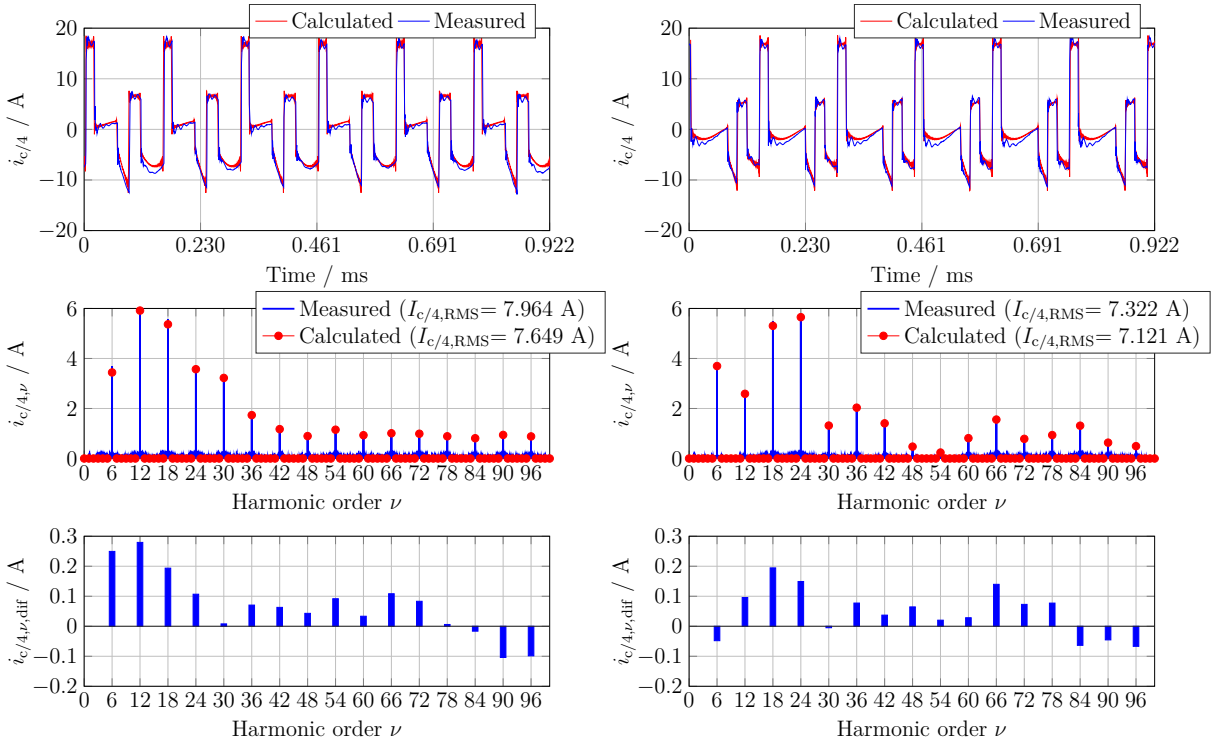

(a) $\boldsymbol{\alpha}_{\text{iso}}$. (b) $\boldsymbol{\alpha}_{\text{aniso}}$.

Figure 3.42: *Capacitor current in OP7 using the optimized switching angles (a)* $\boldsymbol{\alpha}_{\text{iso}}$ *and (b)* $\boldsymbol{\alpha}_{\text{aniso}}$.

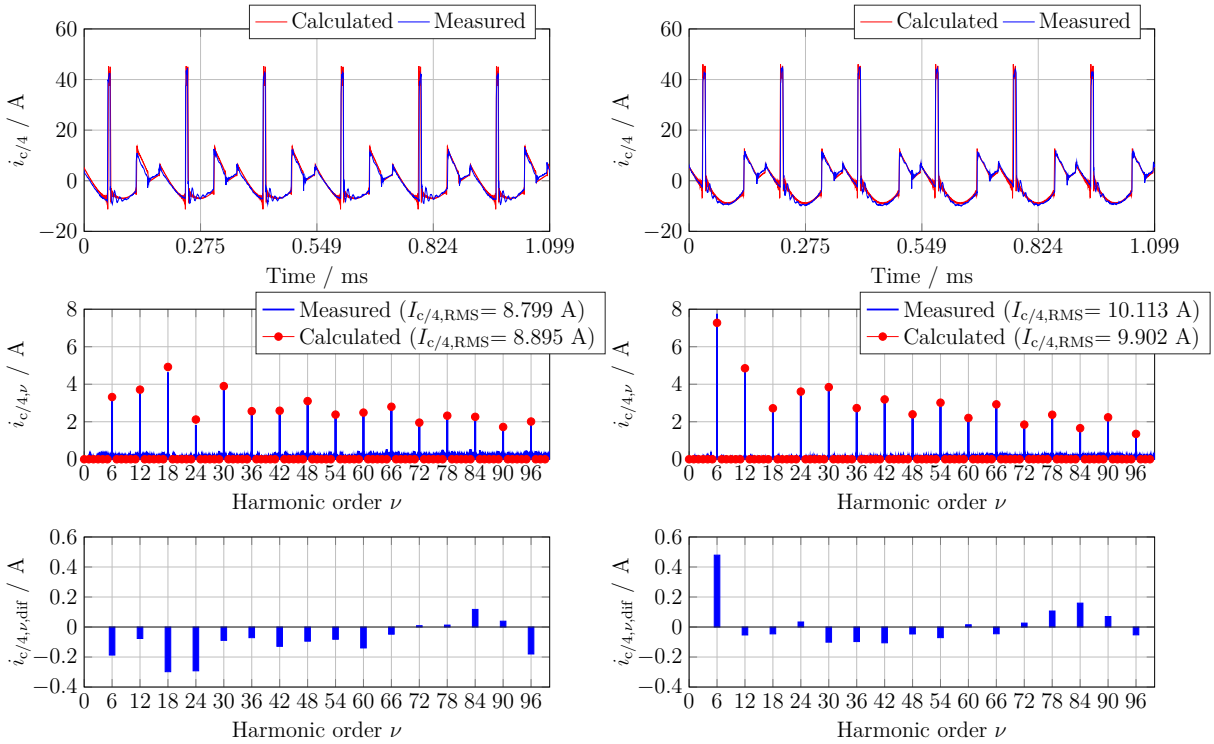

(a) $\boldsymbol{\alpha}_{\text{iso}}$. (b) $\boldsymbol{\alpha}_{\text{aniso}}$.

Figure 3.43: *Capacitor current in OP8 using the optimized switching angles (a)* $\boldsymbol{\alpha}_{\text{iso}}$ *and (b)* $\boldsymbol{\alpha}_{\text{aniso}}$.

Chapter 4

Conclusion and Outlook

In this thesis, the synchronous optimal pulsewidth modulation is employed for the control of an electrical drive system, which consists of a two-level voltage source inverter and an interior permanent magnet synchronous motor with highly operating point dependent magnetic anisotropy.

The advantage of synchronous optimal pulsewidth modulation over the conventional space vector modulation is that the inverter switching events are allowed to take place freely over an electrical period. In this way, the harmonics can be controlled so that different performance criteria can be used for optimization according to the requirements of each application. For this reason, the performance of synchronous optimal pulsewidth modulation mainly depends on the choice and a meaningful formulation of the objective function.

This thesis demonstrates that the performance optimization of an anisotropic interior permanent magnet synchronous motor yields different results from that of an isotropic permanent magnet synchronous motor or induction motor. In this thesis, the analytical expression of the interior permanent magnet synchronous motor phase currents is derived with respect to the inverter switching angles for half-wave symmetric PWM waveforms. Optimization and experimental results are presented considering magnetic saturation and cross-saturation of the motor. It is shown, that the varying anisotropic magnetic properties of the machine and the voltage phase angle have an impact on the machine current harmonic distortion. Suboptimal inverter switching angles and higher current ripple result when magnetic saturation and cross-saturation effects in the machine are neglected. The deviation of the current harmonic distortion when unity anisotropic factor is assumed in the optimization problem formulation to the actual current harmonic distortion depends on the magnetic anisotropic properties of the machine in each operating point.

The disadvantage of this formulation is that the optimization procedure is computationally more expensive, since it has to be repeated for each value of modulation index, machine anisotropic factor and voltage phase angle. Moreover, the optimized inverter switching angles must be stored in three-dimensional look up tables, which increases the hardware memory requirements. On the contrary, one-dimensional look up tables are used when the machine anisotropic properties are neglected in the optimization procedure. Thereafter, this assumption can be justified for industrial applications with limited hardware resources.

Furthermore, the influence of the inverter pulse patterns on the dc-link capacitor current ripple is studied. To this end, the analytical formulation of the dc-link capacitor current is deduced with respect to the inverter switching angles. It is demonstrated that the optimized inverter switching angles, which minimize the motor current harmonic distortion, may lead to increased harmonic currents in the dc-link capacitor. This feature indicates that the choice of objective function in the optimization problem is of crucial importance.

Lastly, the integration of the synchronous optimal pulsewidth modulation scheme into a re-

liable and robust field oriented control scheme with closed-loop current control is investigated in detail. A simple yet very effective fundamental current estimation method is proposed, which allows the implementation of synchronous optimal pulsewidth modulation without the use of a complex observer. The main feature of this method is its implementation simplicity, since the computational effort required is within the capability of a standard industrial digital signal processor system. Moreover, this method can be used also for the control of induction motor drives or inductive loads, since it is independent of the load parameters. These features make the proposed method an attractive alternative to a complex observer for industrial applications, where implementation simplicity is of outmost importance. Furthermore, experimental results demonstrate the dynamic performance of the proposed implementation, which is sufficiently high for automotive applications. Although the inverter is operated at reduced switching frequencies in synchronous optimal pulsewidth modulation in contrast to space vector modulation, a significant degradation of the current control performance is not observed.

Concluding, the better dc-link voltage utilization capability and reduced switching frequency make synchronous optimal pulsewidth modulation an attractive modulation scheme for automotive applications. The torque and power density as well as the efficiency of the drive system can be increased by employing synchronous optimal pulsewidth modulation for inverter control and, in this way, the operating range of electric vehicles can be extended.

The performance of synchronous optimal pulsewidth modulation is examined considering the motor harmonic current distortion. However, a statement regarding the efficiency of the overall drive system cannot be made, since a voltage source inverter with silicon carbide (SiC) semiconductors is utilized for the experimental measurements. For this reason, the main advantage of synchronous optimal pulsewidth modulation regarding reduced inverter switching losses cannot be experimentally confirmed. Future work will focus on testing the performance of synchronous optimal pulsewidth modulation on a voltage source inverter with insulated-gate bipolar transistors (IGBTs), conventionally used in automotive electrical drive systems. Furthermore, the switching frequencies used in this thesis may be too low and, hence, prohibited regarding motor power losses and electromagnetic compatibility. Therefore, the pulse number may need to be increased in future work. Since the improvement of the overall drive system's performance is desired, the thermal stress on both inverter and motor must be considered. For this reason, future work will focus on combining various performance criteria in order to enhance the overall system's performance as well as reduce the size and cost of the dc-link capacitor.

Bibliography

[1] International Council on Clean Transportation (ICCT), "CO_2 emission standards for passenger cars and light-commercial vehicles in the european union," Jan. 2019. [Online]. Available: https://theicct.org/sites/default/files/publications/EU-LCV-CO2-2030_ICCTupdate_201901.pdf

[2] K. Rajashekara, "Present status and future trends in electric vehicle propulsion technologies," *IEEE Journal of Emerging and Selected Topics in Power Electronics*, vol. 1, DOI 10.1109/JESTPE.2013.2259614, no. 1, pp. 3–10, Mar. 2013.

[3] A. Hava, R. Kerkman, and T. Lipo, "Carrier-based PWM-VSI overmodulation strategies: analysis, comparison, and design," *IEEE Transactions on Power Electronics*, vol. 13, DOI 10.1109/63.704136, no. 4, pp. 674–689, Jul. 1998.

[4] Y. C. Kwon, S. Kim, and S. K. Sul, "Six-step operation of PMSM with instantaneous current control," *IEEE Transactions on Industry Applications*, vol. 50, DOI 10.1109/TIA.2013.2296652, no. 4, pp. 2614–2625, Jul.-Aug. 2014.

[5] I. Boldea, L. N. Tutelea, L. Parsa, and D. Dorrell, "Automotive electric propulsion systems with reduced or no permanent magnets: An overview," *IEEE Transactions on Industrial Electronics*, vol. 61, DOI 10.1109/TIE.2014.2301754, no. 10, pp. 5696–5711, Oct. 2014.

[6] M. J. Melfi, S. Evon, and R. McElveen, "Induction versus permanent magnet motors," *IEEE Industry Applications Magazine*, vol. 15, DOI 10.1109/MIAS.2009.934443, no. 6, pp. 28–35, Nov.-Dec. 2009.

[7] P. Kshirsagar and R. Krishnan, "Implementation and experimental validation of efficiency improvement in PMSM drives through switching frequency reduction," *IEEE Applied Power Electronics Conference and Exposition (APEC)*, DOI 10.1109/APEC.2016.7468146, Mar. 2016.

[8] A. Birda, "Evaluation of various pulse width modulation strategies for the automotive sector," *Technical University of Munich (TUM)*, DOI 10.13140/RG.2.2.22090.72644, 2015.

[9] J. Holtz and X. Qi, "Optimal control of medium-voltage drives - an overview," *IEEE Transactions on Industrial Electronics*, vol. 60, DOI 10.1109/TIE.2012.2230594, no. 12, pp. 5472–5481, Dec. 2013.

[10] M. S. A. Dahidah, G. Konstantinou, and V. G. Agelidis, "A review of multilevel selective harmonic elimination PWM: Formulations, solving algorithms, implementation and applications," *IEEE Transactions on Power Electronics*, vol. 30, DOI 10.1109/TPEL.2014.2355226, no. 8, pp. 4091–4106, Aug. 2015.

[11] A. Edpuganti and A. K. Rathore, "A survey of low switching frequency modulation techniques for medium-voltage multilevel converters," *IEEE Transactions on Industry Applications*, vol. 51, DOI 10.1109/TIA.2015.2437351, no. 5, pp. 4212–4228, Sept.-Oct. 2015.

[12] L. Diao, J. Tang, P. C. Loh, S. Yin, L. Wang, and Z. Liu, "An efficient DSP-FPGA-based implementation of hybrid PWM for electric rail traction induction motor control," *IEEE Transactions on Power Electronics*, vol. 33, DOI 10.1109/TPEL.2017.2707639, no. 4, pp. 3276–3288, Apr. 2018.

[13] B. K. Bose and H. A. Sutherland, "A high-performance pulsewidth modulator for an inverter-fed drive system using a microcomputer," *IEEE Transactions on Industry Applications*, vol. IA-19, DOI 10.1109/TIA.1983.4504187, no. 2, pp. 235–243, Mar. 1983.

[14] D. Horstmann and G. Stanke, "Die stromrichternahe Antriebsregelung des Steuergerates fur Bahnautomatisierungssysteme SIBAS32," *Sonderdruck aus Elektrische Bahnen*, 1992. [Online]. Available: https://www.g-st.ch/trambasel/spezial/doku/combino/comantri.pdf

[15] J. Holtz, "Pulsewidth modulation-a survey," *IEEE Transactions on Industrial Electronics*, vol. 39, DOI 10.1109/41.161472, no. 5, pp. 410–420, Oct. 1992.

[16] J. Holtz, "Pulsewidth modulation for electronic power conversion," in *Proceedings of the IEEE*, vol. 82, DOI 10.1109/5.301684, no. 8, pp. 1194–1214, Aug. 1994.

[17] E. R. C. da Silva, E. C. dos Santos, and B. Jacobina, "Pulsewidth modulation strategies," *IEEE Industrial Electronics Magazine*, vol. 5, DOI 10.1109/MIE.2011.941120, no. 2, pp. 37–45, Jun. 2011.

[18] A. Aktaibi, M. A. Rahman, and A. Razali, "A critical review of modulation techniques," *Annual Newfoundland Electrical and Computer Eng. Conference (NECEC 2010)*, Nov. 2010.

[19] F. Jenni and D. Wüest, *Steuerverfahren für selbstgeführte Stromrichter*. vdf Hochschulverlag AG at ETH Zurich and B.G. Teubner, 1995.

[20] H. Liu, G. Cho, and S. Park, "Optimal PWM design for high power three-level inverter through comparative studies," *IEEE Transactions on Power Electronics*, vol. 10, DOI 10.1109/63.368462, no. 1, pp. 38–47, Jan. 1995.

[21] Q. K. Nguyen and J. Roth-Stielow, "Analysis and modelling of the losses for the electrical drive system of an electric vehicle," *IEEE Vehicle Power and Propulsion Conference*, DOI 10.1109/VPPC.2014.7007018, Oct. 2014.

[22] C. M. Hackl, J. Kullick, H. Eldeeb, and L. Horlbeck, "Analytical computation of the optimal reference currents for MTPC/MTPA, MTPV and MTPF operation of anisotropic synchronous machines considering stator resistance and mutual inductance," *19th European Conference on Power Electronics and Applications (EPE'17 ECCE Europe)*, DOI 10.23919/EPE17ECCEEurope.2017.8099040, Sept. 2017.

[23] A. Tripathi and G. Narayanan, "Evaluation and minimization of low-order harmonic torque in low-switching-frequency inverter-fed induction motor drives," *IEEE Transactions on Industry Applications*, vol. 52, DOI 10.1109/TIA.2015.2487447, no. 2, pp. 1477–1488, Mar.-Apr. 2016.

[24] A. Tripathi and G. Narayanan, "Torque ripple minimization in neutral-point-clamped three-level inverter fed induction motor drives operated at low-switching-frequency," *International Symposium on Power Electronics, Electrical Drives, Automation and Motion (SPEEDAM)*, DOI 10.1109/SPEEDAM.2016.7525855, Jun. 2016.

[25] M. Fakharmanesh, C. M. Hackl, and R. Perini, "Instantaneous conduction and switching losses in two-level voltage source inverters," *IEEE International Conference on Environment and Electrical Engineering*, DOI 10.1109/EEEIC.2017.7977671, Jun. 2017.

[26] W. Hassan and B. Wang, "Efficiency optimization of PMSM based drive system," *Proceedings of The 7th International Power Electronics and Motion Control Conference*, DOI 10.1109/IPEMC.2012.6258942, Jun. 2012.

[27] J. Kolar, H. Ertl, and F. Zach, "Influence of the modulation method on the conduction and switching losses of a PWM converter system," *IEEE Transactions on Industry Applications*, vol. 27, DOI 10.1109/28.108456, no. 6, pp. 1063–1075, Nov.-Dec. 1991.

[28] P. Enjeti, P. Ziogas, and J. Lindsay, "Programmed PWM techniques to eliminate harmonics: a critical evaluation," *IEEE Transactions on Industry Applications*, vol. 26, DOI 10.1109/28.54257, no. 2, pp. 302–316, Mar.-Apr. 1990.

[29] F. G. Turnbull, "Selected harmonic reduction in static D-C - A-C inverters," *IEEE Transactions on Communication and Electronics*, vol. 83, DOI 10.1109/TCOME.1964.6541241, no. 73, pp. 374–378, Jul. 1964.

[30] H. S. Patel and R. G. Hoft, "Generalized techniques of harmonic elimination and voltage control in thyristor inverters: Part i - harmonic elimination," *IEEE Transactions on Industry Applications*, vol. IA-9, DOI 10.1109/TIA.1973.349908, no. 3, pp. 310–317, May 1973.

[31] H. S. Patel and R. G. Hoft, "Generalized techniques of harmonic elimination and voltage control in thyristor inverters: Part ii - voltage control techniques," *IEEE Transactions on Industry Applications*, vol. IA-10, DOI 10.1109/TIA.1974.349239, no. 5, pp. 666–673, Sept. 1974.

[32] G. S. Buja and G. B. Indri, "Optimal pulsewidth modulation for feeding ac motors," *IEEE Transactions on Industry Applications*, vol. IA-13, DOI 10.1109/TIA.1977.4503359, no. 1, pp. 38–44, Jan. 1977.

[33] Y. Wang, X. Wen, F. Zhao, and X. Guo, "Selective harmonic elimination PWM technology applied in PMSMs," *IEEE Vehicle Power and Propulsion Conference*, DOI 10.1109/VPPC.2012.6422564, pp. 92–97, Oct. 2012.

[34] Y. Wang, X. Wen, and F. Zhao, "Vector control of six-phase PMSMs with selective harmonic elimination PWM," *IEEE Conference and Expo Transportation Electrification Asia-Pacific (ITEC Asia-Pacific)*, DOI 10.1109/ITEC-AP.2014.6940654, Aug.-Sept. 2014.

[35] F. Mink, K. Peter, H. Kasten, and S. Beineke, "Feedback control of high - speed PMSM with synchronous optimal PWM," *18th European Conference on Power Electronics and Applications (EPE'16 ECCE Europe)*, DOI 10.1109/EPE.2016.7695470, Sep. 2016.

[36] K. Peter, F. Mink, and J. Boecker, "Model-based control structure for high-speed permanent magnet synchronous drives," *IEEE International Electric Machines and Drives Conference (IEMDC)*, DOI 10.1109/IEMDC.2017.8002284, pp. 1–8, May 2017.

[37] Z. Zhang, X. Feng, and J. Xu, "Closed-loop control of PMSM based on optimal synchronous pulse patterns," *International Power Electronics and Application Conference and Exposition*, DOI 10.1109/PEAC.2014.7037940, Nov. 2014.

[38] J. Holtz, G. da Cunha, N. Petry, and P. J. Torri, "Control of large salient-pole synchronous machines using synchronous optimal pulsewidth modulation," *IEEE Transactions on Industrial Electronics*, vol. 62, DOI 10.1109/TIE.2014.2378732, no. 6, pp. 3372–3379, Jun. 2015.

[39] A. R. Rezazade, A. Sayyah, and M. Aflaki, "Modulation error observation and regulation for use in off-line optimal PWM fed high power synchronous motors," *IEEE Conference on Industrial Electronics and Applications*, DOI 10.1109/ICIEA.2006.257214, May 2006.

[40] A. Sayyah, M. Aflaki, and A. Rezazade, "Application of optimal PWM of induction motor in synchronous machines at high power ratings," *IEEE/ASME international conference on advanced intelligent mechatronics*, DOI 10.1109/AIM.2007.4412591, Sept. 2007.

[41] Z. Zhang, X. Ge, Z. Tian, X. Zhang, Q. Tang, and X. Feng, "A PWM for minimum current harmonic distortion in metro traction PMSM with saliency ratio and load angle constrains," *IEEE Transactions on Power Electronics*, vol. 33, DOI 10.1109/TPEL.2017.2723480, no. 5, pp. 4498–4511, May 2018.

[42] M. S. A. Dahidah, G. Konstantinou, N. Flourentzou, and V. G. Agelidis, "On comparing the symmetrical and non-symmetrical selective harmonic elimination pulse-width modulation technique for two-level three-phase voltage source converters," *IET Power Electronics*, vol. 3, DOI 10.1049/iet-pel.2009.0306, no. 6, pp. 829–842, Nov. 2010.

[43] M. S. A. Dahidah and V. G. Agelidis, "Comparative evaluation of symmetrical and non-symmetrical bipolar SHE-PWM techniques," *IEEE Power Electronics Specialists Conference*, DOI 10.1109/PESC.2008.4592332, Jun. 2008.

[44] J. Wells, B. Nee, P. Chapman, and P. Krein, "Selective harmonic control: a general problem formulation and selected solutions," *IEEE Transactions on Power Electronics*, vol. 20, DOI 10.1109/TPEL.2005.857541, no. 6, pp. 1337–1345, Nov. 2005.

[45] J. Wells, P. Chapman, and P. Krein, "Generalization of selective harmonic control/elimination," *IEEE 36th Power Electronics Specialists Conference*, DOI 10.1109/PESC.2005.1581806, Jun. 2005.

[46] G. S. Konstantinou and V. G. Agelidis, "Bipolar switching waveform: Novel solution sets to the selective harmonic elimination problem," *IEEE International Conference on Industrial Technology*, DOI 10.1109/ICIT.2010.5472718, Mar. 2010.

[47] G. S. Konstantinou and V. G. Agelidis, "On re-examining symmetry of two-level selective harmonic elimination pwm: Novel formulations, solutions and performance evaluation," *Electric Power Systems Research*, DOI 10.1016/j.epsr.2013.11.010, Mar. 2014.

[48] F. C. Zach and H. Ertl, "Efficiency optimal control for ac drives with PWM inverters," *IEEE Transactions on Industry Applications*, vol. IA-21, DOI 10.1109/TIA.1985.349569, no. 4, pp. 987–1000, Jul. 1985.

[49] F. Zach, "Comparison of voltage and current spectra using optimized forms of inverter pulsewidth modulation," *IEEE Transactions on Power Electronics*, vol. 4, DOI 10.1109/63.21873, no. 1, pp. 64–72, Jan. 1989.

[50] J. M. D. Murphy and M. G. Egan, "A comparison of PWM strategies for inverter-fed induction motors," *IEEE Transactions on Industry Applications*, vol. IA-19, DOI 10.1109/TIA.1983.4504210, no. 3, pp. 363–369, May 1983.

[51] Y. Wang, X. Wen, X. Guo, F. Zhao, and W. Cong, "The smooth transition research of different PWM modulations for vector control of induction motor in medium voltage high power," *International Conference on Electrical Machines and Systems*, DOI 10.1109/ICEMS.2011.6073517, Aug. 2011.

[52] V. Agelidis, A. Balouktsis, I. Balouktsis, and C. Cossar, "Multiple sets of solutions for harmonic elimination PWM bipolar waveforms: analysis and experimental verification," *IEEE Transactions on Power Electronics*, vol. 21, DOI 10.1109/TPEL.2005.869752, no. 2, pp. 415–421, Mar. 2006.

[53] Y. Zhang, Z. Zhao, and J. Zhu, "A hybrid PWM applied to high-power three-level inverter-fed induction-motor drives," *IEEE Transactions on Industrial Electronics*, vol. 58, DOI 10.1109/TIE.2010.2090836, no. 8, pp. 3409–3420, Aug. 2011.

[54] W. Fei, X. Du, and B. Wu, "A generalized half-wave symmetry SHE-PWM formulation for multilevel voltage inverters," *IEEE Transactions on Industrial Electronics*, vol. 57, DOI 10.1109/TIE.2009.2037647, no. 9, pp. 3030–3038, Sep. 2010.

[55] M. S. A. Dahidah and V. G. Agelidis, "Non-symmetrical selective harmonic elimination PWM techniques: The unipolar waveform," *IEEE Power Electronics Specialists Conference*, DOI 10.1109/PESC.2007.4342290, Jun. 2007.

[56] M. S. A. Dahidah, V. G. Agelidis, and M. V. Rao, "On abolishing symmetry requirements in the formulation of a five-level selective harmonic elimination pulse-width modulation technique," *IEEE Transactions on Power Electronics*, vol. 21, DOI 10.1109/TPEL.2006.883547, no. 6, pp. 1833–1837, Nov. 2006.

[57] J. Meili, S. Ponnaluri, L. Serpa, P. K. Steimer, and J. W. Kolar, "Optimized pulse patterns for the 5-level ANPC converter for high speed high power applications," *IECON - Annual Conference on IEEE Industrial Electronics*, DOI 10.1109/IECON.2006.347555, Nov. 2006.

[58] Y. Zhang, Z. Zhao, and J. Zhu, "A hybrid PWM applied to high-power three-level inverter-fed induction-motor drives," *IEEE Transactions on Industrial Electronics*, vol. 58, DOI 10.1109/TIE.2010.2090836, no. 8, pp. 3409–3420, Aug. 2011.

[59] Y. Zhang, D. Xu, C. Yan, and S. Zou, "Hybrid PWM scheme for the grid inverter," *IEEE Journal of Emerging and Selected Topics in Power Electronics*, vol. 3, DOI 10.1109/JESTPE.2015.2451159, no. 4, pp. 1151–1159, Dec. 2015.

[60] J. Holtz and B. Beyer, "Fast current trajectory tracking control based on synchronous optimal pulsewidth modulation," *IEEE Transactions on Industry Applications*, vol. 31, DOI 10.1109/28.464526, no. 5, pp. 1110–1120, Sep.-Oct. 1995.

[61] A. Tripathi and G. Narayanan, "Optimal pulse width modulation of voltage-source inverter fed motor drives with relaxation of quarter wave symmetry condition," *International Conference on Electronics, Computing and Communication Technologies (CONECCT)*, DOI 10.1109/CONECCT.2014.6740342, pp. 1–6, Jan. 2014.

[62] A. Tripathi and G. Narayanan, "High-performance off-line pulse width modulation without quarter wave symmetry for voltage-source inverter," *International Conference on Advances in Electronics Computers and Communications (ICAECC)*, DOI 10.1109/ICAECC.2014.7002464, pp. 1–6, Oct. 2014.

[63] F. C. Zach, R. Martinez, S. Keplinger, and A. Seiser, "Dynamically optimal switching patterns for PWM inverter drives (for minimization of the torque and speed ripples)," *IEEE Transactions on Industry Applications*, vol. IA-21, DOI 10.1109/TIA.1985.349568, no. 4, pp. 975–986, Jul. 1985.

[64] A. Sayyah, M. Aflaki, and A. Rezazadeh, "Optimization of total harmonic current distortion and torque pulsation reduction in high-power induction motors using genetic algorithms," *Journal of Zhejiang University - SCIENCE A: Applied Physics and Engineering*, DOI 10.1631/jzus.A0820055, pp. 1741–1752, Dec. 2008.

[65] A. Tripathi and G. Narayanan, "Investigations on optimal pulse width modulation to minimize total harmonic distortion in the line current," *IEEE Transactions on Industry Applications*, vol. 53, DOI 10.1109/TIA.2016.2614630, no. 1, pp. 212–221, Jan.-Feb. 2017.

[66] A. Birda, J. Reuss, and C. Hackl, "Synchronous optimal pulse-width modulation with differently modulated waveform symmetry properties for feeding synchronous motor with high magnetic anisotropy," *19th European Conference on Power Electronics and Applications (EPE'17 ECCE Europe)*, DOI 10.23919/EPE17ECCEEurope.2017.8098963, Sep. 2017.

[67] J. Holtz and B. Beyer, "The trajectory tracking approach-a new method for minimum distortion PWM in dynamic high-power drives," *IEEE Transactions on Industry Applications*, vol. 30, DOI 10.1109/28.297922, no. 4, pp. 1048–1057, Jul.-Aug. 1994.

[68] N. Oikonomou and J. Holtz, "Closed-loop control of medium-voltage drives operated with synchronous optimal pulsewidth modulation," *IEEE Transactions on Industry Applications*, vol. 44, DOI 10.1109/TIA.2007.912735, no. 1, pp. 115–123, Jan. 2008.

[69] J. Holtz and N. Oikonomou, "Estimation of the fundamental current in low switching frequency high-dynamic medium voltage drives," *IEEE Industry Applications Annual Meeting*, DOI 10.1109/07IAS.2007.154, Sep. 2007.

[70] J. Holtz and N. Oikonomou, "Synchronous optimal pulsewidth modulation and stator flux trajectory control for medium-voltage drives," *IEEE Transactions on Industry Applications*, vol. 43, DOI 10.1109/TIA.2006.889893, no. 2, pp. 600–608, Mar. 2007.

[71] J. Holtz and N. Oikonomou, "Fast dynamic control of medium voltage drives operating at very low switching frequency - an overview," *IEEE Transactions on Industrial Electronics*, vol. 55, DOI 10.1109/TIE.2007.908540, no. 3, pp. 1005–1013, Mar. 2008.

[72] T. Geyer, N. Oikonomou, G. Papafotiou, and F. Kieferndorf, "Model predictive pulse pattern control," *IEEE Transactions on Industry Applications*, vol. 48, DOI 10.1109/TIA.2011.2181289, no. 2, pp. 663–676, Mar.-Apr. 2012.

[73] T. Geyer and N. Oikonomou, "Model predictive pulse pattern control with very fast transient responses," *IEEE Energy Conversion Congress and Exposition (ECCE)*, DOI 10.1109/ECCE.2014.6954157, pp. 5518–5524, Sept. 2014.

[74] A. K. Rathore, J. Holtz, and T. Boller, "Synchronous optimal pulsewidth modulation for low-switching-frequency control of medium-voltage multilevel inverters," *IEEE Transactions on Industrial Electronics*, vol. 57, DOI 10.1109/TIE.2010.2047824, no. 7, pp. 2374–2381, Jul. 2010.

[75] A. Edpuganti and A. K. Rathore, "Optimal low-switching frequency pulsewidth modulation of medium voltage seven-level cascade-5/3h inverter," *IEEE Transactions on Power Electronics*, vol. 30, DOI 10.1109/TPEL.2014.2313552, no. 1, pp. 496–503, Jan. 2015.

[76] A. K. Rathore, J. Holtz, and T. Boller, "Generalized optimal pulsewidth modulation of multilevel inverters for low-switching-frequency control of medium-voltage high-power industrial ac drives," *IEEE Transactions on Industrial Electronics*, vol. 60, DOI 10.1109/TIE.2012.2217717, no. 10, pp. 4215–4224, Oct. 2013.

[77] A. K. Rathore, J. Holtz, and T. Boller, "Optimal pulsewidth modulation of multilevel inverters for low switching frequency control of medium voltage high power industrial ac drives," *2010 IEEE Energy Conversion Congress and Exposition*, DOI 10.1109/ECCE.2010.5618413, Sep. 2010.

[78] A. Edpuganti and A. K. Rathore, "Fundamental switching frequency optimal pulsewidth modulation of medium-voltage nine-level inverter," *IEEE Transactions on Industrial Electronics*, vol. 62, DOI 10.1109/TIE.2014.2379583, no. 7, pp. 4096–4104, Jul. 2015.

[79] A. Edpuganti and A. K. Rathore, "Optimal low switching frequency pulsewidth modulation of nine-level cascade inverter," *IEEE Transactions on Power Electronics*, vol. 30, DOI 10.1109/TPEL.2014.2298239, no. 1, pp. 482–495, Jan. 2015.

[80] A. Edpuganti and A. K. Rathore, "Fundamental switching frequency optimal pulsewidth modulation of medium-voltage cascaded seven-level inverter," *IEEE Transactions on Industry Applications*, vol. 51, DOI 10.1109/TIA.2015.2394485, no. 4, pp. 3485–3492, Jul.-Aug. 2015.

[81] L. Sobrayen, B. D. Reddy, M. Chai, A. K. Rathore, S. K. Panda, W. Die, and C. Xiaoqing, "Synchronous optimal pulsewidth modulation for marine electric propulsion drives," *IEEE 8th International Power Electronics and Motion Control Conference (IPEMC-ECCE Asia)*, DOI 10.1109/IPEMC.2016.7512748, May 2016.

[82] A. Edpuganti and A. K. Rathore, "Optimal pulsewidth modulation of medium-voltage modular multilevel converter," *IEEE Transactions on Industry Applications*, vol. 52, DOI 10.1109/TIA.2016.2536585, no. 4, pp. 3435–3442, Jul.-Aug. 2016.

[83] D. G. Holmes and T. A. Lipo, *Pulse Width Modulation for Power Converters: Principles and Practice*. John Wiley and Sons, 2003.

[84] A. Edpuganti and A. K. Rathore, "New optimal pulsewidth modulation for single dc-link dual-inverter fed open-end stator winding induction motor drive," *IEEE Transactions on Power Electronics*, vol. 30, DOI 10.1109/TPEL.2014.2353415, no. 8, pp. 4386–4393, Aug. 2015.

[85] J. A. Pontt, J. R. Rodriguez, A. Liendo, P. Newman, J. Holtz, and J. M. S. Martin, "Network-friendly low-switching-frequency multipulse high-power three-level PWM rectifier," *IEEE Transactions on Industrial Electronics*, vol. 56, DOI 10.1109/TIE.2008.2007998, no. 4, pp. 1254–1262, Apr. 2009.

[86] I. Takahashi and H. Mochikawa, "A new control of PWM inverter waveform for minimum loss operation of an induction motor drive," *IEEE Transactions on Industry Applications*, vol. IA-21, DOI 10.1109/TIA.1985.349713, no. 3, pp. 580–587, May 1985.

[87] A. Birth, T. Geyer, and H. du Toit Mouton, "Symmetry relaxation of three-level optimal pulse patterns for lower harmonic distortion," *21th European Conference on Power Electronics and Applications (EPE'19 ECCE Europe)*, DOI 10.23919/EPE.2019.8915078, Sept. 2019.

[88] A. Birth, T. Geyer, H. du Toit Mouton, and M. Dorfling, "Generalized three-level optimal pulse patterns with lower harmonic distortion," *IEEE Transactions on Power Electronics*, vol. 35, DOI 10.1109/TPEL.2019.2953819, no. 6, pp. 5741–5752, Jun. 2020.

[89] N. Oikonomou and J. Holtz, "Stator flux trajectory tracking control for high-performance drives," *Conference Record of the 2006 IEEE Industry Applications Conference Forty-First IAS Annual Meeting*, DOI 10.1109/IAS.2006.256694, pp. 1268–1275, Oct. 2006.

[90] A. Birda, J. Reuss, and C. Hackl, "Synchronous optimal PWM for synchronous machines with highly operating point dependent magnetic anisotropy," *IEEE Transactions on Industrial Electronics*, DOI 10.1109/TIE.2020.2984460, Apr. 2020.

[91] C. Grabher, "Optimized pulse patterns to minimize the current harmonic content in the dc-link of a two-level VSI," *Technical University of Munich (TUM)*, Sept. 2018.

[92] A. Birda, C. Grabher, C. Hackl, and J. Reuss, "Dc-link capacitor and inverter current ripples in anisotropic synchronous motor drives produced by synchronous optimal PWM," *IEEE Transactions on Industrial Electronics*, Manuscript submitted for publication.

[93] A. Birda and J. Reuss, "Strommessverfahren für synchrones Steuerverfahren mit geringer Modulationsfrequenz," Patent application EP18206341.2, submitted to European Patent Office on 14.11.2018.

[94] A. Birda, J. Reuss, and C. M. Hackl, "Simple fundamental current estimation and smooth transition between synchronous optimal PWM and asynchronous SVM," *IEEE Transactions on Industrial Electronics*, vol. 67, DOI 10.1109/TIE.2019.2938490, no. 8, pp. 6354–6364, Sept. 2019.

[95] L. Papula, *Mathematische Formelsammlung für Ingenieure und Naturwissenschaftler*. Springer Verlag, 2014.

[96] MathWorks, "Four-quadrant inverse tangent - MATLAB atan2." [Online]. Available: https://de.mathworks.com/help/matlab/ref/atan2.html

[97] E. Brigham, *The Fast Fourier Transform and its applications*. Prentice Hall, 1974.

[98] E. S. K. Leon, O. Chua, and C. A. Desoer, *Linear and nonlinear Circuits*. McGraw-Hill Book Company, 1987.

[99] C. M. Hackl, *Non-identifier Based Adaptive Control in Mechatronics: Theory and Application*. Springer International Publishing, 2017.

[100] E. Schmidt, "Synchronous reluctance machines with high-anisotropy rotors - comparison of their operational characteristics," *Australasian Universities Power Engineering Conference (AUPEC)*, DOI 10.1109/AUPEC.2014.6966496, pp. 1–6, Dec. 2014.

[101] S. L. Kellner and B. Piepenbreier, "General PMSM d,q-model using optimized interpolated absolute and differential inductance surfaces," *IEEE International Electric Machines & Drives Conference (IEMDC)*, DOI 10.1109/IEMDC.2011.5994848, Aug. 2011.

[102] M. Gasperi, "Life prediction modeling of bus capacitors in ac variable-frequency drives," *IEEE Transactions on Industry Applications*, vol. 41, DOI 10.1109/TIA.2005.858258, no. 6, pp. 1430–1435, Nov.-Dec. 2005.

[103] K. Hasegawa, I. Omura, and S. ichi Nishizawa, "Design and analysis of a new evaluation circuit for capacitors used in a high-power three-phase inverter," *IEEE Transactions on Industrial Electronics*, vol. 63, DOI 10.1109/TIE.2015.2511097, no. 5, pp. 2679–2687, May 2016.

[104] J. Kolar and S. Round, "Analytical calculation of the RMS current stress on the dc-link capacitor of voltage-PWM converter systems," *IEE Proceedings - Electric Power Applications*, vol. 153, DOI 10.1049/ip-epa:20050458, no. 4, pp. 535–543, Jul. 2006.

[105] P. Dahono, Y. Sato, and T. Kataoka, "Analysis and minimization of ripple components of input current and voltage of PWM inverters," *IEEE Transactions on Industry Applications*, vol. 32, DOI 10.1109/28.511653, no. 4, pp. 945–950, Jul.-Aug. 1996.

[106] F. Renken, "Analytic calculation of the dc-link capacitor current for pulsed three-phase inverters," *International power electronics and motion control conference (EPE-PEMC)*, pp. 229–237, 2004.

[107] A. Cross, P. Evans, and A. Forsyth, "Dc link current in PWM inverters with unbalanced and nonlinear loads," *IEE Proceedings - Electric Power Applications*, vol. 146, DOI 10.1049/ip-epa:19990528, no. 6, pp. 620–626, Nov. 1999.

[108] B. P. McGrath and D. G. Holmes, "A general analytical method for calculating inverter dc-link current harmonics," *IEEE Transactions on Industry Applications*, vol. 45, DOI 10.1109/TIA.2009.2027556, no. 5, pp. 1851–1859, Sep.-Oct. 2009.

[109] M. H. Bierhoff and F. W. Fuchs, "Dc-link harmonics of three-phase voltage-source converters influenced by the pulsewidth-modulation strategy - an analysis," *IEEE Transactions on Industrial Electronics*, vol. 55, DOI 10.1109/TIE.2008.921203, no. 5, pp. 2085–2092, May 2008.

[110] J. Hobraiche, J. Vilain, and C. Plasse, "Offline optimized pulse pattern with a view to reducing dc-link capacitor application to a starter generator," *PESC*, DOI 10.1109/PESC.2004.1355065, Nov. 2004.

[111] S. R. Paranjothi, *Electric Circuit Analysis.* New Academic Science, 2010.

[112] MathWorks Switzerland, "Find minimum of constrained nonlinear multivariable function - MATLAB fmincon." [Online]. Available: https://ch.mathworks.com/help/optim/ug/fmincon.html

[113] H. Eldeeb, C. M. Hackl, L. Horlbeck, and J. Kullick, "A unified theory for optimal feedforward torque control of anisotropic synchronous machines," *International Journal of Control*, vol. 91, DOI 10.1080/00207179.2017.1338359, no. 10, pp. 2273–2302, Jul. 2017.

[114] Plexim GmbH, *Plecs: The simulation platform for power electronic systems.* User Manual Version 4.3, 2002-2019.

[115] Analog Devices, "Variable resolution, 10-bit to 16-bit R/D, converter with reference oscillator AD2S1210." [Online]. Available: https://www.analog.com/media/en/technical-documentation/data-sheets/AD2S1210.pdf

[116] J. Szymczak, S. O'Meara, J. S. Gealon, and C. Nelson De La Rama, "Precision resolver to digital converter measures angular position and velocity," Mar. 2014. [Online]. Available: https://www.analog.com/en/analog-dialogue/articles/precision-rtdc-measures-angular-position-and-velocity.html

Appendix A

Test bench

The experimental verification of the SOPWM scheme has been conducted using a test bench, which is equipped with a battery simulator, a two-level VSI with silicon carbide (SiC) semiconductors, an IPMSM and a real-time system. It should be noted, that a VSI with IGBT semiconductor devices, conventionally used in electric vehicles, was not available for use in this thesis. Nevertheless, the contributions of this thesis can still be experimentally validated with the present test bench.

(a) *Two-level VSI.*

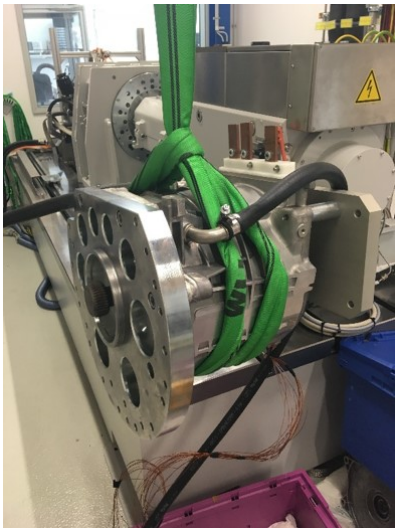

(b) *IPMSM.*

Figure A.1: *Test bench.*

The battery simulator produces a dc voltage u_{bat}, which equals to 400 V in all experimental measurements presented in this thesis. The impedance of the battery simulator and the cable connecting the battery simulator with the VSI can be modelled as a $R_{\mathrm{bat}}L_{\mathrm{bat}}$-element, where $R_{\mathrm{bat}} = 10\,\mathrm{m\Omega}$ and $L_{\mathrm{bat}} = 7.3\,\mu\mathrm{H}$.

The two-level VSI has a rated output current, voltage and power of 379 A, 550 V and 361 kW, respectively (see Table A.1). Four parallel connected capacitors are used in the dc-link with a total capacitance of $C = 320\,\mu\mathrm{F}$ and an equivalent series resistance (ESR) of $R_{\mathrm{ESR}} = 0.4\,\mathrm{m\Omega}$ (see Table A.2).

A six-pole pairs IPMSM is used as a load. Its maximum power and torque are 125 kW and 250 Nm, respectively, while its rated power at 6 000 rpm is 72 kW. The motor can be operated until a maximum speed of 12 000 rpm. The stator resistance R_{s} is approximately equal to 5 mΩ at

20°C. The stator self-inductances as well as the PM flux linkage vary depending on the machine currents in the *dq*-frame (see Table A.3).

The electrical drive system is controlled with a dSpace real-time system. The FOC system is implemented on the DS1007 processor board of the dSpace AutoBox, whereas the modulator for the generation of the gate signals is implemented on the DS5203 field-programmable gate array (FPGA) board. The MSO5204B oscilloscope of Tektronix and GEN7tA transient recorder and data acquisition system of HBM are used for capturing the measured signals with high precision (see Table A.4).

Table A.1: *VSI parameters.*

Parameter	**Value**
rated power	361 kW
rated current	379 A RMS
rated voltage	550 V

Table A.2: *Dc-link capacitor parameters.*

Parameter	**Value**
capacitance C	4x80=320 µF
R_{ESR}	1.6/4=0.4 mΩ
rated voltage	1 200 V

Table A.3: *IPMSM parameters.*

Parameter	**Value**
maximum torque	250 Nm
maximum power	125 kW
rated power	72 kW at 6000 rpm
maximum speed	12000 rpm
pole pairs	6
stator resistance R_{s}	5 mΩ at 20°C
stator self-inductance L_{s}^{d}	42 µH – 88 µH at 20°C
stator self-inductance L_{s}^{q}	75 µH – 289 µH at 20°C
PM flux linkage ψ_{PM}	0.0277 Wb – 0.0399 Wb at 20°C

Table A.4: *Specifications of measurement equipment.*

Equipment	**Parameter**	**Value**
Tektronix MSO5204B oscilloscope	bandwidth	2 GHz
	sample rate	10 GS/s
	vertical resolution	8 bits
Tektronix TCP404XL current probe	bandwidth	2 MHz
	maximum current	500 A RMS
	minimum current	1 A RMS
HBM GEN7tA recorder	sample rate	2 MS/s
	resolution	18 bits

Appendix B

Optimization results

B.1 Optimization results for a pulse number of 5

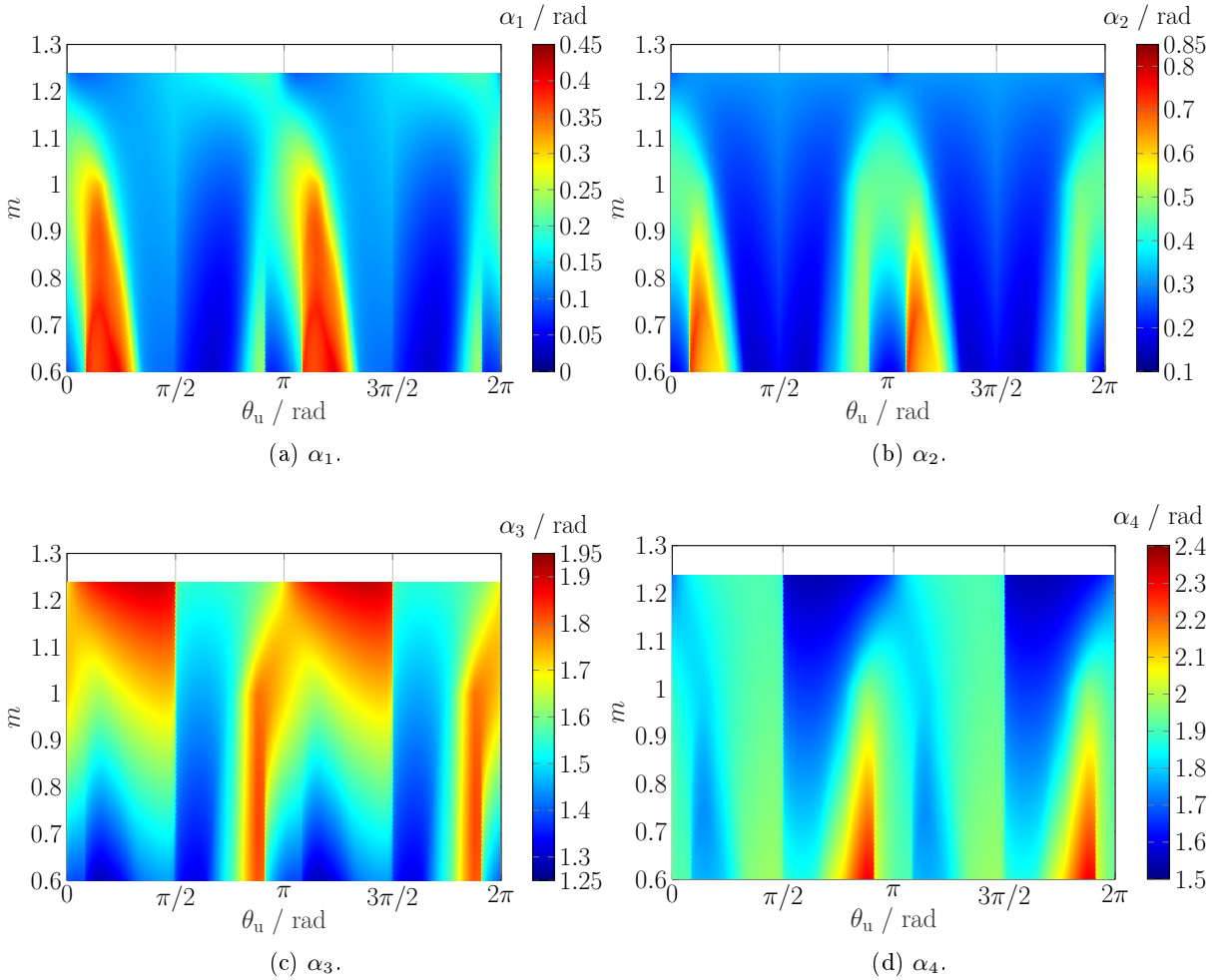

(a) α_1. (b) α_2.

(c) α_3. (d) α_4.

Figure B.1: *Optimized inverter switching angles for* $q = 5$ *and* $\lambda = 2.5$.

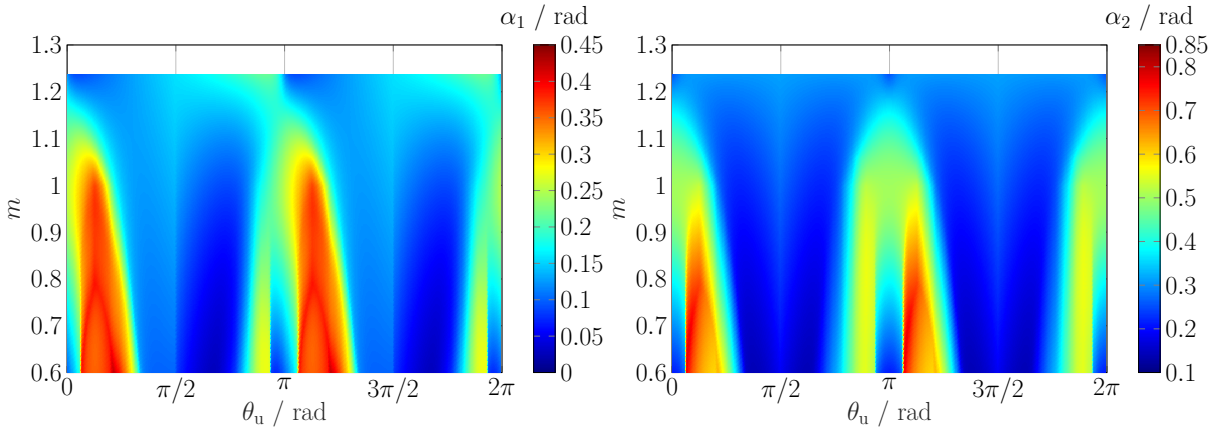

(a) α_1. (b) α_2.

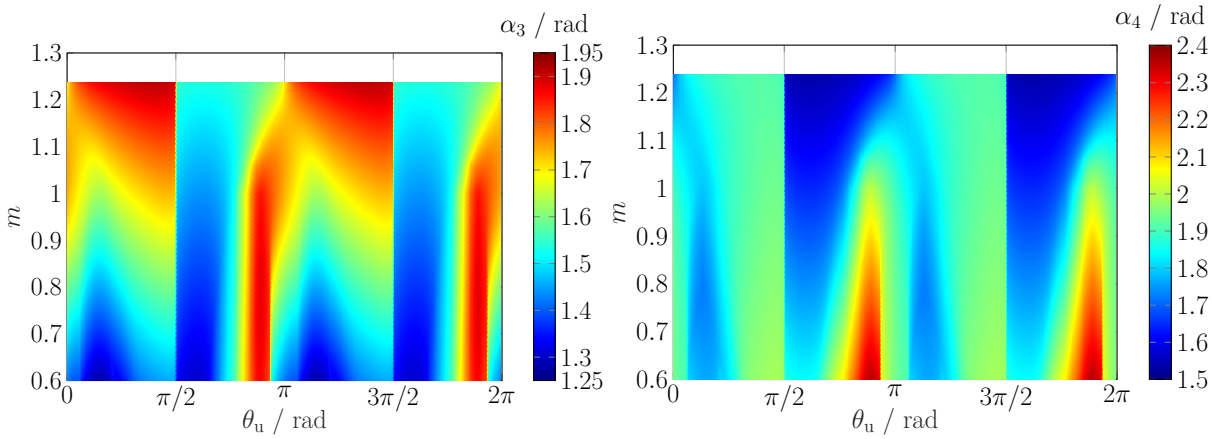

(c) α_3. (d) α_4.

Figure B.2: *Optimized inverter switching angles for* $q = 5$ *and* $\lambda = 2.85$.

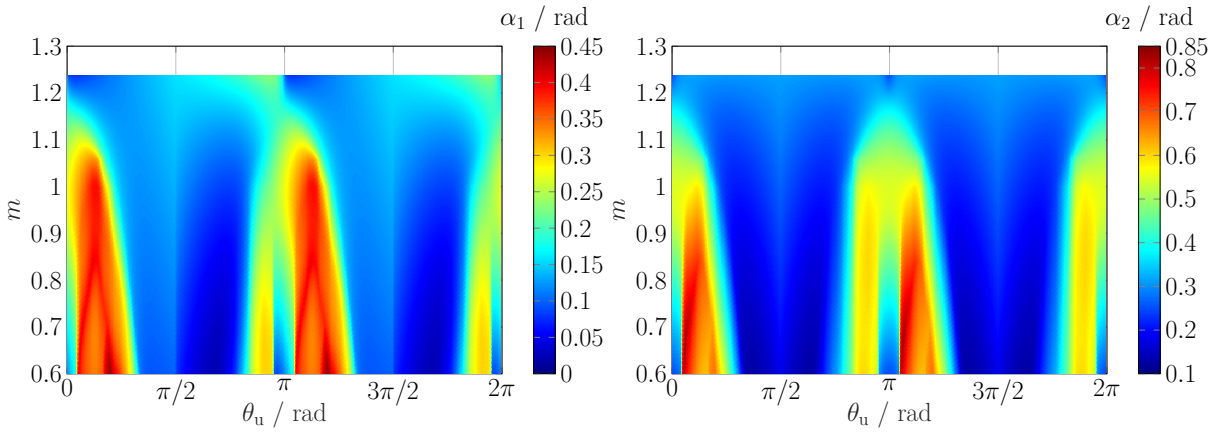

(a) α_1. (b) α_2.

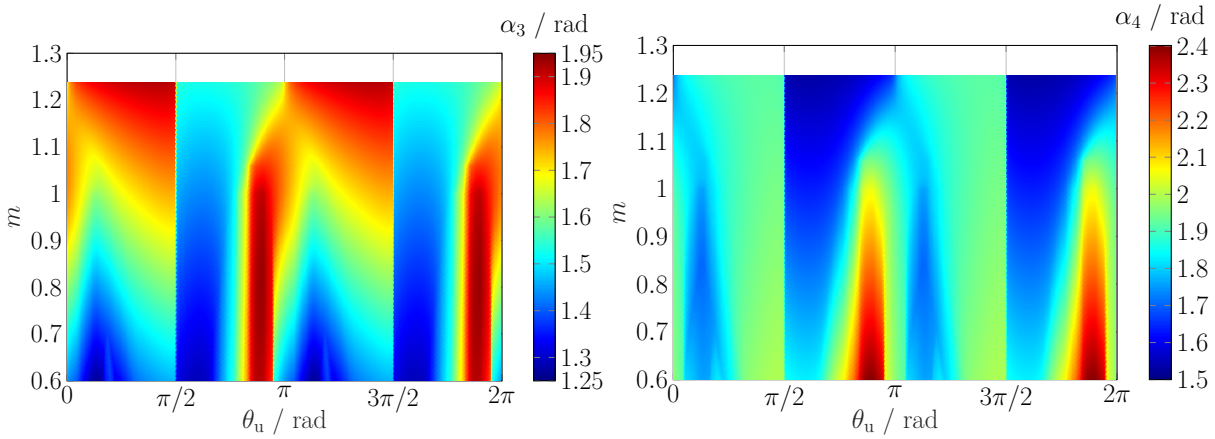

(c) α_3. (d) α_4.

Figure B.3: *Optimized inverter switching angles for* $q = 5$ *and* $\lambda = 3.2$.

B.2 Optimization results for a pulse number of 9

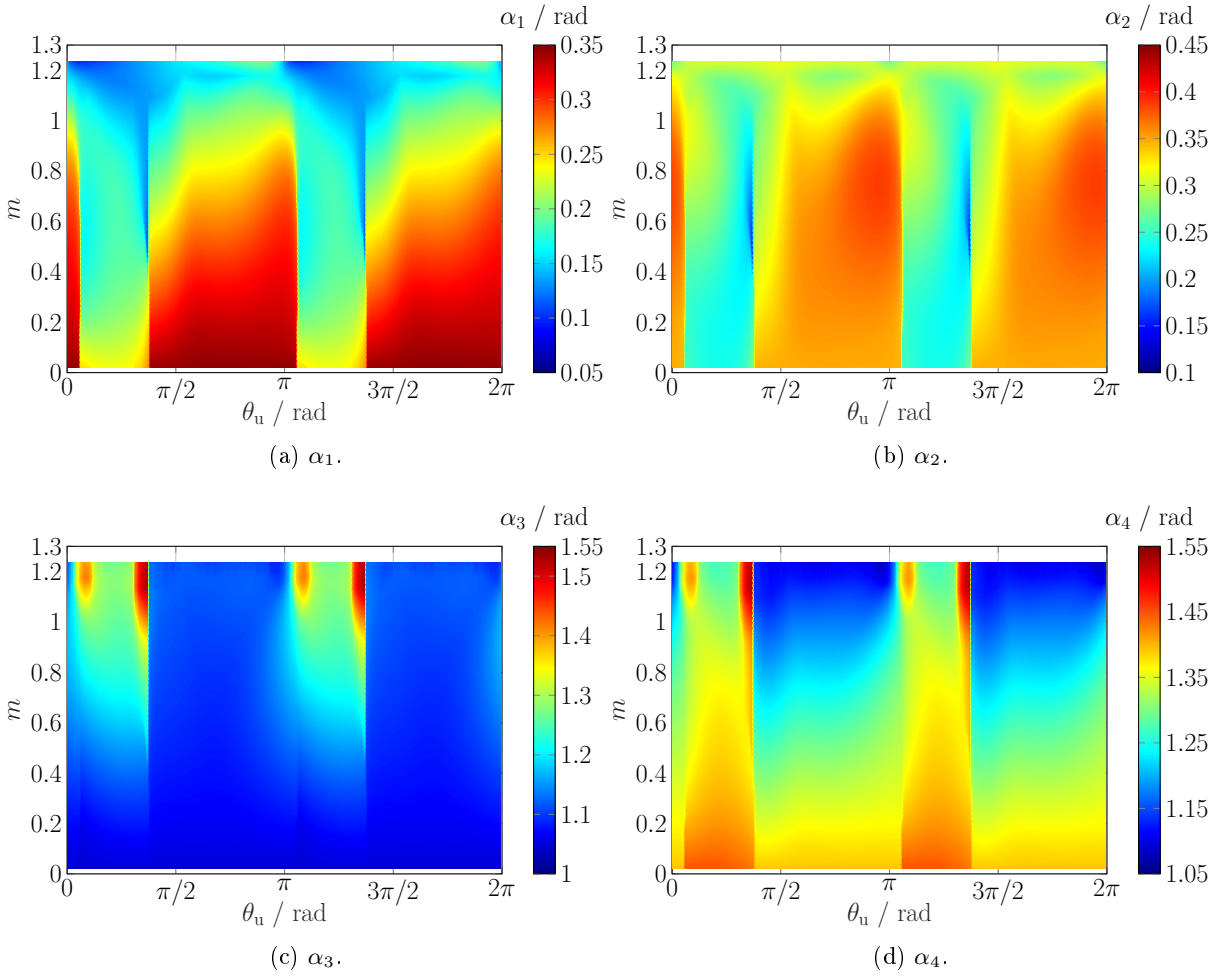

(a) α_1. (b) α_2.

(c) α_3. (d) α_4.

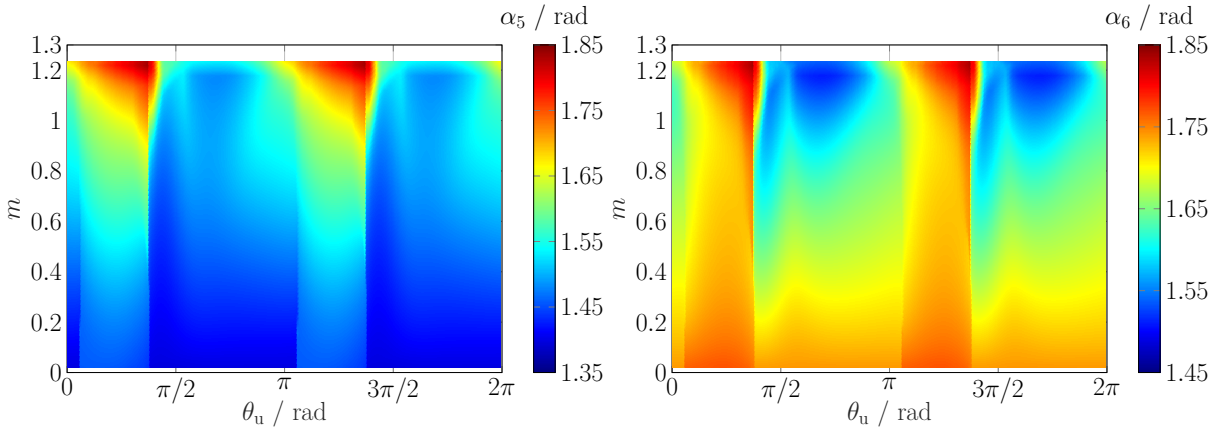

(e) α_5. (f) α_6.

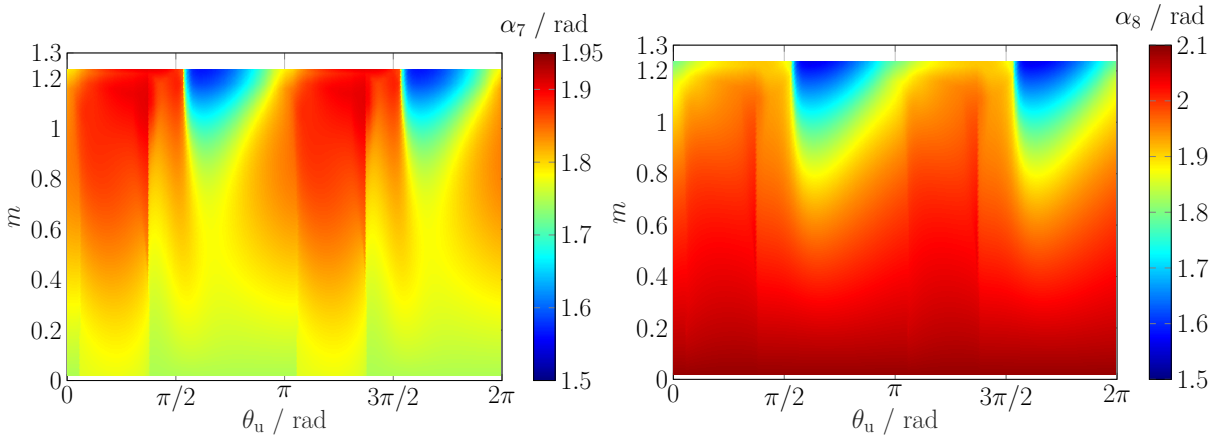

(g) α_7. (h) α_8.

Figure B.4: *Optimized inverter switching angles for* $q = 9$ *and* $\lambda = 2.5$.

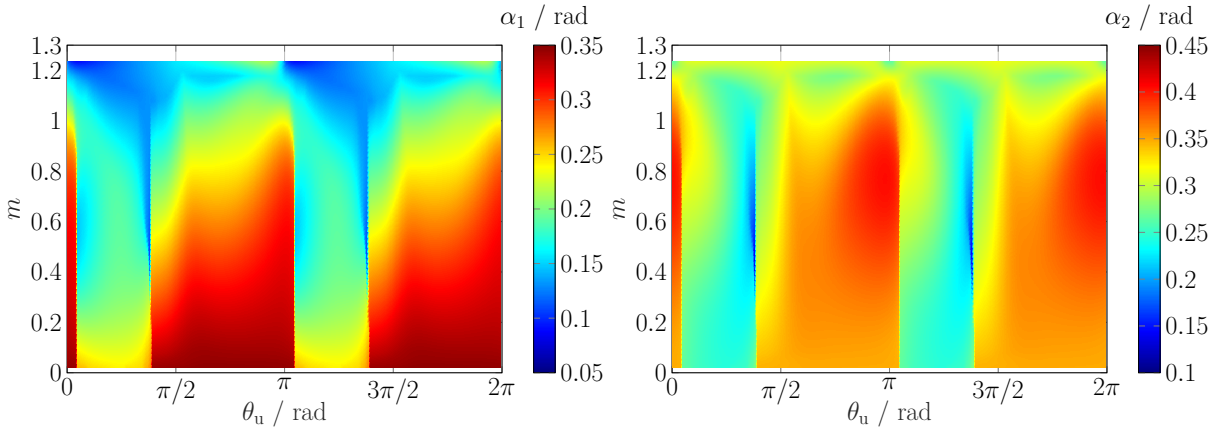

(a) α_1. (b) α_2.

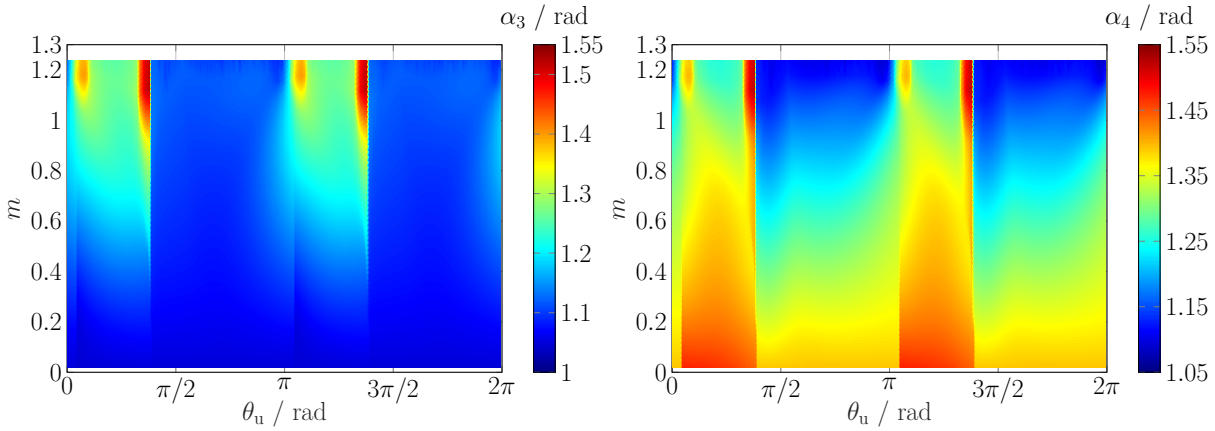

(c) α_3. (d) α_4.

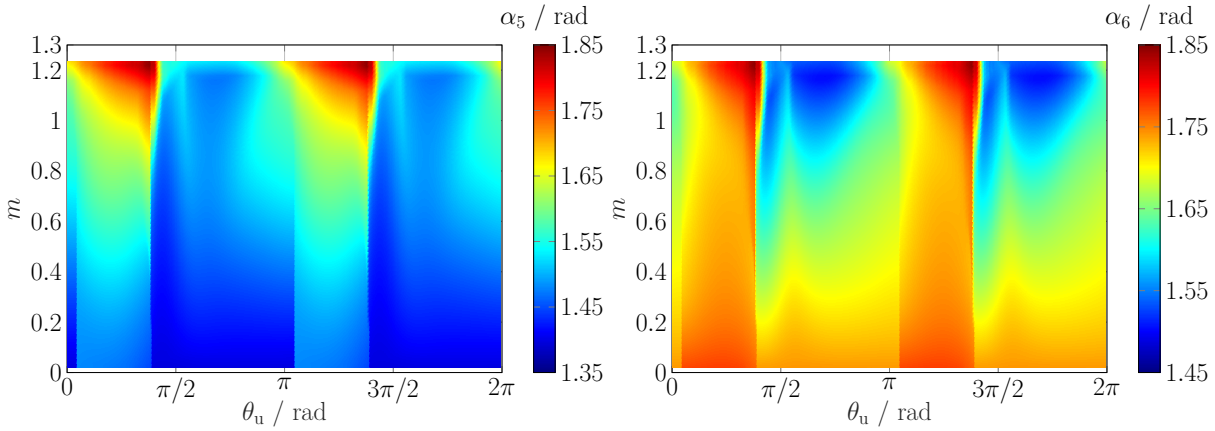

(e) α_5. (f) α_6.

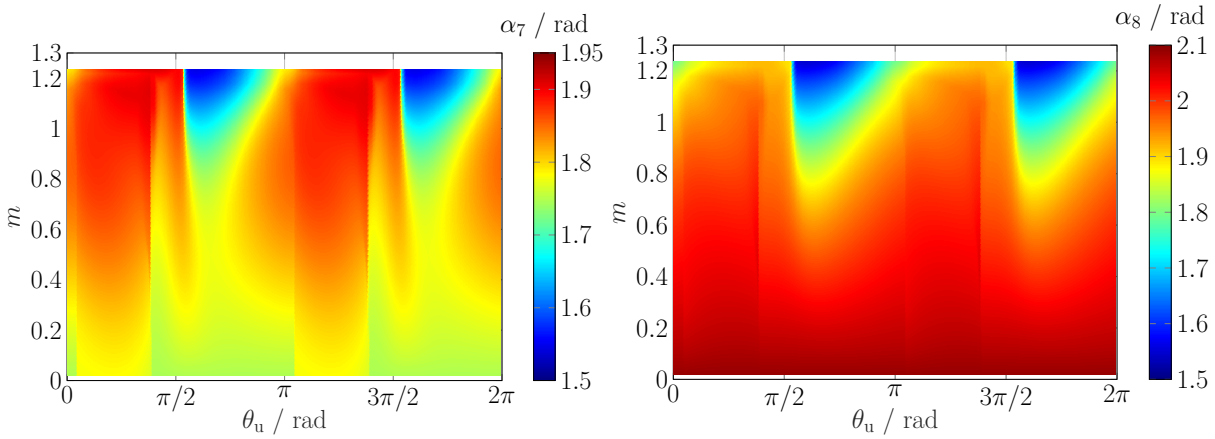

(g) α_7. (h) α_8.

Figure B.5: *Optimized inverter switching angles for* $q = 9$ *and* $\lambda = 2.85$.

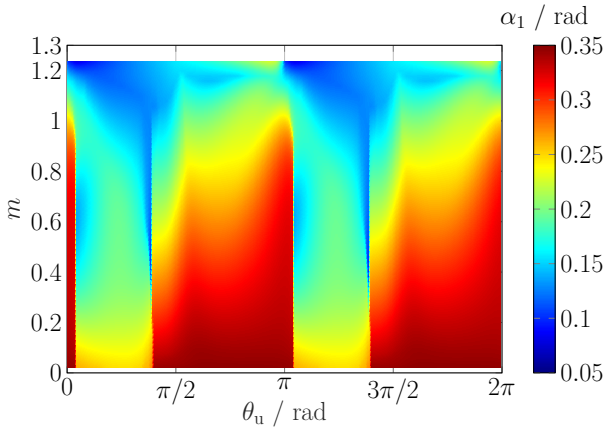

(a) α_1.

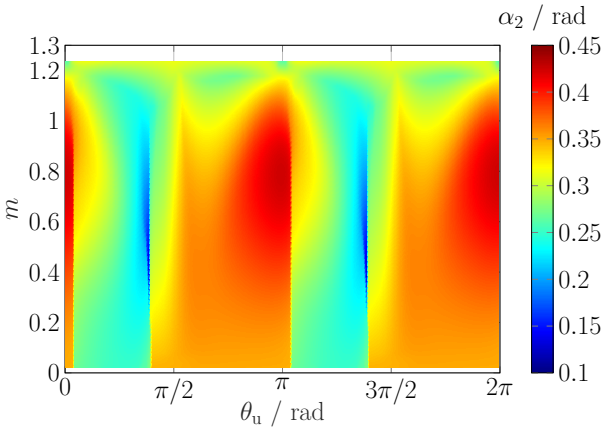

(b) α_2.

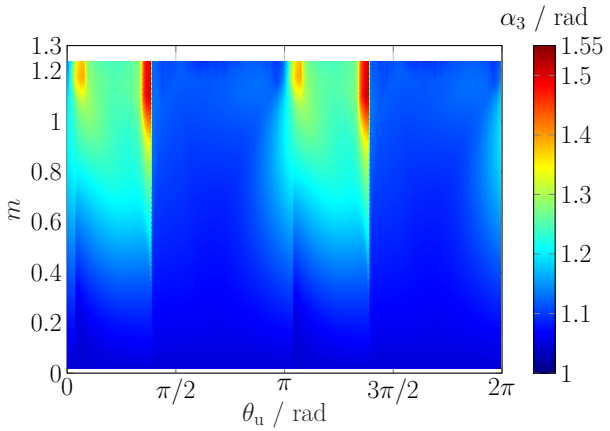

(c) α_3.

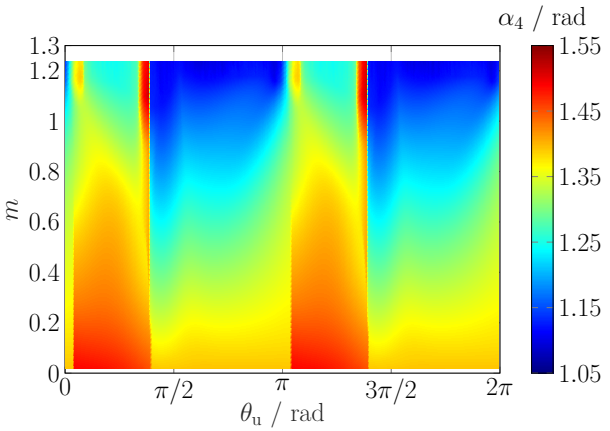

(d) α_4.

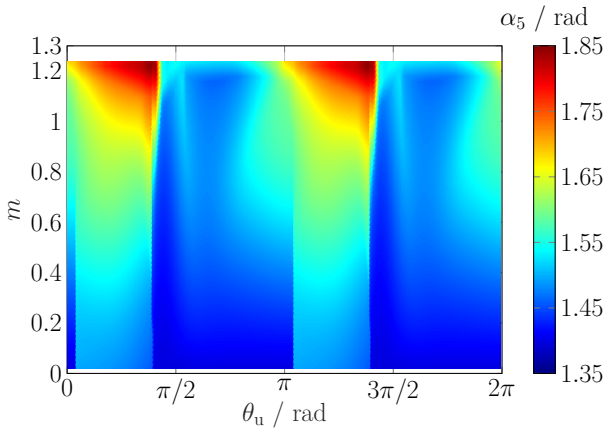

(e) α_5.

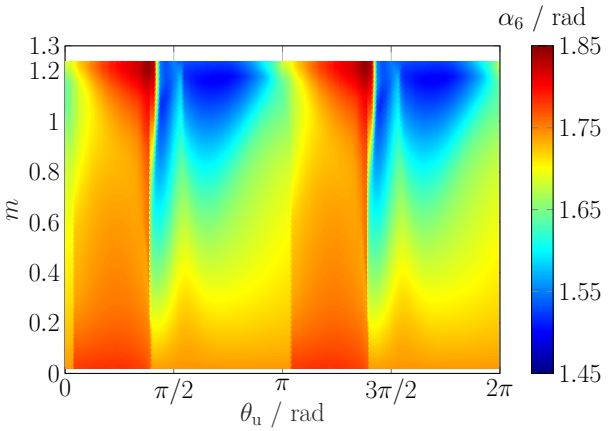

(f) α_6.

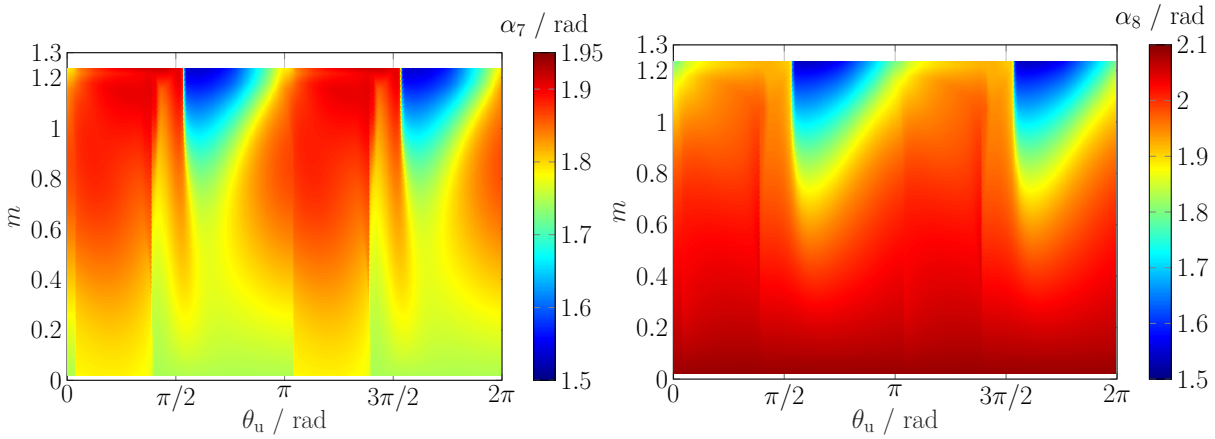

(g) α_7.

(h) α_8.

Figure B.6: *Optimized inverter switching angles for* $q = 9$ *and* $\lambda = 3.2$.